Time-Resolved Photoelectron Imaging of Model Biological Chromophores

by

James O. F. Thompson

Submitted for the degree of Doctor of Philosophy

Heriot-Watt University

School of Engineering & Physical Sciences,
Institute of Photonics & Quantum Sciences

4th May 2015

Abstract

Investigating the underlying forces that have a key role in light-matter interactions is crucial to understanding many fundamental processes that occur in nature. This thesis describes a series of experiments investigating model biological chromophores, providing an insight into the photochemistry of "ultraviolet self-protection" schemes, invoked in many molecules involved in the protection of flora and fauna from the potentially damaging effects of excess ultraviolet radiation. These experiments are achieved through the application of time-resolved photoelectron imaging (TR-PEI) supported by high-level computational chemistry calculations. This thesis will set out both the motivation for the work, consisting of a comprehensive literature review of the subject, as well as an in-depth description of the optical set-up, laser system and spectrometer, as well as non-trivial data handling approaches involved in performing the experiments. This will lead on to work concerning the model chromophore aniline (and several aniline derived systems), guaiacol and finally a series of tertiary aliphatic amines. To conclude, various potential avenues of future work are discussed, considering both the experimental methodology and possible molecules of interest building upon the work described within this thesis.

Acknowledgements

I would first like to start off by thanking my supervisor, Dr Dave Townsend, for his continuous support, encouragement and constantly challenging me to perform my best at whatever I set out to achieve. Secondly, I would like to thank Prof. Martin J. Paterson for his instruction in the arts of computational chemistry and allowing acsess to the HPC6 cluster. Next I would like to thank Dr Ruth A. Livingstone for getting me started on the long road to this point, giving me fantastic instruction in the use of the VMI spectrometer, laser systems and for writing the REPEITS program which proved to be invaluable in interpreting the experiments outlined in this thesis. I would also like to thank Liv Klein, Dr Therese Bergendahl, Dr Omair Ghafur, Dr Marco Candelaresi, Magdalena Zawadzki, Victoria Parkes and Stuart Crane for their useful discussion and contribution to the work presented in this thesis. Further thanks go to Heriot-Watt University for the doctoral training award allowing me to pursue this work by financing me personally, as well as providing support in terms of equipment and travel expenses. And finally, I would like to thank my parents, Anne and Bryan Thompson, as well as my partner Rebecca McIntyre, for their moral support and encouragement throughout my PhD and writing of this thesis.

Finally, food for thought on recruiting prospective students for a laser based PhD in Scotland

"Men and Women wanted for hazardous journey. Low wages, bitter cold, long hours of complete darkness. Safe return doubtful. Honour and recognition in event of success"

Adapted from Sir Ernest Henry Shackleton,
Newspaper advert for South pole expedition (ca ~1900)

ACADEMIC REGISTRY
Research Thesis Submission

Name*:*	JAMES OLIVER FRANK THOMPSON		
School/PGI:	School of Engineering and Physical Science		
Version: *(i.e. First, Resubmission, Final)*	FINAL	Degree Sought (Award **and** Subject area)	Doctor of Philosophy, Physics

Declaration

In accordance with the appropriate regulations I hereby submit my thesis and I declare that:

1) the thesis embodies the results of my own work and has been composed by myself
2) where appropriate, I have made acknowledgement of the work of others and have made reference to work carried out in collaboration with other persons
3) the thesis is the correct version of the thesis for submission and is the same version as any electronic versions submitted*.
4) my thesis for the award referred to, deposited in the Heriot-Watt University Library, should be made available for loan or photocopying and be available via the Institutional Repository, subject to such conditions as the Librarian may require
5) I understand that as a student of the University I am required to abide by the Regulations of the University and to conform to its discipline.

* *Please note that it is the responsibility of the candidate to ensure that the correct version of the thesis is submitted.*

Signature of Candidate*:*		Date:	

Submission

Submitted By *(name in capitals):*	
Signature of Individual Submitting:	
Date Submitted:	

For Completion in the Student Service Centre (SSC)

Received in the SSC by *(name in capitals):*			
Method of Submission *(Handed in to SSC; posted through internal/external mail):*			
*E-thesis Submitted (**mandatory for final theses)***			
Signature:		Date:	

Please note this form should bound into the submitted thesis.

Updated February 2008, November 2008, February 2009, January 2011

Papers arising from thesis work

R.A. Livingstone, J.O.F. Thompson, M. Iljina, R.J. Donaldson, B. Sussman, M.J. Paterson & D. Townsend, *Time-resolved photoelectron imaging of excited state relaxation dynamics in phenol, catechol, resorcinol and hydroquinone*, J. Chem. Phys., **137**, 18, 184304, (2012)

J.O.F. Thompson, R.A. Livingstone & D. Townsend, *Following the relaxation dynamics of photoexcited aniline in the 273-266 nm region using time-resolved photoelectron imaging*, J. Chem. Phys., **139**, 3, 034316, (2013)

S.E. Greenough, M.D. Horbury, J.O.F. Thompson, G.M. Roberts, T.N.V. Karsili, B. Marchetti, D. Townsend & V.G. Stavros., *Solvent induced conformer specific photochemistry of guaiacol*, Phys. Chem. Chem. Phys., **16**, 30, 16187-16195, (2014)

J.O.F. Thompson, L. Saalbach, S.W. Crane, M.J. Paterson & D. Townsend, *Ultraviolet relaxation dynamics of aniline, N, N-dimethylaniline and 3,5-dimethylaniline at 250 nm*, J. Chem. Phys., **142**, 11, 114309 (2015)

J.O.F. Thompson, L.B. Klein, T.I. Sølling, M.J. Paterson & D. Townsend, *Excited state interactions in simple tertiary amines: A time-resolved photoelectron imaging study*, (2015, To be submitted)

Contents:

Chapter 2 – Experimental

Chapter 3 – The photoelectron spectroscopy of aniline at the $S_2(3s/\pi\sigma^*)$ origin

Chapter 4 – Relaxation dynamics of aniline, *N,N*-dimethylaniline & 3,5-dimethylaniline

Chapter 5 – The photoelectron spectroscopy of guaiacol

Chapter 1 – Introduction

1.1 – Overview of chemical dynamics

1.1.1 – Understanding chemical processes

The field of ultrafast chemical dynamics is that of the "*real time*" exploration, and understanding, of chemical processes that occur on picosecond and femtosecond timescales. Over the past few decades, this emerging field has developed a more subtle and complex understanding of the physical pathways through which photochemical reactions take their course. Through this understanding it is possible to predict chemical interactions more successfully and design more sophisticated processes that utilise the fundamental links between chemical structure and chemical dynamics to achieve ideal chemical functionality.[1, 2] Chemical dynamics is, however, not a new concept. Scientists have, for many years, been interested in the study of the timescales of chemical processes and using this information to design more efficient reactions. Put simply, chemical dynamics is the study of the progress of a chemical reaction from reactant to product as illustrated in Figure 1.1. As such, chemical dynamics can be used to understand chemical reactivity of synthetic reactions that have been undertaken for many decades. However, over the last 50 years or so the focus of modern chemical dynamics has moved from the investigation of the rates of chemical reactions (as in traditional organic synthesis) to in-depth understanding of the electrical forces involved in the flow of energy from one quantum state to another through non-adiabatic coupling.[3] To illustrate this idea, we will use the Diels-Alder (DA) reaction (a chemical process familiar to all undergraduate chemistry students)[4] as an example, to illustrate some of the basic concepts behind why we would want to perform a time-resolved study.

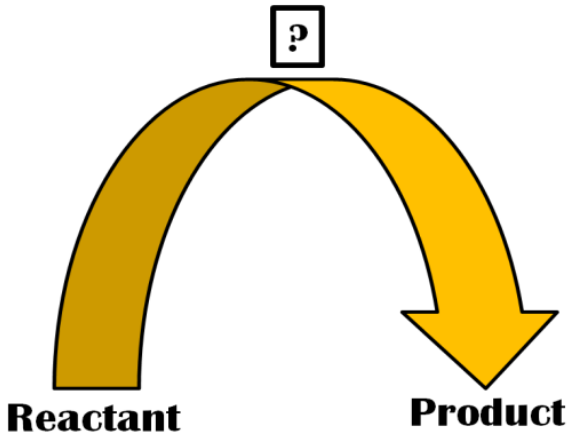

Figure 1.1 – "The arrow of chemistry"

The DA reaction is a process that forms a cyclohexene-like ring structure using a conjugated carbon double bond system and an independent carbon double bond system

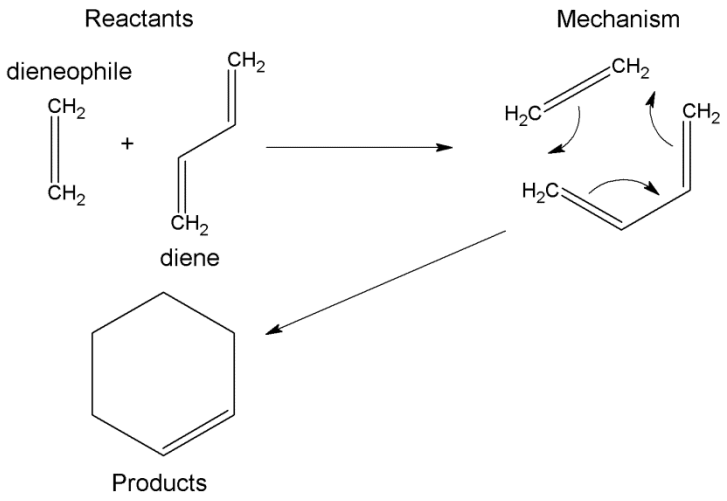

Figure 1.2 – Mechanism of the Diels-Alder reaction, adapted from Ref [5]

as the reagents, as shown in the reaction scheme in Figure 1.2. To discuss the dynamics of this reaction, we start by considering the work by Storer *et al.*,[5] who performed a theoretical study of the DA mechanism to provide new insights to how the reaction progresses. It is this mechanistic understanding of reactions that motivates time-resolved studies. Storer and co-workers discussed two possible mechanisms of how the DA reaction progressed. One of these suggested that bond formation was achieved through a stepwise mechanism involving two transition states along the reaction coordinate, whilst the other suggested a concerted mechanism in which all bond formation is done in a single step. This study compared theoretical models to experimental results and in doing so came to the conclusion that the mechanism was concerted, rather than stepwise. This insight into the reaction dynamics provided an explanation of the stereochemistry of the products of the DA reaction,[4] i.e. the successful prediction of a specific product conformer (syn or anti).

In general, time-resolved studies provide an excellent platform to investigate the dynamics of chemical reactions; however, these experiments are usually restricted to investigating single molecules as processes that involve multiple molecules are typically hard to follow using this approach. This is because it is essential that the time at which a process begins is well defined, which is difficult to establish with intermolecular interactions. However, it is possible to investigate analogous processes by using an equivalent intramolecular reaction. Returning to the previous example of the DA reaction, Zewail and co-workers[6, 7] performed time-resolved studies of retro DA reactions, as a method of investigating the mechanism at play. It was found (in agreement with Storer and co-workers)[5] that the reaction scheme was in fact concerted and not stepwise. This conclusion was based upon the timescale of the vibrational motion of the molecule with respect to the rotational motion of the system, i.e. the bond breaking and formation occurs on a sub-picosecond timescale and is therefore much

faster than rotational motion. These measurements demonstrate the understanding that can be attained by such studies. The work by Zewail and co-workers was performed through the use of an ultrafast femtosecond laser system,[6, 7] allowing the "real-time" study of energy redistribution in the molecular systems as reactions progressed. The use of a femtosecond laser system to study energy flow in molecules provides part of the motivation for the experiments performed in this thesis, and will be discussed in great detail later in this chapter. In recent years an increasing amount of work has gone into the investigation of reactions found in nature, trying to understand why nature has evolved particular processes. An overview of this particular type of reaction will be given.

1.1.2 – Photochemistry

For many years, scientists have used light as a source of activation energy for chemical reactions. One of the earliest recorded instances of a light driven process in chemistry was noted by Trommsdorf in 1834[8] in which it was found that when crystals of α-santonin were exposed to sunlight they turned yellow. Light is of great interest to scientists, not only through synthetic photochemical interactions (as discussed in this section) but also through a large variety of photochemical processes that occur in nature. One of the most famous example is that of photosynthesis which occurs in plants[9], which will be outlined in the following section. There are many reasons as to why photochemical reactions are such an attractive prospect to both organic and inorganic chemists. Because sunlight is free, reactions that are instigated by it are more cost effective and therefore desirable to many companies and manufacturers. Light based processes are also attractive as they typically provide a different chemical route to thermally controlled reactions. To this end, consider two different ring closing reactions. This returns us again to the earlier example of the Diels-Alder reaction. Figure 1.3 illustrates the two reaction pathways available in

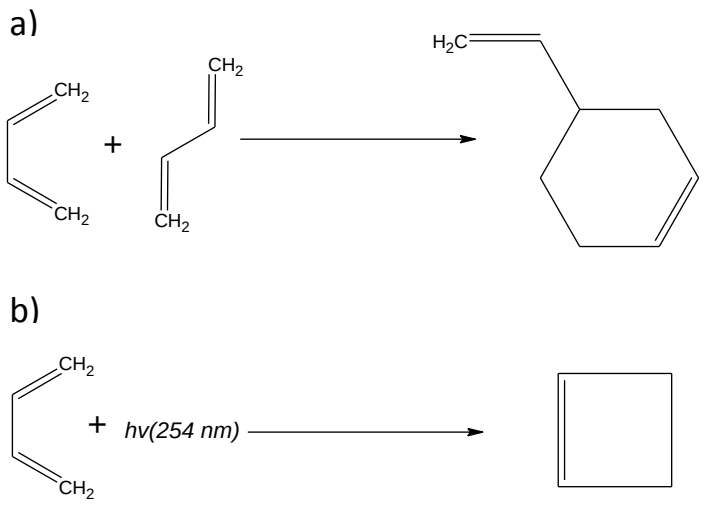

Figure 1.3 – Reaction of 1,3-butadiene showing a) the thermochemical reaction mechanism and b) the photochemical reaction mechanism. From Ref [8]

this reaction.[10] The first scheme, 1.3a, shows that when heated to around 500 – 600 K, 1,3-butadiene undergoes a Diels-Alder cycloaddition (similar to the mechanism shown in Figure 1.2) between cis and trans 1,3-butadiene. However, if irradiated in a solution of cyclohexane using 254 nm light, ring closing can be achieved instead (see Fig 1.3b). It should be noted that this produces cis-cyclobutene, and that the reaction is performed in solution to lower the excitation energy required to access the excited state necessary for the reaction to proceed. This example of two different ring closing reactions highlights the mechanistic differences between thermally driven and light driven processes.

Following from the discussion outlined above, this chapter will expand on many of the themes so far discussed, such as the use of time-resolved studies to investigate reaction dynamics of light-matter interactions involving natural molecules. Furthermore, this chapter will discuss the fundamental quantum mechanics behind these reactions and what types of mechanisms are typically observed in these systems.

1.2 – Light and nature

1.2.1 – Chromophores in nature

Light is one of the most abundant resources on Earth, and the majority of this light is provided by sun. Light is the driving force for a large number of processes that occur in nature. These processes are often initiated at a chromophore; a light absorbing site within proteins and other biological compounds. Typically, it is light in the ultraviolet or visible range that is required to initiate a photochemical reaction. Consider, for example, the process of ATP production in green plants.[9] The first step in this reaction is the absorption of a photon by photosystem II (the structure of which is shown in Figure 1.4), a large protein with multiple component parts.[11] However, the light absorbing site is a much smaller complex involving a magnesium centre attached to the main protein via a long carbon chain. This complex is known as chlorophyll a (see Figure 1.5), and can be thought of as a subunit of photosystem II. What is interesting about this example is that, depending upon plant species, there are a variety of different subunits which perform the same role, all of which are similar in structure to chlorophyll a.[12] The chromophore in these systems is the extended network of pyrrole subunits in a multi-chelating ligand. The absorption of UV light to initiate an electronic excitation within the chromophore provides the initial energy for the multiple charge transfer processes that occurs within photosystem II.[13] This raises an interesting questions relating to how and why this system evolved for this function, and what makes it such an effective design. It is this theme of efficient energy redistribution, common in many systems found in nature, which provides much of the motivation behind the work presented in this thesis.

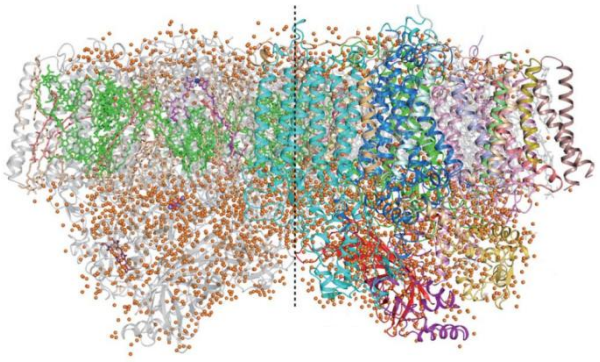

Figure 1.4 Representation of protein photosystem II, adapted from Ref. [11]

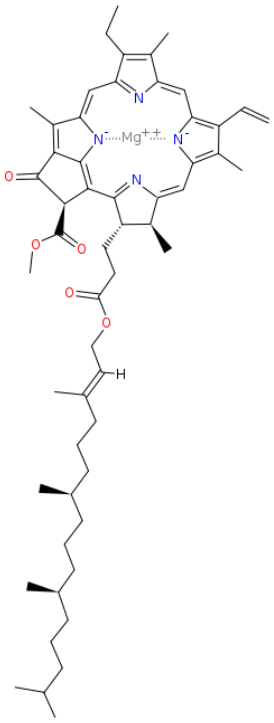

Figure 1.5 structure of chlorophyll a. Adapted from Ref [12]

1.2.2 – Photoprotection

Another example of a natural product involved in a photochemical process is skin pigment. On the surface it might seem like a simple process, in that the skin pigmentation absorbs light thus stopping it from passing into the body. However, where does this energy go? Understanding what the primary mechanistic routes are for energetic relaxation & dissipation is a complex problem. The compound in question for this example is melanin; which is the molecule responsible for the colour of skin pigmentation[14] and is also found in hair and under the iris of human eyes. In humans there are two main types of melanin, eumelanin and pheomelanin.[15] The eumelanin monomer (shown in Figure 1.6a) is comprised of three main components, two of which are indole substituents and the other a derivative of pyrrole. The structure of the monomer of pheomelanin (shown in Figure 1.6b) is more complex than that of eumelanin, with the major difference being that the chromophore components are based on benzene ring structures as opposed to indole type structures. These monomers are the building blocks of a larger system, however, contained within these small subunits are the light absorbing sites, the chromophores. In this case, the function of these compounds is not to absorb light to use as a source of energy, but deny it to other more photosensitive compounds. These molecules act as photoprotectors; they absorb the energy and then release it in a way that is non-detrimental to the surroundings. This is achieved through internal relaxation pathways called the UV "self-photo protection" mechanism.

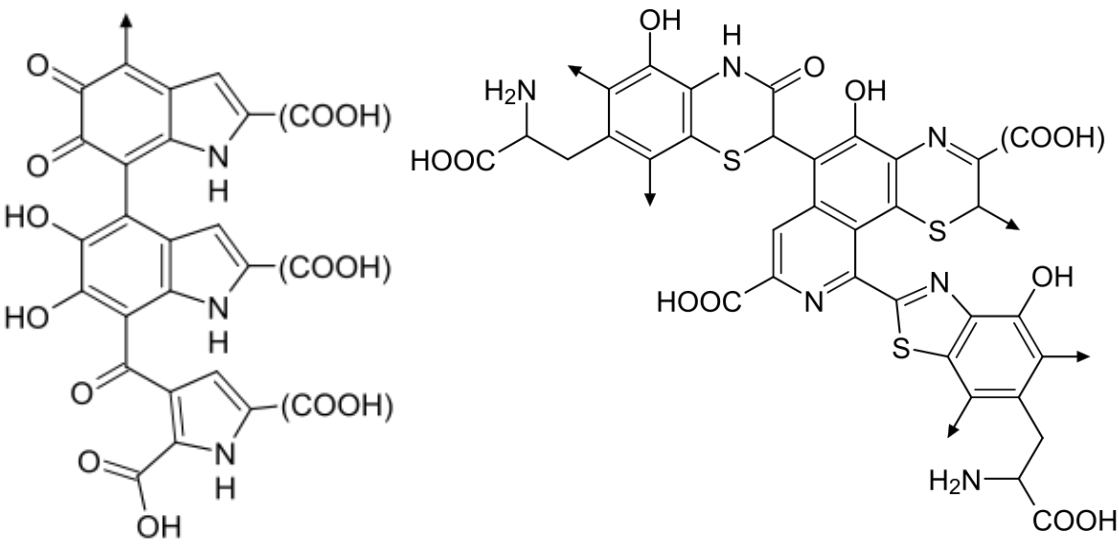

Figure 1.6 – Monomer structure of a) eumalanin and b) pheomelain. From Ref [15]

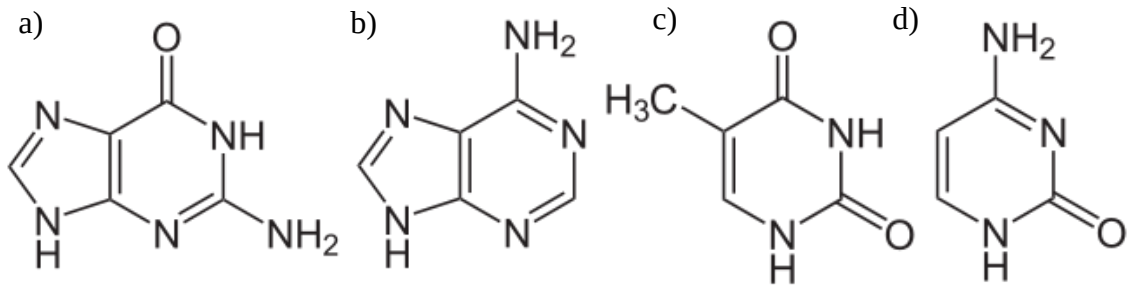

Figure 1.7 – Chemical structures of a) guanine, b) adenine, c) thymine & d) cytosine. Adapted from Ref [14]

There are other molecules in nature that are believed to be photo-resistant by design; one example is that of DNA. The structure of DNA is the famous double helix, as determined by James Watson and Francis Crick in 1953.[16] The backbone of the helix is made of a long chain sugar compound that has chelating base pairs attached internally within the helix by a phosphate group. In DNA, there are four bases; guanine, cytosine, adenine and thymine, as shown in Figure 1.7. These bases are paired up together and form the double helix structure (Figure 1.8). Guanine and adenine have similar purine based structures whilst cytosine and thymine have structures similar to that of pyrimidine. These structures can absorb light in the ultraviolet (UV) region of the electromagnetic spectrum because of their aromatic ring systems; in fact the lowest excited states of these, and similar systems, are often states associated with transitions on these chromophores. In high doses, UV radiation could cause damage to DNA and potentially lead to mutation of the base sequence during cell replication. This is often cited as a possible cause for many different ailments and diseases including various forms of cancers.[14] However, at low levels, it is suggested that DNA is able to absorb light and release the energy in a non-damaging way. This is, in part, one of the possible reasons why the structure of DNA bases may have evolved in their particular manor. Furthermore, when considering this in the context of the early development of life on the planet, this may offer some hints as to its evolution. The younger atmosphere did not contain an

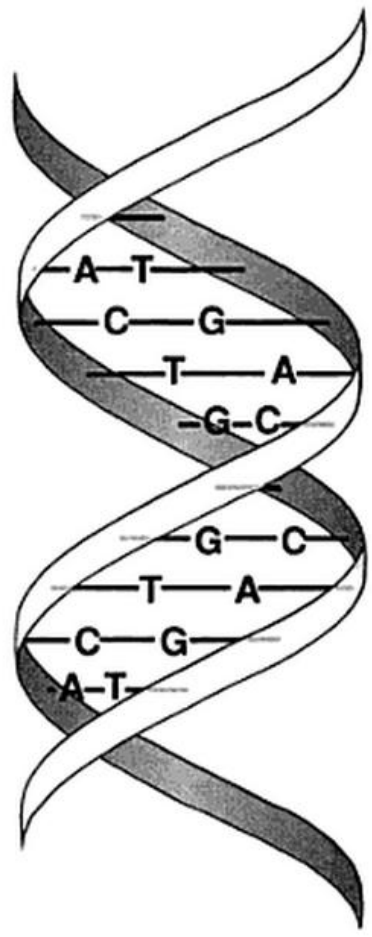

Figure 1.8 – Helical structure of DNA, adapted from Ref [16]

ozone layer to absorb UV radiation from the sun, and as such more UV light was able to irradiate the planet.[17] It is therefore proposed that early life evolved to be UV resistant and so it is not surprising that these similar structures developed in many different organisms.[14]

1.2.3 – Bottom up approach

It is clear to see from the examples discussed in the previous section that chromophores within light absorbing proteins are often a small part of the overall system. Therefore, by simplifying the system, i.e. by trimming away other parts of the protein and leaving just the chromophore, the light absorption process of the larger system can be modelled to investigate how the interaction works in the real system. This method of trying to understand a large complicated biological system by investigating its smallest components and building upwards may be thought of as a "*bottom up approach*". This is illustrated in Figure 1.09 which is adapted from a review by Roberts *et al.*[18]

To expand upon the idea of a bottom-up approach in more detail, we will now consider how this approach can be applied to understand the relaxation dynamics of the DNA base guanine. As alluded to previously, guanine is believed to have photo-resistant properties due to its structure, and as outlined below, can be modelled by using a number of simpler molecules. Figure 1.10 shows examples of these model systems and how this approach can be adopted to achieve understanding of complex molecular systems. Additionally, as we wish to perform experiments on a single molecule, uncoupled from any environmental effects (such as solvent effects), the reduction in size often increases the ease with which these systems can be experimentally investigated in the gas-phase which, from a practical point of view, also adds an attractive prospect to using these model systems. Further understanding can be attained by reducing the chemical functionality of the molecule to understand how the individual functional groups interact with the system, and which group is

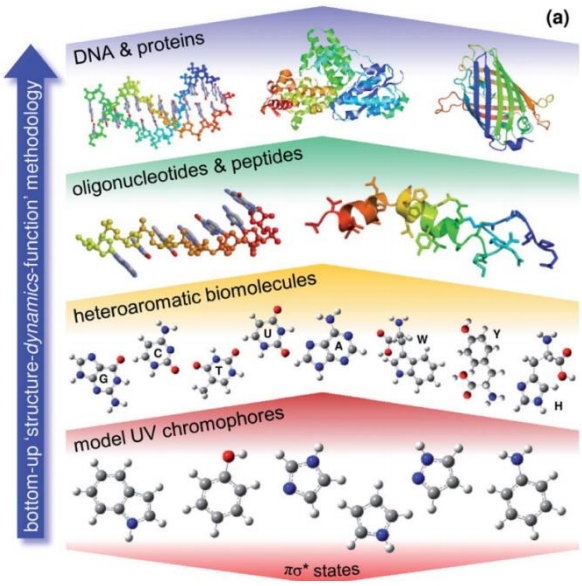

Figure 1.09 – "The bottom up approach", taken from Ref [18]

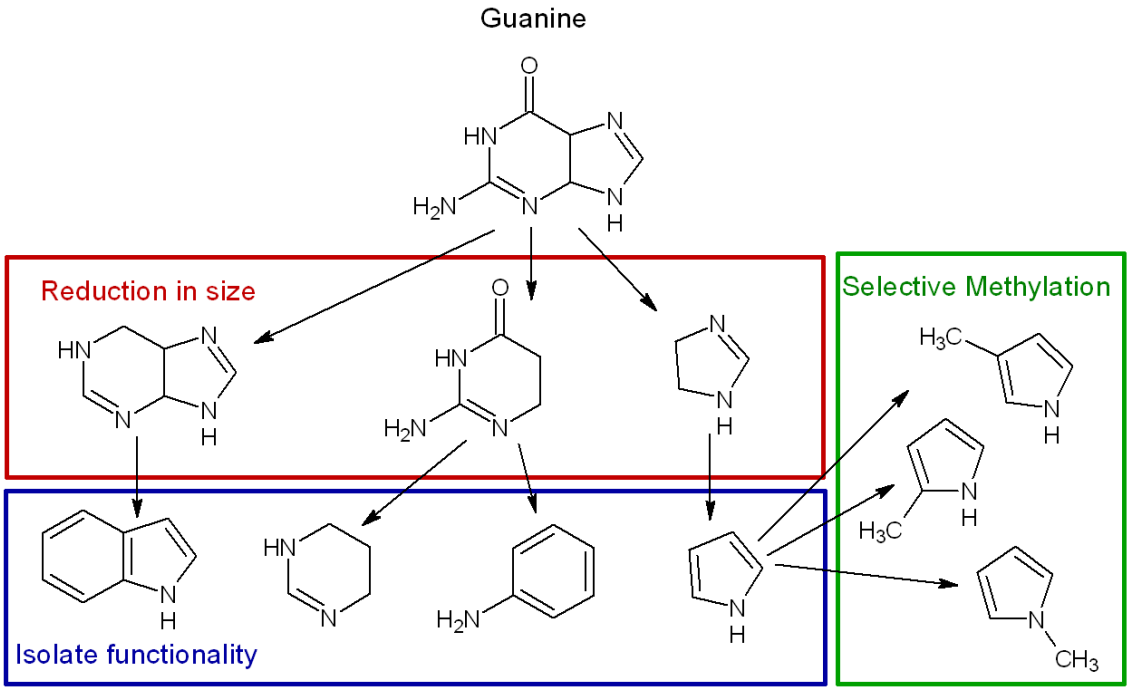

Figure 1.10 – Illustration of different methods that can be employed to understand chemical dynamics of complex systems, using guanine as an example. See text for further details

essential for dynamical process of interest to occur. Finally, to aid in understanding the mechanisms of energy redistribution, selective methylation can be used to interrogate dynamical effects as, by slowing down specific vibrational and rotational modes, it is possible to identify which motions are critical for mechanism to operate efficiently. To summarise, by understanding the pathways in which these smaller model systems absorbs light, this information can be used to understand the processes that occur within the larger system being modelled.

Work investigating the class of systems identified above began to gather pace in the late 1990s and early 2000s, during which Domcke and co-workers[19] identified a possible explanation as to why these molecular systems are potentially so prevalent in nature as light absorbing chromophores. These systems, all of which are small heterocyclic aromatic molecules, have a common set of electronic states called $\pi\sigma^*$ states (discussed in more detail later in this chapter). These states are potentially important to ultrafast energy redistribution, and provide a route for rapid and efficient non-radiative energy relaxation. Figure 1.11 provides an illustration of how this is achieved. It should be noted that this chapter has not yet discussed how such a figure could be described in terms of excited states and the approximations used. However, it is appropriate to mention the features in the figure with respect to the molecules discussed so far. Figure 1.11 depicts a potential energy cut along a single co-ordinate of the multi-dimensional

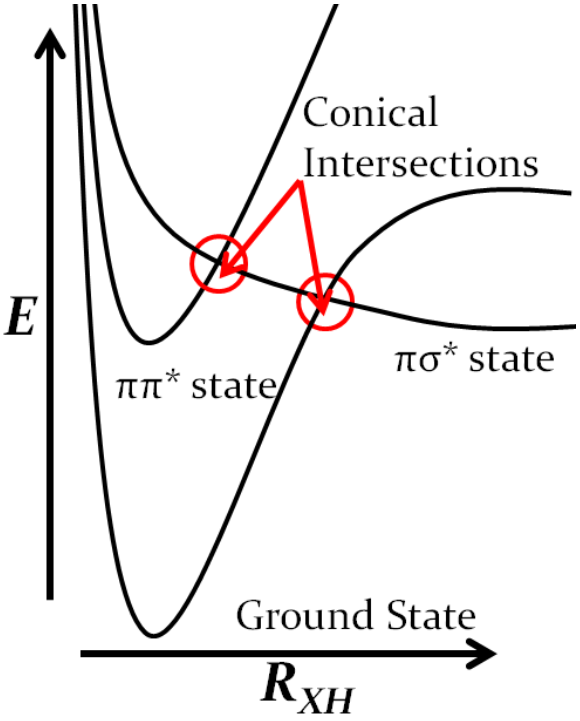

Figure 1.11 – Cartoon schematic of common potential energy surface found in heterocyclic aromatic molecules

potential energy surface of three electronic states. The lowest curve is a cut of the ground state of the system, and the two upper curves are cuts along electronically excited states, labelled as ππ* and πσ*. The πσ* state crosses over the other two states and it is around these regions of the potential energy surface that crossing points can be located, known as conical intersections. A conical intersection is the point at which two different quantum states become degenerate, where, it is possible for energy transfer to occur from one state to another state through non-adiabatic coupling. It is this mechanistic route that is proposed to be the driving force behind the efficient, ultrafast energy redistribution, observed in these systems. This will be expanded upon in detail later in this chapter.

1.3 – Molecular transitions

1.3.1 – Born – Oppenheimer approximation

This section will address the basic quantum mechanical principles required to provide an adequate framework for discussing ideas covered in the previous section in more detail.

The principle photochemical reactions of interest are those concerning the excitation of a model chromophore to an electronic excited state through the absorption of UV light. To understand this transition it is necessary to consider the wavefunction of the initial and the final state of the molecule and the energy difference between the two states. First, the energy of the initial state is calculated through the use of the time-independent Schrödinger wave equation as shown below in Eq. 1.1.[20]

$$E\Psi = \hat{H}\Psi \tag{1.1}$$

Here E is the total energy of the system, $\hat{H}$ is the Hamiltonian operator and Ψ is the wavefunction of the system. This equation can be broken up into components that describe different types of motion, as shown by Eq 1.2

$$\Psi_{Total} = \psi_n \times \psi_e \tag{1.2}$$

Where Ψ_{Total} is the wavefunction of the system, and the component ψ terms are the wavefunctions describing the nuclear and electronic contributions, respectively. This method of separating the nuclear and electronic components of the wavefunction is called the Born-Oppenheimer approximation (BO). This assumes that the individual components of the total wavefunction do not couple or interact due to the large difference in mass between the nuclei and the electrons.[21] This in turn is linked to the difference in the timescale at which different processes occur. For example, electronic motion typically occurs on an attosecond time scale (10^{-18} s), whilst vibrational motion occurs on a relatively slower timescale of femtoseconds (10^{-15} s). Therefore, by solving the Schrödinger equation for each uncoupled wavefunction, and adding the energies together, the combined energy should be the total energy of the system (as shown in Eq. 1.3).

$$E_{Total} = E_n + E_e \tag{1.3}$$

Where E_{Total} is the total energy of the system, E_n is the energy corresponding to the nuclear wavefunction and E_e is the energy corresponding to the electronic wavefunction. This approach can also be expanded further through the use of the rigid rotor approximation, which states that within the nuclear part of the wavefunction, the vibrational and rotational contributions can be separated due to the difference in timescale on which the two motions occur. Vibrational motion, as previously mentioned, occurs on the timescale of femtosecond (10^{-15}) and rotational motion on a picosecond (10^{-12}) timescale. This adiabatic approach to understanding these systems is extremely useful as it provides a framework which leads to the concept of a potential energy surface (PES).[22] This surface is a multi-coordinate landscape which describes an electronic state and the various vibrational and rotational modes associated with it.

Figure 1.12 shows an example of a simple electronic transition between two potential energy surfaces. In the example, the transition is between its ground state and an electronically excited state. It should be noted that the cut shown in Figure 1.12 (as well as the illustrative cartoon shown in Figure 1.11 in Section 1.2.3) shows one of the 3N – 6 (where N is the number of nuclei in the system) dimensions (or degrees of freedom) that exist within a many-body system. As such, these cuts only provide an insight into a small part of the multidimensional landscape. However, as will be demonstrated in subsequent chapters, it is still useful to consider these cuts so long as the dimension investigated is critcal to the non-adiabatic coupling occuring within the molecules of interest. In fact, identifying

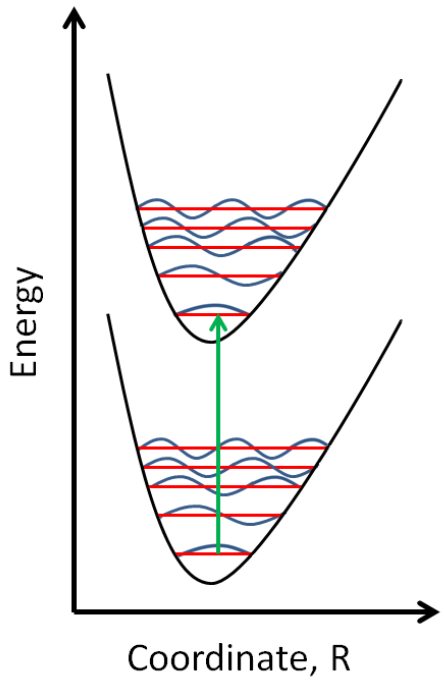

Figure 1.12 – Example transition from a ground state to an excited state visualised as 1D PES. Within each electronic state a number of vibrational levels have been drawn. It should be noted that within each of these vibrational levels would be a number of rotational levels.

which of the 3N-6 co-ordinates are important to the relaxation dynamics is oftern critical to better understanding the relaxation dynamics of these systems

1.3.2 – Molecular orbitals & the Franck-Condon principle

Molecular wavefunctions are constructed using a number of functions to describe the motion of nuclei and electrons. The functions used to describe the position of the electrons in atoms mathematically describe the shape of simple atomic orbitals. However, in the case of molecules, molecular orbitals need to be considered instead of atomic orbitals.

Using molecular orbital theory, molecular orbitals maybe created from a Linear Combination of Atomic Orbitals (LCAO)[10, 23] as shown below:

$$\phi_{MO} = \sum_i c_i \phi_i \tag{1.4}$$

where ϕ_{MO} is the molecular orbital produced from the linear combination of atomic orbitals ϕ_i and c_i is the corresponding coefficient of that orbital. In general, molecular transitions are described by

$$P = \int \psi_1^* \hat{\mu}.\hat{E}\psi_2 d\tau \tag{1.5}$$

where P is the probability amplitude of the transition, $\psi_1$and ψ_2 are the two wavefunctions involved in the transition, where 1 is the initial state and 2 is the final state, $\hat{\mu}$ is the transition dipole moment operator and $\hat{E}$ is the electric field. For an allowed transition the above integral must be non-zero. When the BO approximation is considered, the following occurs:

$$P = \int \psi_{1e}^* \psi_{1v}^* \psi_{1s}^* (\hat{\mu}_e.\hat{E} + \hat{\mu}_n.\hat{E}) \psi_{2e}\psi_{2v}\psi_{2s} d\tau \tag{1.6}$$

$$= \int \psi_{1e}^* \psi_{1v}^* \psi_{1s}^* \hat{\mu}_e.\hat{E}\psi_{2e}\psi_{2v}\psi_{2s} d\tau + \int \psi_{1e}^* \psi_{1v}^* \psi_{1s}^* \hat{\mu}_n.\hat{E}\psi_{2e}\psi_{2v}\psi_{2s} d\tau$$

$$= \int \psi_{1v}^{*}\,\psi_{2v} d\tau_n \int \psi_{1e}^{*}\hat{\mu}_e.\hat{E}\psi_{2e}\,d\tau_e \int \psi_{1s}^{*}\psi_{2s}\,d\tau_s + \int \psi_{1e}^{*}\psi_{2e} d\tau_e \int \psi_{1v}^{*}\hat{\mu}_n.\hat{E}\psi_{2v} d\tau_v \int \psi_{1s}^{*}\psi_{2s} d\tau_s \quad (1.7)$$

From Eq 1.6 we can derive Eq 1.7. It should be noted that the initial and final state wavefunctions (1 & 2 respectively) have been broken into its component vibrational (*v*), electronic (*e*) and spin (*s*) parts. As $\int \psi_{1e}^{*}\psi_{2e} d\tau_e$ can be assumed to be constant and therefore neglect the second half of the contribution,[24] then the first half of the expression contains the information determining whether or not the transition probability it large. The probabilities defined by the integrals $\int \psi_{1e}^{*}\hat{\mu}_e.\hat{E}\psi_{2e}\,d\tau_e$, $\int \psi_{1s}^{*}\psi_{2s}\,d\tau_s$, $\int \psi_{1v}^{*}\,\psi_{2v} d\tau_n$ serve as the mathematical basis of the electronic selection rule, spin selection rule and the Franck-Condon factor (FC).[10] If the three integrals are non-zero then the transition is formally allowed. Any other outcome means that the transition probability is small. From this it is possible to define some simple selection rules. Put simply, electronic selection rules define allowed transitions as occurring between orbitals of the same electronic character, such as π*←π or σ*←σ, but generally formally forbids transitions such as π*←σ. The spin selection rule states that for formally allowed transitions, the spin of the initial and final state must be the same, for example a singlet state to another singlet state, and formally forbids transitions between different spin configurations such as singlet to triplet transitions. The Franck-Condon factor describes the vibrational overlap of the starting vibrational state and the excited vibrational state, the Franck-Condon principle states that for the probability of a transition to be high and formally "allowed" the overlap between vibrational states needs to be high.[24] Figure 1.13 shows two examples of this using 1D PES's. In Figure 1.13a the vibrational mode of the

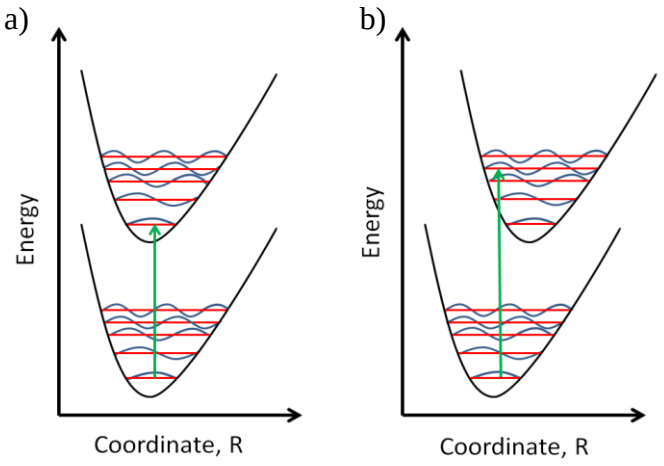

Figure 1.13 – Illustrative examples of the principle behind Franck-Condon overlap. a) illustrates a diagonal transition in which Δ*v* = 0, and b) shows a transition that is off diagonal

ground and excited state are well overlapped and so the excitation occurs to ν = 0 in the excited state. Figure 1.13b shows the PES of a molecule that has undergone a significant geometry change from the ground to excited state, meaning the transition now occurs from the ground state to a progression of vibrational modes in the excited state due to the FC factors. In this particular example, the majority of the population is placed into ν = 3 in the excited state.

1.3.3 – Time-dependant wavepacket motion

So far, this chapter has described the preparation of an excited quantum state by an optical transition. However, this discussion has only considered these processes in a time-independent framework. The experiments presented in Chapters 3 through 6, the initial excitation and subsequent ionisation process will occur using a femtosecond laser pulse (as described in more detail in Section 1.5), and as such, it is also necessary to discuss how this affects the prepared excited state. To describe the dynamical evolution of the optically prepared state it is necessary to operate in a time-dependent framework. The femtosecond laser pulse, by its very nature, has a large frequency bandwidth (as conversely it has a well-defined short temporal duration as consequence of the uncertainty principle). The bandwidth of the laser pulse (when mapped onto the potential energy surface) will typically encompass a large number of vibrational levels within a given electronic state. Therefore, it is no longer correct to describe the prepared state as a single quantum level, but as a superposition of numerous rotational and vibrational levels within the electronic state. This coherently prepared superposition is called a wavepacket, with its general composition given by Eq. 1.8.[25-27]

$$|\Psi(t)\rangle = \sum_n A_n e^{-i[E_n t/\hbar + \phi_n]} |\psi_n\rangle \tag{1.8}$$

The wavepacket (given by $|\Psi(t)\rangle$) is described as a linear combination of exact quantum states $|\psi_n\rangle$, which have a time-dependant phase given by $e^{-i[E_n t/\hbar + \phi_n]}$, where E_n is the energy of the particular quantum state and ϕ_n is its initial phase. The final part of this description is the expansion coefficients term A_n, which is an amplitude term relating how the state is populated (it should also be noted that A_n is P in Eq. 1.6). This depends upon the degree of overlap between the quantum state and the laser pulse. As time progresses, a number of processes may occur within the wavepacket.[28] Firstly, the

relative phases of the individual quantum states within the wavepacket will evolve with time. As such, it is possible, for the quantum states (as described by Eq. 1.8) to cause constructive or destructive interference, which can impact on the observables of experiments. For example, if the quantum states in the wavepacket are interfering constructively then the probability of an ionisation event could increase, resulting in an observed increase of signal in the experiment. And in turn, destructive interference can lead to a decrease in observed signal intensity. This phenomena is referred to as a "quantum beat".[28, 29] The process of photoelectron ionisation will be covered further in the following section. Secondly, population transfer between the various quantum states within the wavepacket may occur through non-adiabatic coupling. This transfer of population from one set of vibrational modes within the wavepacket to another is referred to as intramolecular vibrational energy redistribution (IVR). With this in mind, in the time-dependent picture it is more formal to consider A_n as $A_n(t)$.[30, 31] Wavepacket dynamics in polyatomic systems, such as those investigated in this thesis, can be very complex and challenging to describe as the quantum states that make up the superposition, $|\psi_n\rangle$ are often hard to define. Further approximations are therefore often needed to approximate the eigenstates.

1.3.4 – The role of πσ states in UV photoprotection*

With the framework in place to adequately describe how potential energy surfaces can be constructed and the types of processes which may occur upon them, the next section of this chapter will provide a review of recent work which motivates the experiments performed for this thesis.

In these systems, the ground state is primarily either a π-bonding molecular orbital or a non-bonding orbital located on a heteroatom such as nitrogen or oxygen. However, for the remainder of this section we shall focus on the π-bonding orbital systems. From this there are a number of orbitals to which excitation is possible; such as σ* and π* orbitals, which are examples of anti-bonding orbitals. In most cases the singlet channel excitations, such as π* ← π is an allowed transition whereas the σ* ← π is formally forbidden (or weakly allowed through some vibronic coupling). Through this formalism we can consider the allowed transitions as "bright states" and the forbidden transitions as "dark states".

Optically dark states may potentially be accessed through non-adiabatic coupling from an optically prepared state, this allows a transfer of population from, for example, the ππ* into πσ* state via a conical intersection (CI). In most of these systems, the πσ* can

either cause dissociation to occur, or relax non-radiatively back to the ground state through another conical intersection in systems where the πσ* potential energy surface crosses that of the ground state.[19] It is this ability to relax via non-radiative processes, as discussed previously, that has been postulated as the reason why the structure of melanin, and other systems, contain chromophores built around common structures.[14] There are three main approaches to the study of the reaction mechanisms of these systems; frequency-resolved measurements, time-resolved measurements and theoretical studies. To illustrate the differences in the insights provided by these different approaches, it is convenient to consider the work undertaken on the molecule indole (shown in Figure 1.14). Indole is a good choice for this first discussion due to the large amount of work existing on the system, [32-34] and is model chromophore for tryptophan and eumelanin. The structure of the molecule (shown in Figure 1.14), is made up of an aromatic ring system that contains a 5-membered ring fused onto a 6-membered ring. Within the 5-membered ring is located an N-H group, on which the πσ* state of interest is located. Indole has three main excited states which are believed to be important to the internal relaxation of the photo excited species; these are the L_a $^1\pi\pi^*$, L_b $^1\pi\pi^*$ and $^1\pi\sigma^*$ states. The two ππ* states occur at similar energy, with the difference between them is one state having a larger oscillator strength then the other.

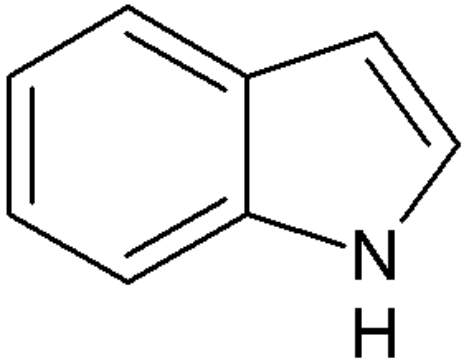

Figure 1.14 – Structure of indole

Frequency resolved measurements often use nanosecond laser systems to interrogate excited state species in order to determine the energy required to overcome potential barriers to different processes. An example of this is in the work of Nix *et al.*,[32] in which indole was investigated through the use of H atom photo fragmentation spectroscopy. However, due to the large temporal width of the pulse (1-3 ns), any dynamical temporal evolution showing non-adiabatic coupling of electronic quantum states is lost due to the large difference in timescale between the laser pulse and the time in which these processes occur (on the order of femtoseconds). As such, frequency resolved measurements cannot provide any temporal information on how the photochemical reaction progresses, which can be achieved through a time-resolved study. An example of a time-resolved study performed on indole is that by Livingstone

et al.,[34] in which indole was investigated through the use of time-resolved photoelectron spectroscopy using a magnetic bottle spectrometer.[35, 36] The key advantage of these time-resolved measurements is that they typically employ picosecond (~10^{-12} s) or femtosecond (~10^{-15} s) laser pulses to investigate these ultrafast processes and thus can perform direct measurements of their kinetics. However, due to the large spectral bandwidth of short pulses of light (typically around 500 cm^{-1}), fine quantum structure information is lost as large numbers of rovibrational states are excited simultaneously. Finally, an example of using high performance computational methods, to predict the energies of molecular excited states and model the coupling of the electronic states on indole is that by Domcke and co-workers.[37] In this example, potential energy surface calculations are performed to investigate the conical intersections as a method for internal energy redistribution and, as such, a mechanism for electronic relaxation within indole and other similar systems. For the remainder of this section, a literature review of a selection of work on similar systems will be provided to further illustrate the scope of this field, investigating heterocyclic systems that contain the electronic state configuration of interest.

Ashfold and co-workers have investigated indole and a number of hydroxyindole species, including 5-hydroxyindole to identify which πσ* state would be active.[38] 5-hydroxyindole is another molecule of interest as a more complex model chromophore found in eumelanin and tryptophan. The addition of the OH group adds an extra layer

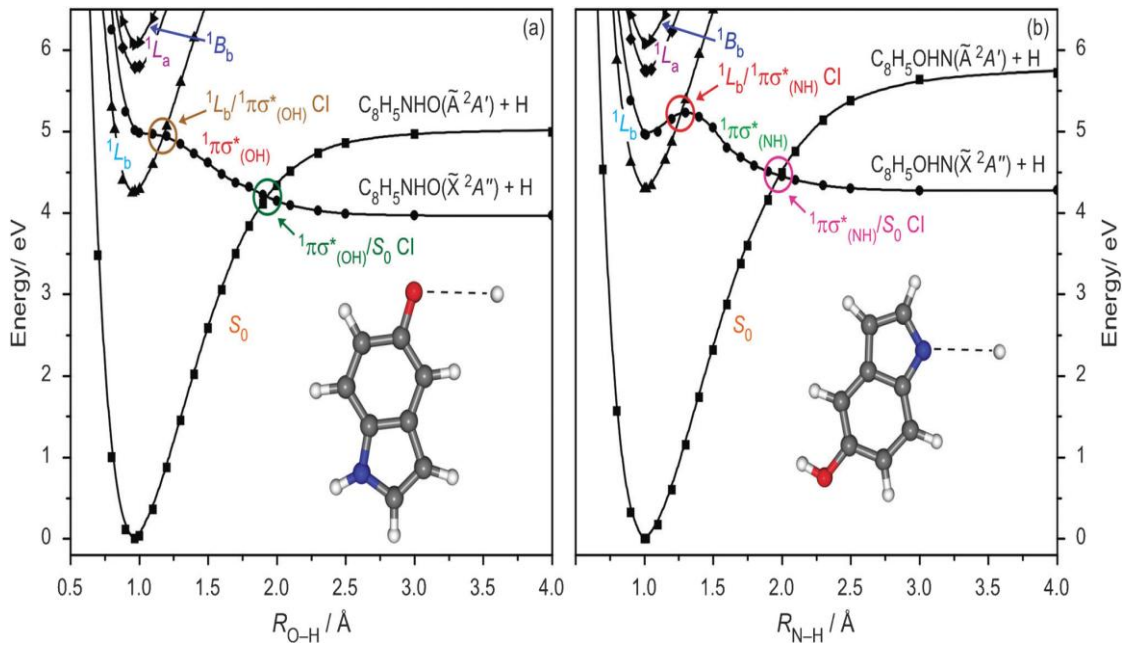

Figure 1.15 – Potential Energy Surfaces of 5-hydroxyindole along the OH coordinate (a) and along the NH coordinate (b). Taken from Ref [39]

of functionality and by comparing this to the base indole molecule is a prime example of the "*bottom-up approach"* at work. In the non-substituted indole no tunnelling H-atoms were detected from the lower $L_b(\pi\pi^*)$ state into the $^1\pi\sigma^*$ state. However in the case of the substituted system, tunnelling H-atoms are detected. As there are two possible dissociative valence states available, this work used computational modelling to predict which competing dissociation pathway was preferred for H atom release, either the oxygen or nitrogen site. The conclusion of this work suggested that the propensity for dissociation either via OH or NH was dependent upon the position of the alcohol group on the 6-membered ring. In the case of 4-hydroxyindole tunnelling occurs from the OH group and not the NH group, whilst conversely in 5-hydroxyindole the tunnelling occurs along the NH group not the OH group. Figure 1.15 (taken from the same paper) shows the 2D potential energy surface of 5-hydroxyindole. By investigating the shape of the potential cuts it can be shown that the barrier to dissociation through H-atom tunnelling along the NH coordinate is smaller than along the OH coordinate. The investigation of potential energy barriers for H-atom tunnelling as a crucial step in the mechanism of internal relaxation has been noted in other studies.[39, 40] A time-resolved study of indole and 5-hydroxyindole was performed by Livingstone *et al.*[34] In this study it was proposed that at wavelengths above the conical intersection (as predicted by Ashfold and co-workers)[38] it is possible for the prepared wavepacket to sample the geometry to allow population to be transferred from the $\pi\pi^*$ to the $\pi\sigma^*$. However, at lower energy wavelengths the $\pi\sigma^*$ still plays a role, as the state can be accessed via a quantum tunnelling mechanism. It was further proposed that the reason that the frequency resolved study did not record photoionisation events from H-atom tunnelling was due to a second conical intersection being active, transferring population from $\pi\sigma^*$ to the ground state, thus no dissociation was observed.

Another example of a well-studied system is pyrrole (as shown in Figure 1.16). Pyrrole is a substituted 5-member ring system with a NH group in the ring. This molecular species can be considered a simplistic model of the indole molecule or a subunit of the ring system that makes up the chromophore within chlorophyll a (as outlined previously). Of particular interest concerning the pyrrole system is that the first two excited states are optically dark singlet $\pi\sigma^*$ states (labelled as $S_1(\pi\sigma^*)$ and $S_2(\pi\sigma^*)$ respectively), whilst the first optically

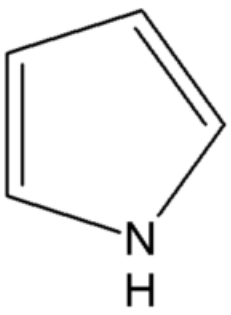

Figure 1.16 –Structure of pyrrole

bright state is the third singlet state, labelled $S_3(\pi\pi^*)$. This system has been studied extensively by Ashfold and co-workers,[41-43] Domcke and co-workers[44, 45] and also by Barbatti and co-workers.[46, 47] From these studies it was suggested that the non-adiabatic coupling is promoted by ring deformation and N-H bond extension, which causes H-atom dissociation. It was determined that this is the key process which underpins the relaxation dynamics of pyrrole. The work of Ashfold and co-workers,[38-40] determined that at excitation wavelengths less than 240 nm, pyrrole shows signal attributed to H-atoms formed from dissociation from the $\pi\sigma^*$ state.

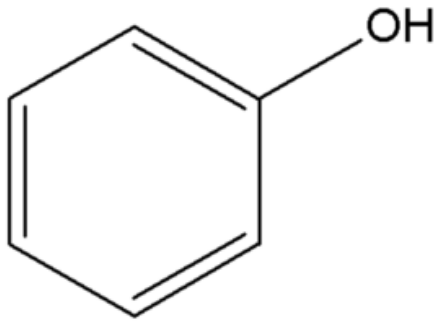

Figure 1.17 – Structure of phenol

To conclude this discussion, studies on the molecule phenol (as pictured in Figure 1.17) will be considered. Phenol serves as both motivation and relevant discussion for much of the work reported in this thesis in results Chapters 3, 4 and 5. Phenol is an aromatic structure that provides a good example of the non-adiabatic coupling between $^1\pi\pi^*$ to $^1\pi\sigma^*$. As reported by Ashfold and co-workers,[48] there is a barrier to the crossing from $^1\pi\pi^*$ to $^1\pi\sigma^*$ which has an onset threshold to cross of around 247 nm. Above the barrier, the wavepacket can freely move from $^1\pi\pi^*$ to $^1\pi\sigma^*$ by an internal conversion mechanism via a conical intersection. Interestingly however, below the barrier it is found that the crossing from the $^1\pi\pi^*$ to the dissociative $^1\pi\sigma^*$ state is still possible. The H-atom tunnelling through the potential energy barrier was promoted via the H-atom stretching mode and the $16a^1$ vibrational mode[49] (using Mulliken notation).[50] This work has also been backed up by the theoretical work of Domcke and co-workers.[51] Other groups have also looked at the timescales of such processes using ultrafast measurements and identified the onset of the release of the H-atoms from the OH bond on phenol.[52, 53] Phenol was also investigated by the Townsend group, and is described more in the report by Livingstone *et al.*,[39] which will be discussed in further detail in Chapter 5.

The next section of this chapter will discuss the experimental techniques employed in the investigation of these types of heterocyclic aromatic systems. Further discussions on the theoretical techniques employed may be found later in Section 1.6.

1.4 –Spectroscopic techniques

So far in this chapter, we have discussed the motivation behind the work presented in this thesis. We have described the framework to understand what processes can potentially occur and reviewed recent work discussing the various relaxation mechanisms in molecules of interest. However, we have yet to discuss how these experiments are performed and what observables are used in investigating the relaxation dynamics of small biological chromophores. As such, this next section will provide a basic overview of the experimental technique used in this thesis. A more detailed discussion of exactly how the experiments reported in this thesis are performed is presented in Chapter 2.

1.4.1 – Laser spectroscopy

Spectroscopy is defined as the study of light-matter interactions, for which there are a number of different experimental techniques which may be employed. Early experiments investigated the lifetimes of prepared excited states by measuring the fluorescence and phosphorescence lifetimes of molecules.[54] However, increasing numbers of experiments that investigate the properties of interactions between light and matter tend to use photoelectron spectroscopy techniques. Photoelectron spectroscopy takes advantage of the photoelectric effect[55] where, through the application of light, it is possible to ionise molecules and cause emission of photoelectrons. In the 1950s and 60s, examples of experiments that utilised the photoelectric effect in this manor investigated molecular systems by direct UV excitation, through the use of discharge lamps. An example of this can be seen in Setlow *et al*.[56] This example, however, utilises a single photon process for ionisation and as such lacks the ability to interrogate excited states. This changed in the 1960s and 70s with the commercialisation of the laser. These sources of narrow bandwidth light made it possible to perform laser spectroscopy and investigate electronic excited states in detail, with the ability to excite either a single rovibrational mode or a small number of rovibrational modes. An example of this progress can be seen in a technique known as Resonance Enhanced Multi Photon Ionisation (REMPI),[57] in which a molecule is prepared in a specific rovibrational level within an electronic excited state, by one or more photons, and then subsequently ionised with further photons as shown in Figure 1.18. This technique provides information on the rovibrational structure of the excited state by scanning the wavelength of the excitation pulses. The principle behind the technique is as follows; as the laser frequency scans over a resonant transition, the absorption of light dramatically

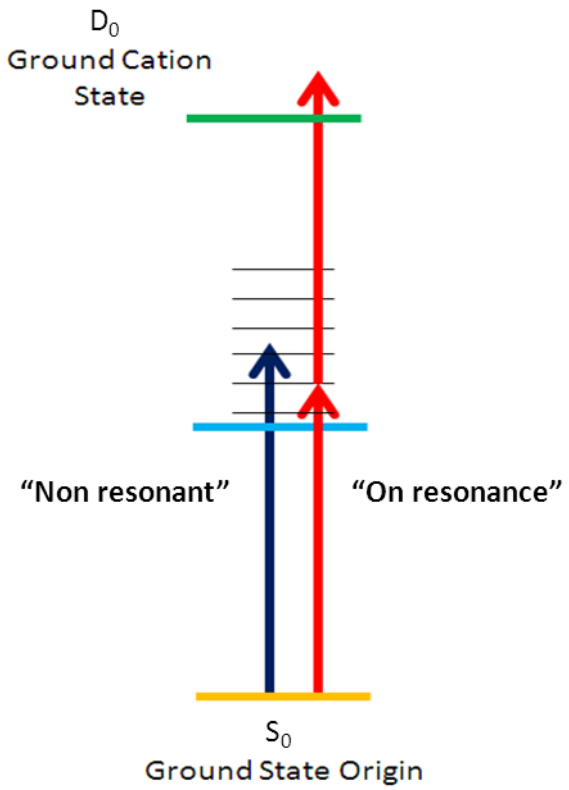

Figure 1.18 – A cartoon schematic of REMPI. The red arrow describes a wavelength that is on resonance with a vibrational level within the excited state and thus subsequently exhibits a strong signal from the [1+1] "pump-probe" ionisation scheme whereas the blue arrow describes a wavelength that is off resonance with a vibrational level and so exhibits much weaker signal from the subsequent ionisation

increases with respect to the extinction coefficient, thus the subsequent ionisation becomes more efficient. By effectively measuring the number of ionisation events at each wavelength, it is possible to produce a spectrum of the excited state.[57] This approach can be taken a step further by considering time-resolved measurements. It is necessary in time-resolved studies to accurately delay the arrival of one laser pulse with respect to the other, allowing measurements to be taken at a series of time delays and in doing so build up an understanding of how energy flows within the molecular system. This type of multiphoton ionisation can be thought of as a "pump-probe" technique. There are a wide variety of experimental approaches that employ this technique for spectroscopic and dynamical interrogation; these will be discussed later in this thesis.

One type of spectroscopy uses charged particles as the observable to investigate how the photochemical reaction is progressing. These charged particle detecting methods can be placed into two categories; photoion spectroscopy or photoelectron spectroscopy. Photoion spectroscopy involves the detection of the charged ions that are produced as a result of photoionisation, such as dissociative fragments or the parent cation species. Photoelectron spectroscopy, which detects the electrons that are ejected from a molecule as it is ionised. This technique can be used to investigate photochemical reactions by observing how much energy is imparted to the outgoing photoelectron ejected by ionisation. It should be noted that charged particle techniques are not exhaustive in the field of understanding chemical dynamical processes. Techniques such as Laser Induced Florescence (LIF),[58, 59] fluorescent up-conversion spectroscopy,[60] or transient absorption spectroscopy[61] are just a few examples of alternative techniques. However,

due to the nature of the work reported in this thesis, only a subset of charged particle techniques will be considered in detail any further.

1.4.2 – Velocity map imaging (VMI)

There are many successful modern photoelectron/photoion spectroscopic techniques, each with their own set of advantages and disadvantages.[45, 62-72] However, for the remainder of this section, the discussion will focus on imaging techniques. Charged particle imaging was developed by Chandler and co-workers[73] (although the first imaging study was performed by Solomon)[74] as a method to combine time-of-flight mass spectroscopy with a 2D detector to investigate the dynamics of photofragmentation. However, the technique encountered difficulties with the resolution of the fragment signals.[75] This technique, however, served as the basis for what came next, Velocity Map Imaging.[76] This variant was first demonstrated by André Eppink and David H. Parker in 1997.[76] The novel improvement to this technique was

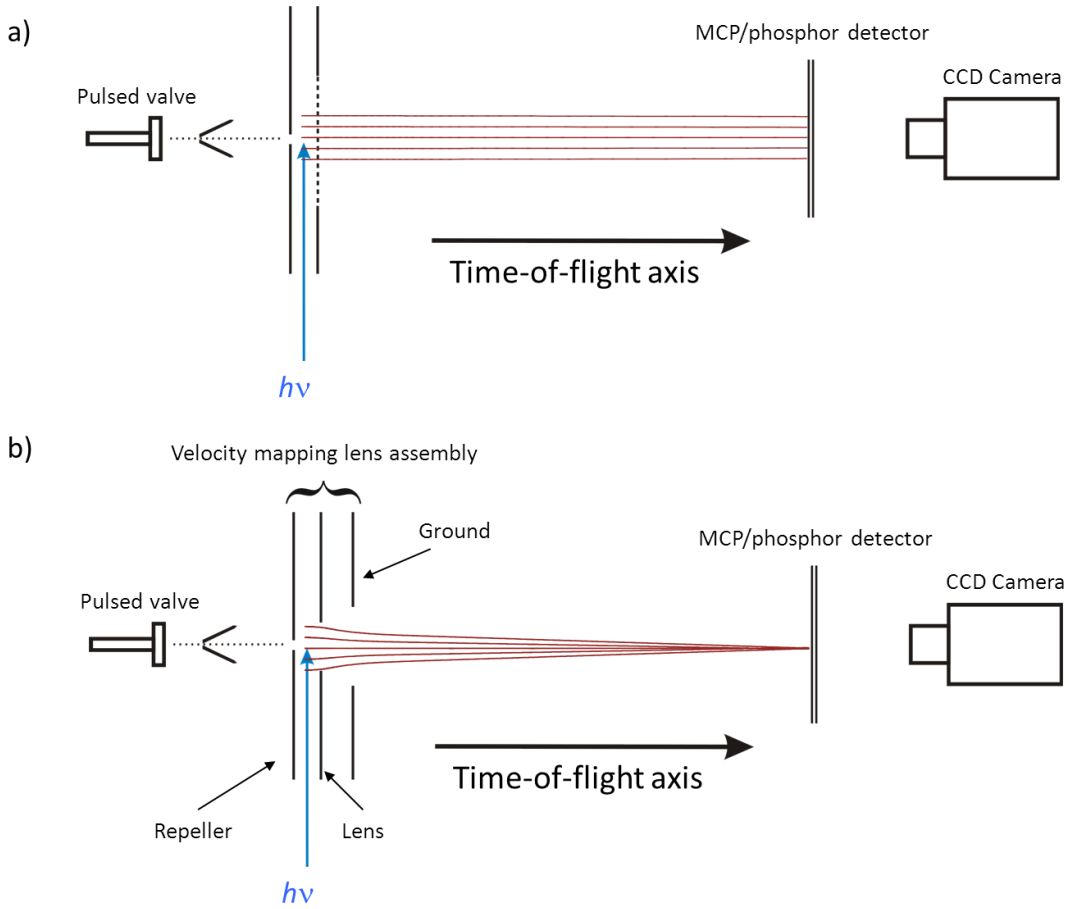

Figure 1.19 – Illustration of the advantage of VMI over charged particle imaging. The upper panel (a) shows the set up for a charged particle imaging experiment. The lower panel shows the basic velocity map imaging set up. The mapping lens is set of electrodes made up of a repeller (the back plate), lens (the middle plate). This set-up has also included a grounding plate. The use of an electrostatic lens set up is able to focus the charge particles, shown as vectors in red.

the introduction of an einzel lenses to focus the charged particles onto a position sensitive detector, as demonstrated in Figure 1.19. This improvement meant that all particles with the same velocity were mapped to the same spatial point on the detector, greatly increasing the resolution of the experiment. In Eppink and Parker's paper,[76] it was shown that this technique could be employed to investigate the photodissociation of molecular oxygen, and generated images of the ions in one configuration and images of electrons by changing the polarity of the lens assembly using the set-up (but not in a co-incident scheme). Figure 1.19(b) shows the basic schematic of a VMI spectrometer, which consists of a few key components. First of all are the aforementioned electrostatic lenses which are used to focus the charged particles along a time-of-fight axis. The plates, as shown in the figure, are typically labelled repeller (the back plate) and lens (the middle plate), and produce an electric field which focuses the charged particles onto a sensor. This sensor is a 2D imaging detector, typically consisting of a microchannel plate coupled with a phosphor screen, with the ability to capture the 2D distribution of electrons and produce an image on the phosphor screen. Typically the sensor is mounted inside the vacuum system. The third component is an actual camera to record the image from the phosphor screen. The camera is typically mounted outside the vacuum system.

An important consequence of the nature of this technique is the need for image reconstruction to extract the data from the raw image. This is because the raw images collected are produced from a flattened 3D object projected onto a 2D plane. The experiments performed for this thesis employed a variation of the Abel transform to reconstruct a 2D slice of the 3D distribution of particles. This particular reconstruction method and a full discussion on the necessity of image reconstruction will be discussed in detail in Chapter 2; however, this section will now give a general

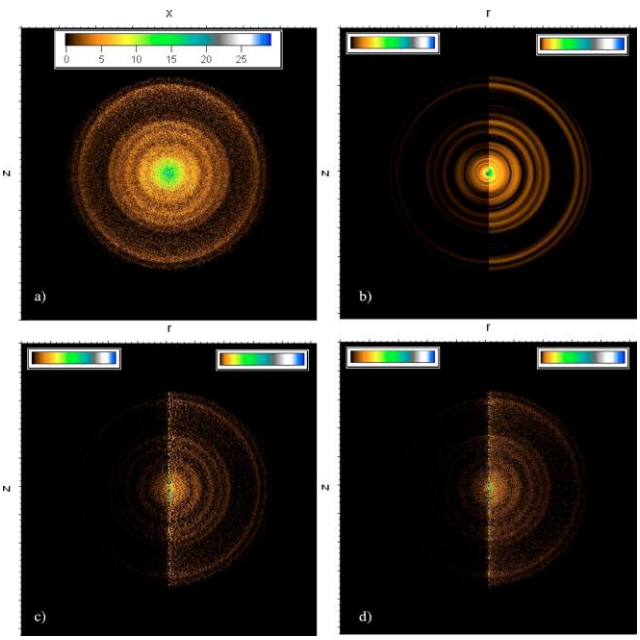

Figure 1.20 – differences in transform inversion methods with a) being the raw image, b) P-BASEX inversion, c) BASEX inversion and d) Abel inversion. Taken from Ref [81]

overview of the techniques available for image reconstruction. The Abel transform method was the first reconstruction method used for image processing.[77] This process seemed to be very effective and simple to implement, however, the process introduces a significant amount of artificial noise into the image, as shown in Figure 1.20d. As such, there has been significant development over the years into alternative inversion methods, so as to improve upon this limitation and extract higher resolution spectra from these images, as well as reducing noise in the inversion process. These techniques include: Onion-Peeling,[78] BASEX,[79] Polar Onion-Peeling (POP),[80] P-BASEX[81] and the specific technique employed in this thesis, the matrix Abel Inversion.[39] Each of these techniques has its merits and advantages, not just in terms of resolution, but also in terms of the computational power required to process the image. Figure 1.20 shows a selection of different inversion methods, operating on the same image, to demonstrate the differences in the resolution of these techniques.

1.4.3 – Photoelectron angular distribution

In addition to spectral information, VMI also allows the investigation of the angular distributions of these systems. Photoelectron angular distributions (PADs) provide insight into electronic structure. PADs are given by the following general equation[82]

$$I(\theta,\phi) \propto \sum_{L=0}^{L_{max}} \sum_{M=-L}^{L} B_{LM} Y_{LM}(\theta,\phi) \tag{1.8}$$

where $Y_{LM}(\theta,\phi)$ is a spherical harmonic function, and B_{LM} is a coefficient and depends upon the process involved in the photoionisation, the photoionisation energy, the molecular or atomic orbital from which the electron was ejected, the spatial distribution of the sample in the experiment and the experimental geometry. The equation is given this particular form when considering the interference of photoelectron partial waves (with orbital angular momenta of *l and l'*) which give rise to the term *L*, where *L* can take values between 0 and *l* + *l'*. When Eq 1.8 is expanded, the first term (B_{00}) is proportional to the intensity of the photoelectron signal integrated over all angles. As such it is convenient to divide the other parameters by this to generate a normalised anisotropy parameter, β.

In the experiments described in later chapters, laboratory frame measurements are made of the PADs, taken from the VMI data. These measurements are laboratory frame, as the point of reference used to determine the PADs is the polarisation axis of the laser light, as opposed to a molecular frame measurement in which a molecular axis is employed as the coordinate of reference. When considering the lab frame measurement, assuming that the sample has an isotropic distribution (a good assumption when considering the molecular beam from which the sample is carried to the interaction region, to be discussed in Chapter 2), the maximum value *L* can take is twice the total number of photons involved in photoionisation. Additionally, only even number *L* terms are required in the expansion, as odd terms *L* are only considered for molecules that are chiral or those that are orientated in space. Further to this, *M* can take values between –*L* and +*L*. However due to the relationship between the polarisation vector of each photon absorbed to the molecular axis, the number of terms can be further limited to *M* being zero. This is due to the symmetry restrictions imposed on the molecule by the restrictions of the lab frame measurement which also removes the dependence on the angle ϕ. As such, the value of B_{LM} will depend on how strongly the sample is aligned. Utilising the restrictions described above, it is possible to express the PADs produced by an experiment using two parallel linearly-polarised photons with the terms B_{00}, B_{20} and B_{40}. As B_{00} is not angle dependent, but rather dependent on the experimental conditions, Eq. 1.8 can be simplified and normalised which gives rise to the following equation Eq 1.8[83]

$$I(\theta) \propto 1 + \beta_2 P_2(cos\theta) + \beta_4 P_4(cos\theta) \tag{1.9}$$

where β_n is the normalised anisotropy parameter, P_n is the Legendre polynomial to the order *n*. It should also be noted that the intensity is given in terms of the angle with respect to the lab frame axis. In fitting the anisotropy parameters it is possible to gain an understanding of the vibronic structure of the state interrogated and, in time-resolved studies, how this state character changes as a function of time.

1.5 – Femtosecond lasers

Now that the technique employed to investigate the molecular systems of interest has been discussed, this section will now consider the type of light source required for the experiments and present an overview of how the laser system operates.

1.5.1 – Modelocking laser

In the field of investigating photochemical reactions, a huge range of possibilities opened up in the 1950s with the invention of the laser.[84] With this coherent monochromatic light source, it became possible to produce highly controlled radiation to be used for a variety of applications. However, what we focus on here is the fact that it can be used to irradiate molecules and instigate photochemical interactions. Over the years, this technology has progressed and enabled new experiments to investigate dynamical processes on various timescales. During the 1960s and 70s nanosecond and picosecond lasers became widely available, which made high resolution spectroscopy of molecular systems and dynamical studies of energy redistribution and charge transfer possible.[85] In the 1980s, laser technology produced its first femtosecond light pulse, however, femtosecond technology did not become widely available until the development of Ti:Sapphire systems in the 1990s.[86]

Ti:Sapphire laser systems, like other short pulsed systems, use a process called mode locking to achieve ultra-short pulses.[86] In a lasing cavity there are a number of longitudinal modes that make up the lasing action. These modes are, generally speaking, are produced normally by minor power fluctuations within the pumping action of the laser medium or through rapid alterations of the laser cavity and have a random phase. It is possible, over time, to build up a large number of modes within the cavity which may be locked together to form short laser pulses, as shown in Figure 1.21.[87] The number of longitudinal modes within a laser cavity required to produce a femtosecond laser pulse, using a Ti:Sapphire crystal as the gain medium, is on the order 10^4. The process that allows these modes to lock together is the optical Kerr lens effect, in which the high power of the laser causes a modification in the refractive index of the lasing medium. This induces a self-focusing effect that constricts the beam diameter. In conjunction with a slit to cut out the lower energy background, this self-focusing is the initiation of passive modelocking and allows only the narrow pulsed light to gain in the cavity.[87] However, most modern mode locking lasers use a combination of active and passive mode locking to achieve pulsing mode. Unlike passive mode locking that takes advantage of random power fluctuations within the lasing action, active mode locking

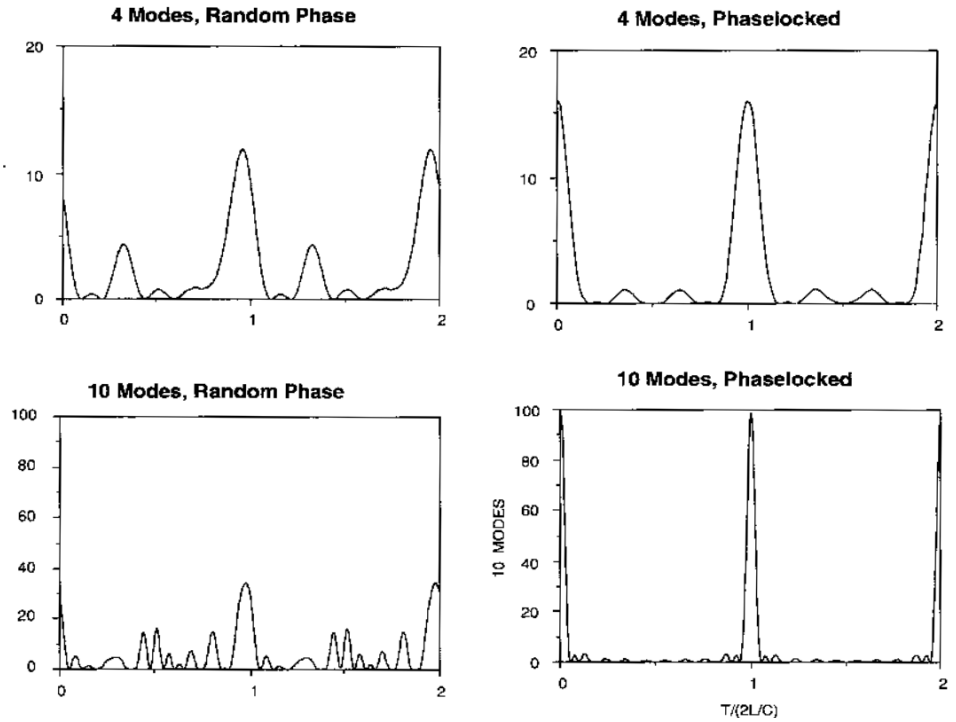

Figure 1.21 – Effects of locking continuous laser modes into a single pulse. Taken from Ref [89]

introduces fluctuations to the path length of the cavity. This results in new modes being produced and shortens the time required to attain enough modes for mode locking. Additionally, once mode locking has been achieved most systems no longer need to actively produce new modes and allow passive mode locking to continue the pulse generating process. A standard, modern day femtosecond laser system consists of an oscillator, which produces a seed light of the correct temporal bandwidth of light pulse, which is then amplified through the use of a regenerative amplifier system. A regenerative amplifier is used to increase the pulse energy of the output of femtosecond lasers from hundreds of milliwatts to tens of watts. It is not feasible to directly produce high power femtosecond pulses as the peak power of these pulses would damage the optical material within the amplifier system in the process. The process used in order to amplify the power of the light is known as chirped pulse amplification.[88] The practicalities of how this is performed discussed in Chapter 2. The Ti:Sapphire laser produces light centred around 800 nm and, as such, has a variety of uses. However, for the rest of this section, focus will be on uses relevant to the work outlined in this thesis.

1.5.2 – Nonlinear optics

The field of nonlinear optics came to be in the 1960s[89] and is the study of how high power electric fields interact with nonlinear materials. This interaction can be described by the non-linearity effect as shown in Eq. 1.10.[90] Mathematically this may be expressed as a Taylor series expansion, where polarisation density $\tilde{P}(t)$ is given in terms

of the electric field $\tilde{E}(t)$ and the materials susceptibility coefficient $\chi^{(n)}$ to various orders of power

$$\tilde{P}(t) = \epsilon_0\left[\chi^{(1)}\tilde{E}(t) + \chi^{(2)}\tilde{E}(t) + \chi^{(3)}\tilde{E}(t) \ldots\right] \tag{1.10}$$

where the electric field vector of a beam of light made up of two frequencies (ω_1 and ω_2) with amplitudes (E_1 and E_2) can be described as

$$\tilde{E}(t) = E_1 e^{-i\omega_1 t} + E_2 e^{-i\omega_2 t} \tag{1.11}$$

Non-linear effects occur when light interacts with a non-linear medium (all types of matter). However, for the types of interactions that are of use for the purposes of the experiments outlined in this thesis, only the second order ($\chi^{(2)}$) effects will be considered. Materials that are suitable for enhancing 2nd order non-linear effects are birefringent (i.e. a material that's refractive index that also depends upon the polarisation of lights propagating as well as wavelength).[90] These materials typically have no long range structural order in one or more axis. Examples of non-linear media include fluids and gasses, as they inherently have no long range ordering due to the random nature of their movement. Solid crystal structures that only exhibit longer range ordering on one or two of their crystal axis instead of all three can also be non-linear media. An example medium is BBO β-Barium Borate (BaB_2O_4), which is often used for frequency doubling.

Frequency doubling or Second Harmonic Generation (SHG) is a process in which a nonlinear crystal spontaneously absorbs two photons of light and re-emits the energy as a single photon of the combined sum frequency of the inputs. This is enhanced by a phase matching angle, where the electric field of the birefringent crystal is aligned to that of the incoming photons in order to fulfil the phase matching condition. This process is governed by a second order susceptibility, which when derived from Eq. 1.11 substituting into Eq. 1.10[90, 91] gives the following equation (Eq. 1.12) to describe a four-wave mixing process.

$$P^{NL} = \varepsilon_0 \chi^{(2)} E^2(t)$$
$$= \varepsilon_0 \chi^{(2)} \left[|E_1|^2 e^{-i2\omega_1 t} + |E_2|^2 e^{-i2\omega_2 t} + 2E_1 E_2 e^{-i(\omega_1+\omega_2)t} \right.$$
$$\left. + 2E_1 E_2^* e^{-i(\omega_1-\omega_2)t} + 2(|E_1|^2 + |E_2|^2) \right] \quad (1.12)$$

This contains components of $|E_1|^2 e^{-i2\omega_1 t}$, $|E_2|^2 e^{-i2\omega_2 t}$, $2E_1 E_2 e^{-i(\omega_1+\omega_2)t}$, $2E_1 E_2^* e^{-i(\omega_1-\omega_2)t}$ and $2(|E_1|^2 + |E_2|^2)$, which is the mathematical description of second harmonic generation (SHG) with either the first or second frequency, sum frequency generation (SFG) of the two frequencies, difference frequency generation (DFG) of the two optical frequencies and optical reflectivity of the light pulses respectively. Additionally, the efficiency of these processes depend heavily upon the polarisation of the electric field with respect to the optical medium (i.e. components of $\chi^{(2)}$), as a phase matching acceptance angle is required to drive this interaction. What is fairly apparent from this is that all these processes are driven by a second order dependence upon the electric field strength and the strength of the interaction with the material. As such, the process becomes more efficient with higher intensity light and with longer crystal axis in which to propagate in. However, longer crystals cause difficulties with femtosecond lasers due to their large spectral bandwidth, with chirp introduced by the temporal walk of the different spectral ends of the pulse. Consider a pulse that is comprised of a large range of wavelengths. In the crystal, the laser pulse undergoes a temporal broadening as the blue and red ends separate from each other. This effectively lowers the peak power of the pulse, and lowers the conversion efficiency. As such, the non-linear optical crystals used in femtosecond lasers must be thin, typically between 0.1 and 0.5 mm thick, to maximise conversion efficiency whilst not compromising the temporal duration of the pulse.

1.5.3 – Uses of ultrafast lasers

The main use of a femtosecond laser, with respect to the aims and objectives of this thesis, is for investigating ultrafast chemical dynamics. This is achieved through the use of femtosecond light pulses to interrogate molecular systems in real time and by describing the dynamical evolution of the excited state utilising pump-probe spectroscopy. This work has been well received in recent years and was the subject matter of the 1999 Nobel Prize in Chemistry, in which Nobel Laureate Prof. Ahmed Zewail was awarded the prize for his work in developing the field of

"Femtochemistry".[92] However, there are many other useful properties of femtosecond lasers that can be used to investigate many other chemical interactions.

An example of the use of a femtosecond laser is the control of chemical reactions through modification of the potential energy surfaces with a high field strength laser pulse.[89, 93-95] Additionally, the light can be used to produce XUV or soft X-ray light through high harmonic generation.[89] Further to this, femtosecond lasers can be used to produce supercontinums through a combination of the optical Kerr effect and four wave mixing.[90] Finally, the high peak flux generated from femtosecond laser pulses may be used to modify the refractive index of materials using a technique called ultrafast laser inscription (which is based on the optical Kerr effect), which may be used to guide electromagnetic waves, otherwise known as an optical waveguide.[96, 97]

1.6 – Theoretical chemistry

1.6.1 – Quantum chemistry

For many of the experiments described in the result chapters of this thesis, theoretical quantum chemistry calculations were performed to aid our understanding of processes observed. This section will provide a background of the various theoretical methods employed to this effect.

Quantum chemistry is the result of the natural progression from a classical mechanics to a quantum picture, using a highly developed methodology to aid chemical understanding. Quantum chemistry is broadly separated into two types of methodologies; semi-empirical methods and *ab initio* methods. *Ab initio* calculations are entirely based on solving the Schrödinger wave-equation and use many approximations and approaches to this end. In general, quantum chemical calculations use an assembled set of functions, collectively known as basis set (discussed in the following section), to describe a series of occupied and virtual atomic or molecular orbitals in a specific system. From this, the energy of different electronic state configurations is evaluated against different geometries of the molecular system, and produces an insight into the potential energy surface (PES) of the molecule. These methods are also able to find an optimum molecular geometry from the movement of atoms, finding a structure with the minimum energy based on bonding and non-bonding interactions. For the remainder of this section, a number of theoretical techniques and applications will be discussed which are relevant to the work presented in this thesis.

1.6.2 – Basis sets

All *ab initio* quantum chemical calculations require a wavefunction (an eigenfunction of an operator) in order to perform a calculation. In molecular systems, this wavefunction is considered to be a linear combination of atomic orbitals (LCAO), as shown below in Eq 1.13[98]

$$\psi_i = \sum_{i=1}^{N} c_i \phi_i \tag{1.13}$$

Where ϕ_i is the atomic wavefunction and c_i is its contribution to the molecular wavefunction ψ_i. Each individual atomic orbital may also be described as an atomic

wavefunction. As such, the set of atomic functions ϕ_i are used to produce a molecular wavefunctions are referred to as the "basis set". In the work discussed in this thesis, there are two main types of basis that are used; these are Pople basis sets and Dunning basis sets.

Pople basis sets consist of a combination of slater and primitive Gaussian functions,[99] which, in practice is written in the form "A-BCG", where A is the number of functions used to describe core orbitals (i.e. non interacting orbitals), B and C are two separate sets of functions used to describe valence orbitals in which the values represent the number of functions per set and G is a letter stating that the functions are Gaussian. An example function of this would be "4-31G" where by the core orbitals are described with 4 functions and valence orbitals are represented with a double split valance (called a double zeta split) using three functions and one function. Additionally, extra diffuse functions (nominally marked with a +) can be added which are used to describe larger orbitals or polarisation functions (normally marked with a *) to describe orbitals of a higher order of angular momenta. Typically, for a good standard calculation, the basis set will take the form of "6-311++G*".[100] Dunning basis sets use a combination of primitive, contracted and polarisation functions to describe molecular orbitals and are often referred to as correlation consistent sets, as these are corrected to account for the instantaneous motion of an electron. These basis sets take the from "cc-pV#Z", where cc-p represents that the functions are correlation consistent polarised, meaning the extra functions added to the basic Hartree-Fock core orbitals increase in both size and angular momentum as additional shells are added, V means that the basis set only describes the valence states and the # can take the form of D, T, Q etc. for double zeta, triple or quadruple zeta, in combination with the Z. On top of this, this basis set can be augmented with additional diffuse functions, normally noted as an "aug-" preceding the "cc-pV#Z".[101]

1.6.3 – Hartree-Fock method

The simplest *ab initio* calculations are based on the Hartree-Fock scheme,[55, 102] in which it is assumed that the multi-body Hamiltonian can be approximated by many one body Hamiltonians, as shown in Eq. 1.14.[98]

$$\hat{H} = \sum_{i=1}^{N} h_i \tag{1.14}$$

Where *H* is the Hamiltonian, *N* is the number of electrons and *h* is the one electron Hamiltonian. In this way, it is possible to solve a many-body wavefunction without having to solve for the electron-electron interaction. Eq. 1.15 presents the one electron Hamiltonian.[98]

$$h_i = -\frac{1}{2}\nabla_i^2 - \sum_{k=1}^{M}\frac{Z_k}{r_{ik}} \tag{1.15}$$

In which ∇_i^2 is the Laplacian operator, *Z* is the molecular charge, M is the number of nuclei, k is the number of electrons and *r* is the distance between the two electrons. Eigenfunctions of this one electron Hamiltonian must satisfy the one-electron Schrödinger equation, as seen in Eq. 1.16.

$$h_i\psi_i = \varepsilon_i\psi_i \tag{1.16}$$

As the Hamiltonian is separable into many single electron Hamiltonians, the many-electron eigenfunction may be constructed by the product of the one-electron eigenfunctions, given by Eq 1.16.

$$\Psi_{HP} = \psi_1\psi_2 \ldots \psi_n \tag{1.17}$$

A wavefunction that takes the form in Equation 1.17 is called the "Hartree-product" wavefunction. This wavefunction, however, currently has no correction for electron-electron interaction. By applying variational calculus, it can be shown that each orbital, ψ_i, which minimises $\langle\Psi_{HP}|H|\Psi_{HP}\rangle$ is an eigenfunciton of its own operator h_i, taking the form:[98]

$$h_i = -\frac{1}{2}\nabla_i^2 - \sum_{k=1}^{M}\frac{Z_k}{r_{ik}} + V_i\{j\} \tag{1.18}$$

This Hamiltonian, depending upon $V_i\{j\}$, is referred to as the "Hartree-Fock" Hamiltonian if the respective eigenfunction of this Hamiltonian is antisymmetric. Below, in Equation 1.19, gives an example of the $V_i\{j\}$ component of the function.

$$V_i\{j\} = \sum_{j \neq i} \int \frac{\rho_i}{r_{ij}} d\boldsymbol{r} \tag{1.19}$$

Here ρ is the probability density associated with electron j. The issue of trying to calculate this electron correlation correction is solved using a self-consistent field approach, employing initial trial wavefunctions, operating upon them to produce new, more accurate wavefunctions in the result of the calculation. This approach is variational, as well as self-consistent; meaning any change to the input which lowers the energy of the system is an improvement. From this, a HF calculation can iteratively search for the lowest energy configuration of an arrangement of electrons. However, as illustrated above, this approach uses many approximations and, as well as being unable to calculate the energy of electron-electron interactions, it is also limited to a single electron configuration. Therefore, it is unable to account for the energy associated with the probability of multiple electrons assuming a different configuration, often an issue for excited states, which results in the calculation being inaccurate. That being said, HF is able to calculate a variety of properties for medium sized systems with reasonable levels of accuracy depending upon the basis set used.

1.6.4 – Post Hartree-Fock methods

Many modern calculations perform additional corrections to the results of the HF calculation. These "post" HF calculations often add in correction terms for the approximations made by the HF method.[103] The main aim of post HF methods is to approximate the "electron correlation" term in the HF wavefunction, which can be divided into dynamical and static electron correlation. Dynamical correlation considers the interdependent motion of electrons, whilst static correlation is used to describe states which require more than one electronic configuration.

First, considering methods that measure static configuration of electrons in orbitals, it is possible to construct wavefunctions with multiple electron configurations. By allowing additional configurations to contribute to the ground state wavefunction, the result more

accurately describes the energy of the system, through the inclusion of static correlation. This is the basis of configuational interaction theory, where the user may calculate any number of configurations of electrons in orbitals to obtain a result with a greater level of accuracy. However, this calculation is still only a single reference method, which means that the orbitals involved in the calculation are only optimised for the original single configuration HF calculation. To improve upon this, the method must be extended to incorporate orbitals that are optimised for as many electron combinations as required to fully describe the chemical process of interest, which in combination leads to a greater level of accuracy when calculating the energy of the system. This approach is known as multi-reference configuational interaction (MR-CI), however for large systems this technique becomes too computationally expensive.

To get around this issue CASSCF, or Complete Active Space (CAS) Self Consistent Field theory can be employed.[98] CASSCF allows the user to design an active space (a set of orbitals which are critical to forming the states of interest), using orbitals generated from HF or another appropriate method as a starting guess. CAS then optimises these orbitals for every configuration of electrons within this active space. Using this active space, CAS then performs a multi-configuational calculation to calculate the energy of the system. It should be noted that all other molecular orbitals are treated as either fully occupied (in the case of occupied orbitals), or fully empty (in the case of virtual orbitals). This process significantly reduces the computational power required to perform this type of calculation whilst still being able to calculate a more accurate PES than using HF alone.

For chemical dynamics, CAS provides attractive benefits over regular HF. CAS is able to investigate dynamics around bond formation with the capability to plot potential energy surfaces out to extreme bond lengths, as well as the ability to investigate features of potential energy surfaces interacting with one another. An example of such an interaction is a conical intersection (CI).[22] This will be discussed in more detail in Section 1.6.6.

The final class of post HF methods that will be discussed in this chapter is Coupled Cluster (CC) theory.[104] This uses the HF output to produce a multi-electron wavefunction using the exponential cluster operator to account for electron correlation energy. What is important to note here is that this method is perturbative and so generates highly accurate dynamical correlation. This is described in Eq. 1.20.[98]

$$\psi = e^{\boldsymbol{T}}\psi_{HF} \tag{1.20}$$

Here $\boldsymbol{T}$ is the cluster operator and is defined in Eq. 1.21, with Figure 1.22 showing the different types of configurations described by the Taylor expansion.

$$e^{\boldsymbol{T}} = 1 + \mathbf{T}_1 + \frac{\mathbf{T}_1^{\,2}}{2} + \frac{\mathbf{T}_1^{\,3}}{3!} \ldots \mathbf{T}_2 + \frac{\mathbf{T}_2^{\,2}}{2} + \frac{\mathbf{T}_2^{\,3}}{3!} \ldots \tag{1.21}$$

Where $\mathbf{T}_1$ is the Taylor expansion for singles, $\mathbf{T}_2$ is the Taylor expansion for doubles and so on. This cluster operator is given as a series of functions up to the number of electrons within the system, becoming more accurate as the number of excitation operators in the exponential increases, i.e. allowing for double and triple excitations as well as singles. In principle, as higher order transitions are added to the series (triples, quadruples etc.), the closer the result is to the full configuration interaction and, thus, the true energy of the Hamiltonian. However, as the number of expansions increases in the Taylor series, the computational costs increase exponentially, requiring an excessively large amount of computing power and time to achieve. Fortunately, in most cases, only calculating the single and double transitions is necessary to get a significant improvement on the energy (although a further improvement cam be made with triples corrections). Additionally, the Taylor expansion naturally truncates to the quadratic term in the series. This is due to the probability of spontaneous movement of one electron being significantly higher than spontaneous motion of two, three or four

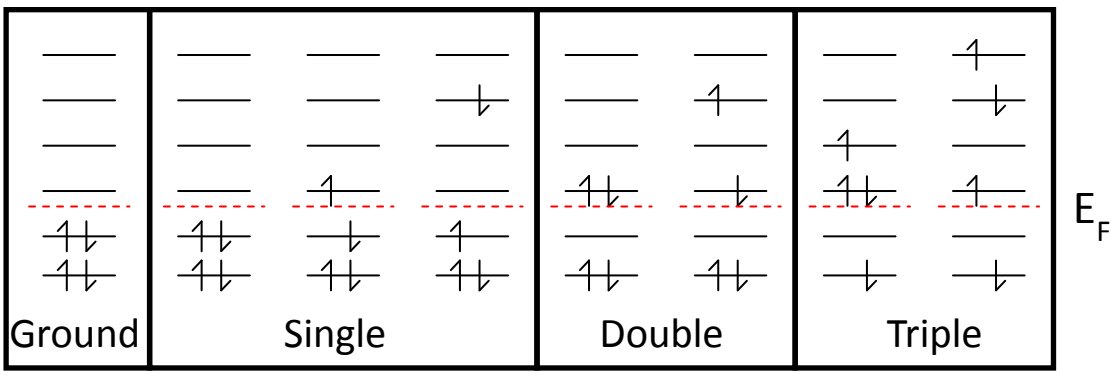

Figure 1.22 – Visualised examples of single, double and triple excitation. The red dashed line represents the Fermi Energy.

electrons respectively. This results in each order of correction applying a smaller alteration to the energy than the previous one.

1.6.5 – Density functional theory

One of the biggest steps forward in quantum chemistry came with the implementation of density functional theory (DFT).[105, 106] DFT can overcome some of the challenges associated with solving the Schrödinger equation in many body systems by forming wavefunctions based upon electron density, rather than electron location probability. DFT is based upon the Thomas-Fermi model, in which statistical models are used to describe the electron distribution around an atom and are able to calculate the energy through use of a kinetic model. DFT, in simple terms, may be derived starting from Eq. 1.22.[103]

$$\hat{H}\psi = \left[\hat{T} + \hat{V} + \hat{U}\right]\psi \tag{1.22}$$

Here, E is represented by $\hat{T}$, the kinetic energy, $\hat{V}$, the potential energy associated with external energy from the nuclei, and $\hat{U}$, the electron-electron interaction energy. It is the term equivalent to $\hat{U}$ that cannot be solved for a many body system in Hartree-Fock (HF) theory. DFT, however, removes this problem by calculating Kohn-Sham (KS) orbitals, based on electron density, instead of the HF, or based on electron location probabilities, removing the issue of electron correlation. Using the particle density $n(\vec{r})$, it is possible to equate the energy functional of a given KS wavefunction by the following:[103]

$$E_s[n] = \left\langle \psi_s[n] \middle| \hat{T} + \hat{V}_s \middle| \psi_s[n] \right\rangle \tag{1.23}$$

Where $E_s[n]$ is the KS energy with respect to the particle density, $\psi_s[n]$ is the KS wave function, and $\hat{V}_s$ is the external effective potential. From this, it is then possible to solve the KS equations to give the following:

$$\left[-\frac{\hbar^2}{2\pi}\nabla^2 + V_s(\vec{r})\right]\phi_i(\vec{r}) = \varepsilon_i\phi_i(\vec{r})$$

(1.24)

This generates KS orbitals, ϕ_i, which reproduce the electron density of the many-body system, $n(\vec{r})$ through a linear combination of single electron densities. From this it is possible to substitute equation Eq 1.25 into Eq. 1.24 and generate the single particle potential, given in Eq. 1.26.[103]

$$n(\vec{r}) \stackrel{\text{def}}{=} n_s(\vec{r}) = \sum_i^N |\phi_i(\vec{r})|^2 \cdot \tag{1.25}$$

$$V_s(\vec{r}) = V_s + \int \frac{e^2 n_s(\vec{r}')}{|\vec{r} - \vec{r}'|} d^3r' + V_{XC}[n_s\vec{r}] \tag{1.26}$$

The most interesting part of this equation is the second integral term, $V_{XC}[n_s\vec{r}]$, which is often referred to as the Hartree component. This is the part of the functional that describes the electron-electron interaction. V_{XC} is referred to as the exchange correlation potential and is the part of DFT which is most diverse. There are numerous DFT functionals available, each utilising different methods of describing the exchange correlation potential. These include methods such as local density approximations (LDA), generalising gradient approximations (GGA) or hybrid functionals, which use some Hartree-Fock potentials as a correction to the functionals.[107] Due to the wide range of functionals that exist, DFT is used in a variety of calculations in both chemistry and materials sciences.

1.6.6 – Excited states & internal conversion

Finally, to finish off this section, the discussion will now focus on excited state calculations and how to describe energy transfer between states using *ab initio* methods. The majority of the theoretical work reported in this thesis comprises calculating transitions to electronic excited states, which involves investigating the response of the ground state wavefunction to an electric field. This methodology is known as response theory. The manor of how this technique works is quite complex and beyond the scope of this discussion, however there are many articles on how this process is understood.[108-112] Using this method, it is possible to calculate the transition energies of various states and how they change as a function of variation in the ground state

wavefunction. This is the how the 1D potential energy surfaces shown in this chapter and later chapters are generated.

Additionally, through manipulation of the ground state wavefunction, it is possible to find positions on potential energy surfaces at which two surfaces intersect. It is at, or close to, these points which conical intersections (CI), avoided crossings or if the two potentials have different spin, where intersystem crossing (ISC) seams may be located. CIs are points at which two different potential energy surfaces (of the same electron spin) become degenerate, due to the geometrical movement of nuclei.[22, 113, 114] To give a simple example of how this process is allowed,[114] consider a system in which a solution is known for all but two of the electronic parts of the Schrödinger equation and ϕ_1 and ϕ_2 are two functions (whose solutions have an energy of E_1 and E_2 respectively) which, with the additional known solutions, make a complete orthonormal set. To locating a crossing point between the states with energy E_1 and E_2, it is possible to express the two remaining electronic eigenfunctions in the following form[22, 114]

$$\Psi = c_1\phi_1 + c_2\phi_1 \tag{1.27}$$

This results in the following secular equation[22, 114]

$$\begin{bmatrix} H_{11} - E & H_{12} \\ H_{21} & H_{22} - E \end{bmatrix} \begin{bmatrix} c_1 \\ c_2 \end{bmatrix} = 0 \tag{1.28}$$

Where each matrix element in Eq. 1.28 is given in Eq. 1.28[22, 114]

$$\begin{aligned} H_{11} &= \langle \phi_1 | H | \phi_1 \rangle \\ H_{22} &= \langle \phi_2 | H | \phi_2 \rangle \\ H_{12} &= H_{21} = \langle \phi_1 | H | \phi_2 \rangle \end{aligned} \tag{1.29}$$

From Eq. 1.28, it is possible to express the energies of E_1 and E_2 by the following[22, 114]

$$E_1 = \frac{1}{2}\left[(H_{11} + H_{22}) - \sqrt{(H_{11} - H_{22})^2 + 4H_{12}^2}\right]$$
$$E_2 = \frac{1}{2}\left[(H_{11} + H_{22}) + \sqrt{(H_{11} - H_{22})^2 + 4H_{12}^2}\right]$$

(1.30)

To bring these two states to degeneracy, there are two separate conditions that must be fulfilled as shown in Eq. 1.31[114]

$$H_{11} = H_{22}$$
$$H_{12} = H_{21} = 0$$

(1.31)

To allow this to occur, at least two nuclear motions are required. These motions can be understood by a combination of two vectors with which, from calculations, it is possible to determine the size and direction of the nuclei movement that is required. These two vectors are known as the derivative coupling and the associated gradient difference. The derivative coupling vector is large when the two states are of the same spin, and the magnitude of this vector is what drives the population transfer between the states. The gradient difference vector is the difference in energy between the initial and final states, which must also be large to facilitate rapid population transfer from one surface to another. The subspace on the potential energy surface which is described by these two vectors is called a "branching space".[114] At the CI, population transfer from one PES to another may occur through the process of "internal conversion". This process allows for the relaxation of excited states to lower level excited states, or even the electronic ground state and is important for excited state dynamical processes. This includes photochemical reactions, combustion and explosions. An avoided crossing is when two states become close to degeneracy but never truly meet. Population transfer is still possible, however, as the wavepacket must move from one surface to another via a "surface hop".[22] Population transfer through avoided crossings is, therefore, generally much slower than through a conical intersection as the transfer occurs through a tunnelling-like mechanism. Finally, intersystem crossing (ISC) may occur between states of different electron spin in a similar manor to the above discussion on CI, however, in the systems investigated in this thesis, is generally not observed due to the low order spin orbit coupling in systems without heavy atoms.[115]

1.7 Thesis outlook

Following on from this review of chemical dynamics, specifically regarding the internal energy transfer of model chromophore systems, the remainder of this thesis will discuss several investigations into processes involving number of different chromophore species.

Chapter 2 provides an overview the experimental set-up; including the velocity map imaging (VMI) spectrometer, the optical set-up and the femtosecond laser system that provided the short pulsed wavelengths of light employed in the experiment. It will also describe the programs used in the data acquisition, processing and interpretation of the experiments.

Chapter 3 provides a discussion of experiments performed on the molecule aniline when excited close to the origin of its πσ* state (267 nm). A number of wavelengths are employed to assess the dynamical lifetimes of the ππ* and πσ* states.

Chapter 4 continues the investigation of aniline by interrogating the molecule with 250 nm light. In an attempt to understand the dynamics, the additional molecules 3,5-dimethylaniline and *N*,*N*-dimethylaniline are also investigated, to gain an insight into the behaviour of this chromophore.

Chapter 5 discusses experiments investigating the relaxation dynamics of guaiacol using gas-phase photoelectron imaging, alongside complimentary solution-phase transient absorption measurements provided by the group of Dr V. Stavros at the University of Warwick. Additionally, previous work by the Townsend group on hydroxybenzene systems will also be drawn upon for discussion.

Chapter 6 provides a discussion of experimental and theoretical investigations of a set of aliphatic amines. These experiments investigate a number of tertiary amines following excitation at 200 nm.

Finally, Chapter 7 will form a general conclusion of the work discussed in the previous chapters and suggest ideas for further investigations in this field to follow on from this work.

1.8 – References

1. A. H. Zewail, J. Phys. Chem. **100** (31), 12701-12724 (1996).
2. W. H. Miller, Ann. Rev. Phys. Chem. **65**, 1-19 (2014).
3. A. J. Alexander and R. N. Zare, Acc. Chem. Res. **33** (4), 199-205 (2000).
4. J. Clayden, N. Greeves and S. Warren, *Organic Chemistry*, 2nd ed. (Oxford, 2012).
5. J. W. Storer, L. Raimondi and K. N. Houk, J. Am. Chem. Soc **116** (21), 9675-9683 (1994).
6. B. A. Horn, J. L. Herek and A. H. Zewail, J. Am. Chem. Soc **118** (36), 8755-8756 (1996).
7. E. W. G. Diau, S. De Feyter and A. H. Zewail, Chem. Phys. Lett. **304** (3-4), 134-144 (1999).
8. A. Natarajan, C. K. Tsai, S. I. Khan, P. McCarren, K. N. Houk and M. A. Garcia-Garibay, J. Am. Chem. Soc. **129** (32), 9846-9847 (2007).
9. N. Nelson and C. F. Yocum, in *Ann. Rev. Plant Biol.* (Annual Reviews, Palo Alto, 2006), Vol. 57, pp. 521-565.
10. A. Gilbert and J. Baggott, in *Essentials of Molecular Photochemistry* (Blackwell Science, London, 1991).
11. Y. Umena, K. Kawakami, J. R. Shen and N. Kamiya, Nature **473** (7345), 55-U65 (2011).
12. H. C. Chow, R. Serlin and C. E. Strouse, J. Am. Chem. Soc **97** (25), 7230-7237 (1975).
13. G. A. Swan, Fortschr. Chem. Org. Naturst. **31** (0), 521-582 (1974).
14. M. Brenner and V. J. Hearing, Photochem. Photobiol. **84** (3), 539-549 (2008).
15. A. Slominski, D. J. Tobin, S. Shibahara and J. Wortsman, Physiol. Rev. **84** (4), 1155-1228 (2004).
16. J. D. Watson and F. H. Crick, Nature **171** (4356), 737-738 (1953).
17. I. Cnossen, J. Sanz-Forcada, F. Favata, O. Witasse, T. Zegers and N. F. Arnold, J. Geophys. Res.-Planets **112** (E2) (2007).
18. G. M. Roberts and V. G. Stavros, Chem. Sci. **5** (5), 1698-1722 (2014).
19. A. L. Sobolewski, W. Domcke, C. Dedonder-Lardeux and C. Jouvet, Phys. Chem. Chem. Phys. **4** (7), 1093-1100 (2002).
20. E. Schrodinger, Phys. Rev. **28** (6), 1049-1070 (1926).
21. C. Eckart, Phys. Rev **46** (5), 0383-0387 (1934).
22. D. Wales, *Energy Landscapes*. (Cambridge Molecular Science, Cambrisge, 2003).
23. J. Simons, *An Introduction to Theoretical Chemistry*. (Cambridge University Press, Cambridge, 2003).
24. A. S. Coolidge, H. M. James and R. D. Present, J. Chem. Phys. **4** (3), 193-211 (1936).
25. A. Stolow, Philos. T. R. Soc. A **356** (1736), 345-362 (1998).
26. W. Domcke and G. Stock, Adv. Chem. Phys. <D> **100**, 1-169 (1997).
27. E. J. Heller, J. Chem. Phys. **62** (4), 1544-1555 (1975).
28. G. Wu, P. Hockett and A. Stolow, Phys. Chem. Chem. Phys. **13** (41), 18447-18467 (2011).
29. Y. Yamada, N. Mikami and T. Ebata, J. Chem. Phys. **121** (23), 11530-11534 (2004).
30. E. J. Heller, J. Chem. Phys. **64** (1), 63-73 (1976).
31. G. A. Worth and L. S. Cederbaum, Annu. Rev. Phys. Chem. **55**, 127-158 (2004).
32. M. G. Nix, A. L. Devine, B. Cronin and M. N. Ashfold, Phys. Chem. Chem. Phys. **8** (22), 2610-2618 (2006).

33. A. Iqbal and V. G. Stavros, J. Phys. Chem. A **114** (1), 68-72 (2010).
34. R. Livingstone, O. Schalk, A. E. Boguslavskiy, G. Wu, L. T. Bergendahl, A. Stolow, M. J. Paterson and D. Townsend, J. Chem. Phys. **135** (19) (2011).
35. P. Kruit, M. J. Vanderwiel and F. H. Read, Aip. Conf. Proc. (90), 390-394 (1982).
36. S. Lochbrunner, J. J. Larsen, J. P. Shaffer, M. Schmitt, T. Schultz, J. G. Underwood and A. Stolow, J. Electron. Spectrosc. **112** (1-3), 183-198 (2000).
37. A. L. Sobolewski and W. Domcke, Chem. Phys. Lett. **315** (3-4), 293-298 (1999).
38. T. A. A. Oliver, G. A. King and M. N. R. Ashfold, Phys. Chem. Chem. Phys. **13** (32), 14646-14662 (2011).
39. R. A. Livingstone, J. O. Thompson, M. Iljina, R. J. Donaldson, B. J. Sussman, M. J. Paterson and D. Townsend, J. Chem. Phys. **137** (18), 184304 (2012).
40. S. E. Greenough, M. D. Horbury, J. O. Thompson, G. M. Roberts, T. N. Karsili, B. Marchetti, D. Townsend and V. G. Stavros, Phys. Chem. Chem. Phys. **16** (30), 16187-16195 (2014).
41. B. Cronin, M. G. D. Nix, R. H. Qadiri and M. N. R. Ashfold, Phys. Chem. Chem. Phys. **6** (21), 5031-5041 (2004).
42. A. J. van den Brom, U. M. KapeliosDepartment of Chemistry, T. N. Kitsopoulos, N. H. Nahler, B. d. Cronin and M. N. R. Ashfold, Phys. Chem. Chem. Phys. **7** (5), 892 (2005).
43. G. A. King, T. A. Oliver, M. G. Nix and M. N. Ashfold, J. Chem. Phys. **132** (6), 064305 (2010).
44. V. Vallet, Z. Lan, S. Mahapatra, A. L. Sobolewski and W. Domcke, J. Chem. Phys. **123** (14), 144307 (2005).
45. Z. G. Lan and W. Domcke, Chem. Phys. **350** (1-3), 125-138 (2008).
46. M. Barbatti, M. Vazdar, A. J. Aquino, M. Eckert-Maksic and H. Lischka, J. Chem. Phys. **125** (16), 164323 (2006).
47. B. Sellner, M. Barbatti and H. Lischka, J. Chem. Phys. **131** (2), 024312 (2009).
48. M. G. Nix, A. L. Devine, B. Cronin, R. N. Dixon and M. N. Ashfold, J. Chem. Phys. **125** (13), 133318 (2006).
49. R. N. Dixon, T. A. Oliver and M. N. Ashfold, J. Chem. Phys. **134** (19), 194303 (2011).
50. R. S. Mulliken, Science **157** (3784), 13-24 (1967).
51. Z. Lan, W. Domcke, V. Vallet, A. L. Sobolewski and S. Mahapatra, J. Chem. Phys. **122** (22), 224315 (2005).
52. G. M. Roberts, A. S. Chatterley, J. D. Young and V. G. Stavros, J. Phys. Chem. Lett. **3** (3), 348-352 (2012).
53. C. M. Tseng, Y. T. Lee and C. K. Ni, J. Chem. Phys. **121** (6), 2459-2461 (2004).
54. J. L. Kinsey, Annu. Rev. Phys. Chem. **28**, 349-372 (1977).
55. J. Lowe, *Quantum Chemistry*. (Academic Press, London, 1978).
56. R. B. Setlow, W. L. Carrier and F. J. Bollum, Proc. Natl. Acad. Sci. USA **53** (5), 1111-1118 (1965).
57. C. E. H. Dessent and K. Muller-Dethlefs, Chem. Rev. **100** (11), 3999-4021 (2000).
58. R. N. Zare, Annu. Rev. Anal. Chem. **5**, 1-14 (2012).
59. K. L. King, G. Paterson, G. E. Rossi, M. Iljina, R. E. Westacott, M. L. Costen and K. G. McKendrick, Phys. Chem. Chem. Phys. **15** (31), 12852-12863 (2013).
60. J. Xu and J. R. Knutson, Methods. Enzymol. **450**, 159-183 (2008).
61. R. Berera, R. van Grondelle and J. T. Kennis, Photosynth Res **101** (2-3), 105-118 (2009).

62. E. Wrede, S. Laubach, S. Schulenburg, A. Brown, E. R. Wouters, A. J. Orr-Ewing and M. N. R. Ashfold, J. Chem. Phys. **114** (6), 2629-2646 (2001).
63. C. Z. Bisgaard, O. J. Clarkin, G. Wu, A. M. Lee, O. Gessner, C. C. Hayden and A. Stolow, Science **323** (5920), 1464-1468 (2009).
64. R. Crespo-Otero, M. Barbatti, H. Yu, N. L. Evans and S. Ullrich, Chemphyschem **12** (17), 3365-3375 (2011).
65. S. Deb, B. A. Bayes, M. P. Minitti and P. M. Weber, J. Phys. Chem. A **115** (10), 1804-1809 (2011).
66. A. Stolow, A. E. Bragg and D. M. Neumark, Chem. Rev **104** (4), 1719-1757 (2004).
67. D. Townsend, S. A. Lahankar, S. K. Lee, S. D. Chambreau, A. G. Suits, X. Zhang, J. Rheinecker, L. B. Harding and J. M. Bowman, Science **306** (5699), 1158-1161 (2004).
68. S. Hammerum, K. Norrman, T. I. Solling, P. E. Andersen, L. B. Jensen and T. Vulpius, J. Am. Chem. Soc **127** (17), 6466-6475 (2005).
69. M. Staniforth and V. G. Stavros, Proc. Roy. Soc. A. Math. Phys. Eng. Sci. **469** (2159) (2013).
70. T. Suzuki, Annu. Rev. Phys. Chem. **57**, 555 (2006).
71. K. Muller-Dethlefs and E. W. Schlag, Angew. Chem. Int. Edit. **37** (10), 1346-1374 (1998).
72. X. Yang, Phys. Chem. Chem. Phys. **13** (18), 8112-8121 (2011).
73. D. W. Chandler and P. L. Houston, J. Chem. Phys. **87** (2), 1445-1447 (1987).
74. J. Solomon, J. Chem. Phys. **47** (3), 889-& (1967).
75. P. L. Houston, in *Imaging in molecular dynamics*, edited by B. Whitaker (Cambridge University Press, Cambridge, 2003).
76. A. T. J. B. Eppink and D. H. Parker, Rev. Sci. Instrum. **68** (9), 3477-3484 (1997).
77. R. N. Strickland and D. W. Chandler, Appl.Opt. **30** (14), 1811-1819 (1991).
78. M. J. J. Vrakking, Rev. Sci. Instrum. **72** (11), 4084-4089 (2001).
79. B. Jones and C. L. Ruiz, Rev. Sci. Instrum. **84** (7), 073510 (2013).
80. G. M. Roberts, J. L. Nixon, J. Lecointre, E. Wrede and J. R. Verlet, Rev. Sci. Instrum. **80** (5), 053104 (2009).
81. G. A. Garcia, L. Nahon and I. Powis, Rev. Sci. Inst. **75** (11), 4989-4996 (2004).
82. K. L. Reid, Mol. Phys. **110** (3), 131-147 (2012).
83. K. L. Reid, Annu. Rev. Phys. Chem. **54**, 397-424 (2003).
84. L. J. Radziemski, Spectrochim. Acta B. **57** (7), 1109-1113 (2002).
85. S. Kimel and S. Speiser, Chem. Rev **77** (4), 437-472 (1977).
86. J. Herrmann and W. Bernd, *Lasers for Ultrashort Light Pulses*. (North-Holland Physics Publishing, Berlin, 1987).
87. S. Link, H. A. Durr and W. Eberhardt, J. Phys-Condens. Mat. **13** (34), 7873-7884 (2001).
88. D. Strickland and G. Mourou, Opt. Comm. **55** (6), 447-449 (1985).
89. R. Thomson, C. Leburn and D. Reid, in *Ultrafast Nonlinear Optics* (Springer, London, 2013).
90. R. W. Boyd, Nonlinear Optics, 3rd Edition, 1-613 (2008).
91. H. E, *Optics*, 4 ed. (Addison Wesley, San Francisco, 2007).
92. A. H. Zewail, Chemical Reactions and Their Control on the Femtosecond Time Scale Xxth Solvay Conference on Chemistry **101**, 892-892 (1997).
93. P. J. Bustard, G. Wu, R. Lausten, D. Townsend, L. A. Walmsley, A. Stolow and B. J. Sussman, Faraday Discuss **153**, 321-342; discussion 395-413 (2011).

94. D. Townsend, B. J. Sussman and A. Stolow, J. Phys. Chem. A **115** (4), 357-373 (2011).
95. P. Brumer and M. Shapiro, Annu. Rev. Phys. Chem. **43**, 257-282 (1992).
96. D. G. MacLachlan, R. R. Thomson, C. R. Cunningham and D. Lee, Opt Mater Express **3** (10), 1616-1623 (2013).
97. N. D. Psaila, R. R. Thomson, H. T. Bookey, A. K. Kar, N. Chiodo, R. Osellame, G. Cerullo, A. Jha and S. Shen, Appl. Phys. Lett. **90** (13), 131102 (2007).
98. C. Cramer, *Essentials of Computational Chemistry*, 2nd ed. (Wiley, Chichester, 2008).
99. .
100. R. Krishnan, J. S. Binkley, R. Seeger and J. A. Pople, J. Phys. Chem. **72** (1), 650-654 (1980).
101. T. H. Dunning, J. Chem. Phys. **90** (2), 1007-1023 (1989).
102. J. B. Foresman, M. Headgordon, J. A. Pople and M. J. Frisch, J. Phys. Chem. **96** (1), 135-149 (1992).
103. J. Kohanoff, *Electronic Structure Calculations for Solids and Molecules*. (Cambridge University Press, Cambridge, 2006).
104. J. D. Watts, in *Radiation Induced Molecular Phenomena in Nucleic Acids*, edited by M. Shukla and J. Leszczynski (Springer, 2008).
105. W. Kohn and L. J. Sham, Phys. Rev. **140** (4A), 1133-1138 (1965).
106. W. Kohn, Rev. Mod. Phys. **71** (5), 1253-1266 (1999).
107. A. D. Becke, J. Chem. Phys. **98** (2), 1372-1377 (1993).
108. M. E. Casida, C. Jamorski, K. C. Casida and D. R. Salahub, J. Chem. Phys. **108** (11), 4439-4449 (1998).
109. R. E. Stratmann, G. E. Scuseria and M. J. Frisch, J. Chem. Phys. **109** (19), 8218-8224 (1998).
110. J. F. Stanton and R. J. Bartlett, J. Chem. Phys. **98** (9), 7029-7039 (1993).
111. F. Furche and R. Ahlrichs, J. Chem. Phys. **117** (16), 7433-7447 (2002).
112. M. Petersilka, U. J. Gossmann and E. K. Gross, Phys. Rev. Lett. **76** (8), 1212-1215 (1996).
113. D. R. Yarkony, Rev. Mod.Phys. **68** (4), 985-1013 (1996).
114. M. A. Robb, M. Garavelli, M. Olivucci and F. Bernardi, Rev. Comp. Ch. **15**, 87-146 (2000).
115. M. A. Elsayed, J. Chem. Phys. **38** (12), 2834 (1963).

Chapter 2 – Experimental

There are many key elements to running the velocity map imaging experiment, which together culminate in the ability to produce the data presented in Chapter 3 – 6. This chapter will provide an overview of the experimental methods used to obtain the time-resolved photoelectron imaging (TRPEI) data, as well as the software used to process and analyse the data in a meaningful manner.

2.1 – Optical system

2.1.1 – Laser system

The laser system is one of the key tools used in the experiments described in Chapters 3-6 and, as such, a detailed description is provided here. During the work outlined in this thesis, a significant redesign of the optical table was performed from the previously published description.[1] This was in order to incorporate extra tuneable wavelength ranges to the experiment, as well as to incorporate a new optical parametric amplifier (TOPAS™) beam line. The optical table as a whole is shown in Figure 2.4, and a full description of the optical set-up is given in the following section.

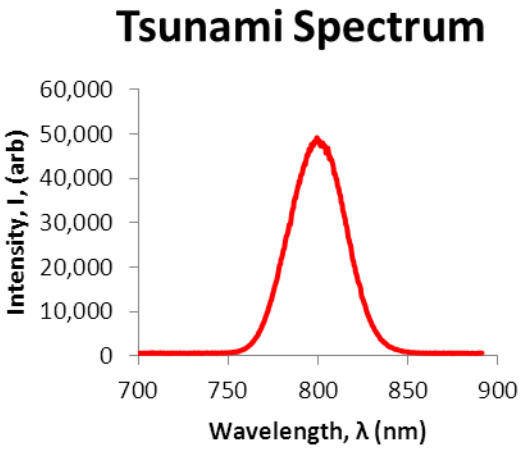

Figure 2.1- Spectrum of Tsunami Output

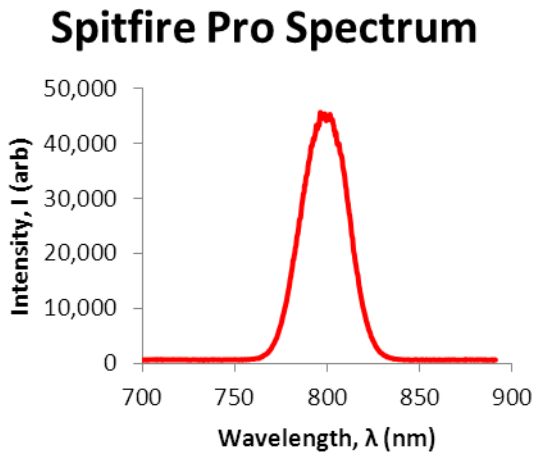

Figure 2.2 – Spectrum of Spitfire Pro

The laser system employed is a regeneratively amplified 800 nm Ti:Sapphire solid state femtosecond pulsed system. It has two distinct sections, the oscillator and the amplifier. The oscillator, which produces the femtosecond pulse seed for the amplifier, is a Spectra Physics Tsunami mode locking laser; pumped by a Millennia CW DPSS 532 nm laser with a 5 W, narrow bandwidth. The central wavelength of the output of the

Tsunami is 800 nm, typically with a power of 400 mW, with a pulse reputation rate of 80 MHz, and a bandwidth of ~40 nm. The spectral profile of this light is shown in Figure 2.1. The amplifier is a Spectra Physics Spitfire femtosecond regenerative system, pumped by a 20 W, 532 nm, Q-switched Nd:YLF laser set to a 1 KHz repetition rate. The amplifier operates as a chirped pulsed amplifier (CPA).[2] As shown in Figure 2.3, CPA consists of three steps. In the first stage, the broadband seed pulse is passed off a set of gratings which stretch the pulse in time. This allows the amplification to occur without damaging the optics inside the cavity due to the high peak power of the amplified pulse. The second stage is amplification, where the stretched seed light and the green pump light are passed through a Ti:Sapphire rod, generating more 800 nm light. The pulse is switched in and out of the cavity by a combination of Pockels cells, which rotate the pulse polarisation, and polarising optics, which reflect or transmit the pulse according to its polarisation. Finally light is passed off a second set of gratings which compress the light back into a femtosecond pulse. This pulse compression process can be optimised by varying the path length between the gratings in the set. The output of the amplifier, the spectrum of which is shown in Figure 2.2, is a beam that is 1 cm in diameter, 4 W in average power, ~30 nm in bandwidth centred at 800 nm with a temporal duration of around 70 fs.

Throughout this chapter, references will be made to different-numbered beam lines, an in-house terminology for conveniently denoting various optical set-ups. The three referred to in this thesis will be named beam line 1, 2 and 3, all of which were used for the work described in Chapter 3-6.

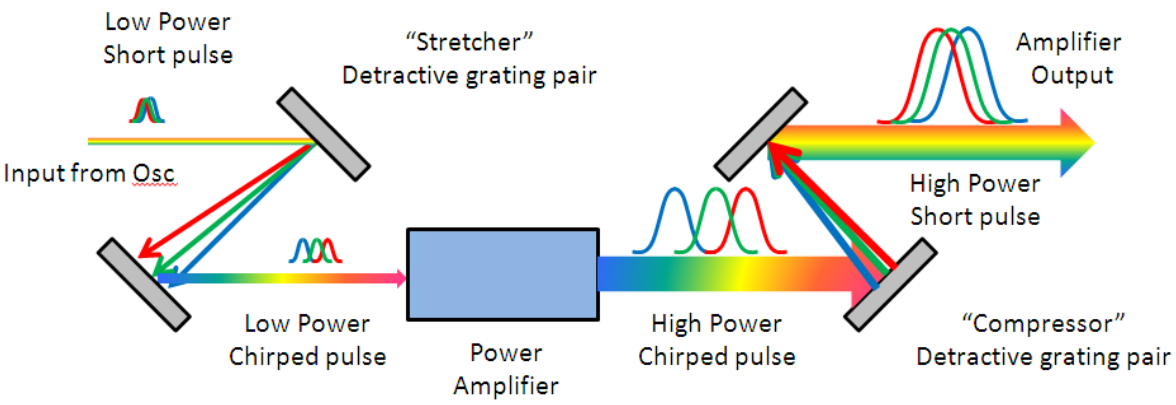

Figure 2.3 – Illustrative cartoon of a chirped pulse amplifier (CPA).

2.1.2 – Optical table set-up

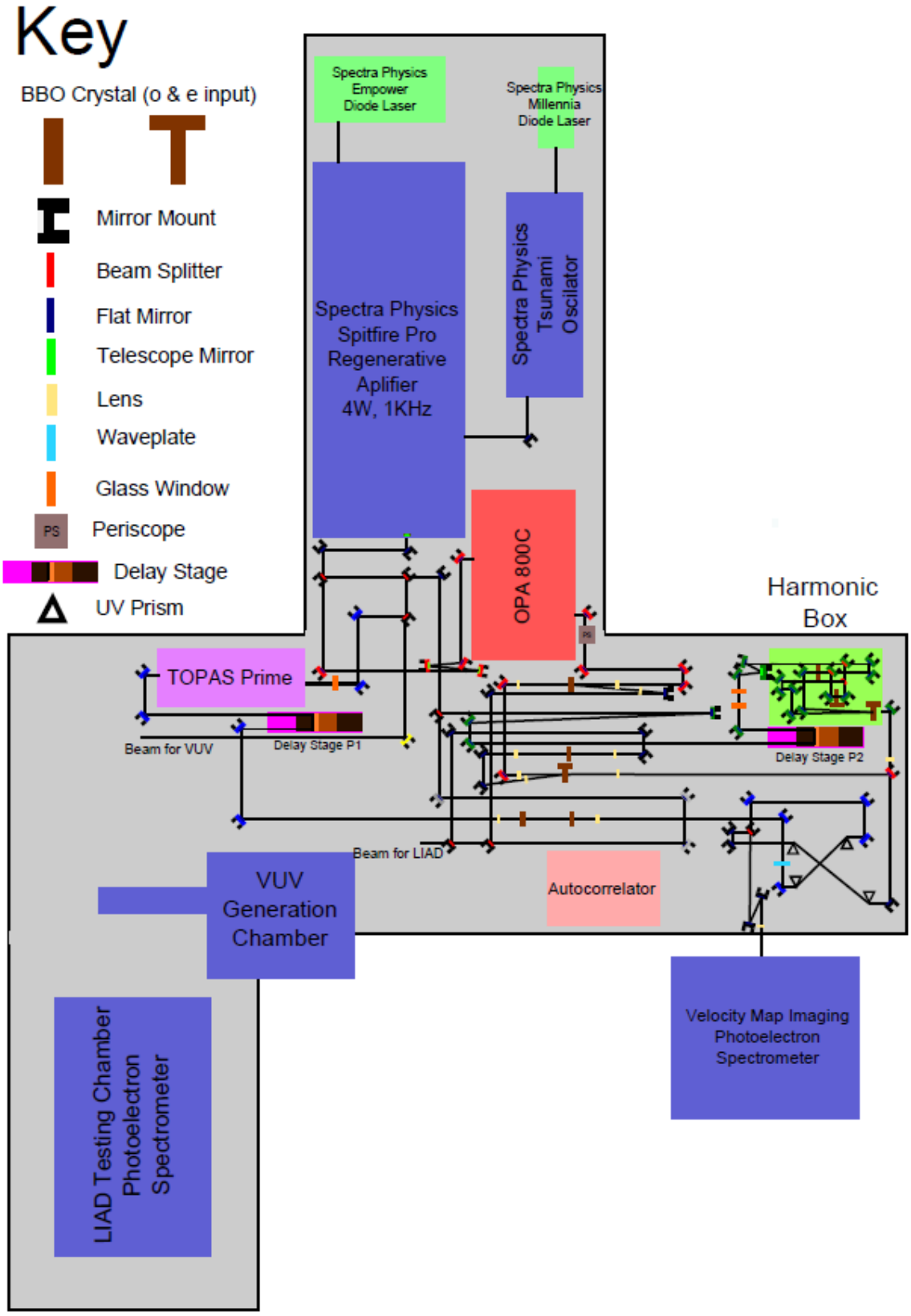

Figure 2.4 – Scale drawing of optical table set up. A key for various components is shown on the top left. Mirror mount colours represent different beam paths. Beam paths for other projects are not shown on this diagram and have been colour coded to match the in-house terminology outlined in this chapter.

2.1.3 – Beam line 1 set-up

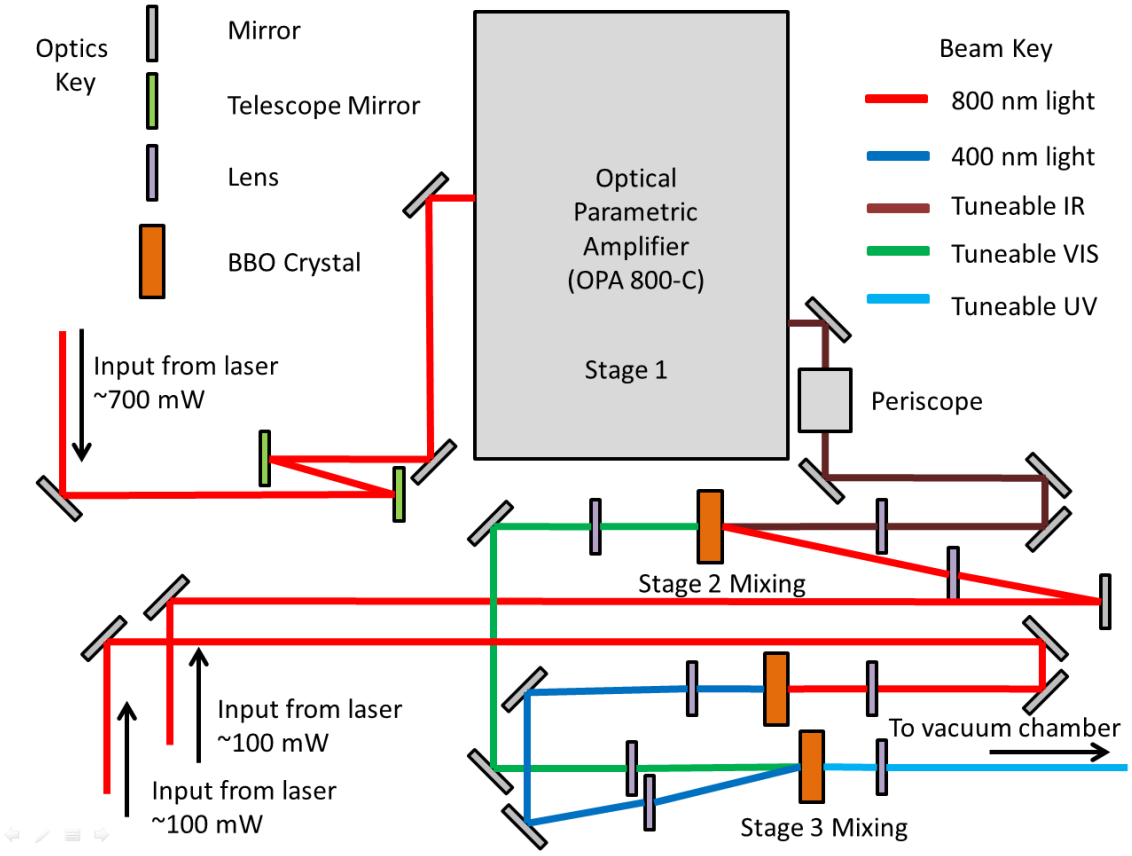

Figure 2.5 – Schematic of beam line 1

The primary role of beam line 1 is to produce high energy tuneable pulses of UV light for use as the pump for many of the experiments performed by the group. Figure 2.5 shows the various stages of this beam line. Stage 1 utilises a Spectra Physics OPA-800C to produce tuneable IR pulses in the range of 1.2 – 2.5 µm using either the signal or idler output. The OPA is pumped by an 800 nm beam (800 µJ/pulse) which, prior to entering the OPA, is passed through a 3:2 telescope. The output power of the OPA depends upon where on the OPA tuning curve the selected signal or idler wavelength lies. Typically, the output power of the signal from the OPA is in the region of 50 – 80 µJ/pulse. The IR output of the OPA is focused with a f = 20 cm BK7 anti reflection (AR) coated lens through a 0.2 mm thick BBO crystal cut at 29°, and is sum frequency mixed (SFM) with an additional beam of 800 nm light (150 µJ/pulse) which is focused using a f = 30 cm BK7 lens through the BBO crystal (this process is shown as stage 2 in Figure 2.5). The resulting visible output from this SFM process is re-collimated by an f = 20 cm fused silica lens with an AR coating suitable for the wavelength range. This visible light is then focused using a f = 20 cm AR coated fused silica lens through a second 0.2 mm thick BBO crystal cut at 65° and is frequency doubled into the UV

(stage 3 in Figure 2.5). This frequency doubling step can also be configured to mix an additional beam of 400 nm light (35 μJ/pulse), if deeper UV light is required. The resulting ultraviolet beam is re-collimated using a f = 20 cm fused silica lens and is then passed through a pair of fused silica prisms for temporal dispersion control (see Section 2.1.7) and combined with either beam line 2 or beam line 3 before entering the VMI spectrometer.

Depending on the wavelength required for the experiment, combinations of frequency doubling or mixing with 800 nm light (or 400 nm light) allows the UV wavelength to be tuned over a wide range between 218 - 350 nm. The combinations of processes required to achieve this tuneability is shown in Table 2.1. The generated wavelengths of these processes were calculated using of the SNLO program.[3, 4]

Wavelength Range	OPA output	Stage 2	Stage 3	Average output Power at chamber (mW)*
218 - 228	Sig	SFM (800)	SFM (400)	0.8
229 - 247	Idl	SFM (800)	SFM (400)	--
240 - 264	Sig	SFM (800)	SHG	1.3
269 – 324	Idl	SFM (800)	SHG	--
300 – 388	Sig	SHG	SHG	1.5
412 – 850	Idl	SHG	SHG	--

Table 2.1 – Wavelength range of beam line 1 by combinations of either Sum Frequency Mixing (SFM) or Second Harmonic Generation (SHG). *The Idler combinations have not been tested and as such no power measurements have been made. However their wavelength range have been generated using the SNLO[3, 4] program for completeness. Maximum wavelength used from the idler was 3400 nm due to the cut off in SNLO[3, 4].

2.1.4 – Beam line 2 set-up

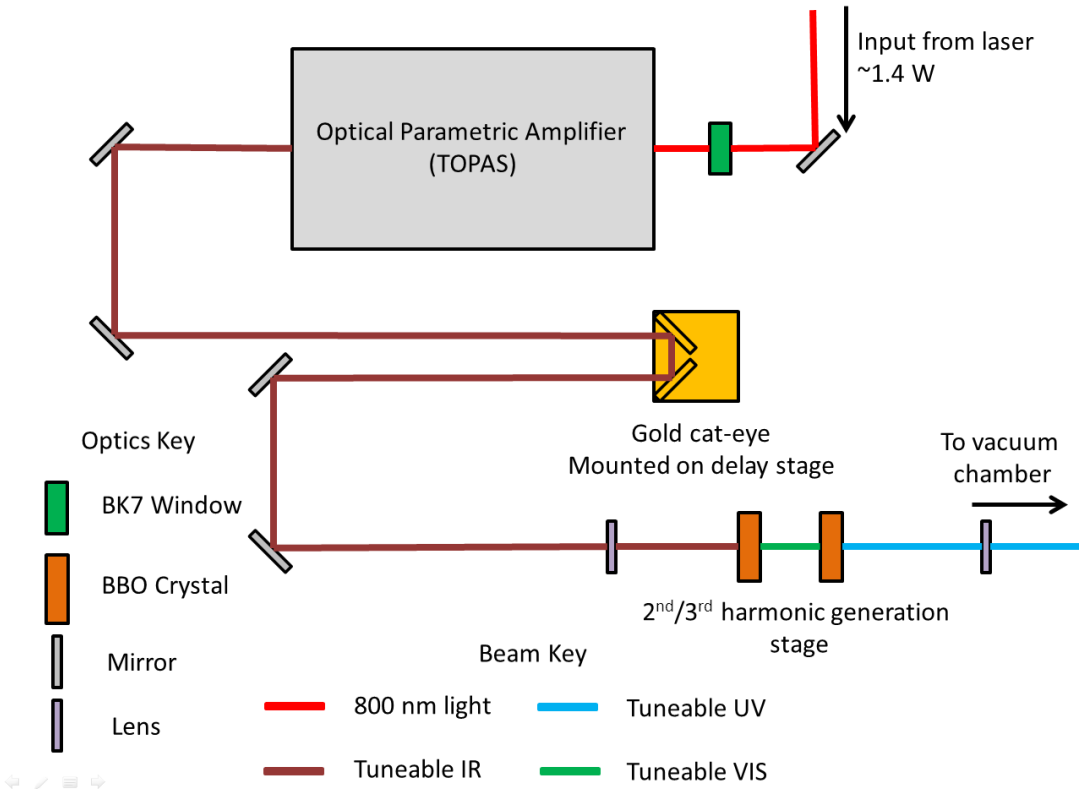

Figure 2.6 – Schematic of beam line 2

Beam line 2 provides the main source of tuneable light between 300 nm and 350 nm, usually for the "probe" in the TRPEI experiments. Figure 2.6 shows the general schematic of the beam line. The OPA, (TOPAS, Light Conversion) is pumped by 1.4 mJ/pulse of 800 nm (at 1 KHz) to generate tuneable IR from 1.16 – 2.5 µm. Prior to its input into the TOPAS, the 800 nm pump beam passes through a 10 mm BK7 glass window. This introduces the appropriate chirp into the 800 nm pulse for maximum UV generation. The signal output of the OPA is produced with an average power of 300 µJ/pulse at 1.2 µm. The TOPAS output is focused using a f = 20 cm BK7 AR coated lens through a pair of BBO crystals, the first being a 0.5 mm thick and cut at 29° and the second being a 0.1 mm crystal and cut at 45°. The focus of the IR is located in-between the two crystals. The UV is collimated by a 20 cm AR coated fused silica lens. The generated UV beam then passes through a 303 nm λ/2 waveplate to rotate the UV polarisation to horizontal (as is required for the VMI set-up) and then through a pair of calcium fluoride (CaF_2) prisms for temporal dispersion control. The beam is then combined with beam line 1 or 3 and passed through a lens and into the spectrometer. Beam line 2 is capable of producing a 3.5 µJ/pulse of 300 nm light at the vacuum chamber entrance.

2.1.5 – Beam line 3 set-up

Beam line 3 is used to generate the 3rd and 4th harmonic of the 800 nm fundamental output from the Ti:Sapphire laser system. Figure 2.7 presents a schematic of this beam line. The line is pumped by a beam of 800 nm light (with an energy of 280 µJ/pulse), which prior to entering the "harmonic generator box" passes through a set of 5 mm BK7 glass plates set to an angle of 35° (with respect to the propagating direction), this introduces the appropriate chirp into the 800 nm pulse for maximum UV generation. The 800 nm beam is then focused by an f = 1.5 m focusing mirror through the harmonic generator box as shown in Figure 2.7, with the focal point located just after the final BBO crystal. The 800 nm input beam is split by a pair of beam splitters, the first being 80% reflecting and the second being 20% reflecting. The beam that passed through the second beam splitter is then frequency doubled, in a 0.5 mm 29° cut BBO crystal, to generate 400 nm light. This 400 nm light is then co-linearly combined with another 800 nm beam (which passed through the first beam splitter) to generate 267 nm light in a 0.2 mm 45° cut BBO crystal using sum frequency mixing (SFM). The generated 267 nm beam is then SFM with another beam of 800 nm (the beam reflected of the second beam splitter) in a non collinear geometry in a 0.2 mm 65° BBO crystal, generating the 200 nm light. The 200 nm beam (or 267 nm beam if the final step is not used) is then collimated using a f = 75 cm fused silica lens. The harmonic box produces 2.5 µJ/pulse

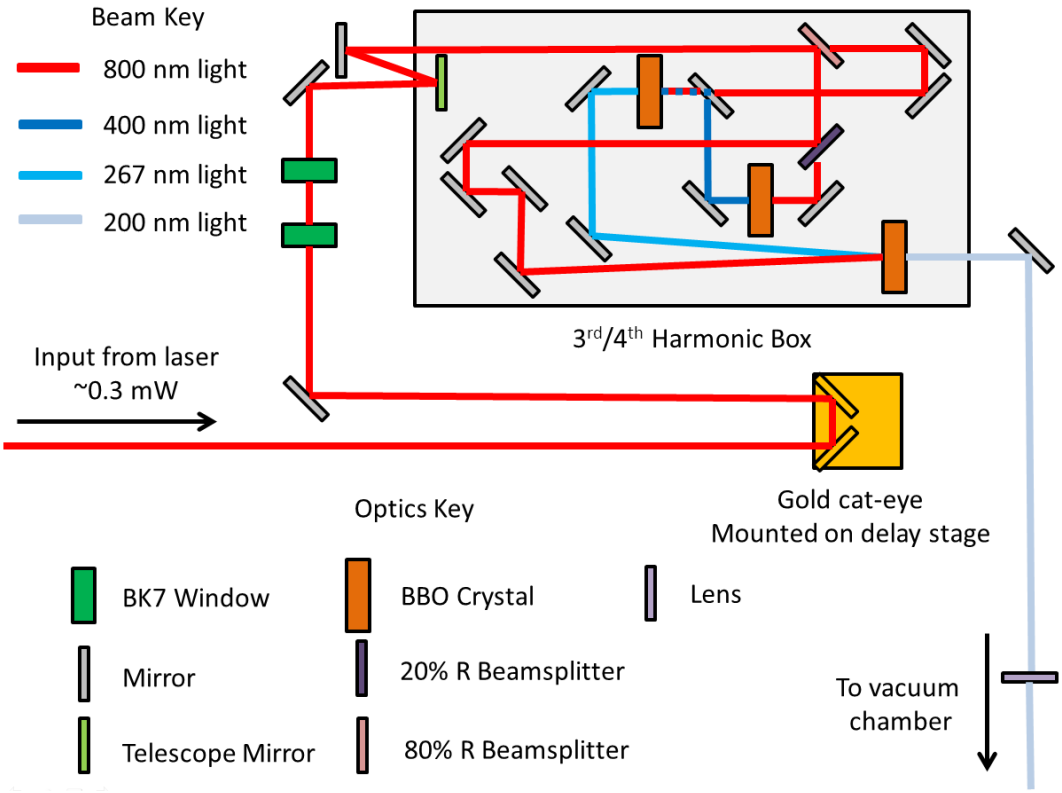

Figure 2.7 – Schematic of beam line 3

of 267 nm or 0.7 µJ/pulse of 200 nm for use in the TRPEI experiment.

This design of the harmonic generator box is a more streamlined version of a previous set-up used by the group,[1] with this version occupying only half the previous bench area, and requiring a significantly lower input power for an equivalent level of output.

2.1.6 – Beam compression & chirp control

Prior to entering the vacuum chamber used for the TRPEI experiments, the beams are passed through independent single pass prism compressors, as illustrated schematically in Figure 2.8. The prism compressors apply a negative chirp to the pulse in order to compensate for the various dispersing processes that occur along the beam line.[5, 6] This is in order to achieve the optimum temporal pump-probe resolution measured *in situ* of 100 - 130 fs. Dispersion management is necessary due to the large spectral bandwidth of the femtosecond pulses. The compressors are comprised of a matched pair of either calcium fluoride (CaF_2) or fused silica prisms. Beam line 1 or 3 passes through the CaF_2 compressor and beam line 2 passes through the fused silica compressor. These compressors operate in the following manner. As light passes through varous optics such as BBO crystals, lenses and beamsplitters, the light is "chirpped". This is due to the fact that different wavelengths propagate through optical materials at different speeds. As such, the "redder" or lower energy part of the pulse will travel faster through the material than the "bluer" higher energy part. If uncorrected, this chirp may result in pulse durations (in the spectrometer) which are 100 fs longer than the shortest possible durations achievable with the measured frequency bandwidth. The amount of chirp applied by the compressor is dependent on the tip-to-tip path length, *l*, between the two prisms and the amount of material the light passes through in the second prism, measured as *d*, the distance from the prism tip, (see Figure 2.8). In principle, the tip-to-tip seperation, *l*, for attaining the shortest pulse duration can be calculated by using Eq. 2.1[1, 5]

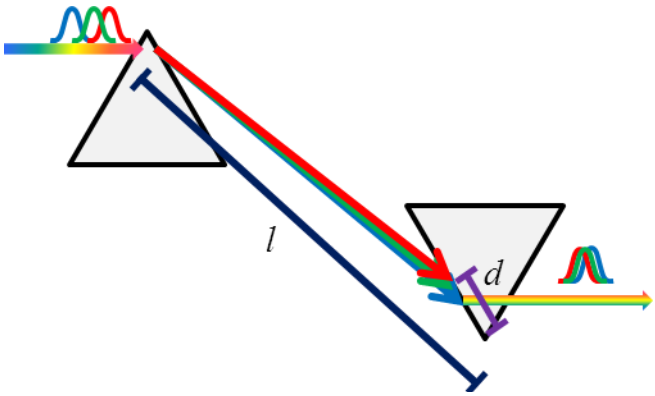

Figure 2.8 – Illustration of prism compressor set-up. The tip-to-tip distance between the prisms has been identified as *l*, and the distance from the prism tip the beam passes through the second prism is labelled as *d*. Both of these values are critical to the dispersion control process, see text for more details

$$l = \frac{\frac{d^2n}{d\lambda^2} d - \frac{6\pi c^2 GDD_p}{\lambda^3}}{40\left(\frac{d^2n}{d\lambda^2} + \left[2n - \frac{1}{n^3}\right]\left[\frac{dn}{d\lambda}\right]^2\right) sin\left(-2\frac{dn}{d\lambda}\Delta\lambda\right) - 80\left(\frac{dn}{d\lambda}\right)^2 \cos\left(-2\frac{dn}{d\lambda}\Delta\lambda\right)}$$

(2.1)

Here GDD_p is the group delay dispersion inside the prism (given in equation 2.5 and described in more detail later), and $\frac{d^2n}{d\lambda^2}$ is given by the following, beginning with the Sellmeir equation.[5, 7]

$$n(\lambda) = \sqrt{1 + \frac{C_1\lambda^2}{\lambda^2 - C_2} + \frac{C_3\lambda^2}{\lambda^2 - C_4} + \frac{C_5\lambda^2}{\lambda^2 - C_6}}$$

(2.2)

$$\frac{dn}{d\lambda} = \frac{1}{2n} - \frac{2C_1C_2\lambda}{(\lambda^2 - C_2)^2} - \frac{2C_3C_4\lambda}{(\lambda^2 - C_4)^2} - \frac{2C_5C_6\lambda}{(\lambda^2 - C_6)^2}$$

(2.3)

$$\begin{aligned}\frac{d^2n}{d\lambda^2} = \frac{1}{2n^3}\left(\frac{C_1\lambda^3}{[\lambda^2 - C_2]^2} + \frac{C_1\lambda}{\lambda^2 - C_2} - \frac{C_3\lambda^3}{[\lambda^2 - C_4]^2} + \frac{C_3\lambda}{\lambda^2 - C_4} - \frac{C_5\lambda^3}{[\lambda^2 - C_6]^2} + \frac{C_5\lambda}{\lambda^2 - C_6}\right)^2 \\ + \frac{1}{n}\left(\frac{4C_1\lambda^4}{[\lambda^2 - C_2]^3} - \frac{5C_1\lambda^2}{[\lambda^2 - C_2]^2} + \frac{C_1}{\lambda^2 - C_2} + \frac{4C_3\lambda^4}{[\lambda^2 - C_4]^3} - \frac{5C_3\lambda^2}{[\lambda^2 - C_4]^2}\right. \\ \left. + \frac{C_3}{\lambda^2 - C_4} + \frac{4C_5\lambda^4}{[\lambda^2 - C_6]^3} - \frac{5C_5\lambda^2}{[\lambda^2 - C_6]^2} + \frac{C_5}{\lambda^2 - C_6}\right)\end{aligned}$$

(2.4)

Here, C_n are the Sellmeir coefficients of the material used, λ is the wavelength and $n(\lambda)$ is the refractive index as a function of the wavelength.

$$GDD_p = \frac{1}{4ln(2)}\sqrt{\left(\frac{\lambda^2 c_b \Delta t_i}{c\Delta\lambda}\right)^2 - \left(\frac{\lambda^2 c_b}{c\Delta\lambda}\right)^4}$$

(2.5)

Here, c_b is the time-bandwidth product (0.44 for a Gaussian pulse), Δt_i is the initial pulse duration upon entering the prism and $\Delta\lambda$ is the spectral bandwidth of the pulse. Practically, however, there are certain difficulties involved in calculating these values. The initial pulse duration of the UV pulse is extremely difficult to determine without specifically designed UV autocorrelators. Typically, standard autocorrelation methods involving frequency doubling[8] will not work on an open optical bench for a number of reasons. Firstly, frequency doubling UV would produce wavelengths of light in the VUV (vaccum ultraviolet) range, meaning that the light is absorbed by the O_2 in the air. Secondly, non-linear materials other than BBO are required for this process, as the required phase matching angle for doubling UV does not exist for BBO. Thirdly, as the wavelength gets shorter, it is possible to start exciting real transitions within the material, depending upon its bandgap. This being said, more recently, specialised methods of UV autocorrelation have been demonstrated by other groups, an example is that of Hofmann *et al*.[9]

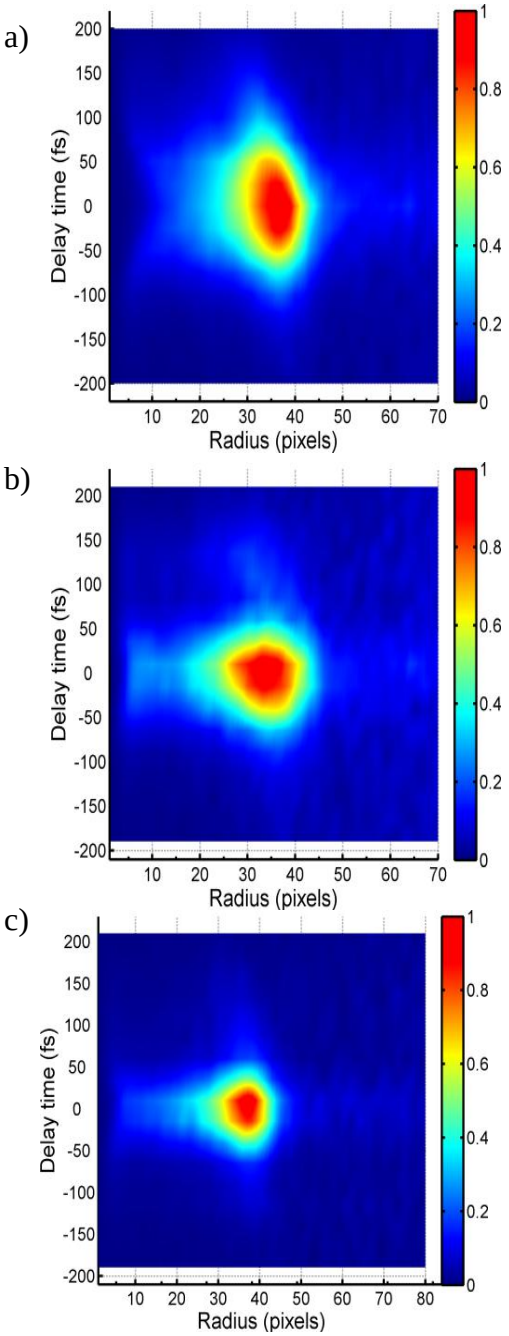

Figure 2.9 – Example cross correlation measurements using the VMI spectrometer. Recorded using 1,3-dutadiene in a [1+1′] using 240 + 310 nm light

It is still possible to characterise short temporal pulses generated for the experiment by using the VMI spectrometer as a crosscorrelator. By using a molecule that does not absorb either the pump or probe wavelengths, but where the combined photon energy is able to ionise the molecule, it is possible to make a measurement in a manner similar to the frequency resolve optical gating technique (FROG).[8] Figure 2.9 shows some examples of this FROG-like trace using the electron kinetic energy spectra of the molecule butadiene. This system is a good choice for taking this measurement as the

molecule used to measure the cross correlation must have a high lying first excited state (which is at 5.92 eV in butadiene)[10] and, ideally, have a reasonably low ionisation potential (9.07 eV in this case).[11] As such, many of the pump-probe wavelength combinations used in experiements disucssed in Chapters 3 – 6 can ionise butadiene in a non-resonant [1+1′] scheme. Figure 2.9a shows an example of an undercompensated chirped pulse, Figure 2.9b gives an example of an compensated–chirped pulse with significant 3rd order dispersion, and finally Figure 2.9c shows an example of a chirp compensated pulse. In practice, the optimum cross correlation is obtained by systematically changing the length of one of the prism compressors (either the pump or probe) until the shortest response is obtained. Once achieved, the other arm is altered to improve the cross correlation. This process is itterated until the compressors have been set at the correct lengths to obtain the shortest experimental temporal resolution. It should noted that the ideal compressor distance is wavelength dependent, thus, this process must be undertaken every time the central wavelength of either beam is tuned.

Finally, for the experiments detailed in this thesis it should be ntoed that great care was taken to ensure that the total intensity of the laser light was controlled to avoid any significant multi-photon or above threshold ionisation schemes. For all the experiements outlined the pulse energy (or peak power) was limited to around 10^{13}-10^{14} W/cm^{-1}.

2.1.7 – Laser beam characterisation

Many of the experiments described subsequently in this thesis required the use of different pump and probe wavelengths; which were measured using an Ocean Optics USB 2000+ spectrometer and viewed using the Ocean Optics Spectra Suite software. All wavelengths quoted have an implicit error of ± 0.2 nm from the spectrometer. Regular monitoring of both the laser bandwidth and wavelength is required in order to maintain the transition energy of the prepared excited state, allowing multiple scans to be summed together for higher signal-to-noise ratios. It is also necessary to monitor the power of these beam lines, in order to ensure consistency during data acquisition. For high energy beams, with an average power >10 µJ/pulse, a Spectra-Physics model 407a analogue power meter, was used to measure the laser power. For average powers below 10 µJ/pulse a Thorlabs PM100A analogue power meter with a standard S120VC photodiode sensor was employed.

2.2 – Velocity map imaging spectrometer

2.2.1 – Vacuum chamber

Figure 2.10 shows a cut through of the vacuum chamber[12] used in the experiments described in the following chapters. The chamber is divided into two sections, a source chamber and main chamber. The source chamber (the lower half of the system) is pumped to a base pressure of 1.8 $\times 10^{-8}$ mbar by a combination of an Edwards turbo molecular pump (2200 l/s pumping speed) and an Edwards M40 rotary pump. This chamber contains an Even-Lavie (EL) molecular beam pulsed valve,[13] used for delivering the target sample to the interaction region. The upper chamber is pumped to a base pressure of 4.2 $\times 10^{-9}$ mbar by a combination of an Edwards's turbo molecular pump (480 l/s pumping speed) and an Edwards M28 rotary pump. This part of the chamber contains a velocity map imaging (VMI) electrostatic lens set-up as well as a MCP/Phosphor detector. To cut out external magnetic fields, the entire time-of-flight region is encased in a double-layered mu-metal shield. It should be noted that the mu-metal shielding is also coated with graphite on the inner surface, to prevent localised charge build up in the flight tube that could distort the VMI image. The pressure in the chamber is determined through the use of two Pirani gauges (base pressure 10^{-4} mbar), measuring the pressure in the backing line between the rotary and turbo pumps, as well as a pair of wide range gauge (base pressure 10^{-9} mbar) located on both the source and main chambers. In both instances, the turbo molecular pump is situated directly on the vacuum chamber, whilst the rotary vacuum pumps are located in a separate pump room to minimise vibrations in the laser lab. Finally, it should be noted that the two halves of the chamber can be isolated through the use of a gate valve, based on the design of Stolow and co-

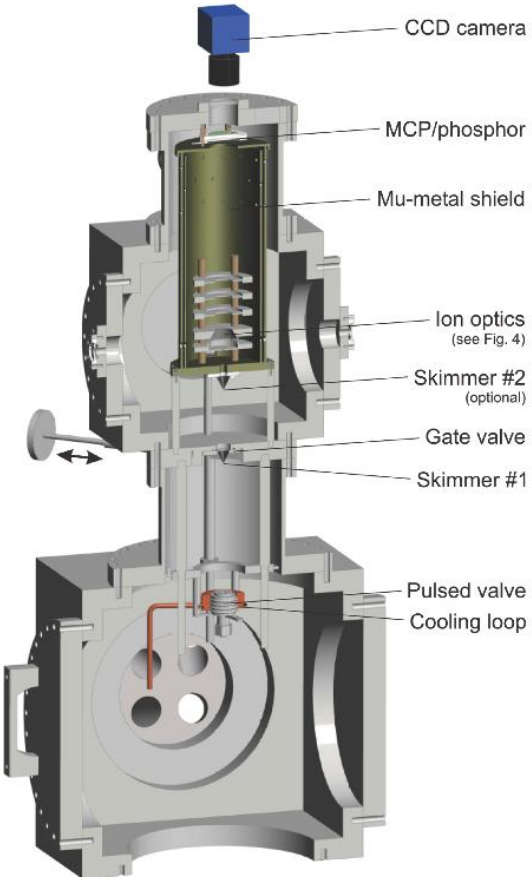

Figure 2.10 – 3D cut through view of VMI spectrometer

workers,[14] which allows for independent venting of the source chamber for a fast turnaround time when changing samples that are loaded directly into the EL valve.

2.2.2 – VMI ion optics & detector

As discussed previously in Chapter 1, a VMI spectrometer consists of set of electrostatic electrodes to focus charged particles onto a position sensitive detector. The design of the ion optics used for all experiments described in Chapters 3 - 6, based on the initial design of Parker *et al.*,[15] have been previously published elsewhere.[12] The design of this lens array was not part of the work for this thesis; however, a brief description is given here. The imaging is performed using a set of grade 316 stainless steel electrodes, as shown in Figure 2.11, which map the charged particles onto a 40 mm micro channel plate (MCP)/ phosphor screen detector (Photonis, APD 2 PS 40/12/10/12 I 46:1 P47). In Figure 2.11, electrode A is the "repeller" plate, which directs the particles towards the MCP, B is the "lens", which focuses the charged particles onto the MCP and C, D and E are additional electrodes, which may be used in combination with B to focus cations when performing a DC slice imaging experiment.[16] However, for the experiments within this thesis they were not used and therefore grounded.

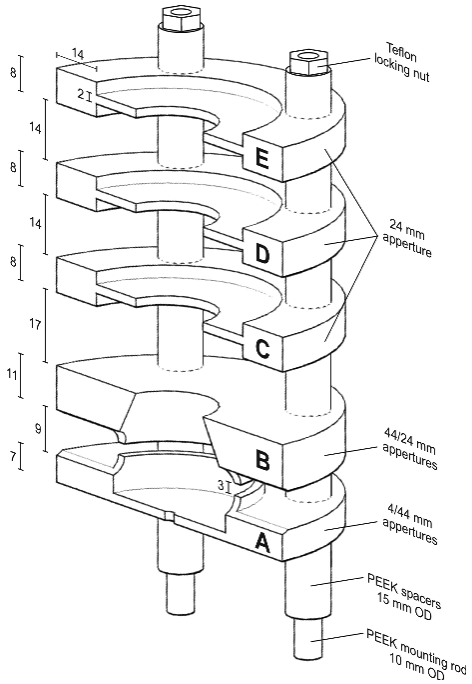

Figure 2.11 – Cut through of VMI optics. All units in mm

The voltage applied to the MCP/phosphor detector is gated to only measure the desired signal using a high-voltage pulser (DEI, PVX-4140). The timing for both the detector gate and the molecular beam firing was provided through the use of a multi-channel delay generator (Stanford DG535), using the Empower laser Q-switch signal as the external trigger. The light emitted by the MCP/Phosphor was captured using a monochrome firewire CCD camera (The Imaging Source, DMK 21BF04) without any additional processing (it should be noted that the camera and the laser pulse bandwidth (typically 2 nm in the UV) is the limiting factor of the resolution on the experiement.

2.2.3 – Sample delivery

Molecular samples are delivered into the vacuum chamber via an Even-Lavie (EL) pulsed molecular valve with a 200 µm diameter conical nozzle.[13] The temperature of the valve was controlled using a Neslab RTE-110 external chiller, containing a refrigerant of 50:50 ethylene glycol and water, connected to the EL valve via a copper cooling loop. The valve produces a pulsed molecular beam with a firing rate that matches the repetition rate of the laser (usually 1 KHz). The molecular beam travels from the lower source chamber to the upper main chamber through a 1 mm diameter skimmer, where, in the main chamber, it interacts with the laser beams. The molecular beam expansion typically cools the sample molecules to 10-30 K, however the experimental set-up does not allow direct measurement of the temperature. The cooling effect of the supersonic expansion is described by the following formula[17]:

$$\frac{T}{T_0} = \left(1 + \frac{\gamma - 1}{2} M^2\right)^{-1} \tag{2.6}$$

Where T is the translational temperature of the molecular beam, T_0 is the initial molecule temperature, γ is the ratio of the heat capacities and M is the Mach number (which is dependent upon the speed of sound and can be assumed to be very small in a vacuum). The molecular beam conditions are optimised by altering the pressure of the carrier gas (typically 1 - 3 bar). High pressures can produce enough supersonic cooling

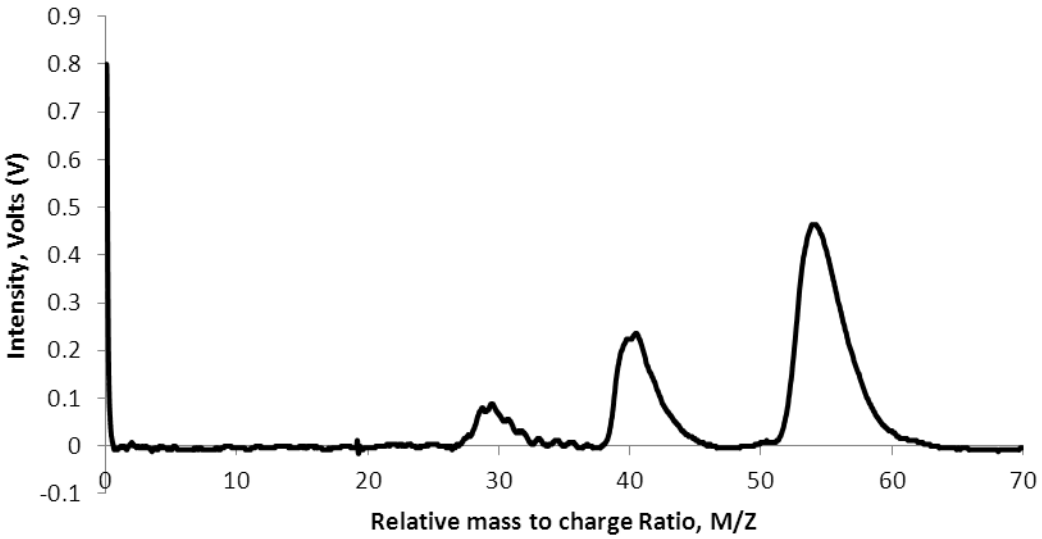

Figure 2.13 – Calibrated time-of-flight signal of 1,3-butadiene. Four main features are identified in the spectrum as a scattered light signal at 0 M/Z used as a zero reference point, and three fragment signals that come at 26, 39 and 54 M/Z identified as the C_2H_2 fragment, C_3H_3 fragment and the parent C_4H_6 respectively.

to allow cluster formation. The presence of clusters can be identified by recording a time-of-flight ion yield trace, an example of such a measurement may be seen in Figure 2.13 (although it should be pointed out that this trace shows only fragments of the parent as opposed to clusters which lie at a higher M/Z value). This data was captured using a SensL MicroFM-10035-X18 Photodiode detector, acquiring signal from the MCP/Phosphor detector and displayed using a Tektronix TDS1002B 60 MHz oscilloscope. These clusters may be removed through careful tuning of the molecular beam conditions.

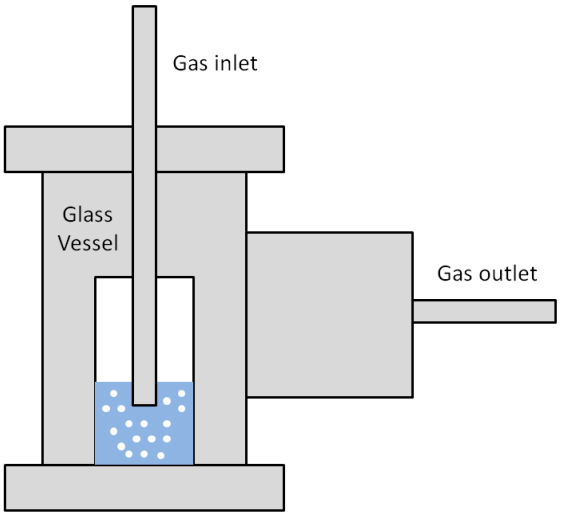

Figure 2.14 – Schematic of the external bubbler. The blue area represents the liquid or solid sample in the bubbler.

The sample can be carried into the chamber using a variety of different carrier gasses (usually helium) with a controllable backing pressure. The sample itself is either loaded directly into the back of the EL valve if the sample is a solid or low vapour pressure liquid (absorbed onto filter paper), or into an external bubbler, as shown in Figure 2.14, if the sample has a high enough vapour pressure (on the order of 0.5 mbar or more at 25 °C).

2.2.4 – Data handling & the REPEITS program

The data was recorded, processed and interpreted using a modified version of the REPEITS software written by Dr Ruth Livingstone and extensively described in her PhD thesis.[1] The current version has been updated to run on a later version of Matlab (Matlab2012a). The operation of the program remains unchanged but a brief description of the functionality of the program is given here. The software can be separated into three main programs named “Acquire”, “Process” and “Analyse”. The Acquire program records the VMI images and integrates a computer controlled stage (Physik Instrumente, M-403.62S stage controlled by a Physik Instrumente, Mercury Step), control of two Thorlabs shutters (Thorlabs, SH05 shutters with a Thorlabs, TSC001 controller) and image acquisition using the firewire CCD camera all into one program. Additionally, each collection cycle (or scan) acquires each image for a short amount of time in each instance, however, the photoelectron images at the same pump-

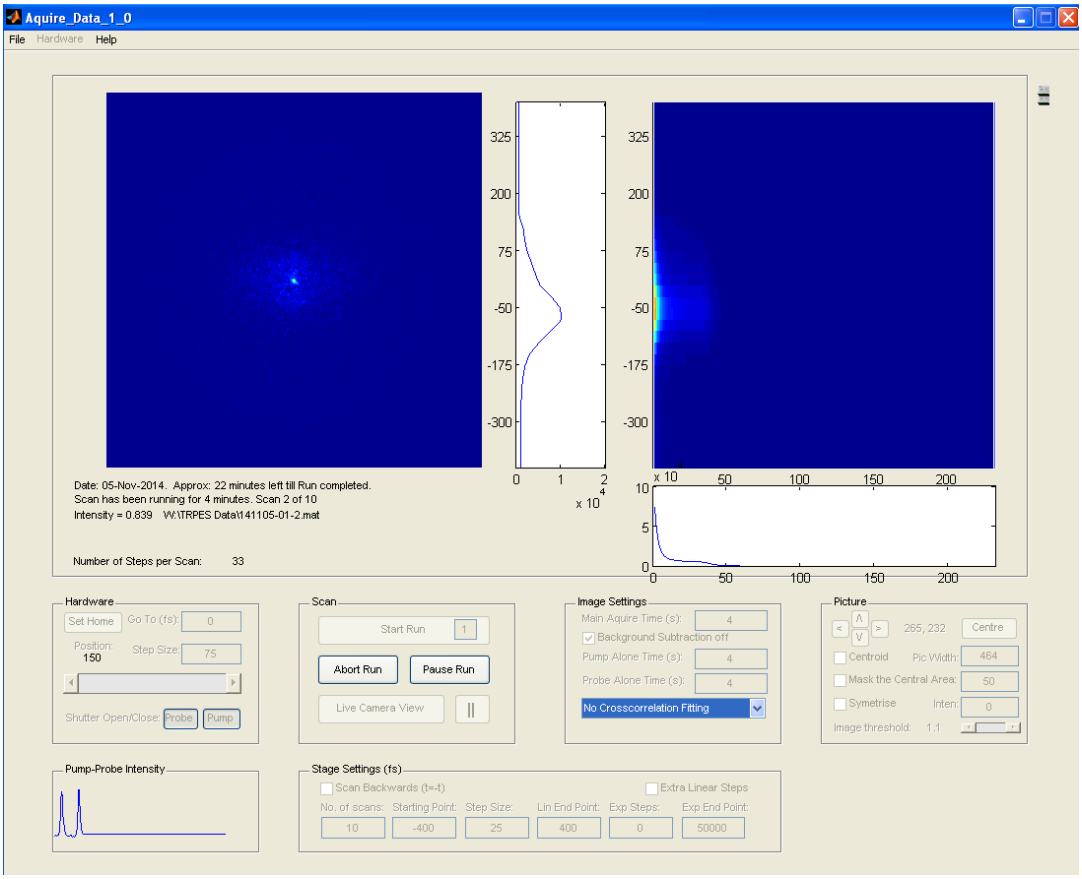

Figure 2.15 – GUI of "Acquire" image acquisition software. The image is taken during a scan of 1,3 butadiene running from -400 fs to +400 fs in step sizes of 25 fs. On the left is the raw image from the previous acquisition, the trace in the middle depicts the total intensity of the signal as a function of pump probe delay and the right shows a map of the signal with respect to radial position of the electron signal and the pump probe delay.

probe time delay in each scan can be added together to produce a set of higher quality images using the REPEITS program.

The GUI (graphical user interface) is shown in Figure 2.15. The Acquire program also has the ability to perform some processing on the live image to improve resolution through centroiding.[18] Centroiding is achieved by recording the brightest pixel in a detected event as the position of the particle instead of the full strike (which may be over several pixels). However, in the experiments described in this thesis, centroiding was not performed.

The Process program is used once the data has been collected by the Acquire program and allows the user to process either a single VMI image or a set of images referred to as a scan. These raw images are typically subject to background subtraction and require additional processing before they can be converted into photoelectron spectra. An overview of different methods available to perform the necessary image inversion has already been provided in Chapter 1, however, this chapter will now provide a discussion of the specific inversion method used in the experiments in the thesis, the matrix Abel

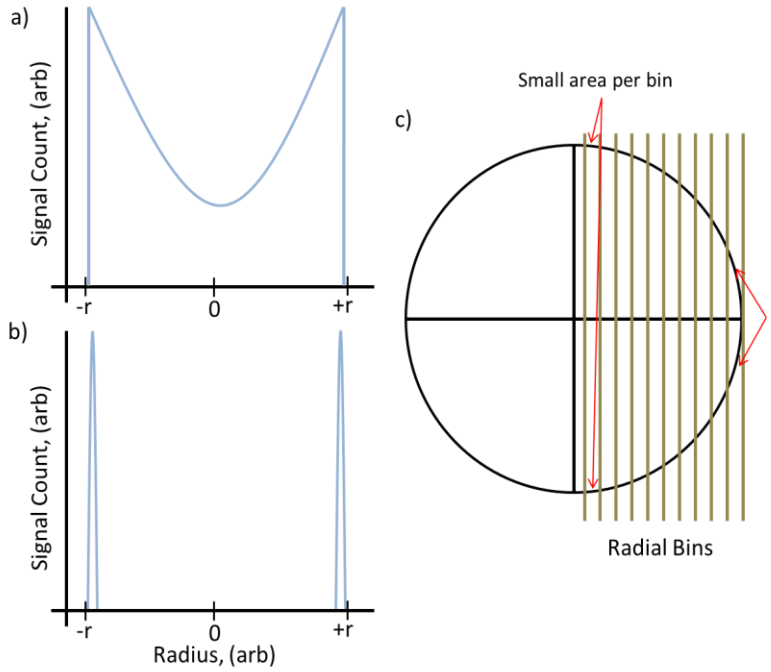

Figure 2.16 – Illustration of the necessity for image reconstruction. a) plots the function of total signal count as a function of area of the 3D sphere flattened onto a 2D surface. b) plots the reconstruction of the 3D image from the flattened image in a). c) shows the idea behind why the flattened 3D image gives the count distribution as shown in a), each section separated by the vertical yellow line describes the area of the sphere which is detected by a single bin in the detector array. Adapted from Ref [18]

transform,[1, 12] and provide an explanation for why an inverse transform method is required to obtain the photoelectron spectrum from the VMI image. For further reading, a general overview of transform techniques can also be found in a number of reviews reviews.[19, 20] The Abel transform is used to reconstruct a 3D object that has been flattened into a 2D plane. Charged particles produced in a VMI experiment following ionisation form a spherical distribution, known as a Newton sphere. When this sphere is crushed onto a 2D plane, in this case the MCP/phosphor detector, the distribution of particles illustrated by Figure 2.16 c) across 1D shown in Figure 2.16 a). In reconstructing the image, an Abel transform (or another appropriate method) produces a distribution similar to the one shown in Figure 2.16 b).

To understand how this is achieved in practice, consider a 2D distribution of charged particles in Cartesian coordinates (x, y) produced when a 3D sphere is compressed onto a 2D plane. This can also be defined in angular coordinates (ρ, z), where $\rho=x^2+y^2$, and z is the altitude of the particle from the detector plane, as shown in E.q. 27

$$I(x,y) \equiv I(\rho,z) \tag{2.7}$$

As such, the projection of the charged particle distribution onto the detector can be given by Eq. 2.8

$$P(y,z) = \int I(x,y,z)dx \tag{2.8}$$

From this, the Abel transform is then given by Eq. 2.9.

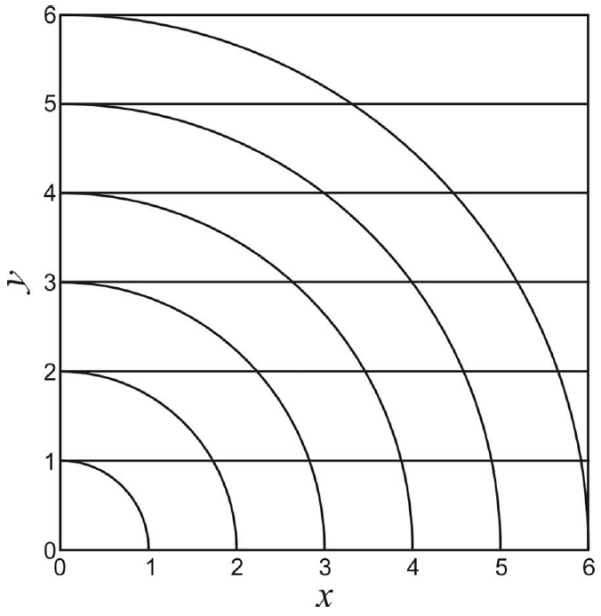

Figure 2.17 – Diagram showing the partitioning of the plane for Abel inversion. Lines of constant radius ρ and y segment the plane with the area of each segment being A_{ij}.

$$I(\rho,z) = \frac{1}{4\pi}\int_y^R \frac{\partial_y P(y,z)}{\sqrt{y^2-\rho^2}}dy \tag{2.9}$$

The main disadvantage to the Abel transform, as discussed in Chapter 1, is the resulting image quality. During the transformation a large amplitude vertical noise line is added to the resulting image. This is due to the derivative of the numerator in Eq. 2.9, and is particularly prevalent in data with poor signal-to-noise ratios.

The matrix Abel transform method is a variation upon the standard Abel transform and was developed by Townsend and co-workers.[12] It should be noted that a similar approach is also used by Cho and Na in the field of plasma diagnostics.[21] To describe the matrix Abel transform method, starting with the Abel transform as denoted in Eq 2.9, consider a particular altitude *z* of the true 3D charged particle distribution. This may be transformed by partitioning the *xy*-plane into a number of sections using $I(\rho, z) \rightarrow I_{ij}$. This partitioning is done using lines of constant *y* and ρ with an index *i* that denotes the maximum radius of a segment of the image and *j* which denotes the maximum value of *y* of each segment. An example of this segmentation is illustrated in Figure 2.17. As such, the area of the segments in contact with the *x* axis (i.e. when $i = j$) is given by Equation 2.11, where the area of each segment is given by A_{ii}

$$A_{ii} = \int_{i-1}^{i}\int_0^{\sqrt{i-y^2}} dxdy = \int_{i-1}^{i}\sqrt{i^2-y^2dy}$$

$$= -\frac{1}{2}i\sqrt{-1+2i} + \frac{1}{2}\sqrt{-1+2i} - \frac{1}{2}i^2 \times arcsin\left(\frac{i-1}{i}\right) + \frac{1}{4}i^2\pi$$

(2.10)

And in all other cases the area of the segment A_{ij} is given by the following

$$A_{ij} = \int_{i-1}^{i} \int_{\sqrt{(j-1)-y^2}}^{\sqrt{j-y^2}} dxdy = \int_{i-1}^{i} \sqrt{j^2 - y^2} - \sqrt{(j-1)^2 - y^2} dy$$
$$= \left(-\frac{1}{2}j^2 + j - \frac{1}{2}\right) arcsin\left(\frac{i}{j-1}\right) + \left(\frac{1}{2}j^2 - j + \frac{1}{2}\right) arcsin\left(\frac{i-1}{j-1}\right)$$
$$+ \frac{1}{2} i\sqrt{j^2 - 2j + 2i - i^2} - \frac{1}{2} i\sqrt{j^2 + 2i - 1 - i^2} - \frac{1}{2}\sqrt{j^2 - 2j + 2i - i^2}$$
$$+ \frac{1}{2}\sqrt{j^2 + 2i - 1 - i^2} + \frac{1}{2} i\sqrt{j^2 - i^2} - \frac{1}{2} j^2 \times arcsin\left(\frac{i-1}{j}\right)$$
$$+ \frac{1}{2} j^2 arcsin\left(\frac{i}{j}\right) - \frac{1}{2} i\sqrt{j^2 - 2j + 1 - i^2}$$

(2.11)

From this, the projection of the 3D distribution onto the 2D plane at large values of *x* is then simply given as

$$P = 2AI$$

(2.12)

As such, the inverse Abel transform is given by the following

$$I = \frac{1}{2} A^{-1} P$$

(2.13)

It should be pointed out that, as the Abel transform method assumes that the image is cylindrically symmetrical about an axis which is parallel to the imaging plane. As such, great care must be taken in ensuring that the laser polarisation is parallel to the MCP detector, otherwise the reconstruction method is no longer valid for reproducing the correct radial distribution of photoelectrons, a key component of the data, for reasons outlined in Chapter 1.

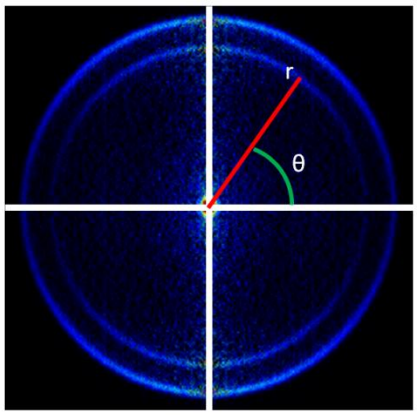

Figure 2.18 – Cartoon of the definition of *rsin(θ)*

Using the matrix Abel transform, it is possible to process a large volume of data rapidly. As an example quoted in Livingstone *et al.*,[12] this method is able to reconstruct 100 images with dimensions of 300 × 300 pixels in a single second using standard matrix inversion routes available in MATLAB (version 7.4.0, 2007a) on a PC with a 2.67 GHz processor. Due to this speed, it is the ideal approach for the data collected in this thesis discussed in Chapters 3 – 6 as typically; a data set can contain over 150 images per scan. Post transformation the data is weighted by $rsin(\theta)$, where r is the radial position of the pixel and θ is the angle with respect to the centre line axis (as shown in Figure 2.18) to regain the full velocity distribution. The interface of the Process program may be seen in Figure 2.19. In the process program the data can be further treated to simplify the overall analysis of the data. This treatment is highlighted in Figure 2.20. The first panels of Figure 2.20 (a-c) shows the raw photoelectron data of 3,5-dimethylaniline alongside the "pump alone" and "probe alone" background images. The process program is able to the background subtraction by directly subtracting both the pump and probe alone images from the main image. The results of this are shown in panel d) of Figure 2.20. Finally, the program is able to symmetrise this data around a 4-

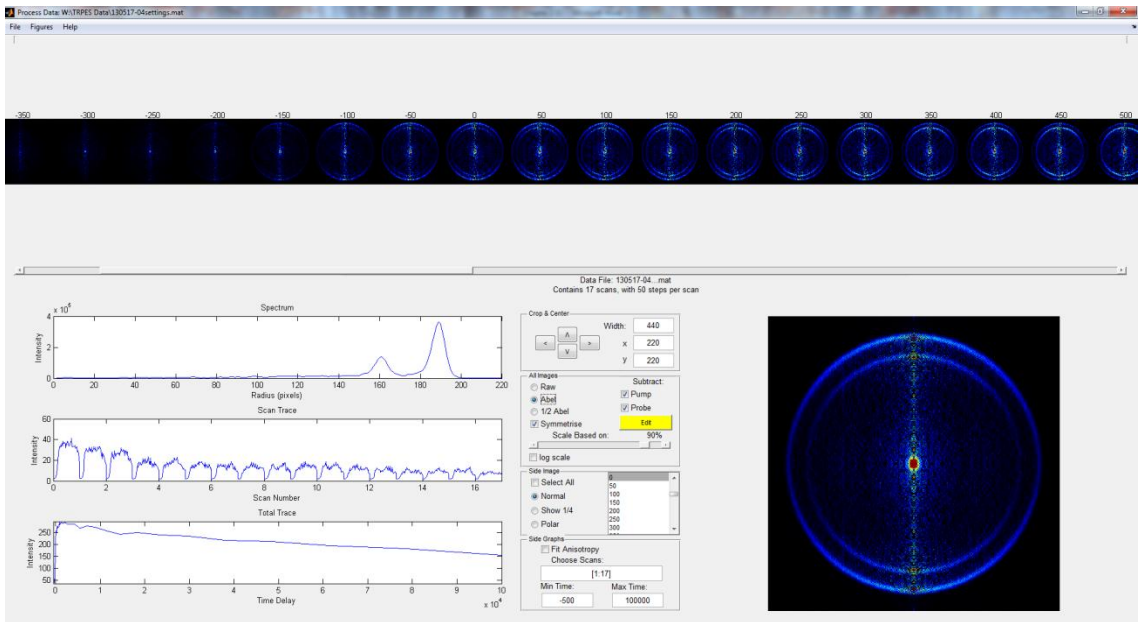

Figure 2.19 – Process data GUI. Data from *N*,N-dimethylpropylamine (DMPA) used as an illustrative example. Images have been background subtracted and matrix Abel inverted

fold axis to improve the overall statistics of the data (as each quadrant should contain the same information as the others). Panel e) of Figure 2.20 shows the data post symmetrisation. Once the images have been processed and any background signal has been removed, the data can then be inverted using the matrix abel transform (the results of which are shown in Figure 2.20 f)) and can be exported to the "Analysis" program.

The "Analysis" program has several key functionalities used to aid interpretation of the data. The first is the ability convert the processed image data from velocity space (i.e. the ring size and spacing in terms of pixels) to kinetic energy space. This is achieved by calibrating the image against another image collected from a molecule with a well-known ionisation potential (IP) that produces clear, well resolved features under the same VMI conditions. The energy scale may then be further modified such that the spectrum is plotted in terms of internal binding energy. An illustrative example of these transformations are shown in Figure 2.21, using time-resolved photoelectron spectrum

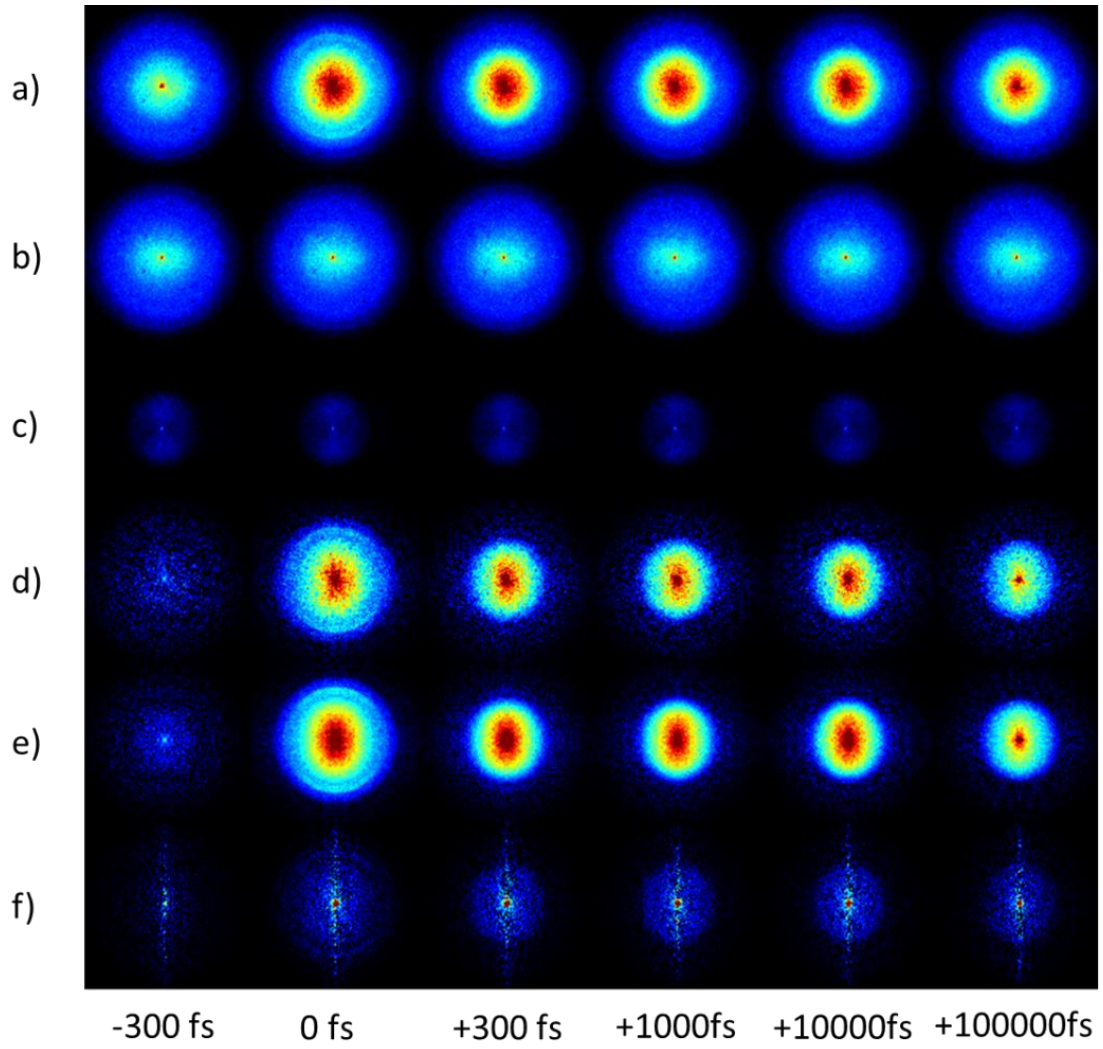

Figure 2.20 – Images of 3,5-dimethylaniline in various stages of processing. Set a) shows the raw VMI images, b) shows the pump alone images, c) shows the probe alone images, d) shows the background subtracted VMI images, e) shows the background subtracted VMI images after a 4-fold symmetrisation and finally f) shows the abel inverted background subtracted symmetrised images.

a)

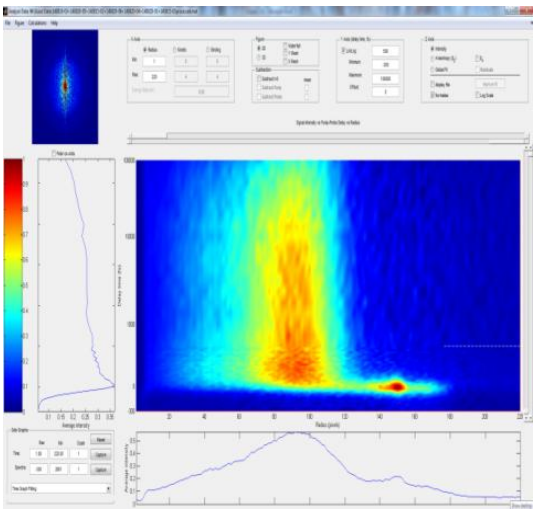

b)

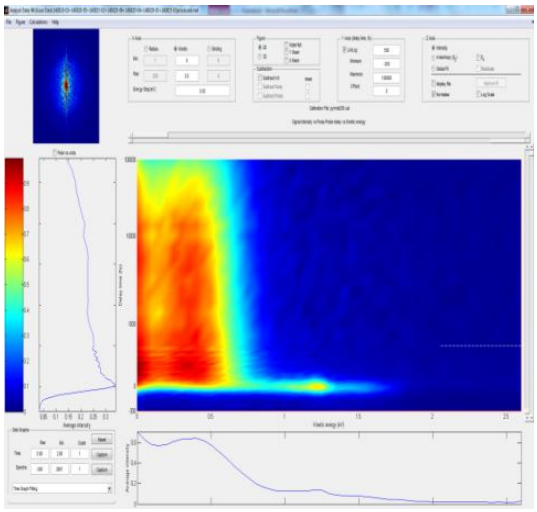

c)

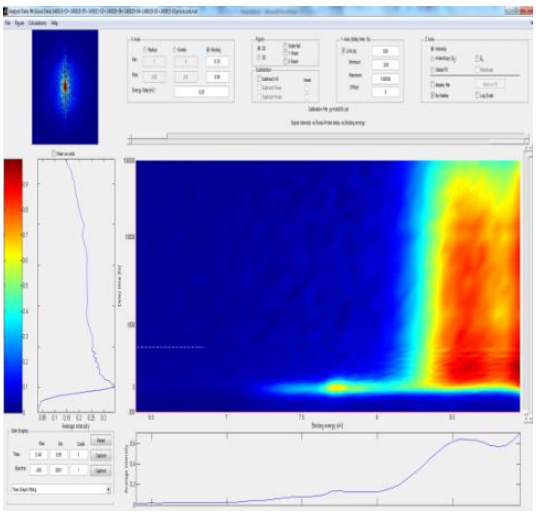

Figure 2.21 – demonstration of scale transformation using *N*,*N*-dimethylaniline showing a) velocity, b) electron kinetic energy & c) cation binding energy

data for *N*,*N*-dimethylaniline, which will be discussed in more detail in Chapter 4. Mathematically, this conversion between velocity space and kinetic energy space is given by Eq. 2.14 (with the limits r_1 and r_2 shown in Eq. 2.15 and Eq. 2.16).

$$I(E,t) = \sum_{i=r_1}^{r_2} I(r_i,t) \tag{2.14}$$

$$r_1 = \sqrt{A(E + \Delta E - E_0)} + r_0 \tag{2.15}$$

$$r_2 = \sqrt{A(E - E_0)} + r_0 \tag{2.16}$$

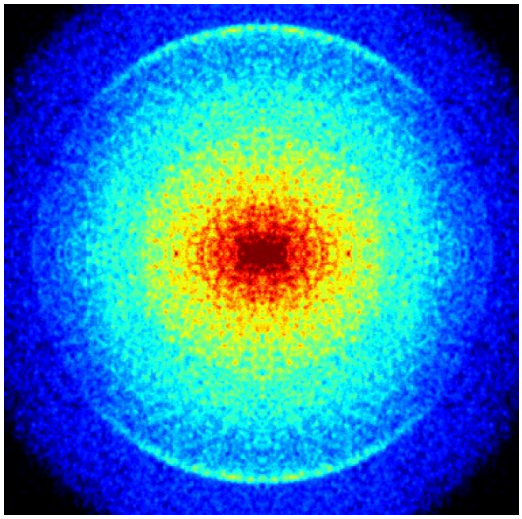

Figure 2.22 – Calibration image of xenon. It should be noted that the image has been 4 fold symmetrised for presentation purposes

Where $I(E,t)$ is intensity in terms of energy and time, $I(r_i,t)$ is intensity in terms of radius and time, E is the electron kinetic energy, r is the radial position of the electron on the image, A is the conversion factor between radius and energy, E_0 and r_0 are the minimum known electron energy and its radial position respectively, and ΔE is the size of the energy binning. It should be noted that for all the data in this thesis the energy binning is set to 0.05 eV. Once converted into electron kinetic energy space, a further conversion can be performed to convert the photoelectron spectrum from electron kinetic energy, E_k, into binding energy, E_b, as shown in Eq. 2.17.

$$E_b = \frac{hc}{\lambda_{pump}} + \frac{hc}{\lambda_{probe}} - E_k \tag{2.17}$$

In practise to calibrate the raw VMI data an image of a well characterised molecule is required. An example of this process is given as follows. In chapters 3 – 6 the majority of the calibration images are generated using either xenon or 1,3-butadiene. These molecules are ideal as they produce images with well resolved rings and the ionisation potential of these systems are very well known. Figure 2.22 shows a 4-folded symmetrised image of xenon, acquired for 230,000 laser shots. By identifying the positions of the rings, (i.e. $r1$ and $r2$ in equations 2.15 and 2.16) it is possible to calculate the conversion factor, A, and calibrate all photoelectron data generate with the same specific VMI conditions, such as electrostatic lens voltages and laser focal conditions.

The second function of the analysis program is its ability to undertake fits to the photoelectron data. This procedure is performed globally, meaning that the spectrum is analysed with a number of user defined functions over all regions of the spectrum simultaneously. These functions are iteratively optimised (using a least-squares fitting routine) until the best model of the photoelectron data is produced. Exponential functions used in the fit are convoluted with an additional Gaussian component, defined

by the cross correlation response of the VMI spectrometer (recorded separately). The fitting function (a summation of *n* functions defined by the user) is given by Eq. 2.18 and Eq. 2.19[1]

$$I(E,t) = \sum_{i=1}^{n} A_i(E)\left(e^{-\frac{t}{\tau_i}}.cc(t)\right) \tag{2.18}$$

$$cc(t) = \frac{1}{2}\left(1 + erf\left(\frac{2\sqrt{\ln(2)}\,t}{\tau_{cc}}\right)\right) \tag{2.19}$$

a)

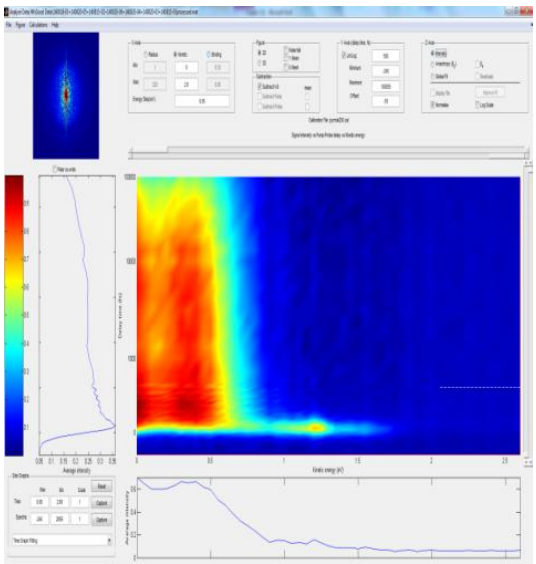

b)

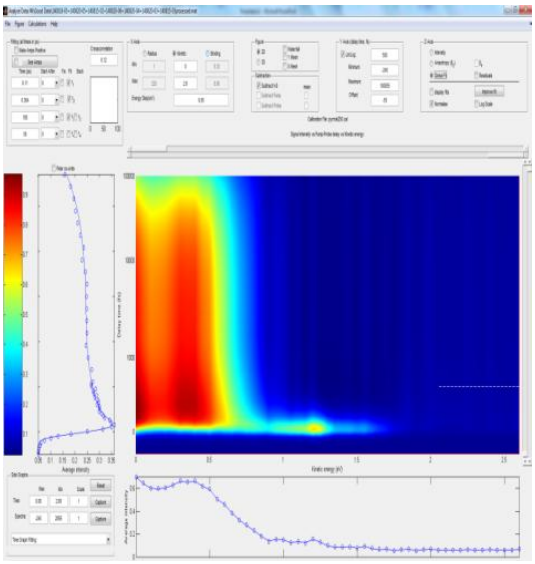

c)

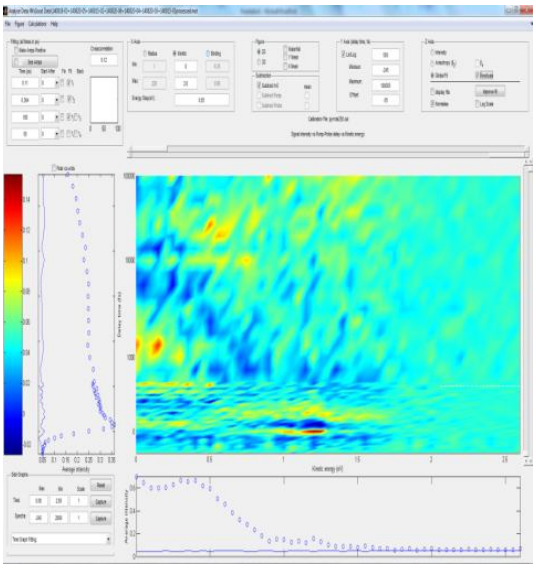

Figure 2.23 – demonstration of the fitting function using *N,N*-dimethylamine fitted with three exponentials. a) shows the raw data, b) displays the globally fitted data & c) shows the associated residual of the fit,

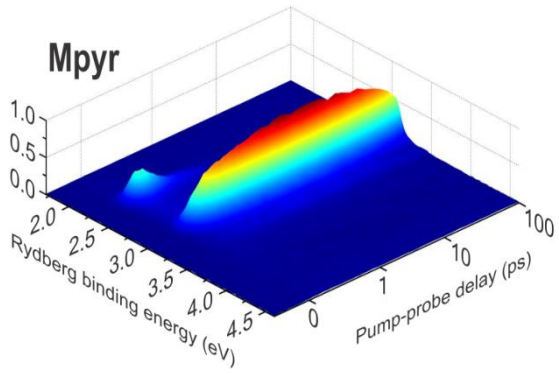

Figure 2.24 - 3D photoelectron spectra of the Mpyr. The delay times are given on lin-log time scales, changing over at 1000 fs.

Where A_i is the amplitude in each energy region associated with the time constant τ, and $cc(t)$ is the rise due to the cross correlation given by Eq. 2.19, where τ_{CC} is the cross correlation response of the spectrometer. The error function, *erf*, also contains a factor of $2\sqrt{\ln(2)}$ to convert the Gaussian standard deviation into a full width at half maximum. This fitting procedure is used in Chapters 3 - 5. Using *N*,*N*-dimethylaniline again as an illustrative example, Figure 2.23 displays the raw spectrum (a), fitted spectrum (b) and residual (the difference between the raw and fitted spectrum) (c). Using the fits to identify the processes occurring as the molecule relaxes; it is convenient to plot the fitted data parameters as a Decay Associated Spectra (DAS). The DAS shows the amplitude (A_i) in each energy region associated with the time constant τ. From the DAS the experimental data can be interpreted and mechanistic pathways may be deduced.

To explain the use of a DAS, the photoelectron data of *N*-methylpyrrolidine (Mpyr), a tertiary amine system which will be discussed later in Chapter 6, will be used as an illustrative example. Figure 2.24 shows the time resolved photoelectron spectrum of Mpyr, plotted in 3D. As evident from the spectra, it is clear that there is some interplay between the high and lower binding energy features. Figure 2.25 shows the DAS of Mpyr, fitted with two exponential functions using the procedure discussed previously (see Eq 2.18). The DAS plot shows the amplitude of the exponential functions in various regions of the spectrum. From Figure 2.25, it is clear that there are two main regions with a large amount of photoelectron signal, as shown by the positive amplitude peaks in each spectrum. In addition, there is also a negative amplitude feature that is spectrally overlapping a positive amplitude

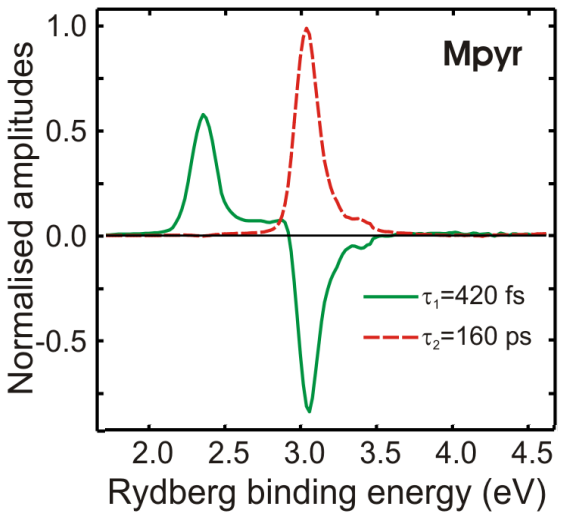

Figure 2.25 – Decay associated spectra of Mpyr using a two exponential global fit model. Each time constant is plotted in parallel and originates from $t = 0$

feature. As the exponential fitting functions all originate from t = 0, negative amplitude exponentials model an onset to the rise of a photoelectron signal. This allows the user to identify potentially kinetically sequential dynamics without inferring it prior to the application of the fitting model, as discussed by Stolow and co-workers.[22] Figure 2.26 illustrates how the photoelectron data is fitted. Figure 2.26 a) shows a slice of the photoelectron spectrum from Figure 2.24 at 2.3 eV Rydberg binding energy. As can be seen in the figure, this feature rises with the Gaussian cross correlation function and exponentially decays in 420 fs. This feature is adequately modelled by a single exponential decaying function (plotted in green in Figure 2.26 a)). The second exponential function (plotted in red in Figure 2.26) has no significant amplitude in this region. Figure 2.26 b), shows a slice of the photoelectron spectrum at 3.1 eV, in which the data does not rise with the Gaussian cross correlation. Therefore, as alluded to previously, a negative amplitude exponential function (plotted in green in the Figure 2.26) has been used in order to model the delayed rise of the signal, whilst a positive amplitude function models that signal at long time (plotted in red in the Figure 2.26).

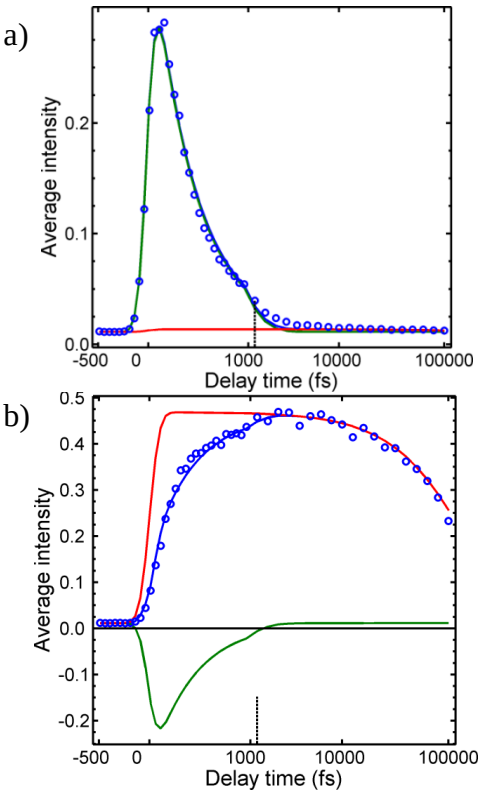

Figure 2.26 – Average intensity against time graphs in specific energy bins of Mpyr, depicting the raw photoelectron data (blue circles) and traces of the exponential functions (green and red lines) required to fit the data. a) plots a slice at 2.3 eV and b) a slice at 3.1 eV. The vertical dotted line indicates when the linear scale ends and the logarithmic scale begins. See text for more details

However, a non-sequential method can struggle to fit multiple time constants in the same spectral region that have very similar lifetimes. This is because the fits begin to artificially mirror each other in a non-meaningful manner. As such, it is occasionally necessary to resort to a different fitting procedure, in which, instead of fitting exponentials in parallel, they are fitted in series (i.e. a model in which a sequential kinetic model is assumed from the beginning). The relevant fitting function is now given by:

$$I(E,t) = \sum_{i=1}^{n} A_i(E)\left(e^{-\frac{t}{\tau_i}} \otimes r_i(t).cc(t)\right)$$

(2.20)

In which $r_i(t)$ is given by

$$r_i(t) = 1 - e^{-\frac{t}{\tau_j}}$$

(2.21)

In this method, which is also supported in REPEITS, an additional term, $r_i(t)$ is introduced which adds an offset to the rise of the function (where τ_j is the time constant of the previous function). This fitting procedure is used in Chapter 6. An example of the difference in this fitting procedure from the previous is shown in Figure 2.27, once again using the photoelectron spectra Mpyr as an example. Here, it is clear to see that the rise of each component in the DAS occurs sequentially and is fitted with three functions (plotted as green, red and light blue respectively in Figure 2.27). The drawback to this method is that the user must *assume* that all processes are sequential whereas the parallel method often identifies sequential processes as discussed previously.

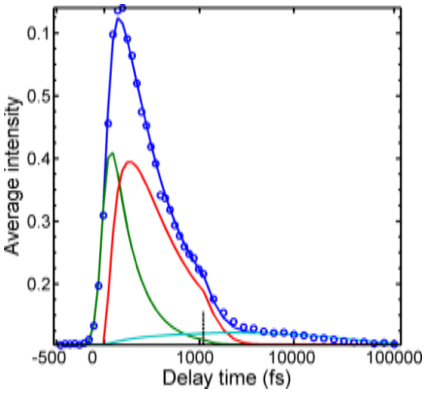

Figure 2.27 – Average intensity vs time graph of Mpyr averaged between 2.1 – 2.6 eV. The data is plotted by the dark blue circles. The green, red and light blue lines show the components of the three exponentials in the model (the fit is shown in the dark blue). This fit was generated using a sequential model. The vertical dotted line indicates when the linear scale ends and the logarithmic scale begins. See text for more details

The third feature of the analysis program is the ability to fit and plot the anisotropy parameters β_2 and β_4[23] as a function of energy and time. These parameters are discussed in more detail in Chapter 1. If we considering each photoelectron image at each "pump-probe" time delay rescaled onto an energy axis, then we can rewrite Eq. 1.9 into Eq. 2.22

$$I(E,t,\theta) \propto 1 + \beta_2(E,t)P_2(\theta) + \beta_4(E,t)P_4(\theta)$$

(2.22)

Where β_n is the normalised anisotropy parameter, P_n is the Legendre polynomial to the order *n*. The amplitudes are fitted using the least squares method[1] and this results in the ability to interrogate the angular distributions of the photoelectron data in each energy bin at all pump-probe time delays which, as will be discussed in Chapters 3 – 6, can provide additional insights into the dynamics of the target molecules.

2.2.5 – Error analysis

Throughout this section of the thesis we have so far omitted a discussion on errors arising from the methods employed in the data collection and analysis. For the work presented here a full rigorous error analysis has not been performed as it is the author's belief that the single largest source of error is from the temporal instrument response function of the spectrometer. As such the error for the time constants generated are on the order of 10's of femtoseconds (assuming a cross correlation for ~120 – 180 fs), and as such the error for time constants identified in the data presented in chapters 3 – 6 as ±10%.

However, this being said it is possible to perform a more rigorous error analysis as discussed in the thesis of Adam Chatterley (University of Warwick), in which a support plane analysis technique was used.[24]

2.3 – Conclusion

This chapter has provided a detailed description of the state-of-the-art velocity map imaging spectrometer which is used to investigate model biological chromophores using time resolved photoelectron imaging. Furthermore, a detailed description of how the laser light is generated and dispersion is controlled in order to perform the experiments is also given. Additionally, this chapter has discussed the methods used in data acquisition; and how the data is processed using a matrix Abel transform method. Finally, details on how the data is plotted and interpreted, through the use of global fitting functions and decay associated spectra (using the REPEITS program) are also considered.

Following on from this, the thesis will now describe several experiments performed using this experimental and computational infrastructure. Each chapter will contain specific information with regards to parameters from individual experiments performed, as well as a detailed account of the results and discussion. Chapters 3 and 4 will discuss investigations into the relaxation dynamics of aniline. Chapter 5 will present data on the molecule guaiacol and will provide details of both a time-resolved photoelectron imaging experiment as well as complementary solution phase experiments performed by Stavros and co-workers at the University of Warwick.[25] Chapter 6 will discuss work investigating the relaxation dynamics of a set of aliphatic amines. The final chapter (Chapter 7) will then present ideas for future work to further improve this experimental set up or to expand upon the work reported in Chapters 3 through 6, alongside some concluding remarks.

2.4 – References

1. R. Livingstone, Heriot Watt University, 2012.
2. D. Strickland and G. Mourou, Opt. Comm. **55** (6), 447-449 (1985).
3. A. V. Smith, (AS-Photonics, Albuquerque).
4. A. V. Smith and M. S. Bowers, J. Opt. Soc. Am. B **12** (1), 49-57 (1995).
5. M. Rosete-Aguilar, F. C. Estrada-Silva, N. C. Bruce, C. J. Roman-Moreno and R. Ortega-Martinez, Rev. Mex. Fis. **54** (2), 141-148 (2008).
6. O. E. Martinez, J. P. Gordon and R. L. Fork, J. Opt. Soc. Am. A **1** (10), 1003-1006 (1984).
7. W. Sellmeier, Ann. Phy. Chem **219**, 272 (1871).
8. R. Trebino, K. W. DeLong, D. N. Fittinghoff, J. N. Sweetser, M. A. Krumbugel, B. A. Richman and D. J. Kane, Rev. Sci. Instrum. **68** (9), 3277-3295 (1997).
9. C. Homann, N. Krebs and E. Riedle, Appl. Phys. B-Lasers. O. **104** (4), 783-791 (2011).
10. B. Saha, M. Ehara and H. Nakatsuji, J. Chem. Phys. **125** (1), 014316 (2006).
11. A. C. Parr and F. A. Elder, J. Chem. Phys. **49** (6), 2659-2664 (1968).
12. R. A. Livingstone, J. O. Thompson, M. Iljina, R. J. Donaldson, B. J. Sussman, M. J. Paterson and D. Townsend, J. Chem. Phys. **137** (18), 184304 (2012).
13. U. Even, J. Jortner, D. Noy, N. Lavie and C. Cossart-Magos, J. Chem. Phys. **112** (18), 8068-8071 (2000).
14. A. Stolow, J. Vac. Sci. Technol. A **14** (4), 2669-2670 (1996).
15. A. T. J. B. Eppink and D. H. Parker, Rev. Sci. Instrum. **68** (9), 3477-3484 (1997).
16. D. Townsend, M. P. Minitti and A. G. Suits, Rev. Sci. Instrum. **74** (4), 2530-2539 (2003).
17. W. Christen, K. Rademann and U. Even, J. Chem. Phys. **125** (17), 174307 (2006).
18. Y. Ogi, H. Kohguchi, D. Niu, K. Ohshimo and T. Suzuki, J. Phys. Chem. A **113** (52), 14536-14544 (2009).
19. A. T. J. B. Eppink;, S. Wu; and B. J. Whitaker, in *Imaging in Molecular Dynamics, Technology and Applications*, edited by B. J. Whitaker (Cambridge University Press, Cambridge, 2003), Vol. 1, pp. 65-112.
20. M. N. Ashfold, N. H. Nahler, A. J. Orr-Ewing, O. P. Vieuxmaire, R. L. Toomes, T. N. Kitsopoulos, I. A. Garcia, D. A. Chestakov, S. M. Wu and D. H. Parker, Phys. Chem. Chem. Phys. **8** (1), 26-53 (2006).
21. Y. T. Cho and S. J. Na, Meas. Sci. Technol. **16** (3), 878-884 (2005).
22. O. Schalk, A. E. Boguslavskiy and A. Stolow, J. Phys. Chem. A. **114** (12), 4058-4064 (2010).
23. K. L. Reid, Annu. Rev. Phys. Chem. **54**, 397-424 (2003).
24. A. Chatterley, Warwick, Durham, 2013.
25. S. E. Greenough, M. D. Horbury, J. O. Thompson, G. M. Roberts, T. N. Karsili, B. Marchetti, D. Townsend and V. G. Stavros, Phys. Chem. Chem. Phys. **16** (30), 16187-16195 (2014).

Chapter 3 – The photoelectron spectroscopy of aniline at the $S_2(3s/\pi\sigma^*)$ origin

3.1 – Introduction

Over the past three decades, a significant number of experimental and theoretical studies have been performed to investigate systems that model more complex chromophore sites in large polypeptide protein systems. An overview is given in Chapter 1 of this thesis. This chapter will report work on the molecule aniline, a system which has been subject to a large number of studies both computationally and experimentally.[1-6] Aniline, the structure of which is shown in Figure 3.1, is found as a subunit in a large number of biological molecules; most notably amino acids. Aniline has two major absorption bands between 300 nm and 220 nm. These two bands have been assigned previously as $\pi\pi^*$ transitions.[7] However, more recent work has identified an additional "dark state" between these two "bright states". This weak transition corresponds to excitation of a $\pi\sigma^*$ valence state which is dissociative along the N-H coordinate, and is strongly coupled to a bound 3s Rydberg state located on the nitrogen.[8] For more details see Chapter 1. Interestingly, and in contrast to many molecules that have $3s/\pi\sigma^*$ states, this state in aniline exhibits vibrational structure due a small bound region along the N-H co-ordinate. This is caused by the relatively low ionisation potential (IP) of the system when compared with many molecules of similar structure. For instance, the IP of aniline is around 0.8 eV lower than phenol, aniline's

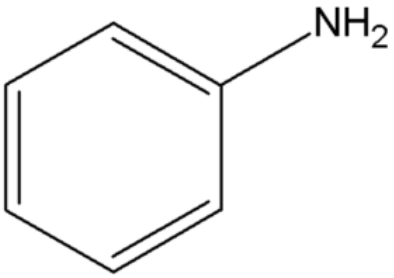

Figure 3.1 – Structure of Aniline

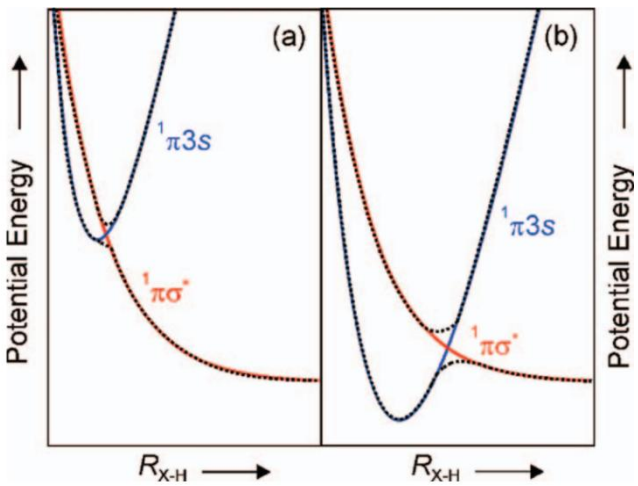

Figure 3.2 - An illustration of the adiabatic potentials arising from the interaction between the 3s Rydberg state, and σ* state curve configurations in two contrasting cases. In panel a), the two states are near degenerate in the vFC region, whereas in panel b), the Rydberg configuration is stabilized at short RX–H relative to the valence state. The two configurations show the lower adiabatic product is manifest as the "effective" πσ* PES on which dissociation proceeds. Taken from Ref [2]

isoelectronic alcohol equivalent, which does not support any vibrational structure on its $S_2(3s/\pi\sigma^*)$ state.[9] The low IP of the system leads to a reduction of the energy of the Rydberg series and, as such, lowers the energy of the 3s Rydberg state relative to the $\pi\sigma^*$ valence state, resulting in a region of this state to be quasi-bound. Ashfold and co-workers[1] have produced a schematic of the resulting interaction shown in Figure 3.2 as an illustrative cut along the X-H (where X is some heteroatom) coordinate.

For the rest of this chapter the two lowest singlet states in aniline will be defined as $S_1(\pi\pi^*)$ and $S_2(3s/\pi\sigma^*)$. The origin of the $S_2(3s/\pi\sigma^*)$ state has been experimentally determined to be at 269.5 nm.[8] Initial excitation within the vertical Franck-Condon region will primarily prepare a wavepacket within the part of the state dominated by 3s Rydberg electronic character. However, as the N-H bond extends, the electronic character evolves so that valance σ^* character dominates.[10] This will be expanded upon further in Chapter 4. Figure 3.3, also from Ashfold and co-workers,[1] shows a potential energy cut of aniline along the N-H coordinate. Considering the potential energy cuts in Figure 3.3,[1] it is possible for any direct excitation to result in either relaxation through a purely dissociative mechanism leading to H-atom loss, or through non-adiabatic coupling from the $S_2(3s/\pi\sigma^*)$ state to other electronic states via a conical intersection (CI). Since one of the accessible states through a conical intersection (specifically the one at large N-H distance) is the S_0 ground state, it is proposed that the $S_2(3s/\pi\sigma^*)$ can be used as a route for fast internal relaxation from electronically excited states to the electronic ground state.[10] It is this mechanism that is put forward as a method of "photo-protection" in nature, by facilitating rapid energy transfer from an electronically excited chromophore to its surrounding environment, as discussed in Chapter 1.

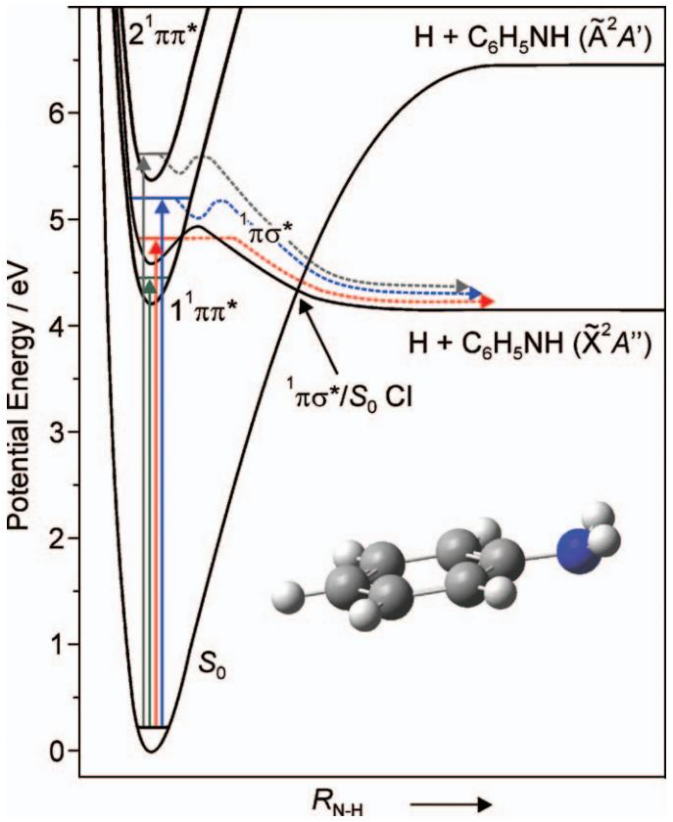

Figure 3.3 – Potential energy cuts of aniline along the NH coordinate showing the electronic S_0 ground state, the $S_1(\pi\pi^*)$, $S_2(3s/\pi\sigma^*)$ & S_3 states and the respective conical intersections. Taken from Ref [1]

Over the last decade, there have been a number of investigations into gas-phase UV excitation dynamics of aniline reported by a number of different groups, all using different techniques along with different associated observables. However, for the purposes of this discussion, this chapter will focus on four of these studies. These publications serve as motivation for this work and provide useful points for the interpretations discussed later.

The first of these experiments is that undertaken by Ashfold and co-workers.[1] In this work, H-Rydberg atom photofragmentation translational spectroscopy was employed to investigate the excitation region spanning 293.3 nm to 193.3 nm. Results from this work showed that at wavelengths longer than 269.5 nm (i.e. below the $S_2(3s/\pi\sigma^*)$ origin), as indicated by the green arrow in Figure 3.3, only a broad, low energy H-atom loss feature was observed in the total kinetic energy release (TKER) spectra, which was assigned as signal arising from excitation to the $S_1(\pi\pi^*)$. This signal showed no signs of any significant recoil anisotropy, indicating a long dissociation lifetime of the state. However, at wavelengths shorter then 269.5 nm (the origin of the $S_2(3s/\pi\sigma^*)$ state), as indicated by red, blue and grey arrows in Figure 3.3, new sharp high kinetic energy H-atom loss features were observed. These features were assigned as signal arising from excitation to quasibound vibrational levels within the shallow bound potential well of the $S_2(3s/\pi\sigma^*)$ state in the Franck-Condon (FC) region. From this work, it was proposed that following excitation to the $S_2(3s/\pi\sigma^*)$ state, H-atom tunnelling occurs through the potential barrier on the $S_2(3s/\pi\sigma^*)$ surface, thereby allowing for fast H-atom loss. The H-atom recoil anisotropy parameter of β = -0.5 associated with this feature is evidence that this process is extremely rapid. This is as a result of the H-atom dissociation occuring before the molecules are able to rotate out of alignment induced by lasers electric field. As the wavelength is shortened further (<260 nm), a broad, unstructured, high TKER continuum appeared in place of the sharp features. This structural change to the TKER spectrum was attributed to excitation to the $S_1(\pi\pi^*)$ state with subsequent internal conversion to the $S_2(3s/\pi\sigma^*)$ state via a concial intersection (CI).

A time-resolved ion yield study performed by Longarte and co-workers,[2] investigated aniline in the region between 294-234 nm, utilising multiphoton ionisation schemes and varying polarization geometries. With excitation energies lying between the $S_1(\pi\pi^*)$ and $S_2(\pi\sigma^*)$ origins, the parent ion transient signal observed was long lived. This signal was attributed to direct excitation to the $S_1(\pi\pi^*)$ state. However, at wavelengths between 269.5 nm and 240 nm, a very weak, rapid signal was seen (with a lifetime

attributed to it of 165 fs). This was associated with direct excitation to the $S_2(3s/\pi\sigma^*)$ state, which subsequently decayed. It was postulated that this decay was mediated by population transfer to the $S_1(\pi\pi^*)$ state, however the authors were unable to be definitive in their mechanistic argument. At excitation wavelengths shorter than 240 nm, additional decaying componants appeared in the transient ion signal, attributed to dynamics associated with highier-lying excited states.

Further time-resolved work was also performed by Stavros and co-workers.[3] The H-atom elimination channels in aniline were investigated using time-resolved velocity map ion-imaging following excitation at a range of wavelengths between 294 - 240 nm. In contrast to the two aforementioned studies, this work did not see any direct excitation to the $S_2(3s/\pi\sigma^*)$ state at wavelengths below 250 nm. However, this lack of signal was attributed to the large bandwidth of the femtosecond laser pulse used in this study. As the spectral features of the $S_2(3s/\pi\sigma^*)$ state are very narrow and are formally single photon forbidden, the large spectral bandwidth of the laser pulse provides very little popualtion in the $S_2(3s/\pi\sigma^*)$ state, relative to the much more strongly absorbing $S_1(\pi\pi^*)$ transition, following excitation. Nevertheless, at excitation wavelengths $\leq$250 nm, there was evidence of signal arising from the $S_2(3s/\pi\sigma^*)$ state with a <1 ps lifetime. It was proposed that this signal originated from the $S_2(3s/\pi\sigma^*)$ state operating as a pathway for non-adiabatic relaxation from the directly excited $S_1(\pi\pi^*)$ state. Furthermore, at pump wavelengths directly exciting the highier lying state above the S_2 (at wavelengths above 240 nm), a two stage sequential decay pathway was identified involving non-adiabatic coupling between the S_3 state and via both $S_1(\pi\pi^*)$ and $S_2(3s/\pi\sigma^*)$.

The final piece of work to comment on here is that by Fielding and co-workers.[4, 5] In this study, time-resolved photoelectron imaging (TRPEI) was employed to investigate the dynamics of aniline in the region between 269 - 236 nm. This work concluded that, following excitation at 269 nm, both the $S_1(\pi\pi^*)$ and the $S_2(3s/\pi\sigma^*)$ were both directly populated. They also went on to suggest that both the 3s Ryberg and $\pi\sigma^*$ componants of the $S_2(3s/\pi\sigma^*)$ were directly excited. These two components were found to have lifetimes of 230 fs and 0.9 ps, which were attributed to non-adiabatic coupling to the $S_1(\pi\pi^*)$, and direct dissociation of the NH bond, respectively. When the excitation wavelength was moved to 250 nm, however, the signal observed was attributed to direct excitation to the 3s and $\pi\sigma^*$ components of $S_2(3s/\pi\sigma^*)$, with no direct excitation to the $S_1(\pi\pi^*)$. Finally, at wavelengths shorter than 240 nm, extra features were observed and attributed to signal from highier lying excited states.

From these four pieces of work,[1-4] it is clear that there are some discrepancies. In order to attempt to resolve this, a study was performed using time-resolved photoelectron velocity map imaging.[11] Four excitation wavelengths were carefully selected to investigate the dynamics around the $S_2(3s/\pi\sigma^*)$ origin. These wavelengths were selected based upon a [2+2] REMPI spectrum taken by Ebata and co-workers,[8] shown in Figure 3.4. Specifically, they were 273 nm, which sits below the $S_2(3s/\pi\sigma^*)$ origin by 3.5 nm, 269.5 nm, the position of the $S_2(3s/\pi\sigma^*)$ origin itself, 267.7 nm, a region in between the first two resonant transitions attributed to $S_2(3s/\pi\sigma^*)$, and 265.9 nm, a broad resonant feaure in the $S_2(3s/\pi\sigma^*)$ absorption spectrum, as shown in Figure 3.4. The rest of this chapter will discuss the results of the time-resolved velocity map imaging experiments.[11]

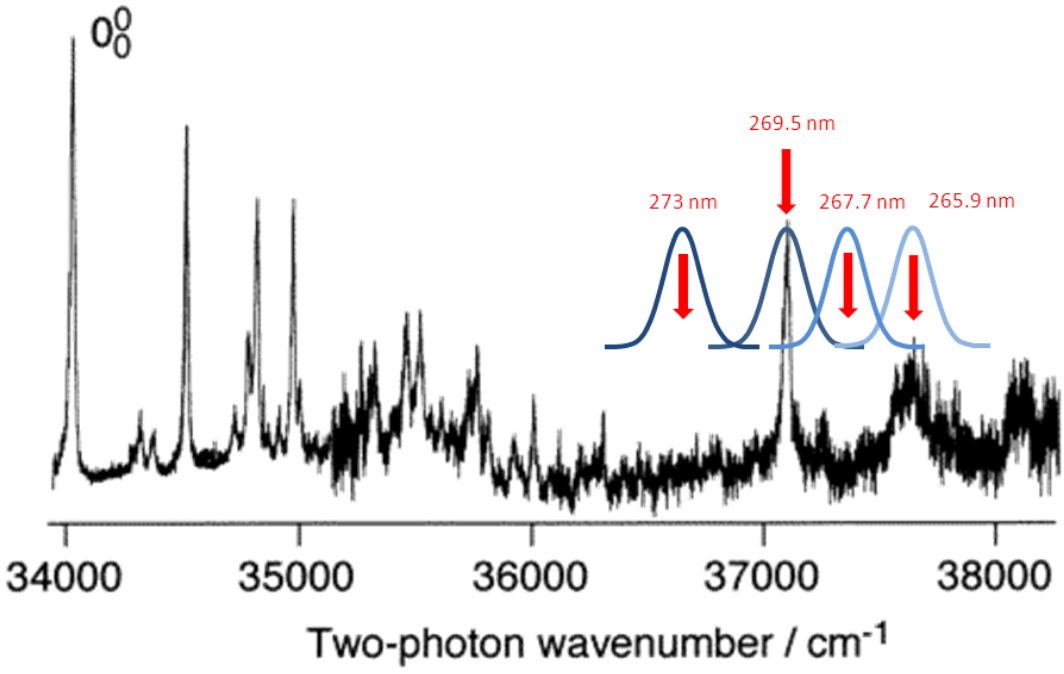

Figure 3.4 – [2+2] REMPI spectrum of aniline. The feature assigned as 0_0^0 is attributed to the origin of the S_1 state. The spectral feature labelled 37104 cm^{-1} is assigned as the origin of the S_2 state. The arrows identify the spectral regions (and the wavelength in nm) pumped for the TR-PES experiment. The gaussians shown in blue represent the bandwidth of the laser at each excitation, with a FWHM of 1.8 nm. Adapted from Ref [8]

3.2 – Experimental

The set up for this experiment has been previously described in detail in Chapter 2 of this thesis and elsewhere.[12] Aniline, was purchased from Sigma-Aldrich (99% purity). This sample was directly loaded into the Even-Lavie valve[13] and seeded into a molecular beam with a carrier gas of He (at 3 bar). The sample was maintained at 50 °C to provide adequate vapour pressure and a good signal to noise ratio. In the interaction region of the velocity map imaging (VMI) spectrometer,[14] the skimmed molecular beam was intersected by two UV laser pulses.

For this experiment, the 3rd harmonic of the laser system was used as the pump wavelength, generated using beam line 3. The central wavelength output of the Ti:Sapphire laser system was tuned between 819 nm and 798 nm to generate the tuneability for this experiment, providing a UV tuning range of 273 nm – 266 nm with an average attenuated power at the spectrometer of 0.2 μJ per pulse. The probe wavelength was set to 305 nm and was generated using beam line 1. 305 nm was selected as the probe wavelength to avoid direct excitation to the $S_1(\pi\pi^*)$ and possible "probe-pump" ionisation. The pump and probe beams were combined on an appropriate dichroic mirror and focussed into the chamber using a 25 cm focal length lens. For the results described in the following section, the cross correlation achieved in the measurement was recorded as 180 fs, obtained by a [1+1′] non-resonant direct ionisation of 1,3-butadiene and were also calibrated using 1,3-butadiene image recorded at 250 nm (in a [1+1] scheme).

Linear time steps of 33.3 fs were used for the time region between -300 fs and +1000 fs, followed by additional linear time steps of 200 fs from +1000 fs to 3600 fs. For each of the 53 images recorded, the data shown was comprised of 30 – 40 scans, in order to provide satisfactory statistics at each pump – probe delay time. In the data presented in this chapter, each image was acquired for 200,000 laser shots.

3.3 – Results

3.3.1 – Time zero velocity map images

Figure 3.5 shows 4-fold symmetrised single background subtracted (as described in Chapter 2) images of aniline at the four excitation wavelengths investigated at zero pump-probe delay. The left hand side of each image shows half the raw image whilst the right hand side shows half the image after the matrix Abel transform (as discussed in Chapter 2). It is clear to see that at wavelengths resonant with transitions on the $S_2(3s/\pi\sigma^*)$ state there is a narrow ring on the outer edge of the photoelectron image (Figure 3.5b & 3.5d).

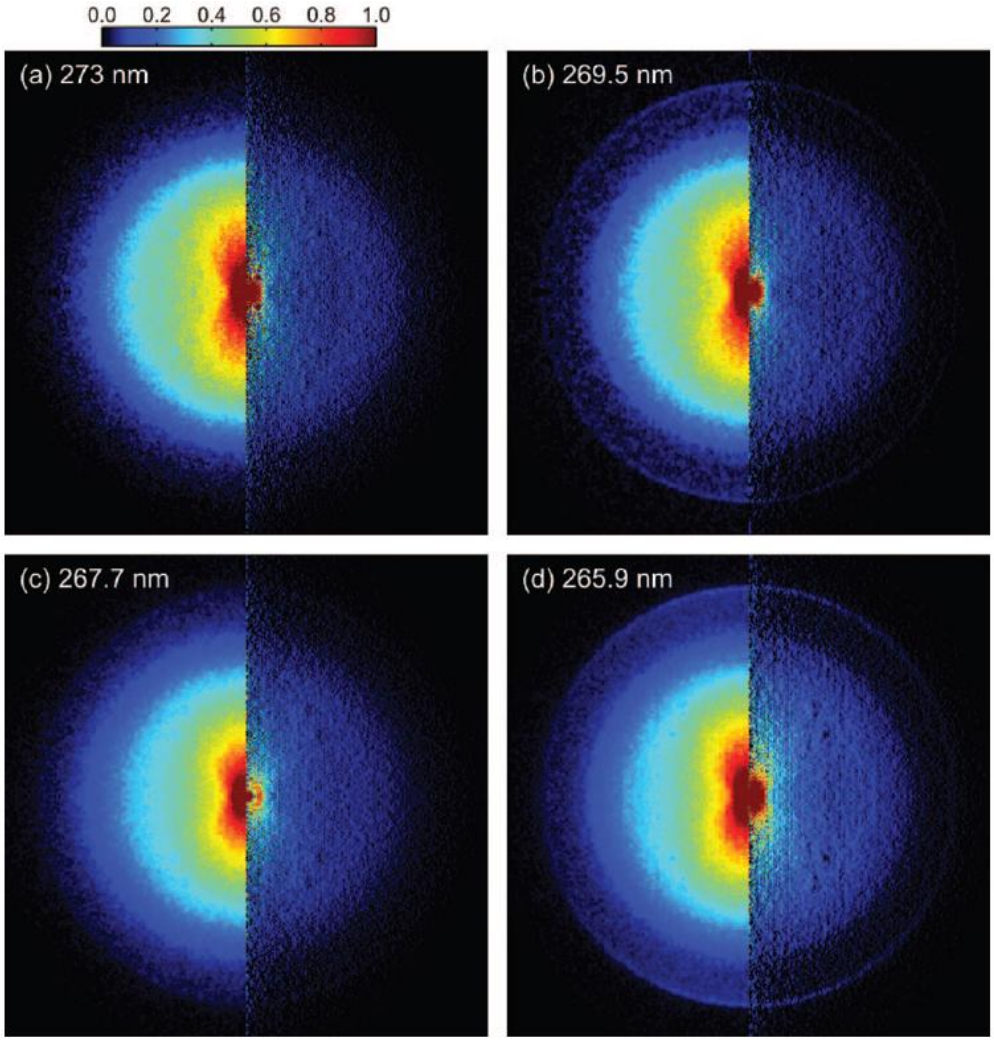

Figure 3.5 – Time zero images of aniline recorded at pump wavelengths of 273 nm, 269.5 nm, 267.7 nm and 265.9 nm (images (a)-(d) respectively). The images have been 4-fold symmetrised and are shown as a half Abel image. The left hand side of the images show raw image, whilst the right hand side of the image displays the Abel transformed image.

3.3.2 – Time-resolved photoelectron spectra

Figure 3.6 shows the time-resolved photoelectron spectra of aniline taken at the four pump wavelengths, along with a residual and fit for the spectrum of 269.5 nm. The data was fitted with a global fitting function defined in Eq 3.1[12, 15] as explained in more detail in Chapter 2, with three exponential functions.

$$I(E,t) = \sum_{i=1}^{n} A_i(E)\left(e^{-\frac{t}{\tau_i}}.cc(t)\right) \tag{3.1}$$

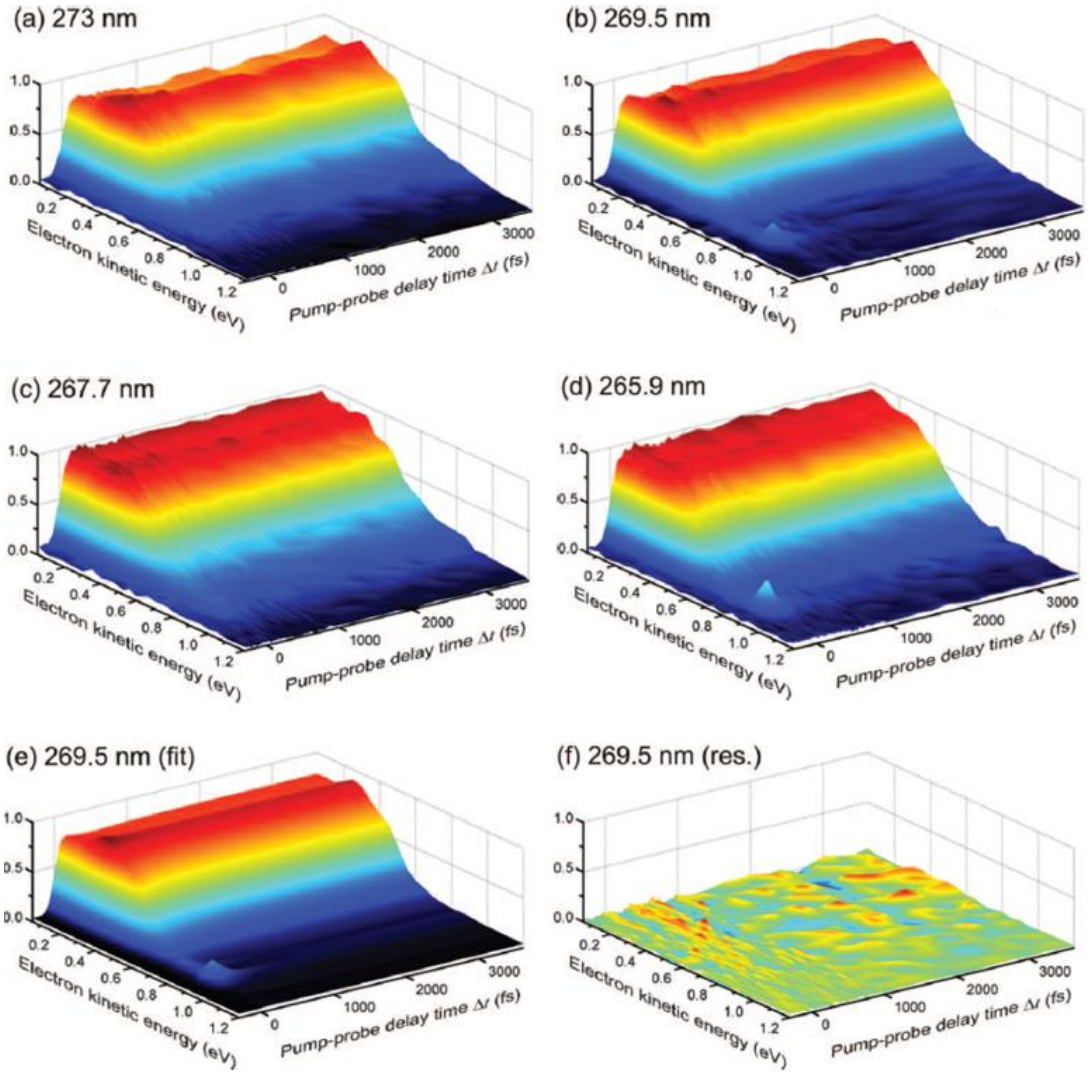

Figure 3.6 – The time-resolved photoelectron spectra of aniline at a) 273 nm, b) 269.5 nm, c) 267.7 nm and d) 265.9 nm. An example fit and residual is shown in the figure where e) is the fit of the 269.5 nm spectrum and f) is the corresponding residuals to the fit. For the displayed fit three decaying exponential functions were used.

It is immediately clear that there is a difference in the spectra at the four different excitation wavelengths. As seen in Figure 3.6, when the excitation wavelength is set to 269.5 nm and 265.9 nm there is evidence of a small feature at around 1.0 eV. This feature is not present at 273 nm and 267.7 nm. This is assigned as resulting from direct excitation to $S_2(3s/\pi\sigma^*)$ based upon the [2+2] REMPI by Ebata and co-workers[8] and in agreement with Fielding and co-workers.[5] Furthermore, this feature corresponds to the narrow ring identifiable in Figure 3.5b and Figure 3.5d. This narrow feature is indicative of a spectral feature with Rydberg character, due to its propensity to ionise to $\Delta v=0$ in the cation. It should also be noted that, due to the wavelengths selected, any ionisation of aniline will only access the first cation state $D_0(\pi^{-1})$. This is because the $D_0(\pi^{-1})$ ionisation energy is 7.72 eV[16, 17] and the $D_1(\pi^{-1})$ cation state ionisation energy is at 9.18 eV,[18] which is well above the total photon energy of 8.5-8.6 eV (pump + probe) for this experiment.

3.3.3 – Decay associated spectra

The four spectra in Fig 3.6 were fitted (as per Eq. 3.1) with three exponential functions (or two in the case of 273 nm). In each case, these fits were plotted as decay associated spectra (DAS) as shown in Figure 3.7. It should be noted that in all cases, the quoted uncertainty in the values of τ_1 and τ_2 is ± 10%. The DAS for the 273 nm data is fitted with two exponential functions, exhibiting lifetimes of τ_2 = 640 fs and τ_3 = >1 ns. The lack of a τ_1 exponential is to maintain a common nomenclature with the DAS of the other three excitation wavelengths.

The DAS generated from the 269.5 nm, 267.7 nm and 265.9 nm excitation data were fitted with three exponential functions. The time constants for 269.5 nm are reported as τ_1 = 180 fs, τ_2 = 510 fs and τ_3 = >1 ns. The lifetime of τ_1 at 269.5 nm of 180 fs is in good agreement with previously reported lifetimes by both Fielding and co-workers,[4] and Longarte and co-workers[2] (230 fs and 165 fs respectively). For 267.7 nm, the reported time constants are τ_1 = 110 fs, τ_2 = 760 fs and τ_3 = >1 ns. It was found when fitting this spectrum that a third exponential fit gave rise to a small non-zero amplitude fit in the region of 0.9 – 1.0 eV. This was attributed to a small amount of excitation to resonant $S_2(3s/\pi\sigma^*)$ transitions induced by the wings of the broad pump laser pulse. This produced a better residual than fitting with two exponentials, which skewed the τ_2 lifetime and produced an unsatisfactory result. Finally, the DAS at 265.9 nm was fitted with functions yielding lifetimes of τ_1 = 130 fs, τ_2 = 400 fs and τ_3 = >1 ns. From these DAS, it is clear that they all have similar relative shapes and amplitudes in the region of

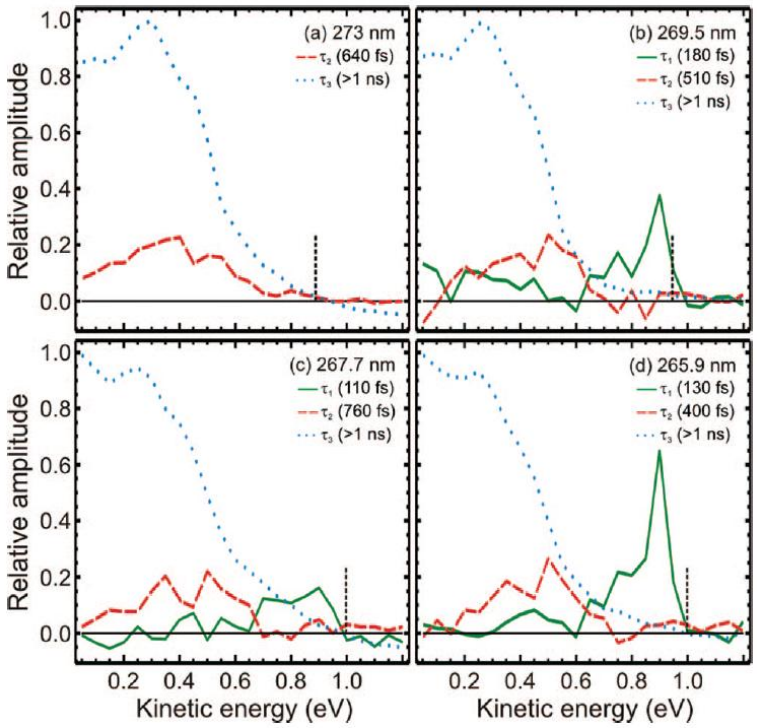

Figure 3.7 – Decay associated spectra of aniline at the four excitation wavelengths. The spectrum has been plotted in electron kinetic energy. In each spectrum the amplitudes have been normalised independently of all other wavelengths. The vertical dotted line represents the energetic cut off based upon the wavelengths used for the [1+1'] ionisation of aniline.

the spectrum between 0 – 0.6 eV. In this region, at all four wavelengths there is a long lived feature with a smaller amplitude feature superimposed upon it (τ_2 and τ_3). At wavelengths on resonance with a transition assigned to $S_2(\pi\sigma^*)$ there is a large, narrow feature that rapidly decays away. This spectral feature in the DAS was therefore assigned as resulting from $S_2(\pi\sigma^*)$, whilst the long lived feature and its superimposed weaker feature were assigned as $S_1(\pi\pi^*)$. The lifetime of >1 ns for τ_3 was identified by additional exploratory data taken out to 100 ps delay time.

Although the time constants reported in this work are in strong agreement with previously reported time-resolved photoelectron spectroscopy measurement by Fielding and co-workers,[4, 5] there is a difference in the relative amplitudes of the shortest time constant fit. In the work presented here there is no negative amplitude in any region of the DAS, whilst in the previous reported work by Fielding and co-workers[4] a negative amplitude feature between 0 – 0.6 eV was observed in the feature that is attributed to τ_1 here. It is worth noting that in the work by Fielding and co-workers,[4, 5] a different method of fitting the data was employed. However, the absence of any negative amplitude features in the DAS from this work would seem consistent with other findings in this study. These will be further discussed later in this chapter.

3.3.4 – Photoelectron angular distribution

Figure 3.8 displays the anisotropy parameter β_2 as a function of electron kinetic energy at three different time regions for both 273 nm and 265.9 nm. As the experiment was performed using a [1+1′] ionisation scheme with linearly polarised light, the following

equation (Eq. 3.2)[19, 20] was used to calculate the photoelectron angular distribution, as discussed in Chapter 2.

$$I(E,t,\theta) \propto 1 + \beta_2(E,t)P_2(\theta) + \beta_4(E,t)P_4(\theta) \tag{3.2}$$

From fitting the anisotropy parameters at all times and all energies it was concluded that β_4 was effectively zero at all points, and as such will not be considered any further. The normalised anisotropy parameter β_2 was investigated as both a function of energy (as shown in Figure 3.8), and as a function of time (as shown in Figure 3.9). From these figures it is clear that the β_2 parameter is heavily energy dependent. Considering only the short time region shown in Figure 3.8a and 3.8d, the low energy region of 0 – 0.3 eV has a β_2 of 0.6, whilst in the region between 0.3 – 0.6 eV β_2 gradually falls from 0.6 to 0. In the high energy region of Figure 3.8d there is a β_2 feature between 0.9 – 1.0 eV which matches up with the feature in the photoelectron spectra assigned to $S_2(3s/\pi\sigma^*)$. This feature has a high degree of anisotropy with a β_2 of ~1.1 (in good agreement to the value identified by Fielding and co-workers of 1.2).[4] Furthermore, when the longer time regions of 60 – 900 fs and 3.0 – 3.6 ps are considered, it is clear that the shape of the feature between 0.0 – 0.6 eV has undergone very little change in terms of β_2 as a function of time. Figure 3.9 shows β_2 as a function of time between 0 – 0.3 eV and 0.3 – 0.6 eV, and in 265.9 nm between 0.9 – 1.0 eV regions. As is evident from Figure 3.9, the value of β_2 is invariant as a function of time at all energies. It should also be noted that the same procedure was performed on the 269.5 nm and 267.7 nm spectra, and the results were nearly identical to those presented here for 265.9 nm and 273 nm. The significance of the invariance of the β_2 parameter as a function of time at these four wavelengths will be discussed further on in this chapter.

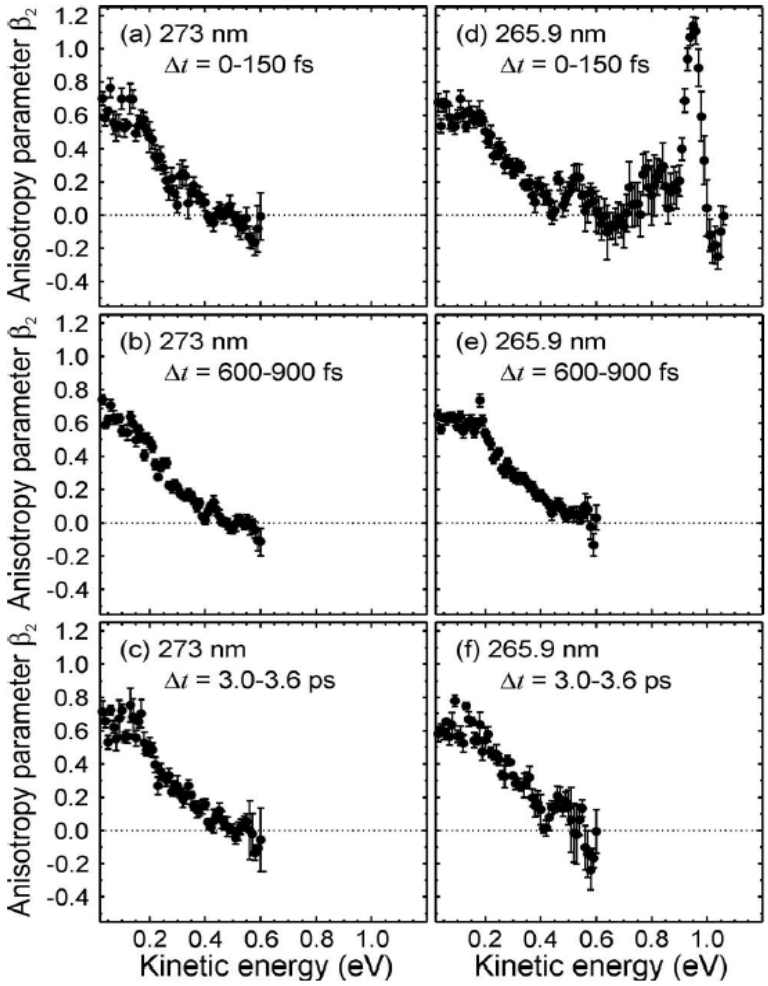

Figure 3.8 – Normalised anisotropy parameter β_2 as a function of electron kinetic energy at the three time regions of 0 – 150 fs, 600 – 900 fs and 3.0 – 3.6 ps at 273 nm (spectra a) – c) respectively) and 265.9 nm (spectra d) – f) respectively).

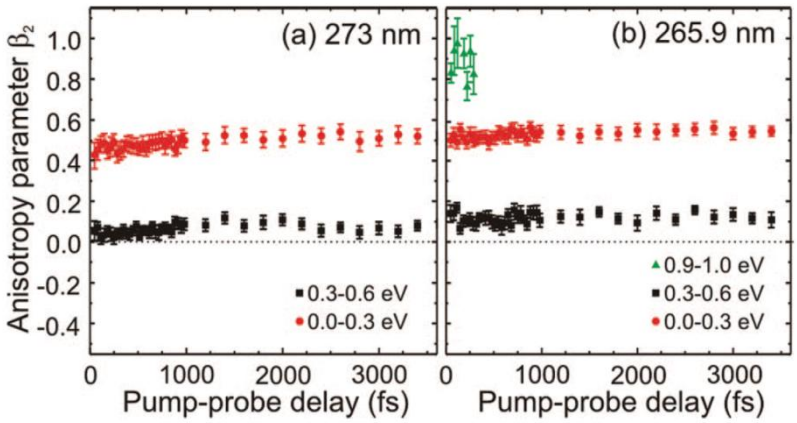

Figure 3.9 – The normalised anisotropy parameter β_2 plotted as a function of pump/probe delay. a) displays the parameter from the 273 nm spectrum, the value for β_2 has been taken as the average of two energy regions 0 – 0.3 eV, and 0.3 – 0.6 eV. b) shows the β_2 value as a function of pump/probe delay in the 265.9 nm spectrum. The β_2 values for this spectrum have been taken as an average of three energy regions 0 – 0.3 eV, 0.3 – 0.6 eV and 0.9 – 1.0 eV. These regions were selected to match the spectral regions with different amplitudes in the DAS (and have been coloured to match the colours used in figure 3.7

3.4 – Discussion

3.4.1 – Dynamics of the $S_1(\pi\pi^*)$ state

On the basis of previously reported studies, it is known that excitation with 273 nm only excites the $S_1(\pi\pi^*)$ state of aniline.[1, 8] In addition, it is known that the lifetime of the $S_1(\pi\pi^*)$ state is very long (~6 ns).[21] Therefore, based upon the DAS of the 273 nm data (shown in Figure 3.7a) we assign the long lived feature of τ_3 to the decay of the $S_1(\pi\pi^*)$ state. The decay mechanism of the $S_1(\pi\pi^*)$ state of aniline is not within the scope of this work, however, based upon the work of Weber and co-workers it is suggested that this decay is achieved not only by fluorescence,[22] but, also by an intersystem crossing to the T_1 triplet state identified in a picosecond study following excitation with 294 nm and subsequent ionisation with 200 nm light.[23] As the T_1 feature was only observed with pump + probe energies greater than 9 eV, however, due to the wavelengths used in this study, we are effectively blind to this decay mechanism as the total pump + probe energy provided in this experiment is in the region of 8.6 – 8.7 eV. It should also be noted that Ashfold and co-workers[1] speculated that the $S_1(\pi\pi^*)$ state can decay internally via a conical intersection with the S_0 ground state. However, they went on to say that this is likely to be inefficient at wavelengths >260 nm.

Continuing to consider the DAS resulting from excitation with 273 nm (shown in Fig 3.7a), the feature characterised by τ_2 = 640 fs will now be discussed. In previous work on phenol, catechol, resorcinol, hydroquinone[12] (see also Chapter 5), a feature was observed with similar dynamical timescales. This signal was attributed to ultra-fast intramolecular vibrational energy redistribution (IVR) on the $S_1(\pi\pi^*)$ surface, which in turn lead to a change in the Franck-Condon (FC) factors for ionisation as a function of time, thus leading to a decaying component in the spectrum. It should also be noted that sub-picosecond ultrafast IVR has been reported in the ground state of both benzene and difluorobenzene,[24] as well as the $S_1(\pi\pi^*)$ excited state of chlorobenzene.[25] In the results presented here, the excitation of $S_1(\pi\pi^*)$ is occurring at ~2600 – 3580 cm^{-1} above the $S_1(\pi\pi^*)$ origin. Therefore, it is reasonable to assume that IVR may be active when compared to the experimentally determined onset of IVR in similar systems such as hydroquinone and anisole, with onsets of 1650 cm^{-1} and 940 cm^{-1} respectively.[26, 27] In addition to this, the previously discussed work by Longarte and co-workers[2] also speculated that this process may be occurring on the initially prepared $S_1(\pi\pi^*)$ surface, in order to account for the relatively long lifetime of aniline at excitation wavelengths as short as 240 nm. From this evidence, the feature with the lifetime τ_2 is attributed to

ultrafast IVR on the $S_1(\pi\pi^*)$ surface of aniline. It should be noted though that the fitting method employed is only able to accurately model the IVR component of the overall dynamics is small.

Considering the arguments above, it is clear to see that the DAS of all four measurements are similar in terms of the shape and size of the amplitudes of the fits for τ_2 and τ_3. As such, it is reasonable to conclude that at all four wavelengths studied, the mechanistic pathways described by τ_2 and τ_3 are the same in all cases. This implies that the $S_1(\pi\pi^*)$ state is directly excited at all four wavelengths with ultrafast IVR occurring on a sub-picosecond timescale leading to an apparent change in the ionisation cross-section, followed by a long lived decay of the $S_1(\pi\pi^*)$ state. It should be noted that an alternative explanation for the feature associated with τ_2 is available through a "prefulvenic" conical intersection with the S_0 ground state. This alternative arises due to previously attributed sub-picosecond signal following UV excitation of benzene in the "channel three" region by Fielding and co-workers.[28, 29] However, this mechanism is shown to be unlikely due to a theoretical calculation performed by Stavros and co-workers.,[3] in which complete active space self-consistent field (CASSCF) calculations were performed to predict the energetic onset of prefulvenic conical intersections to connect the S_1 excited state to the S_0 ground state. It was found that this conical intersection lies at an energy of ~5.50 – 5.61 eV above the S_0 minimum. This energy is significantly higher than the excitation energies used in this work (4.54 – 4.66 eV). It should also be noted that Stavros and co-workers[3] inferred that even at excitation energies as high as 200 nm (6.2 eV), there is no strong evidence of prefulvenic pathways playing a role in the decay mechanisms.

3.4.2 – Dynamics of the $S_2(3s/\pi\sigma^*)$ state

At excitations in which the central wavelength is resonant with a transition identified as a bound vibrational level on the $S_2(3s/\pi\sigma^*)$, an additional feature is observed in the DAS in the high kinetic energy region of 0.9 – 1.0 eV, as clearly shown in Figure 3.7. As previously discussed, in the Franck-Condon region of the $S_2(3s/\pi\sigma^*)$ state the electronic character of the state contains a large contribution from the 3s Rydberg state located on the nitrogen. Therefore, ionisation from the $S_2(3s/\pi\sigma^*)$ region would likely lead to high kinetic energy photoelectrons with a narrow energy distribution due to the propensity of Rydberg states to ionise to $\Delta v = 0$. The feature with the lifetime labelled as τ_1 in both 269.5 nm and 265.9 nm is consistent with this, and so this feature is attributed to signal arising from direct excitation to quasi-bound vibrational levels in the

$S_2(3s/\pi\sigma^*)$ excited state. In addition to this, if the photoelectron angular distribution is considered, it is possible to gain further evidence to support this assignment. Consider a single photon ionisation from a state with a large electronic character from a 3s Rydberg orbital. Based upon an atomic orbital approximation the resulting photoelectron partial waves should be p type (considering the angular momentum quantum number, *l*, has to change by ±1), and produce a highly anisotropic distribution of photoelectrons peaking along the laser polarisation axis. As shown in Figure 3.8, the feature between 0.9 – 1.0 eV contains photoelectrons with a high anisotropy of $\beta_{2;}$ ~1.1. This evidence adds weight to the assignment of this feature to $S_2(3s/\pi\sigma^*)$. Additionally, the lifetime of this feature is shorter at 265.9 nm than 269.5 nm. In the work by Ebata and co-workers the REMPI spectrum,[8] displayed in Figure 3.4 showed that the origin transition of the $S_2(3s/\pi\sigma^*)$ at 269.5 nm has a significantly narrower line width then the higher lying vibrational feature at 265.9 nm. This difference, ~35 cm^{-1} for 269.5 nm versus ~150 cm^{-1} 265.9 nm, is a strong indicator of the lifetime of the transitions. Based upon these values the 1/*e* lifetimes were estimated to be ~150 fs for the 269.5 nm transition, and ~35 fs for the transition at 265.9 nm. The estimated value for 269.5 nm is in good agreement with the reported results (~180 fs), but the absolute value reported value 265.9 nm is somewhat larger than what the [2+2′] REMPI spectra would predict. That being said however, this is likely due to a blurring effect as the cross correlation of the instrument response in recording these measurements is too long to accurately measure a lifetime of 35 fs, nevertheless, it is clear to see that the trend is followed. Additionally, this spectrum also provides an explanation for the enhancement of the $S_2(3s/\pi\sigma^*)$ feature in 265.9 nm compared with 269.5 nm. As the feature at 265.9 nm is significantly broader than 269.5 nm, more of the bandwidth of the excitation laser pulse overlaps with it and, as such, more population can be put into $S_2(3s/\pi\sigma^*)$. The work of Stavros and co-workers,[3] discussed earlier in this chapter, reported no evidence of any direct excitation to $S_2(3s/\pi\sigma^*)$ following excitation to the $S_2(3s/\pi\sigma^*)$ origin at 269.5 nm. However, they attribute this to having a large bandwidth, reported in the UV to be around ~500 cm^{-1} (approximately ~200 cm^{-1} larger than the bandwidth used in this study), and as such were unable to get any significant population to this dark state due to its low oscillator strength.

Now, with all the evidence presented previously, the decay mechanism for the $S_2(3s/\pi\sigma^*)$ state will be considered. It was suggested by Ashfold and co-workers[1] that any population within the bound vibrational levels of the shallow potential in the $S_2(3s/\pi\sigma^*)$ surface decays via a tunnelling mechanism under the small potential energy

barrier purely on the $S_2(3s/\pi\sigma^*)$ surface, rather than undergoing population transfer to the $S_1(\pi\pi^*)$ state via non-adiabatic coupling of the two states through a conical intersection. After tunnelling it was suggested that the H-atom reached the purely dissociative part of the $S_2(3s/\pi\sigma^*)$ surface, and that near ballistic N-H bond dissociation would then occur. This mechanism is also supported in a number of different ways by the results presented in this chapter. Firstly by the lifetime of the $S_2(3s/\pi\sigma^*)$ state following excitation at both 269.5 nm and 265.9 nm. The tunnelling rate is dependent upon the size of the potential barrier. The top of this barrier in aniline is located at around ~255 nm based upon the potential energy cuts in Figure 3.2. As such, at higher energy wavelengths, the effective barrier height would become smaller and could potentially increase the tunnelling rate, assuming that the rate determining step is the dissociation of the N-H bond. This idea is described in Figure 3.10 as a schematic illustration. Consider next the DAS plots in Figure 3.7. The lack of any negative amplitude features in the DAS would indicate that the two relaxation mechanisms are independent of one another. This would mean that the decay of the $S_1(\pi\pi^*)$ and $S_2(3s/\pi\sigma^*)$ states are not sequential, but in fact two independent mechanisms over all regions in which both $S_1(\pi\pi^*)$ and $S_2(3s/\pi\sigma^*)$ were excited in this investigation. Considering that the experimentally determined onset for an S_2/S_1 conical intersection is reported to be either <260 nm (from Ashfold and co-workers)[1] or <250 nm (by Stavros

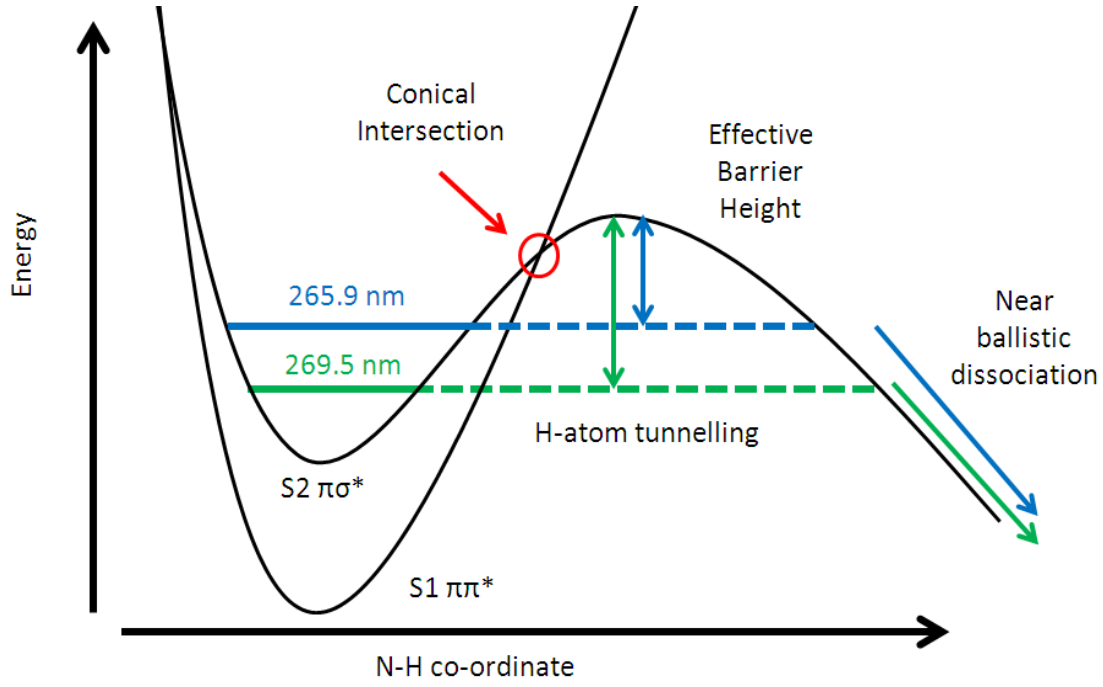

Figure 3.10 – Cartoon schematic of the H-atom tunnelling mechanism beneath the potential energy barrier on the S_2. The green line represents absorption to the S_2 origin at 269.5 nm and the blue excitation to the resonant transition in S_2 at 265.9 nm. Based on the potential energy cut in Figure 3.2

and co-workers),[3] it would seem that this could reasonably be the case. The next piece of evidence to consider is based upon the photoelectron angular distribution (PADs). As stated previously in this chapter, there is no observed change in β_2, the normalised anisotropy parameter, as a function of time in any energy region relating to any of the excitation wavelengths used in this work. As argued in other pieces of work by Townsend and co-workers[12] and by others,[30, 31] when two states non-adiabatically couple together some change in the PADs, as a function of pump-probe delay, due to the evolution of the electronic character, is expected. This can provide a signature that there is some change occurring in the state that the electron is subsequently ionised from, especially if the two electronic states give rise to very different PADs.

In many cases of aromatic or heteroaromatic systems, non-adiabatic coupling of states such as $\pi\pi^*$ and $3s/\pi\sigma^*$ states is achieved through some vibronic coupling, allowing the two states to mix. This is due to the restrictions imposed by the pure electronic symmetry character of the states involved.[32] As such, these vibronic couplings allow for distortions to occur within the molecular framework of the system (commonly through some sort of out-of-plane ring twisting or puckering motion)[33] to induce non-adiabatic dynamical evolution of the initially excited state. Due to the time scales of vibronic motion, it should be possible to monitor and resolve such changes in the electronic character of the state in the type of "ultrafast" measurements described in this chapter. A good example of this is work on several hydroxybenzenes performed by Livingstone *et al.*[12] (which will be discussed in Chapter 5), in which the temporal evolution of the anisotropy parameter β_2 was used as evidence of non-adiabatic coupling between the $S_1(\pi\pi^*)$ and $S_2(3s/\pi\sigma^*)$ states. In that study it was noted that the anisotropy parameter β_2 of the observed $S_1(\pi\pi^*)$ state increased as more 3s Rydberg electronic character from the $S_2(3s/\pi\sigma^*)$ state was mixed into the $S_1(\pi\pi^*)$ state, causing the resulting photoelectrons from subsequent ionisation to contain more p-wave type character. In general, aniline should be no exception to this as the electronic symmetries of the $S_1(\pi\pi^*)$ is B_2 and the electronic symmetry of the $S_2(3s/\pi\sigma^*)$ state of aniline is B_1 within the C_{2v} point group (given its predicted planar geometry in the excited state). Therefore, a vibrational mode with symmetry a_2 would be required to induce any non-adiabatic coupling between the $S_1(\pi\pi^*)$ and $S_2(3s/\pi\sigma^*)$ state, such as the suggested out-of-plane motion. The mediator of this interaction remains unclear at present,[1, 3] but based upon experimental work discussed in the following chapter, it is clear that some motion on the benzene ring in aniline is also required alongside the extension of the N-H bond.

As highlighted previously in this chapter, the onset for this internal conversion between $S_2(3s/\pi\sigma^*)$ and $S_1(\pi\pi^*)$ has been strongly inferred to occur at higher pump energies than those used for excitation in this study. The additional lack of any temporal evolution of the β_2 parameter within the data presented, would suggest that the initially excited $S_2(3s/\pi\sigma^*)$ surface is unable to sample the relevant vibrational modes needed to induce non-adiabatic coupling between the $S_2(3s/\pi\sigma^*)$ and $S_1(\pi\pi^*)$ states. The PADs, therefore, add additional support to the proposed mechanism that the $S_1(\pi\pi^*)$ and $S_2(3s/\pi\sigma^*)$ states decay via independent pathways. However, additional information that is discussed later in Chapter 4 may suggest that this argument maybe more subtle. However, as this is just one part of the justification for identifying the processes involved in the decay mechanism of aniline we postulate that the overall conclusion remains unchanged.

Finally, considering that there is no information on the relative ionisation cross-sections for the $S_1(\pi\pi^*)$ and $S_2(3s/\pi\sigma^*)$ states, it is not possible to quantify the fraction of the contribution these two pathways make to the overall dynamics of aniline at these excitation wavelengths. However, in many respects this would not be a useful comparison to make, as the $S_1(\pi\pi^*)$ state we are sampling is comprised of a broad "continuum-like" set of vibrational levels, whilst the resonant $S_2(3s/\pi\sigma^*)$ state is a narrow feature. As such, each component is largely dependent upon laser bandwidth. Interestingly, from this data it is possible to speculate that the ionisation cross-section of the $S_2(3s/\pi\sigma^*)$ state is significantly larger than that of the $S_1(\pi\pi^*)$ state. This speculation is based on the fact that the absorption cross-section of the $S_1(\pi\pi^*)$ state, from oscillator strengths alone, is four orders of magnitude larger than that of $S_2(3s/\pi\sigma^*)$.[3] That being said, the that fact that the $S_2(3s/\pi\sigma^*)$ feature is observable in the photoelectron spectrum implies that, even with the small population of the initially prepared $S_2(3s/\pi\sigma^*)$ state, the $S_2(3s/\pi\sigma^*)$-to-D_0 ionisation cross-section must be very large indeed. The following chapter, Chapter 4, will expand upon this in more detail by presenting and discussing experiments performed on aniline following excitation at 250 nm, alongside supporting high level theoretical calculations performed to support this work.

3.5 – Conclusion

Time-resolved photoelectron spectroscopy has been employed to investigate the electronic relaxation dynamics of aniline in the region between 273 – 265 nm. From the results presented, the conclusion was reached that at all wavelengths studied the $S_1(\pi\pi^*)$ state is directly populated and undergoes ultrafast IVR on a timescale of around ~500 fs, subsequently decaying on a timescale of >1 ns. With excitation wavelengths centred on resonance with transitions to the bound $S_2(3s/\pi\sigma^*)$, as shown in a previously reported REMPI spectrum,[8] direct excitation to $S_2(3s/\pi\sigma^*)$ is observed. This leads to an extra decay channel being present within the time-resolved spectra and is clearly modelled within the decay associated spectra (DAS). This feature has a high anisotropy of β_2, ~1.1, as expected from a state that contains a large electronic contribution from a 3s Rydberg state. However, within the wavelength range investigated, no evidence of non-adiabatic coupling between the $S_1(\pi\pi^*)$ and $S_2(3s/\pi\sigma^*)$ was observed. This is supported by three main pieces of evidence from the data. Firstly, from the shape of the DAS; the features described with a lifetime of τ_2 and τ_3 (the ultrafast IVR and decay of $S_1(\pi\pi^*)$) were invariant with excitation wavelength. Secondly, there was no evidence of any negative amplitude in the fits in the DAS in the region between 0 – 0.6 eV in all wavelengths studied with direct excitation to the $S_2(3s/\pi\sigma^*)$ state, implying that both $S_1(\pi\pi^*)$ and $S_2(3s/\pi\sigma^*)$ were populated simultaneously, and that the subsequent decay was independent and not sequential. Thirdly, it was observed that there was no dynamical evolution of the photoelectron angular distribution (PADs) at all wavelengths used. This is a strong indication that there is no non-adiabatic coupling occurring within the system at the wavelengths selected. The analysis performed and the conclusions reached regarding the decay mechanisms of aniline in the regions investigated, are largely consistent with the majority of other recent reports investigating the relaxation dynamics of aniline in the same region. However, the results presented in this chapter do differ in interpretation from some previously reported time-resolved photoelectron measurements on aniline.[4, 5]

To conclude this chapter, results were presented and discussed in an attempt to understand the relaxation dynamics around the $S_2(3s/\pi\sigma^*)$ origin. However, this is only a narrow range of the UV absorption region of aniline. To gain a greater understanding of the non-adiabatic coupling and interplay of the $S_1(\pi\pi^*)$ and $S_2(3s/\pi\sigma^*)$ states, it is necessary to investigate this system at higher energy wavelengths. This is discussed in the following chapter.

3.6 - References

1. G. A. King, T. A. Oliver and M. N. Ashfold, J. Chem. Phys. **132** (21), 214307 (2010).
2. R. Montero, A. Peralta Conde, V. Ovejas, R. Martinez, F. Castano and A. Longarte, J. Chem. Phys. **135** (5), 054308 (2011).
3. G. M. Roberts, C. A. Williams, J. D. Young, S. Ullrich, M. J. Paterson and V. G. Stavros, J. Am. Chem. Soc. **134** (30), 12578-12589 (2012).
4. R. Spesyvtsev, O. M. Kirkby, M. Vacher and H. H. Fielding, Phys. Chem. Chem. Phys. **14** (28), 9942-9947 (2012).
5. R. Spesyvtsev, O. M. Kirkby and H. H. Fielding, Faraday. Discuss. **157**, 165-179 (2012).
6. M. Miura, Y. Aoki and B. Champagne, J. Chem. Phys. **127** (8), 084103 (2007).
7. K. Kimura, H. Tsubomura and S. Nagakura, Bull. Chem. Soc. Jpn. **37** (9), 1336-1346 (1964).
8. T. Ebata, C. Minejima and N. Mikami, J. Phys. Chem. A **106** (46), 11070-11074 (2002).
9. R. N. Dixon, T. A. Oliver and M. N. Ashfold, J. Chem. Phys. **134** (19), 194303 (2011).
10. A. L. Sobolewski, W. Domcke, C. Dedonder-Lardeux and C. Jouvet, Phys. Chem. Chem. Phys. **4** (7), 1093-1100 (2002).
11. J. O. F. Thompson, R. A. Livingstone and D. Townsend, J. Chem. Phys. **139** (3), 034316 (2013).
12. R. A. Livingstone, J. O. Thompson, M. Iljina, R. J. Donaldson, B. J. Sussman, M. J. Paterson and D. Townsend, J. Chem. Phys. **137** (18), 184304 (2012).
13. U. Even, J. Jortner, D. Noy, N. Lavie and C. Cossart-Magos, J. Chem. Phys. **112** (18), 8068-8071 (2000).
14. A. T. J. B. Eppink and D. H. Parker, Rev. Sci. Instrum. **68** (9), 3477-3484 (1997).
15. O. Schalk, A. E. Boguslavskiy and A. Stolow, J. Phys. Chem. A. **114** (12), 4058-4064 (2010).
16. Kobayash.T and S. Nagakura, B. Chem. Soc. Jpn. **47** (10), 2563-2572 (1974).
17. M. A. Smith, J. W. Hager and S. C. Wallace, J. Chem. Phys. **80** (7), 3097-3105 (1984).
18. J. P. Maier and D. W. Turner, J. Chem. Soc. Farad. T 2 (4), 521-531 (1973).
19. K. L. Reid, Annu. Rev. Phys. Chem. **54**, 397-424 (2003).
20. K. L. Reid, Mol. Phys. **110** (3), 131-147 (2012).
21. R. Scheps, D. Florida and S. A. Rice, J. Chem. Phys. **61** (5), 1730-1747 (1974).
22. B. Kim, C. P. Schick and P. M. Weber, J. Chem. Phys. **103** (16), 6903-6913 (1995).
23. J. H. Yeh, T. L. Shen, D. G. Nocera, G. E. Leroi, I. Suzuka, H. Ozawa and Y. Namuta, J. Phys. Chem. **100** (11), 4385-4389 (1996).
24. R. S. von Benten, Y. Liu and B. Abel, J. Chem. Phys. **133** (13), 134306 (2010).
25. Y. Z. Liu, C. C. Qin, S. Zhang, Y. M. Wang and B. Zhang, Acta. Phys-Chim. Sin. **27** (4), 965-970 (2011).
26. G. N. Patwari, S. Doraiswamy and S. Wategaonkar, J. Phys. Chem. A. **104** (37), 8466-8474 (2000).
27. R. Matsumoto, K. Sakeda, Y. Matsushita, T. Suzuki and T. Ichimura, J. Mol. Struct. **735**, 153-167 (2005).
28. R. S. Minns, D. S. N. Parker, T. J. Penfold, G. A. Worth and H. H. Fielding, Phys. Chem. Chem. Phys. **12** (48), 15607-15615 (2010).

29. D. S. N. Parker, R. S. Minns, T. J. Penfold, G. A. Worth and H. H. Fielding, Chem. Phys. Lett. **469** (1-3), 43-47 (2009).
30. C. Z. Bisgaard, O. J. Clarkin, G. Wu, A. M. Lee, O. Gessner, C. C. Hayden and A. Stolow, Science **323** (5920), 1464-1468 (2009).
31. Y.-I. Suzuki, T. Horio, T. Fuji and T. Suzuki, J. Chem. Phys. **134** (18), 184313 (2011).
32. M. N. Ashfold, G. A. King, D. Murdock, M. G. Nix, T. A. Oliver and A. G. Sage, Phys. Chem. Chem. Phys. **12** (6), 1218-1238 (2010).
33. M. G. Nix, A. L. Devine, B. Cronin, R. N. Dixon and M. N. Ashfold, J. Chem. Phys. **125** (13), 133318 (2006).

Chapter 4 – Relaxation dynamics of aniline, *N*,*N*-dimethylaniline & 3,5-dimethylaniline

4.1 – Introduction

The work in this chapter follows directly from that in Chapter 3 in which the time resolved photoelectron dynamics of aniline in the region 273 – 266 nm were investigated.[1] This region was selected to understand the dynamics around the onset of direct excitation to the $S_2(3s/\pi\sigma^*)$ state.[2] This chapter documents additional work that was subsequently undertaken to further investigate the potential non-adiabatic coupling in aniline in an excitation regime above the theoretically and experimentally determined $S_2(3s/\pi\sigma^*)/S_1(\pi\pi^*)$ conical intersection at 250 nm.

As discussed in Chapter 3, the $S_2(3s/\pi\sigma^*)$ state in aniline exhibits considerable electronic character of a 3s Rydberg state in the vertical Franck-Condon region. However, as the N-H bond length increases, this electronic character falls away and the electronic character becomes more "valence-like".[3] As also discussed in the previous chapter, systems that contain $3s/\pi\sigma^*$ states are often found as chromophore sites in biologically relevant species, and it has been proposed that this allows these systems to rapidly and efficiently transfer energy, allowing rapid relaxation from an electronic excited state to the electronic ground state.[4, 5]

Work on aniline described here is motivated not only by its interesting photostability properties, but due to the fact that the exact mechanisms involved in the relaxation dynamics are unclear, even with a large body of work published by other groups. It was previously noted that the dynamics surrounding excitation around the $S_2(3s/\pi\sigma^*)$ origin were of particular contention. However, this discrepancy in the absolute nature of the relaxation mechanism of aniline is not just limited to this energy region. At excitation wavelengths around 250 nm there is also a lack of consistency between previously reported studies. In this higher energetic region, excitation still only populates the $S_2(3s/\pi\sigma^*)$ and $S_1(\pi\pi^*)$ excited states of aniline. However, at this wavelength more energy is available to the system (thus exciting a different, higher lying set of vibrational modes) when compared to the study in Chapter 3. It should be noted that the next electronic excited state is not accessible at this wavelength (which has an onset ~240 nm).

The next part of this chapter will discuss a set of four previous studies on aniline following excitation around 250 nm. Ashfold and co-workers,[6] and Stavros and co-

workers[7] have concluded that there is active non-adiabatic relaxation mechanism at work in the system allowing the initially excited $S_1(\pi\pi^*)$ state to decay via population transfer to the $S_2(3s/\pi\sigma^*)$ state through rapid internal conversion via a conical intersection. In the work of the former study, it was inferred that one of the critical co-ordinates involved in the motion required to promote the state mixing was an out-of-plane ring distortion on the benzene ring of the aniline system. This was deduced by examining the vibrational structure and recoil anisotropies of the H-atom total energy release spectrum generated using H-atom Rydberg tagging spectroscopy. In the latter work, time resolved H-atom velocity map imaging was employed to investigate the onset point for signal from high kinetic energy H-atoms, along with highly accurate complete active space self-consistent field (CASSCF) calculations. This study found that the onset of such signal was observed following excitation with 250 nm light. The appearance time of this signal was measured as <1 ps, and was treated as further evidence to support the mechanism of $S_1(\pi\pi^*)/S_2(3s/\pi\sigma^*)$ population transfer through a conical intersection. In addition to these two studies, work performed by Longarte and co-workers,[8] using time-resolved ion yield spectroscopy, also deduced that the conical intersection was active. However, they were unable to confidently define the directionality of the population transfer between the $S_2(3s/\pi\sigma^*)/S_1(\pi\pi^*)$. Finally, Fielding and co-workers performed time-resolved photoelectron imaging (TR-PEI) investigating the dynamics of aniline following excitation at 250 nm.[9] At this wavelength, the authors suggest that all excitation is exclusively to the $S_2(3s/\pi\sigma^*)$ state, in which both the 3s and $\pi\sigma^*$ components are populated. These two components then decay with lifetimes of 200 fs and 1.6 ps respectively. The faster time constant is attributed to decay to the $S_1(\pi\pi^*)$ state via non-adiabatic coupling, and the slower time constant is associated with N-H bond dissociation (or potentially an internal conversion to the S_0 electronic ground state). This proposed mechanism is the reverse of the process suggested by Ashfold and co-workers and Stavros and co-workers, however, it is also supported by recent calculations.[10]

Considering the discrepancies in the four previously published studies, it was decided that a new time resolved photoelectron imaging (TR-PEI) experiment should be performed to try and resolve the differences and understand the mechanism involved. In order to further interrogate the possible co-ordinates involved in bringing the two states to degeneracy, complementary measurements have also been performed on the *N*,*N*-dimethylaniline and 3,5-dimethylaniline systems. The structures of all three molecules of interest are shown in Figure 4.1. It has been stipulated previously, that

there are two motions which are key to accessing the $S_2(3s/\pi\sigma^*)/S_1(\pi\pi^*)$ conical intersection.[6, 7] These co-ordinates are motion along the N-H bond stretching mode, and a ring torsion mode on the benzene ring. The selection of the two additional systems has been chosen to provide further mechanistic insight into the importance of these modes 3,5-dimethylaniline was specifically chosen to limit proximity effects of the methyl groups on the amino group.

There have been very few published studies on the two methylated systems. Only two relevant experimental studies on the spectroscopy *N*,*N*-dimethylaniline have been published, which both provide low-resolution UV-VIS spectra.[11, 12] In addition, a single computational study investigating the excited state energies of the system using CASSCF[13] has previously been published. There appears to be no previous work published on 3,5-dimethylaniline. Due to the lack of previous work, any comparison made between the three molecules studied must be done with great care. However, the TR-PEI work presented in this chapter will be augmented by additional preliminary spectroscopic measurements and supporting theoretical calculations. The culmination of this work will help produce an understanding of the $S_1(\pi\pi^*)/S_2(3s/\pi\sigma^*)$ conical intersection mechanism in the three systems of interest.

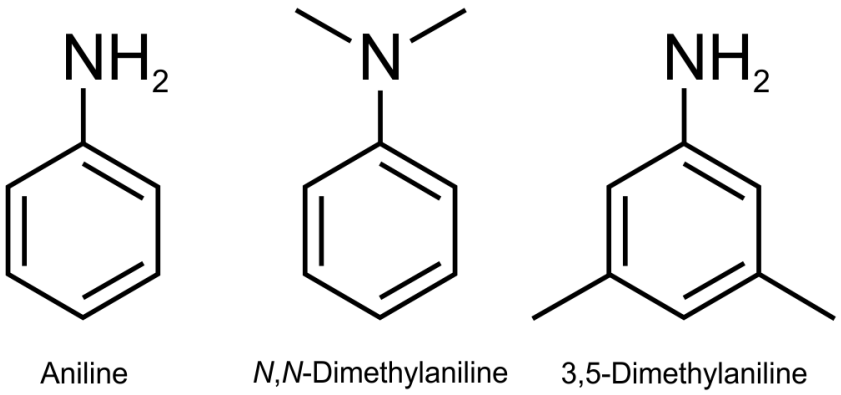

Figure 4.1 – Chemical structures of aniline, *N*,*N*-dimethylaniline and 3,5-dimethylaniline

4.2 – Experimental

4.2.1 – Gas phase UV/VIS absorption spectrometer

In all three cases, the molecules studied were purchased from Sigma-Aldrich (aniline ≥99.5% purity, *N*,*N*-dimethylaniline 99% purity and 3,5-dimethylaniline 98% purity). Initial vapour phase UV/VIS spectra were recorded at room temperature using a commercially available (Shimadzu UV-2550) spectrometer. The spectra were produced using a scan with 0.2 nm step intervals with a 1 mm slit width. The sample was introduced into the spectrometer using a 1 cm diameter quartz (HellmaAnalytics 104.002-QS) cuvette.

4.2.2 – [1+1] REMPI set-up

In order to ensure the wavelengths selected would not cause further complication to the dynamics by accessing additional states other than $S_1(\pi\pi^*)$ and $S_2(3s/\pi\sigma^*)$, preliminary [1+1] resonance enhanced multiphoton ionisation (REMPI) measurements were performed using the velocity map imaging spectrometer described elsewhere.[14] Samples were introduced into the vacuum chamber via an Even-Lavie (EL) pulsed molecular beam valve[15] seeded with helium at a backing pressure of 1.5 bar. The liquid samples were applied to strips of filter paper and loaded directly into the sample cartridge of the valve directly behind the expansion nozzle. The valve was regulated at a temperature of ~45° C (or at ~60° C for 3,5-dimethylaniline) to gain adequate vapour pressure for the measurements. The molecular beam produced by the EL valve passed through a skimmer before reaching the interaction region in the spectrometer, where it was intersected by a laser beam of UV light, tuned between 254 – 240 nm. The light was generated by using "beam line 1" as described in detail in Chapter 2, attenuated to 1.2 μJ/pulse and focused into the VMI spectrometer through a 25 cm fused silica lens. [1+1] REMPI photoelectron images were recorded for all three molecules over a wavelength range of 254 – 240 nm in 2 nm intervals (also the full width half maximum of the UV bandwidth). In each case a single photoelectron image was acquired using the standard VMI set-up described in Chapter 2. In the case of each molecule, the molecular beam conditions were tuned to eliminate any cluster signal by examining a time-of-flight mass spectrum produced in ion detection mode. Finally, the REMPI photoelectron images were processed using the matrix-Abel transform and calibrated using a 240 nm one colour multiphoton image of pyrrole.

4.2.3 –Time resolved photoelectron imaging set-up

TRPEI experiments were performed using the set up discussed in Section 4.2.2 with the following additions. The pump beam for the initial excitation process of all the TRPEI experiments was set to 250 nm (1.2 μJ/pulse). A second co-propagating beam of light set at 305 nm for aniline or 310 nm for *N*,*N*-dimethylaniline or 3,5-dimethylaniline (1.8 μJ/pulse) was used for the probe pulse (generated using "beam line 2" as described in Chapter 2). Prior to combination, the pump and probe UV beams were passed through prism compressors to manage the temporal response of the instrument. The cross-correlation was obtained by non-resonant, two-colour [1+1′] multiphoton ionisation of pyrrole and was measured to be 130±10 fs. The pump-probe time delay for all the TRPEI measurements was scanned between -250 fs to +100 ps, this was partitioned into 25 fs linear steps in the region from -250 fs to +500 fs, and then 17 exponentially increasing time steps. At each pump-probe delay position, time-independent one-colour photoelectron images were recorded of both the pump and probe alone signals in addition to the pump-probe signal. These were used for subsequent background subtraction from the pump-probe signal.

4.3 – Results

4.3.1 – Gas phase UV/VIS absorption spectra

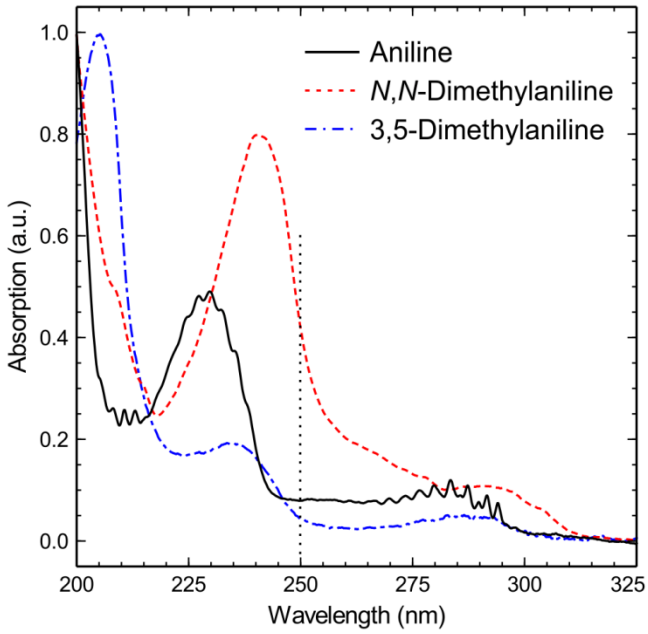

Figure 4.2 – Vapour phase UV/VIS spectra of aniline, *N*,*N*-dimethylaniline and 3,5-dimethylaniline

Figure 4.2 shows the preliminary vapour phase UV/VIS spectra recorded at room temperature of the three systems. The aniline spectrum is consistent with previously reported measurements.[6, 7] The spectra show three regions of major absorption which have been assigned by previous work as the first, second and third ππ* states.[11] The region between 270 nm and 245 nm is where excitation to the previously studied $S_2(3s/\pi\sigma^*)$ state would be anticipated.[1, 2] The second strong absorption band onset is at ~245 nm. Until recently, this state had been assigned as $S_3(\pi\pi^*)$, however, recent theoretical work by Worth and co-workers has suggested that there are two p type Rydberg states that also exist in this energetic region.[16] This assignment is also supported by theoretical calculations performed in this work, outlined in Section 4.3.6. As such, this feature will be labelled as S_3 with no specific molecular orbital state label for the remainder of this chapter.

The spectrum of 3,5-dimethylaniline, is very similar to that of aniline. There is a small red shift in the position of the higher energy bands most likely due to an electron induction effect caused by the methyl groups lowering the excitation energy of the π-system. Due to the similarity, the spectrum of 3,5-dimethylaniline is assigned in the same way as aniline. It is important to note that this work seeks to investigate these systems at a wavelength close to 250 nm where it is believed that the $S_2(3s/\pi\sigma^*)/S_1(\pi\pi^*)$ conical intersection is active. As such, it is important that there is no direct excitation to S_3 for these systems, as the additional state could potentially further complicate the TRPEI data and subsequent interpretation. However, as the absorption of S_3 has only been shifted by ~5 nm, it is unlikely that at 250 nm there would be any significant absorption to the S_3 state.

Considering the need to avoid direct excitation of the S_3 state, and using the highest energy pump wavelength possible to maximise the chance of observing the coupling between the $S_2(3s/\pi\sigma^*)$ and $S_1(\pi\pi^*)$ states, the spectrum of *N*,*N*-dimethylaniline potentially poses a problem as it is clearly quite red shifted with respect to aniline. In fact, the onset of the S_3 state is red shifted by ~20 nm. This shift in the spectrum would suggest that the wavelength choice for the pump beam would have to be different for *N*,*N*-dimethylaniline in order to avoid direct excitation of the S_3 state. However, the spectrum of *N*,*N*-dimethylaniline at room temperature could contain more hot bands than the spectrum of aniline, and thus the origin of the S_3 excited state might potentially appear to be red shifted compared with its true origin. This assumption is based on a comparison of the lowest frequency ground-state vibrational modes of the two systems. In aniline, the lowest frequency vibrational modes in the ground state are >200 cm^{-1} [16, 17] where as in *N*,*N*-dimethylaniline it is predicted that there are vibrational modes (associated with CN and CH_3 torsions) with vibrational frequencies <100 cm^{-1}.[18] To the best of this authors knowledge, the ground state vibrational frequencies for 3,5-dimethylaniline have not been previously reported. However, considering that the low frequency vibrational mode in aniline is associated with the NH_2 group, it is reasonable to assume that the lowest frequency vibrational mode in 3,5-dimethylaniline would be similar, and therefore would have a lowest frequency vibrational mode around <200 cm^{-1}. It is also worth noting that the infrared spectrum of *m*-xylene (or 1,3-dimethylbenzene) has been measured and shows vibrational frequencies around ~100 cm^{-1} which are associated with torsional modes of the CH_3 groups on the benzene ring.[19]

Within the context of this work, it is important to understand that the TRPEI measurements are obtained in a jet-cooled molecular beam. As such, the likelihood of any hot band features in the TRPEI spectrum is significantly reduced, and in principle should not be evident at room temperature. To get a clearer picture of excitation to the onset of the S_3 state in all three molecules, the next section will present the [1+1] REMPI spectra of the three systems using the method described in Section 4.2.2 in this chapter.

4.3.2 – [1+1] REMPI spectra

Figure 4.3 shows the [1+1] REMPI spectra of aniline, *N*,*N*-dimethylaniline and 3,5-dimethylaniline. By comparing the results of the aniline REMPI to the work in Chapter 3 and previous work by Fielding and co-workers,[9, 20] the signals originating from the

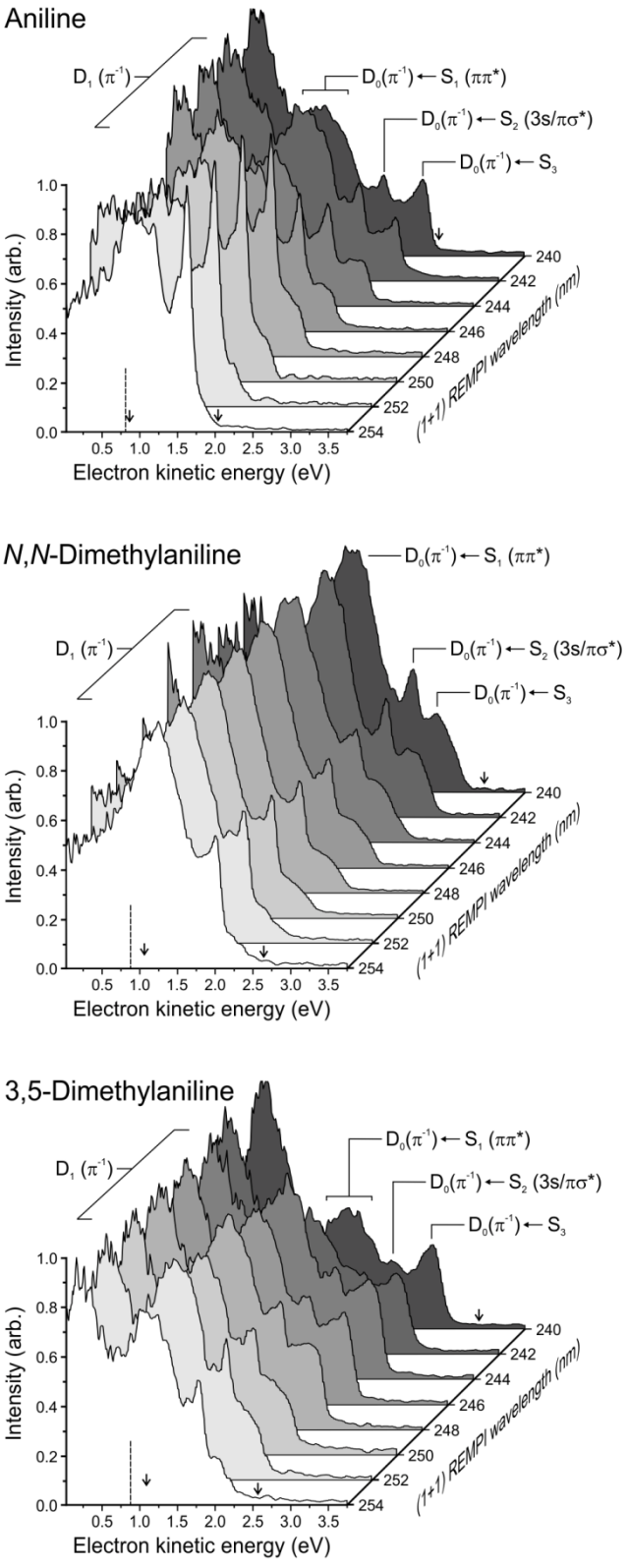

Figure 4.3 – [1+1] REMPI spectra of aniline, *N*,*N*-dimethylaniline and 3,5-dimethylaniline plotted in a waterfall style. The spectra have all been calibrated in the same manner and each spectral feature has been labelled as indicated in the spectra.

$S_1(\pi\pi^*)$, $S_2(3s/\pi\sigma^*)$ and S_3 states are easily identifiable and have been labelled on the figure. For aniline, *N*,*N*-dimethylaniline and 3,5-dimethylaniline, the adiabatic ionisation potentials (IPs) to the D_0 cation states are known and have energies of 7.72 eV,[21, 22] 7.12 eV[23, 24] and 7.2 eV[25] respectively. The energetic cut offs, based upon the total energy indicated by the small arrows on the REMPI photoelectron spectrum. In the case of aniline, the maximum cut off of the kinetic energy photoelectron spectrum agrees well with the values predicted by the IP. However, in the case of the two methylated systems, the agreement is less satisfactory. But it is worth noting that the IPs quoted for the methylated systems are based on band edges of low-resolution He(I) photoelectron spectra, whilst the quoted IP for aniline was obtained using a higher resolution, laser-based measurement. As such, based upon the data presented in Figure 4.3, using the averaged cut off position of the high kinetic energy photoelectrons it has been possible to estimate a revised $D_0(\pi^{-1})$ adiabatic IP for the two methylated aniline systems. There are 7.26±0.05 eV for *N*,*N*-dimethylaniline and 7.48±0.05 eV for 3,5-dimethylaniline.

However, as noted previously in this chapter, the importance of the [1+1] REMPI spectra shown in Figure 4.3 is to investigate the onset of the S_3 state. It is clear in all cases that as the wavelength is shortened a peak becomes pronounced at high kinetic energy. In aniline, this feature becomes highly apparent at wavelengths ≤242 nm and has an onset at 246 nm. Interestingly, at longer wavelengths (≥248 nm) there is a small shoulder on the high kinetic energy edge of the spectra. This narrow peak and small shoulder exist at all wavelengths investigated and is attributed to signal arising from $S_2(3s/\pi\sigma^*)$. The origin of the shoulder signal will be elaborated on in detail further on in this chapter. Both *N*,*N*-dimethylaniline and 3,5-dimethylaniline show behaviour consistent with aniline in terms of the structure of the photoelectron spectra. These systems show the onset of the S_3 signal to be around ~246 nm to 248 nm. It is therefore concluded that excitation at 250 nm may be used for the TRPEI measurements to investigate the potential coupling between the $S_2(3s/\pi\sigma^*)/S_1(\pi\pi^*)$ states in all three systems without any significant excitation to the S_3 state.

In the low kinetic energy region of each spectrum, a feature grows in intensity as the wavelength is shortened with an onset of ~246 nm (except in the case of 3,5-dimethylaniline, where it is present at all wavelengths). This feature can reasonably be attributed to ionisation to the $D_1(\pi^{-1})$ cation state. The vertical ionisation potentials of the $D_1(\pi^{-1})$ cation state (from the ground state) have been previously identified as 9.18 eV, 9.00 eV and 8.55 eV for aniline, *N*,*N*-dimethylaniline and 3,5-dimethylaniline, respectively.[24, 25] Considering the total energy provided in a [1+1] REMPI scheme at 250 nm is 9.92 eV, it is feasible for the $D_1(\pi^{-1})$ cation state to be accessible at all REMPI wavelengths studied. However, excitation with a 250 nm laser pulse (4.96 eV) prepares the $S_1(\pi\pi^*)$ and $S_2(3s/\pi\sigma^*)$ state in high energy vibrational modes (well above the origins of the respective states).[2, 6] As such, using the Franck-Condon principle, it can be speculated that the propensity for ionisation to the $D_1(\pi^{-1})$ cation state from the $S_1(\pi\pi^*)$ and $S_2(3s/\pi\sigma^*)$ states is small. This is largely due to the total energy being applied to the system is not sufficient to access the highly vibrationally excited levels of the $D_1(\pi^{-1})$ cation state where the FC overlap with the highly vibrationally excited $S_1(\pi\pi^*)$ and $S_2(3s/\pi\sigma^*)$ states would be more favourable) That being said, once the threshold for excitation to S_3 has been reached, this state (being prepared in vibrational modes at or close to the origin) should have a more favourable Franck-Condon overlap with the $D_1(\pi^{-1})$ cation state and, therefore, ionisation via S_3 should be able to access the $D_1(\pi^{-1})$ state. In the case of aniline and *N*,*N*-dimethylaniline this seems to be the case, adding additional weight to the argument that at 250 nm there is no direct excitation to

the S_3 state in these systems. For the 3,5-dimethylaniline, the situation is a little different as $D_1(\pi^{-1})$ ionisation is present at all wavelengths. However, when considering the significant lowering in energy of the $D_1(\pi^{-1})$ state when compared to aniline or *N*,*N*-dimethylaniline, it is possible that Franck-Condon overlap between $S_1(\pi\pi^*)$ and $S_2(3s/\pi\sigma^*)$ states with the $D_1(\pi^{-1})$ cation state is increased, allowing more effective ionisation at all wavelengths.

Based upon the UV/VIS vapour phase spectra presented in Figure 4.2, the choice of probe wavelength was made to minimise the risk of any probe-pump excitation to the $S_1(\pi\pi^*)$ state origin. The probe wavelengths were set to 305 nm for aniline, and 310 nm for the two methylated aniline systems. This gives a total energy for the TRPEI measurement of ~9.0 eV when exciting at 250 nm. In Figure 4.3, this is denoted by a vertical dashed line. This position on the spectra is effectively the position of zero kinetic energy for the resulting photoelectron using the TRPEI [1+1′] ionisation scheme. On the basis of this, it is assumed that during the TRPEI measurement only signal originating from ionisation to the $D_0(\pi^{-1})$ cation state should be present.

4.3.3 – Photoelectron images & time-resolved photoelectron spectra

Figure 4.4 presents a selection of velocity map images of aniline, *N*,*N*-dimethylaniline

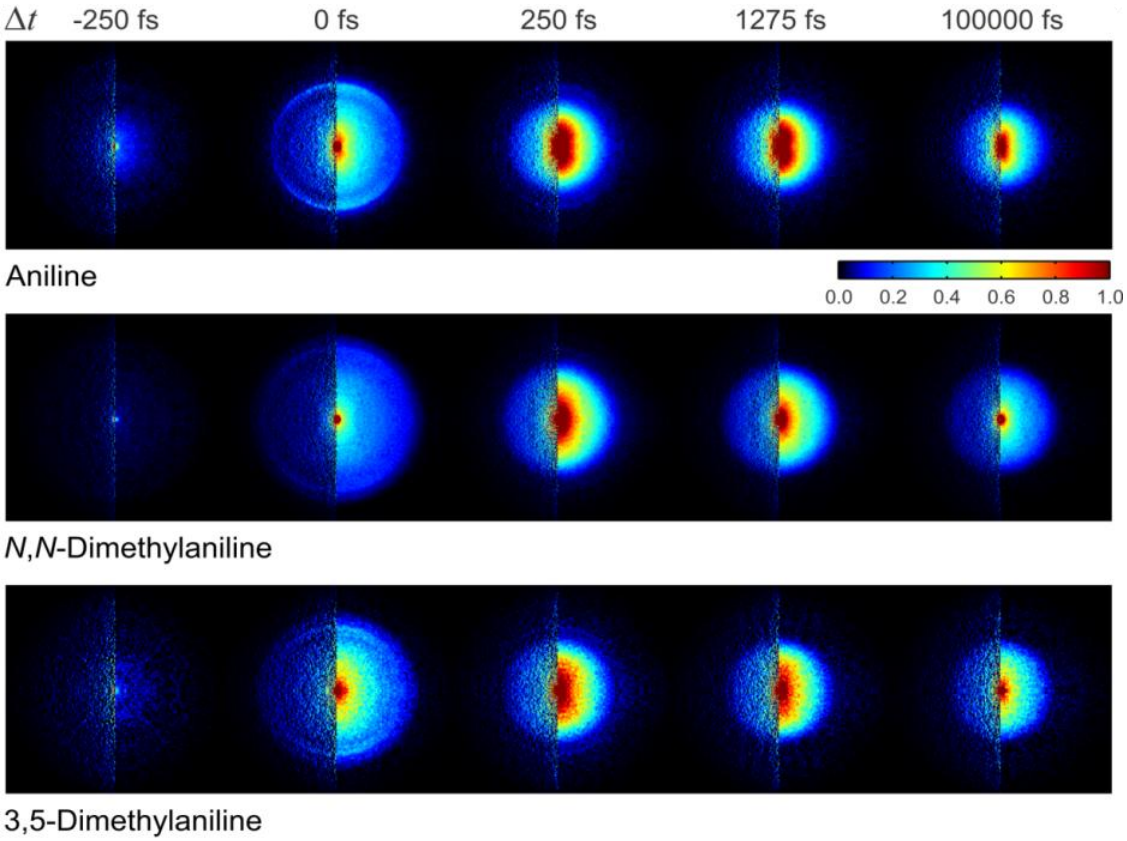

Figure 4.4 – Strip of VMI images of aniline, *N*,*N*-dimethylaniline and 3,5-dimethylaniline taken at a selection of pump-probe time delays, The images have been presented showing both the raw and transformed images (shown as a half and half picture). The left hand side of the image is transformed, whilst the right hand side is raw. The images have been symmetrised on a 4 fold axis and have had any pump or probe alone signals removed by background subtraction.

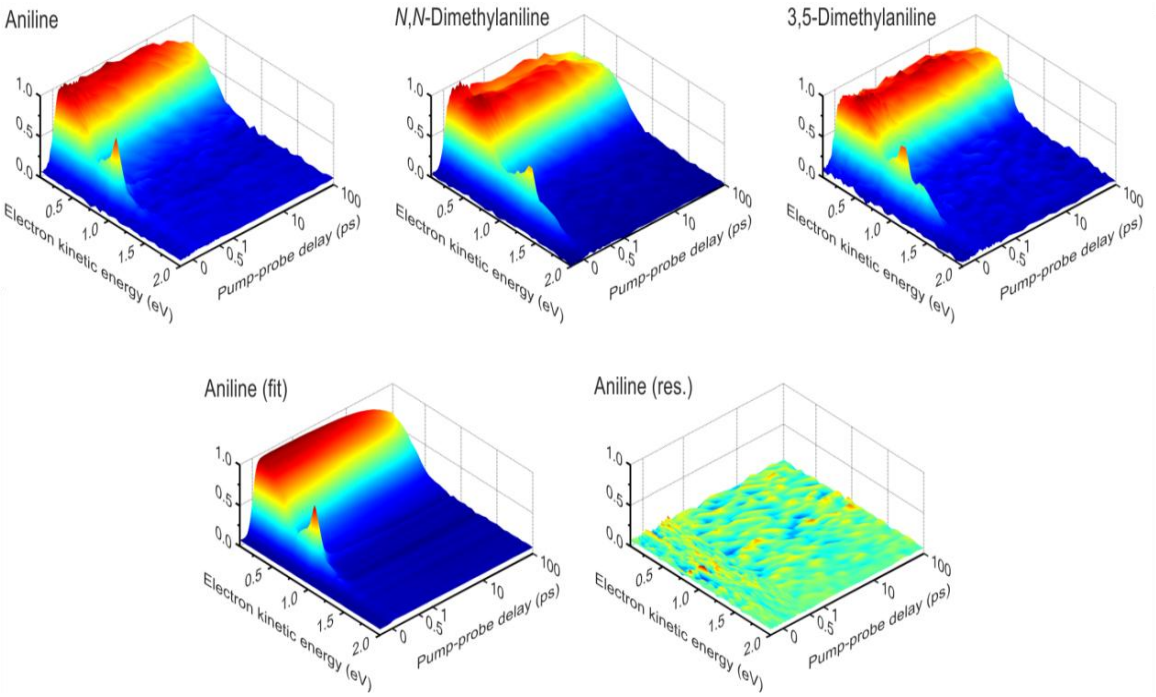

Figure 4.5 – Time resolved photoelectron spectra of aniline, *N*,*N*-dimethylaniline and 3,5-dimethylaniline. The globally fitted aniline spectrum is also shown with its residual fit. The data is presented in a lin/log time axis for presentation purposes. The linear region runs from -250 fs to +500 fs from which point the scale is logarithmic to 100 ps. The data has been partitioned into energy bins of 0.025 eV.

and 3,5-dimethylaniline at various pump-probe time delays. These images were generated by subtracting the pump-alone and probe-alone photoelectron images from the unprocessed pump-probe photoelectron images (shown on the right hand side of the images). These images are then subjected to a matrix Abel-transform to reconstruct the velocity map image (left hand side of the images).

Figure 4.5 shows the time-resolved photoelectron spectra of aniline, *N*,*N*-dimethylaniline and 3,5-dimethylaniline. The data have been plotted on a linear scale between -250 fs and +500 fs and on a log scale from 500 fs to 100 ps. In all three data sets, there are a number of similar spectral features. In the low kinetic energy region of the spectrum between 0 eV and ~0.7 eV, there is a weakly decaying signal on top of a longer lived feature. In addition, at early time delays, all three molecules exhibit a rapidly decaying feature at energies higher than 0.6 eV kinetic energy. This feature has a well-defined narrow peak on top of a large, broad background signal. The spectra are also largely similar to the aniline spectrum at 265.9 nm (as shown in Figure 3.6) in terms of observed spectral features. This will be discussed later in this chapter.

4.3.4 – Decay associated spectra

The time resolved photoelectron spectra were fitted by the global fit function (as discussed in Chapter 2) which, in turn, describes a series of exponentially decaying

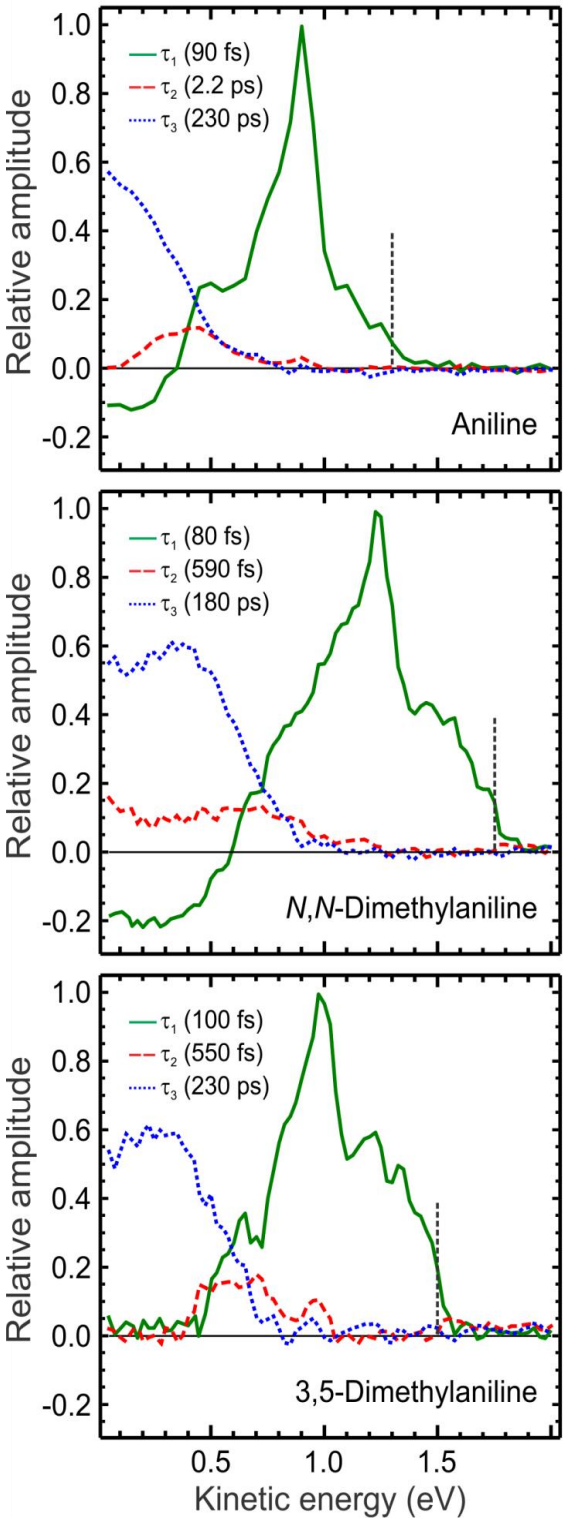

Figure 4.6 – Decay associated spectra of the three molecules. In each case the spectra have been fitted with 3 exponentially decaying functions. The vertical dashed line in each spectrum represents the energetic cut off of each system based upon the IP (which is assumed to be 7.72 eV, 7.26 eV and 7.48 eV for aniline, N,N-dimethylaniline and 3,5-dimethylaniline respectively) and the total pump probe excess energy. The uncertainties of the fits shown in the figure are ±10 % (one standard deviation).

functions (which originate from $\Delta t = 0$). This is then coupled to the experimentally determined Gaussian cross-correlation function. This method is discussed in more detail in Chapter 2 and elsewhere.[26] This fitting method produces a decay associated spectrum (DAS), in which the relative amplitude of each exponential function is plotted against photoelectron kinetic energy. These DAS are plotted in Figure 4.6 for aniline, *N*,*N*-dimethylaniline and 3,5-dimethylaniline. In order to produce a satisfactory fit to the TRPES data shown in Figure 4.5, three exponential functions were required. In all three molecules, the first time constant, τ_1, was fitted as 100 fs or faster. The second time constant, τ_2, describes a longer process in the low kinetic energy region of the photoelectron spectra. These constants somewhat differ from aniline to the methylated systems; changing from 2.2 ps in aniline to 550 fs and 590 fs in 3,5-dimethylaniline and *N*,*N*-dimethylaniline respectively. The third and final time constant, τ_3, decays over a significantly longer time scale of 180 – 230 ps.

The lifetimes obtained for aniline are in reasonable agreement with the previously reported time constants reported by Fielding and co-workers at 250 nm.[20] Additionally, the lifetime of the first time constant follows the trend of decreasing

lifetime as the pump pulse is shortened, as identified in Chapter 3. Although the structure and relative amplitudes of the DAS are broadly similar in appearance in all three spectra, there is a key difference between the 3,5-dimethylaniline and the other two systems. For aniline and *N*,*N*-dimethylaniline, there is a negative amplitude feature in the low kinetic energy region of the spectrum, which is not present in the 3,5-dimethylaniline spectrum. The negative amplitude feature is a strong indication that a sequential dynamical process may be occurring, as discussed already in Chapter 2. The significance of the negative amplitude feature in the DAS of aniline and *N*,*N*-dimethylaniline and the lack of negative amplitude in the DAS of 3,5-dimethylaniline will be expanded upon further in Section 4.4.

4.3.5 - Photoelectron angular distributions

As discussed previously in Chapter 2, and in numerous reviews,[27, 28] the photoelectron angular distribution (PADs) can be obtained by using the function in Eq. 4.1

$$I(E,t,\theta) \propto 1 + \beta_2(E,t)P_2(\theta) + \beta_4(E,t)P_4(\theta) \tag{4.1}$$

Figure 4.7 shows the β_2 value plotted as a function of pump-probe delay time (left) and as a function of kinetic energy at Δt = 0 (right). First considering β_2 as a function of photoelectron kinetic energy at Δt = 0, it is clear to see that the sharp feature in the photoelectron spectrum around ~1 eV has a considerably higher β_2 than other features. This feature is characteristic of 3s Rydberg electronic character associated with the $S_2(3s/\pi\sigma^*)$ state, as previously seen in Chapter 3. Next, considering the left hand panels in Figure 4.7, in all case the β_2 value is averaged over all regions with significant photoelectron signal associated with the third time constant, τ_3, which can be assumed to be between 0.0 eV and 0.7 eV in all cases. Looking at the temporal evolution of β_2 in aniline, it is clear to see that there is no change in the signal as a function of time. This is somewhat different to what was observed in the methylated systems. In the case of *N*,*N*-dimethylaniline, there is an obvious change in the β_2 at early time delays with a rise time of approximately 200 fs. This rise is considerably faster than the one shown in the 3,5-dimethylaniline data. In this system there is a longer rise in the value of β_2, which occurs on the timescale of ~1 ps. The differences in the temporal evolution of β_2 will be considered further in the discussion section of this chapter. At higher kinetic energies (i.e., beyond 0.50-0.80 eV, depending on the system), photoelectron signals are

extremely short-lived and no information relating to their temporal evolution may be reliably obtained. It should also be noted that the value of β_4 was measured to be effectively zero at all energies and times in all three molecules.

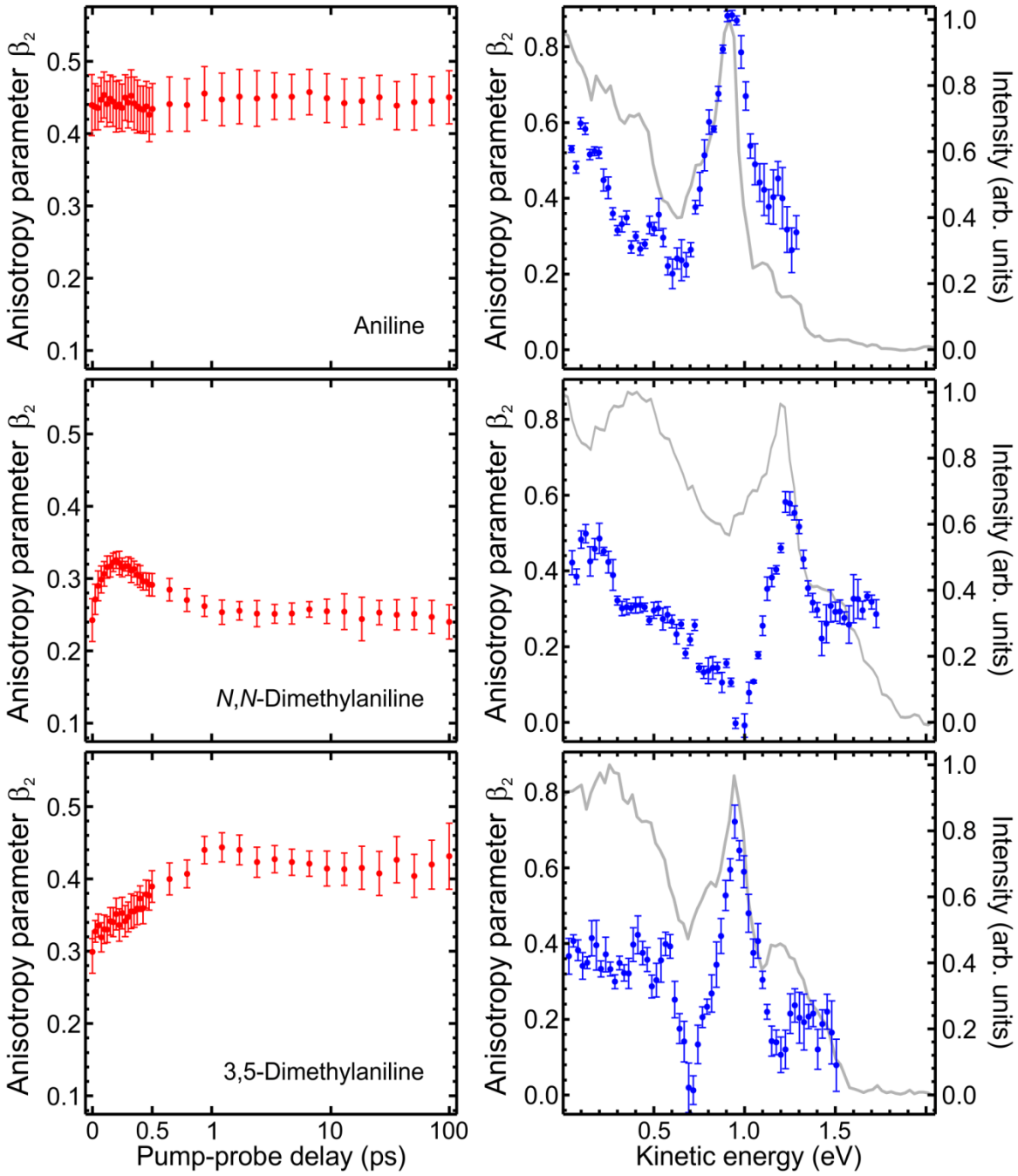

Figure 4.7 – The left hand side of the figure shows the normalised anisotropy parameter β_2 as a function of pump-probe delay (averaged between 0 eV and 0.7 eV). The temporal axis has been plotted as a lin/log scale. The region from 0 fs to +500 fs has been plotted in a linear scale whilst the region from +500 fs to +100 ps has been plotted in a logarithmic scale. The error bars of β_2 represent one standard deviation. The right hand side shows the photoelectron angular distribution of the three systems as a function of energy at $\Delta t = 0$ overlaid with the corresponding photoelectron spectra. The data has been plotted with an energy binning of 0.025 eV.

4.3.6 - Theoretical calculations

In addition to the extensive experimental measurements undertaken for this work, a number of theoretical calculations were performed to aid in the interpretation of the experimental results. These calculations were performed by Prof M Paterson using both Gaussian 09[29] and Dalton 2013.[30] Initial ground state S_0 ground state optimisations were performed using B3LYP using a 6-311(d, p) basis set on all three systems using C_s symmetry. Using these optimised ground states, potential energies of aniline, *N*.*N*-dimethylaniline and 3,5-dimethylaniline were calculated using equation of motion couple cluster theory for singles and doubles (EOM-CCSD) and linear response coupled cluster theory (LR-CCSD). The linear response calculations also received a correction to examine the effects of triples using non-iterative CCSDR(3) corrections.[31] The results of these calculations are shown in Table 4.1.

In all cases, it was found that the triples correction lowered the state energies by less than 0.1 eV, and that the first two electronic excited states were identified as $S_1(\pi\pi^*)$ and $S_2(3s/\pi\sigma^*)$ respectively. However, it should be noted that in the case of *N*,*N*-dimethylaniline, without the triples correction the two state energies are almost

Table 4.1 - Vertical excitation energies (ΔE), oscillator strengths (*f*) and dipole moments (μ) obtained at various levels of theory for the three molecules under study. All ground state optimisation calculations performed using B3LYP/6-311G(d,p) in C_s symmetry. The calculations labelled as A were performed with an aug-cc-pVDZ basis set. The calculations labelled as B were performed with an aug-cc-pVTZ basis set. The calculations labelled as C were performed with iterative triples corrections (CCSDR(3)) with an aug-cc-pVDZ basis set. It should be noted that the ordering of the $S_1(\pi\pi^*)$ and $S_2(3s/\pi\sigma^*)$ state in N,N-dimethylaniline was based upon the ordering from the CCSDR(3) calculation

Aniline		ΔE (eV) A	ΔE (eV) B	ΔE (eV) C	*f* A	*f* B	μ (D) A
S_0		0	0	0	-	-	1.468
S_1 ($1\,^1A''$)	ππ*	4.746	4.754	4.661	0.0235	0.0228	2.277
S_2 ($1\,^1A'$)	πσ* (NH)/Ns Ryd	4.913	5.047	4.890	0.0055	0.0057	7.911
S_3 ($2\,^1A'$)	πσ* (CH)/Cs Ryd	5.585	5.682	5.558	0.0122	0.0507	6.967
S_4 ($2\,^1A''$)	ππ*/Ryd	5.661	5.782	5.647	0.0001	0.0001	3.882
***N*,*N*-Dimethylaniline**							
S_0		0	-	0	-	-	1.911
S_1 ($1\,^1A''$)	ππ*	4.585	-	4.486	0.0406	-	4.201
S_2 ($1\,^1A'$)	πσ* (CN)/Ns Ryd	4.550	-	4.539	0.0231	-	3.504
S_3 ($2\,^1A''$)	πσ* (CH)/Np Ryd	5.136	-	5.131	0.0007	-	1.063
S_4 ($2\,^1A'$)	πσ* (CH)/Cs Ryd	5.173	-	5.163	0.0145	-	4.582
3,5-Dimethylaniline							
S_0		0	-	0	-	-	1.176
S_1 ($1\,^1A''$)	ππ*/Ryd	4.679	-	4.601	0.0247	-	1.782
S_2 ($1\,^1A'$)	πσ* (NH)/Ns Ryd	4.795	-	4.770	0.0034	-	8.478
S_3 ($2\,^1A'$)	πσ* (CH)/Ryd	5.489	-	5.456	0.0089	-	6.100
S_4 ($2\,^1A''$)	πσ* (CH)/Cp Ryd	5.550	-	5.531	0.0008	-	5.856

degenerate, causing a change in the relative ordering of the first and second states when compared to the other two systems. Therefore, for the sake of simplicity, and the lack of experimental data to show the true state ordering, the previously used labels of $S_1(\pi\pi^*)$ and $S_2(3s/\pi\sigma^*)$ will be used in all three systems. When comparing the absolute state energies in Table 4.1 to the recorded absorption spectra in Figure 4.2 it is found that the predicted energy from the calculation is slightly higher than those determined by the band maxima of the UV-VIS absorption spectra by approximately 0.2 eV in all cases. However, the relative spacing between the states appears to be broadly consistent.

Rigid potential energy surface calculations were performed on the three systems using EOM-CCSD/aug-cc-pVDZ. For aniline and 3,5-dimethylaniline the scan was taken

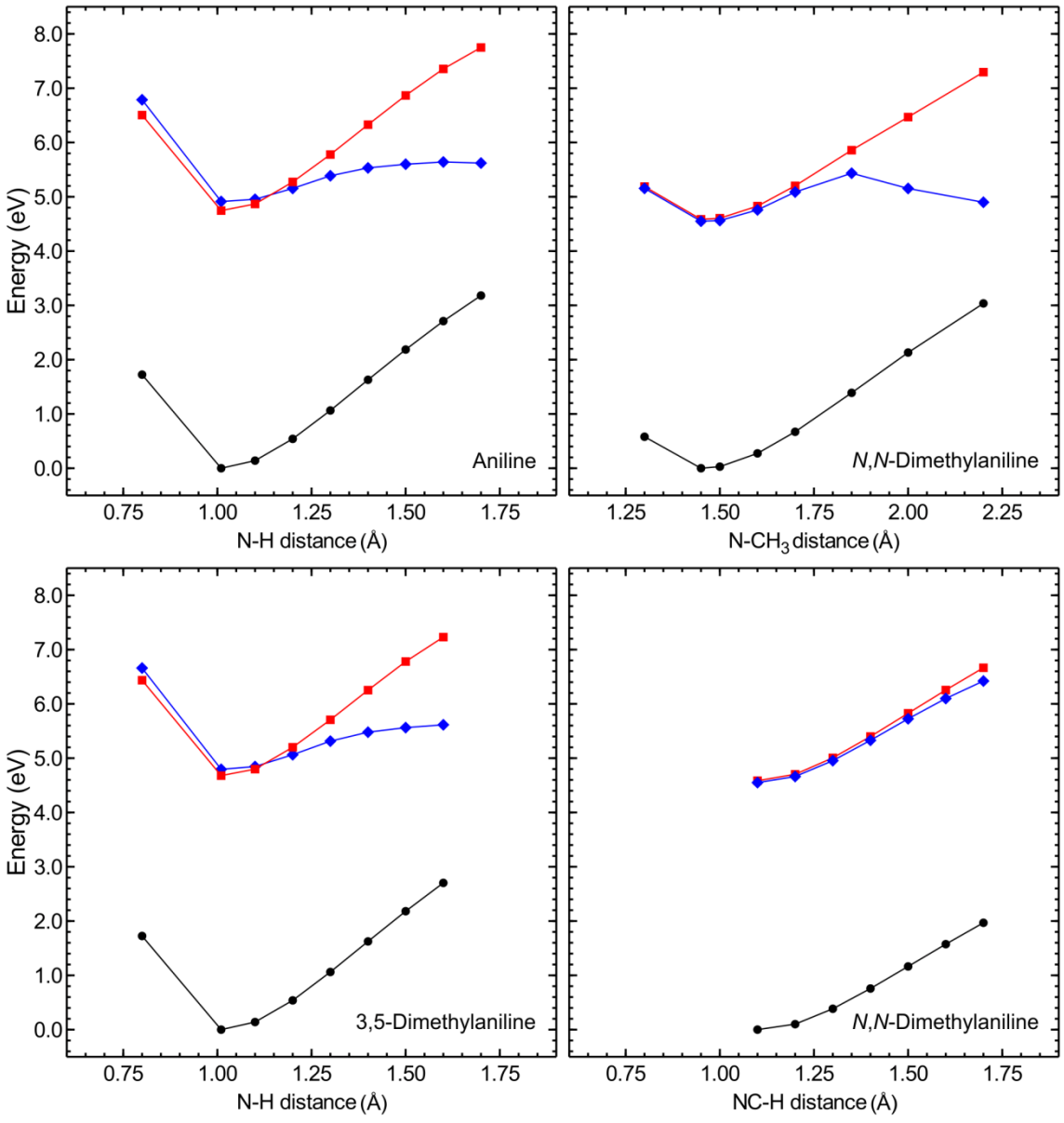

Figure 4.8 - EOM-CCSD/aug-cc-pVDZ potential energy cuts along the N-H stretching coordinate (aniline, 3,5-dimethylaniline) and the N-CH_3 and NC-H stretching coordinates (*N*,*N*-dimethylaniline) for the S_0 (●), $S_1(\pi\pi^*)$ (■) and $S_2(3s/\pi\sigma^*)$ (◆) states. For additional details see the main text.

along the N-H coordinate and for *N*,*N*-dimethylaniline the energy values were determined along the analogous N-CH3 co-ordinate. Additionally, for *N*,*N*-dimethylaniline a scan was conducted along the NC-H co-ordinate. These potential energy cuts are shown in Figure 4.8. Based upon these cuts, it is shown that the co-ordinate mostly likely to be involved dissociation as a route for relaxation in N,N-dimethylaniline is the N-CH3 coordinate, as the S_2 state exhibits a shallow potential well and dissociative character similar to the N-H cuts of aniline and 3,5-dimethylaniline, whilst the NC-H cuts reveal that both states are strongly bound along this co-ordinate.

In addition to the calculations described so far, aniline was also examined further to identify several electronic state properties as a function of the N-H bond length. Figure 4.9 shows a variety of plots describing the evolution of these properties. Figure 4.9(a) shows the normalised EOM-CCSD right eigenvector amplitudes for the orbital transition relating the 3s/πσ* state contribution to the overall S_2 state. It is shown that as the bond length extends, this amplitude falls from 0.7 at 1.01 Å, to 0.32 at 1.7 Å. Figure 4.9(b) shows the magnitude of the un-normalised LCAO coefficient of the 3s basis function within the 3s/πσ* component of the S_2 state (i.e. the N-centred s-type Gaussian basis function with the smallest exponent in the aug-cc-pVDZ basis set,

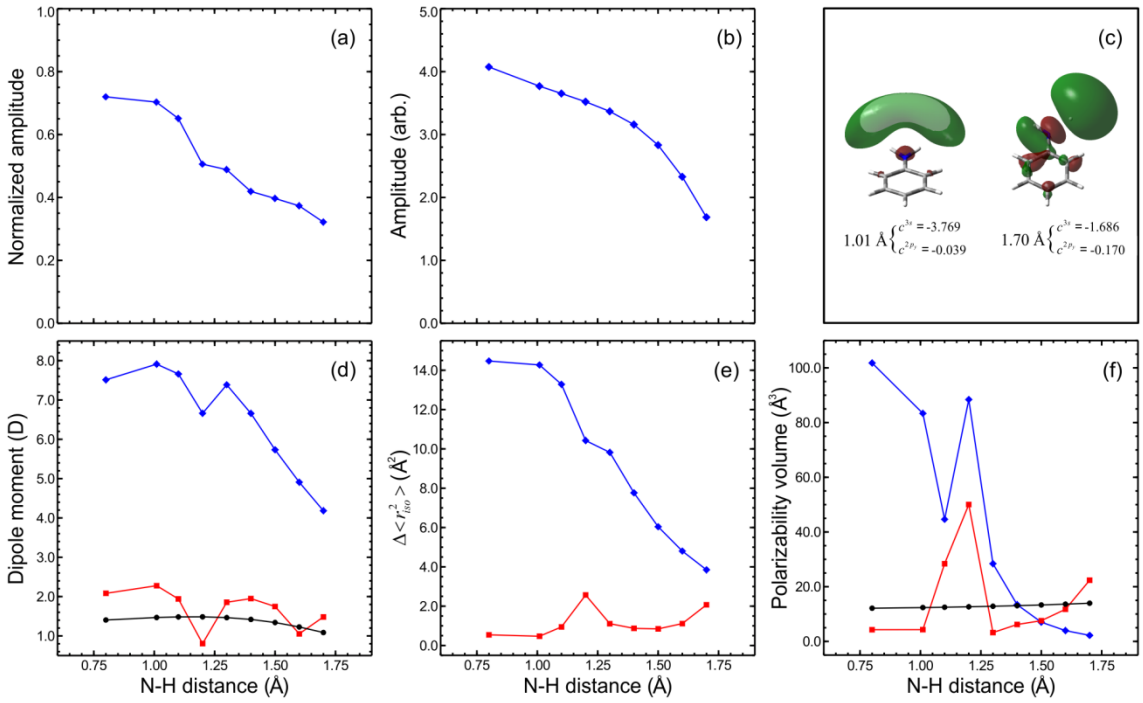

Figure 4.9 - Evolution of electronic state properties for the S_0 (•), $S_1(\pi\pi^*)$ (■) and $S_2(3s/\pi\sigma^*)$ (◆) states of aniline as a function of N-H bond extension, For further details see main text. (a) normalized EOM-CCSD right eigenvector amplitude for the 3s/πσ* state, (b) un-normalized LCAO coefficient of the uncontracted nitrogen 3s basis function within the 3s/πσ* state, (c) 3s/πσ* orbital plot at 1.01 Å and 1.7 Å, (d) dipole moment, (e) isotropic invariant of the excited-state second-moment of the electronic charge distribution with respect to the ground state, (f) isotropic polarisability volume.

ζ=0.06124). When considering the same bond extension it is clear to see that over this region there is a decrease by a factor of ~2.5. When taken in combination, Figure 4.9a & b clearly show that as the N-H bond extends, the relative contribution of the 3s component to the S_2 state falls dramatically. This can be shown qualitatively by comparing the 3s/πσ* orbital at the equilibrium N-H bond length and at an extended bond length (1.01 Å and 1.7 Å respectively), as shown in Figure 4.9(c). At the equilibrium geometry, the electronic character of the orbital is almost entirely governed by the 3s Rydberg orbital contribution, with a very small opposite phase amplitude contribution along the N-H bond. In contrast, as the bond is extended the state becomes more heavily mixed as the 3s contribution drops.

In order to characterize the excited states of aniline along the N-H stretching co-ordinate further, LR-CCSD calculations were performed to obtain excited state dipole moments (as orbital unrelaxed excited-state first-order properties).[32, 33] To provide consistency, ground state calculations were also performed using CCSD to compute the dipole moments, again without orbital relaxation. Figure 4.9(d) plots the changes in the overall dipole moment as a function of N-H bond length. These property surfaces also indicate that valence character increases at the expense of 3s Rydberg character along the N-H stretching co-ordinate. In the case of the ground state and the ππ* excited state, the dipole moment decreases only slightly. This change is tiny compared to the change in the dipole moment of the 3s/πσ* state, which drops from 7.911 D at the FC region (N-H 1.01 Å), to 4.182 D at the extended distance of 1.7 Å. At 1.2 Å there is a pronounced spike in the ππ* and 3s/πσ* data sets in an otherwise smooth trend in the results; this is at the point at which the excited states mix. It should be noted that the S_1(ππ*)/S_2(3s/πσ*) interaction is only really important in a very narrow range of geometries where these states non-adiabatically couple. This means that for our results only those shown at 1.2 Å have any degree of S_1(ππ*)/S_2(3s/πσ*) mixing while all others can be thought of as essentially diabatic state properties.

The excited-state second-moments of electronic charge distribution were also calculated for aniline. These $< \alpha\beta > [\alpha\beta \, \epsilon \, x, y, z]$ have been used as a main tool to investigate Rydberg character in several pioneering studies (see, for example, Ref [3]). What is of particular relevance to the characterization of the excited state Rydberg character is the size of the isotropic invariant of the second-moment tensor of charge distribution in relation to the S_0 ground state $\Delta < r_{iso}^2 >$. For each state $< r_{iso}^2 >$ is obtained from the average of the trace of the second moment tensor, given by Equation 4.2.

$$< r_{iso}^2 > = \frac{1}{3}(< x^2 > + < y^2 > + < z^2 >)$$

(4.2)

As discussed in more detail in a review by Reisler and Krylov,[3] valence states typically exhibit a $\Delta < r_{iso}^2 >$ value close to 1 Å^2, whilst for 3s Rydberg states this value tends to be in the region of around 12 Å^2. Figure 4.9(e) plots the evolution of $\Delta < r_{iso}^2 >$ as a function of N-H bond extension in aniline for both the $S_1(\pi\pi^*)$ and $S_2(3s/\pi\sigma^*)$ states. From this plot it is shown that the value for the $\pi\pi^*$ state is small at all bond lengths (~1 Å^2), however, for the $3s/\pi\sigma^*$ state the value drops dramatically from 14.470 Å^2 to 3.849 Å^2 over the range examined. Once again, this illustrates the large reduction in the Rydberg character of the $S_2(3s/\pi\sigma^*)$ state as the N-H bond extends.

The final way in which the electronic components of the S_1 and S_2 states have been characterized was to investigate the isotropic excited state polarisability volume ($\bar{\alpha}$). This is related to the trace of the polarisability tensor in a similar manner to that which the second moment of charge tensor is related as shown in E.q 4.3. The polarisability volume ($\bar{\alpha}$) is given by

$$\bar{\alpha} = \frac{1}{3}(\alpha_{xx} + \alpha_{yy} + \alpha_{zz})$$

(4.3)

As shown in Figure 4.9(f), the starting value for the polarizability of the $3s/\pi\sigma^*$ is considerably higher than that of the $\pi\pi^*$ and S_0 ground states and, additionally, other than the very strong state-mixing occurring at around 1.2 Å, the $3s/\pi\sigma^*$ state polarisability volume decreases rapidly with the extension of the N-H bond.

All of these trends are consistent with the idea that as the N-H bond length increases, the amount of 3s Rydberg character in the $S_2(3s/\pi\sigma^*)$ state decreases, and the valence character in the state increases. This will be expanded upon further in Section 4.4 as these significant changes in the $3s/\pi\sigma^*$ electronic state character as a function of N-H bond extension have important implications for the interpretation of the experimental results already presented in this chapter.

4.4 – Discussion

4.4.1 – Long-time dynamics in aniline, N,N-dimethylaniline & 3,5-dimethylaniline

The DAS for all three systems are shown in Figure 4.6. From this figure it is clear to see that the spectra for all three systems are broadly similar in terms of numerical time-constants and in the relative shape and amplitude of the spectral features. The only major difference between the spectra of the three molecules is that there is no negative amplitude component in the DAS of 3,5-dimethylaniline. This difference will be discussed in a later part of this chapter. It should also be noted that there are many similarities between the DAS in Figure 4.6 and those reported previously in Figure 3.7 in Chapter 3. As discussed in Chapter 3, following excitation to 265.9 nm, low-lying vibrational levels supported by the shallow potential well along the $S_2(3s/\pi\sigma^*)$ N-H coordinate were excited, in addition to the $S_1(\pi\pi^*)$ state. What is apparent is the striking similarity of the relative amplitudes of both τ_2 and τ_3 of the 265.9 nm data and the 250 nm data. As such, we interpret the τ_2 and τ_3 DAS following 250 nm excitation of all three molecules in a similar fashion as before in Chapter 3. This infers that a component of the initial excitation at 250 nm directly populates the $S_1(\pi\pi^*)$ state, which then undergoes ultrafast intramolecular vibrational redistribution (IVR). This causes a change in the Franck-Condon factors for ionisation, which manifests as a temporal evolution of the ionisation cross-section (0.5 – 2.2 ps, as modelled by τ_2). Ultrafast IVR was previously reported in the $S_1(\pi\pi^*)$ state of chlorobenzene,[34] and in the ground state of both benzene and difluorobenzene.[35] In Chapter 3, we have attributed the same dynamical process to the excited state of aniline in a lower energy region and in the excited state dynamics of phenol and a number of dihydroxybenzenes.[14] In the results presented in this chapter, the excitation energy is in excess of 6000 cm^{-1} above the $S_1(\pi\pi^*)$ origin in all three systems, this is considerably higher than the experimentally determined IVR onset threshold in the excited ($^1\pi\pi^*$) of similar aromatic systems such as anisole (940 cm^{-1}) and hydroquinone (1650 cm^{-1}).[36, 37]

The ultimate fate of the $S_1(\pi\pi^*)$ state is modelled by a decay on a much longer timescale of τ_3 ~200 ps. As discussed in Chapter 3 it is suggested that, on the basis of previous work on aniline, fluorescence,[38] intersystem crossing to lower-lying triplet states[39] and internal conversion back to the S_0 ground state, where the role played by prefulvene-like structures, could be involved in the ultimate decay of the $S_1(\pi\pi^*)$ state.[9, 10, 20] Theoretical work by Fielding and co-workers[10] predicts aniline to have four conical intersections (CIs) connecting the $S_1(\pi\pi^*)$ and S_0 states, the lowest lying of which is

located at ≥4.96 eV above the S_0 minimum energy. The relatively long $S_1(\pi\pi^*)$ state lifetime as shown in the DAS (180 – 230 ps) would seem to indicate that this transition state is not directly accessible following excitation at 250 nm (also 4.96 eV) in any of the systems under investigation.

4.4.2 – Short-time dynamics in aniline, N,N-dimethylaniline & 3,5-dimethylaniline

This section will consider the very short timescale dynamics (~100 fs) observed in all three data sets, and described as τ_1 in Figure 4.6. In all three cases, there is a sharp peak (appearing between 0.9 eV and 1.2 eV, depending on the molecule) which has a relatively high anisotropy parameter, β_2, associated with it (as shown in Figure 4.7, and previously in Chapter 3). As confirmed in Section 4.3.6, the $S_2(3s/\pi\sigma^*)$ state exhibits a large amount of 3s Rydberg electronic character in the vertical Franck-Condon region. As such, single photon ionisation from an orbital possessing this character should give rise to photoelectron partial waves of predominantly p character that peak along the laser polarisation axis, and therefore have a relatively large positive value for the anisotropy parameter β_2. As the state contains a large amount of Rydberg character, a strong propensity for vertical ionisation would also be expected, giving rise to a narrow peak in the photoelectron spectrum. As such, the presence of the $S_2(3s/\pi\sigma^*)$ state is clearly shown in the data for all three systems investigated by this sharp feature in the 0.9 – 1.2 eV region of the τ_1 DAS. It should be noted that the relative amplitude of this feature is significantly greater than was the case in the work outlined in Chapter 3 following excitation at, or just above, the vibrational $S_2(3s/\pi\sigma^*)$ origin. In Chapter 3, excitation was to single vibrational levels supported by the shallow potential well along the N-H stretching co-ordinate in the $S_2(3s/\pi\sigma^*)$ state. As such, only a small fraction of the laser bandwidth associated with the broadband femtosecond pump laser pulse was resonant with the transition. This is in contrast to the $S_1(\pi\pi^*)$ state, in which the full pump bandwidth was potentially resonant as the much higher density of associated vibrational levels in the state acts effectively as a vibrational continuum. At 250 nm, transitions to the $S_2(3s/\pi\sigma^*)$ state also now sample a continuum, as the excitation energy produces a wavepacket above the bound well in a purely repulsive part of the $S_2(3s/\pi\sigma^*)$ potential. As there is now a greater overlap between the pump bandwidth and the vibrational level(s), the effective strength of the signal arising from the $S_2(3s/\pi\sigma^*)$ is increased compared to the measurements in Chapter 3.

The sharp feature in the τ_1 DAS (Figure 4.6) from the Rydberg feature is superimposed on a broader, short-lived background that exhibits a lower value of β_2. This extends

from ~0.5 eV to between 1.3 and 1.7 eV, depending on the molecule in question. As already shown theoretically for the case of aniline, the 3s Rydberg character of the $S_2(3s/\pi\sigma^*)$ state dramatically decreases as the N-H bond length extends. This implies that the evolution of the orbital character should occur extremely rapidly, as the initially prepared wavepacket on the $S_2(3s/\pi\sigma^*)$ potential undergoes ballistic motion along the N-H coordinate, assuming the potential is completely repulsive. When considering this with the 130 fs response of the instrument, it is clear that we are unable to resolve this evolution temporally, even upon replacing the N-H group with N-CH_3, as is the case for *N*,*N*-dimethylaniline. However, the data appears to reflect this evolution in a *spectrally averaged* way as the increase of valence character of the $S_2(3s/\pi\sigma^*)$ state at extended N-CH_3/N-H, distances in conjunction with the reduction in Rydberg character, might well explain this feature due to an expected reduction in the propensity for diagonal ionisation. This would in turn lead to a broadening of the photoelectron feature in the τ_1 DAS and a reduction in the β_2 anisotropy parameter associated with this ionisation signal. This is what appears to be observed in all three systems. As shown in Figure 4.6, the ionisation signal originating from the valence character of the $S_2(3s/\pi\sigma^*)$ state extends to either side of the sharp Rydberg feature. This accounts for the small shoulder on the one-colour ionisation data (shown in Figure 4.3), which is present before the threshold for excitation to S_3 is reached energetically. A discussion on observation of distinct ionisation signatures originating from the Rydberg and valence components of the $S_2(3s/\pi\sigma^*)$ state in aniline have been performed previously by Fielding and co-workers.[9, 10] However, it should be noted that their interpretations are different to the ones presented here. More generally, the reduction in the Rydberg character as a function of bond extension in mixed Rydberg/valence states may have far wider-reaching implications for time-resolved dynamical experiments in other systems. The presence of narrow spectral features with pronounced angular distributions clearly provides a strong and extremely sensitive indicator to the 3s component of a $3s/\pi\sigma^*$ state. However, this would seem to apply only in the vertical Franck-Condon region (i.e. in the short X-H bond extension region, where X is some generalised atom such as N or O etc.), as evident here in the case of direct excitation to $S_2(3s/\pi\sigma^*)$ and indirect population transfer, as was the case in additional work on phenol and dihydroxybenzenes (which will be discussed further in Chapter 5),[14] where the population is trapped at short distances in a potential well resulting from a coupling interaction between the (initially populated) $S_1(\pi\pi^*)$ and $S_2(3s/\pi\sigma^*)$ states. As such, in

situations where 3s/πσ* character states are only accessible via internal conversion at extended X-H bond distances (i.e. not in the FC region), it might not be possible to observe this distinct ionisation signature, which could lead to possible prevention of unambiguous assignment and further complicate any dynamical interpretation.

In the low kinetic energy region of the τ_1 DAS (<0.5 eV) obtained for aniline and for *N,N*-dimethylaniline there is a negative amplitude feature, which is not present in 3,5-dimethylaniline. As discussed previously in Chapter 2, negative amplitude features obtained from a global fitting procedure used to analyse this data are strongly indicative of a sequential population transfer process. In aniline and *N,N*-dimethylaniline the position of the negative amplitude feature overlaps well with the DAS from τ_2 and τ_3, which have been assigned to the $S_1(\pi\pi^*)$ state. In agreement with Fielding and co-workers,[20] we therefore suggest that this feature is a direct consequence of ultrafast $S_2(3s/\pi\sigma^*) \rightarrow S_1(\pi\pi^*)$ internal conversion occurring in ~100 fs. This is in contrast to the previously reported work on aniline (as discussed in Chapter 3) at or just above the $S_2(3s/\pi\sigma^*)$ origin, where no clear evidence of such internal conversion was revealed and tunnelling under the potential barrier along the N-H stretching coordinate on the $S_2(3s/\pi\sigma^*)$ potential surface was implied as the primary route for relaxation of the state.[1]

Even though the relative amplitude of the negative feature in the τ_1 DAS of *N,N*-dimethylaniline is somewhat larger than it is in aniline, we are unable to definitively deduce the relative fraction of population transfer in the two molecules as we have no information regarding the absorption and ionisation cross-sections of the $S_1(\pi\pi^*)$ and $S_2(3s/\pi\sigma^*)$ states, and so are unable to determine their initial relative populations and any differences in sensitivity to probing them. However, the fact that the negative signal does not "mirror" the positive amplitude in the τ_3 DAS means that there is some confidence that both $S_1(\pi\pi^*)$ and $S_2(3s/\pi\sigma^*)$ are directly excited to some extent. In further attempts to expand on this issue, we are able to make some speculative assumptions that at the very least enable us to comment on the relative contributions that the various process may make to the overall dynamics of these systems, in particular for the case of aniline as this molecule has been far more extensively investigated by other groups then the two methylated systems.

On the basis of the calculations described in Section 4.3.6, as well as those reported by other groups,[7, 40] the *absorption cross-section* for single-photon excitation to the $S_2(3s/\pi\sigma^*)$ state is significantly smaller than that of the $S_1(\pi\pi^*)$ based upon the relative

predicted oscillator strengths. However, we suggest that the *photoionisation cross-section* for the $S_2(3s/\pi\sigma^*)$ state in aniline (and by extension the other two systems) is much larger than that of the $S_1(\pi\pi^*)$. This is hinted at by recent work from Vallance and co-workers in which it was established that there was a strong linear correlation between static polarizability and absolute (ground state) electron impact ionisation cross-section.[41, 42] For a large range of small organic molecules, electronic polarizability volumes between 2-15.5 $Å^3$ gave corresponding maxima in the total ionization cross-section of 2.5-23 $Å^2$. Similar correlations in relative ionization cross-section size were also shown to extend over a large range of electron impact energies. To the best of our knowledge, the only investigation looking for similar relationship in low-energy photoionization is that performed by Mullica and co-workers.[43] This report did not claim to show a generalised correlation between the two properties, but it did show a clear trend within groups of molecules with similar chemical functionality. In order to explore this idea for ourselves, we have compared the calculated polarizability volume for 27 of the molecules reported by Vallance and co-workers with experimental photoionisation cross-section information obtained from a number of sources.[44-52] The results of this comparison (for photon energy of 11.5 eV) are shown in Figure 4.10. As shown in the figure, there is a clear positive relationship between these two properties. This is illustrated, for example, by a linear fit to the data which yields a correlation coefficient of r = 0.91 (and a coefficient of determination of R^2 = 0.83). However, we are unable to say for certain if the trend is truly linear, as to do so more data is required, specifically for systems with a polarisability volume >15 $Å^3$ over a larger range of values. Additionally, data for a large number of chemically similar systems would also be desirable to investigate this relationship further in a more detailed and systematic way.

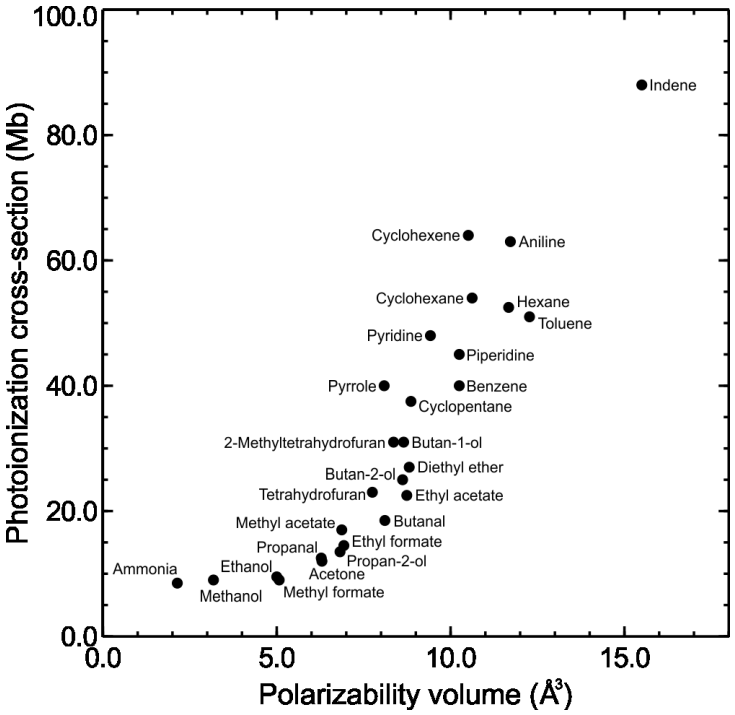

Figure 4.10 - Photoionization cross-section (at a photon energy of 11.5 eV) plotted against polarizability volume for 27 small molecules. Refs [41] & [42] provided the Polarizability data, and Refs [44-52] provided the experimental cross-section data.

That being said, Figure 4.10 establishes a strong positive general trend relating increasing polarizability volume to a larger (relatively low energy) photoionisation cross-section. This result is of relevance in this discussion as the calculations outlined previously predict an extremely large difference in the polarisability volumes for the $S_1(\pi\pi^*)$ and $S_2(3s/\pi\sigma^*)$ states in aniline, particularly in the FC region (e.g. 4.29 $Å^3$ vs. 83.37 $Å^3$, respectively, at the S_0 equilibrium geometry). Neglecting Franck-Condon effects, we therefore suggest that the ionisation cross-section for the $S_2(3s/\pi\sigma^*)$ state may be at least an order of magnitude larger than for the $S_1(\pi\pi^*)$ state, even if the correlation seen in Figure 4.10 does not continue to extend in the same manner to higher values of the polarizability volume, or follow quite the same trend for electronically excited states. As such, given the similar amplitude of the features which are attributed to both the $S_1(\pi\pi^*)$ and $S_2(3s/\pi\sigma^*)$ states in the photoelectron data and in the DAS (Figures 4.5 & 4.6), we conclude that the initial fraction of population prepared in $S_2(3s/\pi\sigma^*)$ is likely to be very small compared to $S_1(\pi\pi^*)$. This means that the population transferred from the $S_2(3s/\pi\sigma^*)$ to the $S_1(\pi\pi^*)$ is small compared to the population prepared in $S_1(\pi\pi^*)$ by the initial excitation of aniline following excitation to 250 nm. With this in mind, we also suggest that although the ionisation-based experiment presented here is very sensitive to population within $S_2(3s/\pi\sigma^*)$, this sensitivity does not enable us to efficiently track the population transfer into $S_1(\pi\pi^*)$. As such, the relatively small negative amplitude in the aniline τ_1 DAS may, in fact, be reflecting a large fraction of population transfer from $S_2(3s/\pi\sigma^*)$.

Following on from the arguments discussed previously, it is worth reiterating, however, that on the basis of the calculations provided here in Section 4.3.6, the efficiency of $S_2(3s/\pi\sigma^*)$ ionisation in aniline with respect to the efficiency of ionising the $S_1(\pi\pi^*)$ state will also evolve rapidly as a function of N-H bond extension. Even though the experiments described here are not able to directly resolve this, the averaging of such effects clearly increases the complexity of the detection sensitivity argument outlined above. Furthermore, it may also be a significant convoluting factor that requires more detailed consideration in any future time-resolved measurements undertaken with a considerably shorter instrument response function. It should also be noted that, as a consequence of the calculations predictions, that tracking the population within the $S_2(3s/\pi\sigma^*)$ as the N-H bond is further complicated by the decrease in the ionisation cross-section, which would lead to an apparent decrease in signal, further complicating effective tracking of the population.

4.4.3 – Internal conversion Vs direct dissociation

Even though the DAS obtained for both aniline and *N*,*N*-dimethylaniline provide very strong evidence of $S_2(3s/\pi\sigma^*) \rightarrow S_1(\pi\pi^*)$ internal conversion, this pathway is not the only possible way for the $S_2(3s/\pi\sigma^*)$ state to relax following excitation at 250 nm. Work on aniline, performed by the Ashfold and Stavros groups have both reported rapid H-atom release in aniline, a mechanistic pathway that the current TR-PEI experiment is effectively "blind" to. This ultrafast H-atom release was inferred from photo-fragmentation recoil anisotropy in the work by Ashfold and co-workers, and reported in a time-resolved photo fragmentation imaging study with an appearance onset time of <1 ps for the H-atom photoproducts by Stavros and co-workers.[5, 7] In both studies, the origin of this process was attributed to H-atoms formed via dissociation along the N-H co-ordinate of the $S_2(3s/\pi\sigma^*)$ state. In contradiction to the interpretation of the results for this work, these groups concluded that population transfer was indeed active, but in the opposite direction, (i.e. that population moved from $S_1(\pi\pi^*)$ to $S_2(3s/\pi\sigma^*)$) via a similar internal conversion mechanism. However, considering the relatively long lifetime of the $S_1(\pi\pi^*)$ state compared to the life time of the $S_2(3s/\pi\sigma^*)$, this pathway would seem to be unlikely purely on the basis of simple kinetic arguments, unless the molecule is only able to sample this $S_1(\pi\pi^*)/S_2(3s/\pi\sigma^*)$ conical intersection for a short amount of time before the $S_1(\pi\pi^*)$ state relaxes, as noted previously by Longarte and co-workers.[8]

The possibility of the existence of an alternative, second decay mechanism for the $S_2(3s/\pi\sigma^*)$ state is also suggested by the fact that the 3,5-dimethylaniline τ_1 DAS contains no feature with a negative amplitude. This provides clear evidence that there is no significant $S_2(3s/\pi\sigma^*) \rightarrow S_1(\pi\pi^*)$ internal conversion occurring in this system. However, that being said, there is obviously still population moving out of this state extremely rapidly when the τ_1 lifetime is considered. Based on the rate at which the signal decays, the most likely mechanism is that of N-H dissociation.

In the case of *N*,*N*-dimethylaniline, the observed lifetime of the $S_2(3s/\pi\sigma^*)$ state is similar to that of the other two systems (≤100 fs). This implies that any dissociation along the N-CH_3 co-ordinate must be direct, instead of being mediated by tunnelling, if it is to compete effectively against an internal conversion relaxation pathway. This appears to be confirmed by the fact that (a) excitation at 250 nm in aniline is almost definitely exciting above the $S_2(3s/\pi\sigma^*)$ N-H barrier, and (b) the calculations predict a similar barrier height but a lower $S_2(3s/\pi\sigma^*)$ origin energy in *N*,*N*-dimethylaniline (as

shown in Figure 4.8). As is the case in aniline, we can assume that both decay pathways (direct dissociation and internal conversion) are active in principle, although we are unable to quantify the relative fraction contributions of these pathways to the overall dynamics of the $S_2(3s/\pi\sigma^*)$ state in either molecule. However, in spite of this limitation, additional insights into the apparent differences as to which process is favoured by the three systems under investigation are revealed through analysis of the angular information, which will be discussed in the following section.

4.4.4 – Photoelectron angular distribution

Recent studies of aniline, both theoretical and experimental, have concluded that the critical internal molecular co-ordinates responsible for allowing non-adiabatic coupling between the $S_1(\pi\pi^*)$ and $S_2(3s/\pi\sigma^*)$ states are a combination of extensions along the N-H co-ordinate and out-of-plane distortions of the aromatic ring system. In fact, the same types of motions have been consistently implicated in mediating similar excited state interactions in a wide range of other aromatic systems such as indoles, pyrroles and hydroxybenzenes. [4, 14, 53, 54] As suggested by our previous work,[14] and also by the work of other groups,[55, 56] non-adiabatic coupling interactions between different states effectively mix their electronic (or vibronic) character. This change in the electronic (or vibronic) character of the state may therefore be reflected in the temporal evolution of the photoelectron angular distributions (PADs) observed in a TRPEI measurement.

As is shown in Figure 4.7, the three molecules investigated undergo different temporal evolution of the β_2 anisotropy parameter. We suggest that this evolution is directly related to change in $S_1(\pi\pi^*)$ electronic character that occurs when each system samples the correct molecular geometry to access the conical intersection with the $S_2(3s/\pi\sigma^*)$ state. Critically, the relative timescales observed appear to be consistent with the assumption that extension along the N-H/N-CH_3 bond and out-of-plane distortions of the aromatic ring system are prerequisites for this interaction to occur. In aniline there is no significant change in β_2 as a function of pump-probe delay, even though there is clear evidence that there is a sequential non-adiabatic population transfer process occurring from $S_2(3s/\pi\sigma^*)$ to $S_1(\pi\pi^*)$, as shown in the DAS presented in Figure 4.6, which must require some state mixing. We therefore must assume that any such interaction is occurring too rapidly to be observed by the temporal resolution of the experiment. As previously discussed, it can also be assumed that in aniline both the internal conversion and direct dissociation pathways operate to some extent in the reduction of $S_2(3s/\pi\sigma^*)$ population following 250 nm excitation. However, we are

unable to determine the relative fraction that each pathway contributes to the total dynamics. Methylation of the N-H groups (*N*,*N*-dimethylaniline) slows down the state mixing between the $S_1(\pi\pi^*)/S_2(3s/\pi\sigma^*)$ states, but to a small extent as the motion along the N-CH_3 co-ordinate is still very fast. It should be assumed however, that any motion associated with the out-of-plane ring deformations would remain unaffected by the methylation of the amine functional group. Nevertheless, the effect of the substitution is sufficient to allow the PAD evolution to be revealed experimentally, with β_2 rising to its maximum value in 200 fs. The timescale of this is still comparable to any direct dissociation and so the internal conversion pathway may be in competition to deplete population from the $S_2(3s/\pi\sigma^*)$ state. Methylation of the aromatic ring (3,5-dimethylaniline) has a much more profound effect on the timescale for accessing the $S_1(\pi\pi^*)/S_2(3s/\pi\sigma^*)$ conical intersection. This is presumably due to the fact that a greater number of larger atomic centres within the molecule need to be displaced to reach the degeneracy point. As shown in Figure 4.7, β_2 now evolves on a much longer timescale (~1 ps). Since the direct $S_2(3s/\pi\sigma^*)$ dissociation pathway is not expected to be slow down in comparison to aniline, simple kinetic arguments would therefore suggest that the majority of the initially prepared population on the $S_2(3s/\pi\sigma^*)$ state will now be depleted via direct dissociation, before the system has a chance to access the $S_1(\pi\pi^*)/S_2(3s/\pi\sigma^*)$ conical intersection. As such, in contrast to aniline and *N*,*N*-dimethylaniline, there is no negative amplitude observed in the 3,5–dimethylaniline τ_1 decay associated spectra, as shown in Figure 4.6. Taken in combination, the observed energy resolved and angle-resolved information provided by the imaging study for the three systems investigated provide a clear and self-consistent picture of the dynamical processes occurring following excitation at 250 nm. Furthermore, the data discussed in this chapter provide an excellent demonstration of the interplay between molecular structure and photochemical dynamics in electronically excited state species. This underlines the importance of the link to chemical functionality that is particularly relevant for a wide range of molecular systems, including those implicated in mediating key processes in photobiology.

To finish, we briefly return to consider the previous arguments made in Chapter 3 regarding the photoelectron dynamics of aniline at, or just above, the $S_2(3s/\pi\sigma^*)$ origin.[1] In this chapter, there was also no observation of any evolution of the β_2 anisotropy parameter as a function of pump-probe delay in aniline. This was then used as an argument to imply that no $S_2(3s/\pi\sigma^*)/S_1(\pi\pi^*)$ interaction was occurring *at those*

specific wavelengths. However, this argument is potentially no longer fully reliable in light of the experiments discussed in this chapter, where we believe that the changes to the β_2 parameter are occurring too fast to be resolved by the instrument response (which is now shorter by ~ 50 fs than the instrument response for the experiment discussed in Chapter 3). It should be stressed that additional evidence of a lack of $S_2(3s/\pi\sigma^*)/S_1(\pi\pi^*)$ interaction also came from the absence of any negative amplitude signal in the τ_1 DAS, which is in contrast to the work presented here following excitation at 250 nm. As such, it is our belief that the conclusion drawn in Chapter 3 still holds. However, considering the arguments invoked regarding the potential differences in the sensitivity of $S_2(3s/\pi\sigma^*)$ and $S_1(\pi\pi^*)$ to ionization detection, the reduced levels of relative initial $S_2(3s/\pi\sigma^*)$ population in the previous chapter may indicate that any fraction of the population internally converting to $S_1(\pi\pi^*)$ may have not been as readily observable by the TR-PEI experiment.

4.5 – Conclusion

Building on work presented in Chapter 3, this chapter has presented work utilising time-resolved photoelectron imaging (TR-PEI) to investigate the potential role of non-adiabatic coupling between the $S_2(3s/\pi\sigma^*)$ and $S_1(\pi\pi^*)$ states in the electronic relaxation of aniline, and two of its methylated substituted derivatives following excitation at 250 nm. The analysis of the temporal evolution presented in the photoelectron angular distributions (PADs) suggests that in all the systems investigated, the non-adiabatic coupling interactions between the $S_1(\pi\pi^*)$ and $S_2(3s/\pi\sigma^*)$ states are in operation at this specific energy. Although from the findings presented in this chapter, this coupling is slowed down by an order of magnitude by targeted methylation of the aromatic ring at the 3 and 5 positions. Fits to our time-resolved photoelectron kinetic energy data appear to indicate that this coupling then provides a potential route for population transfer from the $S_2(3s/\pi\sigma*)$ state to the $S_1(\pi\pi*)$ state (both of which may be populated directly in the initial excitation). Furthermore, the $S_2(3s/\pi\sigma^*)$ state may depopulate via a dissociation along the N-H bond, providing a competing N-H bond fission mechanism (or N-CH_3 for the *N*,*N*-dimethylaniline system). In aniline and *N*,*N*-dimethylaniline, we suggest that both of these pathways may be actively operating, providing competing routes for population loss from the $S_2(3s/\pi\sigma^*)$ state. However, in the case of 3,5-dimethylaniline there is no evidence of any population transfer from the $S_2(3s/\pi\sigma^*)$ state to the $S_1(\pi\pi^*)$ state via an internal conversion process. This can, be rationalised in terms of a simple kinetics argument. Since the relative rates of the two processes are significantly changed following methylation of the aromatic ring (slowing down the $S_2(3s/\pi\sigma^*)/S_1(\pi\pi^*)$ coupling interaction), this process is kinetically ill-favoured as a decay pathway for the $S_2(3s/\pi\sigma^*)$ state in 3,5-dimethylaniline.

In addition, our analysis was supported by a series of high level theoretical investigations of a variety of excited state properties as a function of N-H bond length in aniline. These calculations provide new insight into the evolution of the electronic character of the $S_2(3s/\pi\sigma^*)$ state. Particularly, the 3s Rydberg contribution to the electronic character of the state decreases with increasing N-H bond length and this observation may be used to explain several features in the experimental data. More generally however, we suggest that this observation is likely to be common among many other molecular species which exhibit excited states of mixed Rydberg/valence character. This chapter therefore provides findings that are potentially important when interpreting dynamical data in all such systems.

Finally, initial semi-quantitative arguments relating polarisability volumes to low energy ionisation crossections have been discussed. This has potentially large implications for experiments in which photoionisation methods are used to investigate non-adiabatic dynamics evolving across different states (with different associated detection sensitivities). This potentially provides a useful aid in the interpretation of results presented in this chapter. However, more work is required to fully quantify the relationship between polarizability volume and photoionisation cross-section.

4.6 - References

1. J. O. F. Thompson, R. A. Livingstone and D. Townsend, J. Chem. Phys. **139** (3), 034316 (2013).
2. T. Ebata, C. Minejima and N. Mikami, J. Phys. Chem. A **106** (46), 11070-11074 (2002).
3. H. Reisler and A. I. Krylov, Int. Rev. Phys. Chem. **28** (2), 267-308 (2009).
4. M. N. Ashfold, G. A. King, D. Murdock, M. G. Nix, T. A. Oliver and A. G. Sage, Phys. Chem. Chem. Phys. **12** (6), 1218-1238 (2010).
5. G. M. Roberts and V. G. Stavros, Chem. Sci. **5** (5), 1698-1722 (2014).
6. G. A. King, T. A. Oliver and M. N. Ashfold, J. Chem. Phys. **132** (21), 214307 (2010).
7. G. M. Roberts, C. A. Williams, J. D. Young, S. Ullrich, M. J. Paterson and V. G. Stavros, J. Am. Chem. Soc. **134** (30), 12578-12589 (2012).
8. R. Montero, A. Peralta Conde, V. Ovejas, R. Martinez, F. Castano and A. Longarte, J. Chem. Phys. **135** (5), 054308 (2011).
9. R. Spesyvtsev, O. M. Kirkby, M. Vacher and H. H. Fielding, Phys. Chem. Chem. Phys. **14** (28), 9942-9947 (2012).
10. M. Sala, O. M. Kirkby, S. Guerin and H. H. Fielding, Phys. Chem. Chem. Phys. **16** (7), 3122-3133 (2014).
11. K. Kimura, H. Tsubomura and S. Nagakura, Bull. Chem. Soc. Jpn. **37** (9), 1336-1346 (1964).
12. L. Lagesson-Andrasko and V. Lagesson, *Handbook of Ultraviolet Spectra Vapour Phase 168-330 nm*. (Linköping, Sweden, 2005).
13. I. F. Galván, M. E. Martín, A. Muñoz-Losa and M. A. Aguilar, J. Chem. Theory Comput. **5**, 341 (2009).
14. R. A. Livingstone, J. O. Thompson, M. Iljina, R. J. Donaldson, B. J. Sussman, M. J. Paterson and D. Townsend, J. Chem. Phys. **137** (18), 184304 (2012).
15. U. Even, J. Jortner, D. Noy, N. Lavie and C. Cossart-Magos, J. Chem. Phys. **112** (18), 8068-8071 (2000).
16. F. Wang, S. P. Neville, R. Wang and G. A. Worth, J. Phys. Chem. A **117** (32), 7298-7307 (2013).
17. P. M. Wojciechowski, W. Zierkiewicz, D. Michalska and P. Hobza, J. Chem. Phys. **118** (2003).
18. G. Raja, K. Saravanan and S. Sivakumar, Elixir Comp. Chem. **44**, 7341 (2012).
19. S. Zhang, B. Tang, Y. Wang and B. Zhang, Chem. Phys. Lett. **397**, 495 (2004).
20. R. Spesyvtsev, O. M. Kirkby and H. H. Fielding, Faraday. Discuss. **157**, 165-179 (2012).
21. M. A. Smith, J. W. Hager and S. C. Wallace, J. Chem. Phys. **80** (7), 3097-3105 (1984).
22. J. W. Hager, M. A. Smith and S. C. Wallace, J. Chem. Phys. **83**, 4820 (1985).
23. V. K. Potapov and L. I. Iskakov, High. Energy. Chem. **5**, 237 (1971).
24. J. P. Maier and D. W. Turner, J. Chem. Soc. Farad. T 2 (4), 521-531 (1973).
25. L. Szepes, G. Distefano and S. Pignataro, Ann. Chim. **64**, 159 (1974).
26. O. Schalk, A. E. Boguslavskiy and A. Stolow, J. Phys. Chem. A **114**, 4058 (2010).
27. K. L. Reid, Annu. Rev. Phys. Chem. **54**, 397-424 (2003).
28. T. Suzuki, in *Ann. Rev. Phys. Chem.* (2006), Vol. 57, pp. 555-592.
29. M. J. Frisch, G. W. Trucks, H. B. Schlegel, G. E. Scuseria, M. A. Robb, J. R. Cheeseman, G. Scalmani, V. Barone, B. Mennucci, G. A. Petersson, H. Nakatsuji, M. Caricato, X. Li, H. P. Hratchian, A. F. Izmaylov, J. Bloino, G. Zheng, J. L. Sonnenberg, M. Hada, M. Ehara, K. Toyota, R. Fukuda, J. Hasegawa, M. Ishida, T. Nakajima, Y.

Honda, O. Kitao, H. Nakai, T. Vreven, J. J. A. Montgomery, J. E. Peralta, F. Ogliaro, M. Bearpark, J. J. Heyd, E. Brothers, K. N. Kudin, V. N. Staroverov, R. Kobayashi, J. Normand, K. Raghavachari, A. Rendell, J. C. Burant, S. S. Iyengar, J. Tomasi, M. Cossi, N. Rega, J. M. Millam, M. Klene, J. E. Knox, J. B. Cross, V. Bakken, C. Adamo, J. Jaramillo, R. Gomperts, R. E. Stratmann, O. Yazyev, A. J. Austin, R. Cammi, C. Pomelli, J. W. Ochterski, R. L. Martin, K. Morokuma, V. G. Zakrzewski, G. A. Voth, P. Salvador, J. J. Dannenberg, S. Dapprich, A. D. Daniels, Ö. Farkas, J. B. Foresman, J. V. Ortiz, J. Cioslowski and D. J. Fox, (Gaussian, Inc., Wallingford CT, 2009).

30. K. Aidas, C. Angeli, K. L. Bak, V. Bakken, R. Bast, L. Boman, O. Christiansen, R. Cimiraglia, S. Coriani, P. Dahle, E. K. Dalskov, U. Ekström, T. Enevoldsen, J. J. Eriksen, P. Ettenhuber, B. Fernández, L. Ferrighi, H. Fliegl, L. Frediani, K. Hald, A. Halkier, C. Hättig, H. Heiberg, T. Helgaker, A. C. Hennum, H. Hettema, E. Hjertenæs, S. Høst, I.-M. Høyvik, M. F. Iozzi, B. Jansik, H. J. A. Jensen, D. Jonsson, P. Jørgensen, J. Kauczor, S. Kirpekar, T. Kjærgaard, W. Klopper, S. Knecht, R. Kobayashi, H. Koch, J. Kongsted, A. Krapp, K. Kristensen, A. Ligabue, O. B. Lutnæs, J. I. Melo, K. V. Mikkelsen, R. H. Myhre, C. Neiss, C. B. Nielsen, P. Norman, J. Olsen, J. M. H. Olsen, A. Osted, M. J. Packer, F. Pawlowski, T. B. Pedersen, P. F. Provasi, S. Reine, Z. Rinkevicius, T. A. Ruden, K. Ruud, V. Rybkin, P. Salek, C. C. M. Samson, A. S. d. Merás, T. Saue, S. P. A. Sauer, B. Schimmelpfennig, K. Sneskov, A. H. Steindal, K. O. Sylvester-Hvid, P. R. Taylor, A. M. Teale, E. I. Tellgren, D. P. Tew, A. J. Thorvaldsen, L. Thøgersen, O. Vahtras, M. A. Watson, D. J. D. Wilson, M. Ziolkowski and H. Ågren, WIREs Comp. Mol. Sci. **4**, 269 (2014).

31. O. Christiansen, H. Koch and F. Jorgensen, J. Chem. Phys. **105** (4), 1451-1459 (1996).

32. O. Christiansen, A. Halkier, H. Koch, P. Jørgensen and T. Helgaker, J. Chem. Phys. **108**, 2801 (1998).

33. O. Christiansen, P. Jørgensen and C. Hättig, Int. J. Quantum Chem. **68**, 1 (1998).

34. Y. Z. Liu, C. C. Qin, S. Zhang, Y. M. Wang and B. Zhang, Acta. Phys-Chim. Sin. **27** (4), 965-970 (2011).

35. R. S. von Benten, Y. Liu and B. Abel, J. Chem. Phys. **133** (13), 134306 (2010).

36. G. N. Patwari, S. Doraiswamy and S. Wategaonkar, J. Phys. Chem. A. **104** (37), 8466-8474 (2000).

37. R. Matsumoto, K. Sakeda, Y. Matsushita, T. Suzuki and T. Ichimura, J. Mol. Struct. **735**, 153-167 (2005).

38. R. Scheps, D. Florida and S. A. Rice, J. Chem. Phys. **61** (5), 1730-1747 (1974).

39. B. Kim, C. P. Schick and P. M. Weber, J. Chem. Phys. **103**, 6903 (1995).

40. Y. Honda, M. Hada, M. Ehara and H. Nakatsuji, J. Chem. Phys. **117** (5), 2045-2052 (2002).

41. J. N. Bull, P. W. Harland and C. Vallance, J. Phys. Chem. A **116**, 767 (2012).

42. J. N. Bull, J. W. L. Lee and C. Vallance, Phys. Chem. Chem. Phys. **16**, 10743 (2014).

43. J. A. Beran, A. K. Dhingra, W.-S. Liu and D. F. Mullica, Can. J. Chem. **53**, 1616 (1975).

44. J. A. R. Samson, G. N. Haddad and L. D. Kilcoyne, J. Chem. Phys. **87**, 6416 (1987).

45. T. A. Cool, J. Wang, K. Nakajima, C. A. Taatjes and A. McIlroy, Int. J. Mass. Spectrom. **247** (1-3), 18-27 (2005).

46. J. Wang, B. Yang, T. A. Cool, N. Hansen and T. Kasper, Int. J. Mass. Spectrom. **269**, 210 (2008).

47. Z. Zhou, M. Xie, Z. Wang and F. Qi, Rapid Commun. Mass Spectrom. **23**, 3994 (2009).

48. Z. Zhou, L. Zhang, M. Xie, Z. Wang, D. Chen and F. Qi, Rapid Commun. Mass Spectrom. **24** (9), 1335-1342 (2010).
49. M. Xie, Z. Zhou, Z. Wang, D. Chen and F. Qi, Int. J. Mass. Spectrom. **293**, 28 (2010).
50. J. Wang, B. Yang, T. A. Cool and N. Hansen, Int. J. Mass. Spectrom. **292**, 14 (2010).
51. M. Xie, Z. Zhou, Z. Wang, D. Chen and F. Qi, Int. J. Mass. Spectrom. **303**, 137 (2011).
52. B. Yang, J. Wang, T. A. Cool, N. Hansen, S. Skeen and D. L. Osborn, Int. J. Mass. Spectrom. **309**, 118 (2012).
53. D. J. Hadden, K. L. Wells, G. M. Roberts, L. T. Bergendahl, M. J. Paterson and V. G. Stavros, Phys. Chem. Chem. Phys. **13** (21), 10342-10349 (2011).
54. S. E. Greenough, M. D. Horbury, J. O. Thompson, G. M. Roberts, T. N. Karsili, B. Marchetti, D. Townsend and V. G. Stavros, Phys. Chem. Chem. Phys. **16** (30), 16187-16195 (2014).
55. C. Z. Bisgaard, O. J. Clarkin, G. Wu, A. M. D. Lee, O. Gessner, C. C. Hayden and A. Stolow, Science **323**, 1464 (2009).
56. Y.-I. Suzuki, T. Horio, T. Fuji and T. Suzuki, J. Chem. Phys. **134**, 184313 (2011).

Chapter 5 – The photoelectron spectroscopy of guaiacol

5.1 – Introduction

Following on from the work on aniline, this chapter will discuss a set of experiments performed on the molecule guaiacol, and will begin by discussing some previous work on a similar system, phenol. Phenol has been extensively investigated using theoretical,[1-7] gas-phase[8-19] and liquid-phase studies.[20-22] Phenol is found to be the chromophore in a number of biological systems, such as the amino acid tyrosine.[23] As well as its interesting biological relevance, phenol has been studied for its interesting dynamical properties; in particular the interactions between its optically bright $S_1(\pi\pi^*)$ state, and its optically dark $S_2(3s/\pi\sigma^*)$ state.[4] In contrast to aniline (as discussed in Chapters 3 & 4), this $\pi\sigma^*$ state in phenol is found to be completely dissociative along the O-H bond coordinate; with no bound region of the potential to support vibrational modes. The $3s/\pi\sigma^*$ state is of interest due to the fact that it has been widely recognised as a key component in the relaxation dynamics of many similar systems, as discussed in Chapter 1.

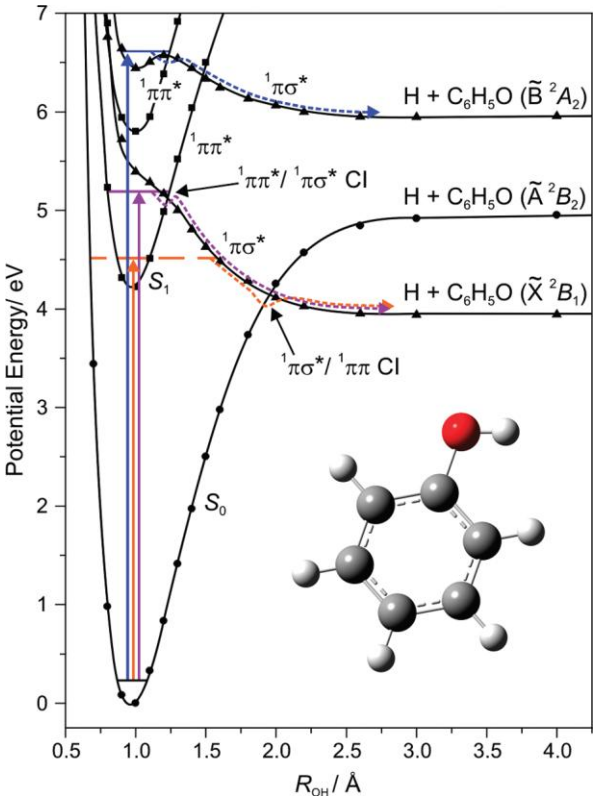

Figure 5.1 – Potential energy surface of phenol taken from Ref [17]. The surface is calculated along the OH coordinate using CASPT2(12/11)/aug-cc-pVTZ

As with a number of similar systems, the $S_2(3s/\pi\sigma^*)$ state in phenol has a large 3s Rydberg character component in the vertical Franck-Condon (FC) region. As the O-H bond is elongated, this contribution to the overall electronic character of the S_2 state disappears as the bond stretches, and ultimately dissociates.[24, 25] This has been discussed in more detail in Chapter 4. Although this state is optically dark, it can be accessed via the $S_1(\pi\pi^*)$ excited state through a conical intersection (CI) as a result of vibronic coupling.[4, 25, 26] This conical intersection, along with a second conical intersection with the S_0 potential energy surface, potentially allows a complete, non-

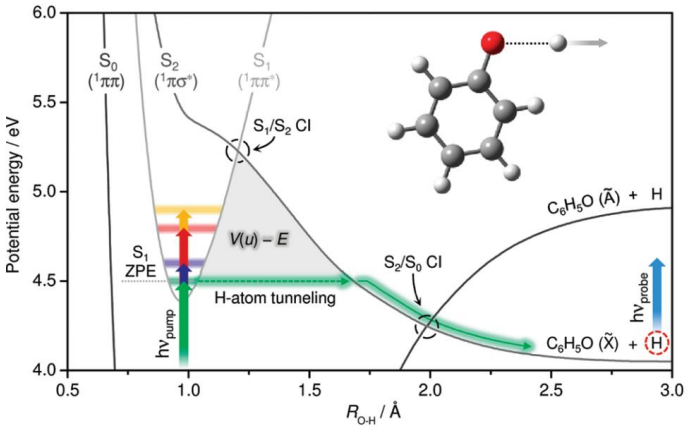

Figure 5.2 – Schematic diagram of a potential energy surface of phenol showing the mechanism of H-atom tunnelling and the size of the barrier. This figure was taken from Ref [9].

radiative decay of the electronically excited phenol species.[4, 6, 13] Figure 5.1 shows a 1D cut through of the potential energy surface (PES) of phenol along the O-H bond coordinate calculated by Ashfold and co-workers[17]. This highlights the crossover points of the different surfaces, and therefore the possible locations of the conical intersections. It should also be noted from the PES that the conical intersection should not accessible at all excitation energies as it lies above the vibrational origin of the $S_1(\pi\pi^*)$ state. However, studies have shown that crossing from $S_1(\pi\pi^*)/S_2(\pi\sigma^*)$ is still possible by quantum tunnelling under a potential energy barrier formed by vibronic coupling (see Figure 5.2), which allows the states to mix. The tunnelling lifetime is dependent upon the relative size of this potential barrier. Stavros and co-workers have modelled this using a Wentzel-Kramers-Brillouin model.[9]

In addition, derivatives of phenol have also been widely investigated. This work has included methylation of the alcohol group,[27-30] replacing the alcohol with a thiol group,[12] and adding more alcohol groups to the system.[8, 31-33] It is the work involving methylation and the addition of alcohol groups that is focused on here, due to its relevance to the guaiacol system. Anisole, otherwise known as methoxybenzene, has been shown to have similar dynamics, albeit slower, to its alcohol-containing counterpart, phenol.[28] This implies that the $S_1(\pi\pi^*)/S_2(3s/\pi\sigma^*)$ conical intersection is active, providing a route for internal non-radiative relaxation of the electronically excited species. Experiments investigating the effects of adding additional alcohol groups to the benzene ring have been performed to understand the effects of these additions on the relaxation dynamics of the system. Catechol (o-dihydroxybenzene), resorcinol (m-dihydroxybenzene), and hydroquinone (p-dihydroxybenzene) have all been previously studied.[8, 31, 32] Of these systems, resorcinol, hydroquinone, and phenol behave very similarly to one another, as will be discussed further in Section 5.2. Catechol, however, is different and has a dramatically shorter lifetime in its $S_1(\pi\pi^*)$ excited state. This is attributed to a change in the potential energy surface with respect

to phenol, causing an increase in the rate of quantum tunnelling from the $S_1(\pi\pi^*)$ to the dissociative $S_2(\pi\sigma^*)$ state, this will be elaborated on in the following section.

Work on competing alcohol/methoxy dynamics has also been performed on 4-methoxyphenol (mequinol). In a study by Hadden *et al.*[28] mequinol was used to examine competing dissociative pathways between the loss of hydrogen or the loss of a methyl group. It was found that within the excitation region of the $S_1(\pi\pi^*)$ state, the dominant dynamical pathway for relaxation was H atom tunnelling in a similar fashion to phenol. Interestingly, in the region of low absorption in the $S_1(\pi\pi^*)$ state, it was possible to directly excite to a quasi-bound level in the vertical Franck-Condon region of the $\pi\sigma^*$ state associated with the dissociation of the O-Me bond. The difference in the shape of these two surfaces is shown in Figure 5.3. Further to this work, and the topic of this Chapter, guaiacol has been investigated to further understand the effects on methylation of dihydroxybenzene systems. Guaiacol is the single methylated analogue of catechol (as mequinol is to hydroquinone).[34] This work was undertaken in collaboration between the Townsend group, and the Stavros group, and has been previously published.[35] This chapter will now present details of previous work on hydroxybenzenes, specifically the theoretical calculations, performed to determine the differences in the photoelectron spectra of the hydroxybenzene systems studied[8], this will focus on the theoretical calculations contribution to the work that was performed by myself rather than the experimental work performed by Dr Ruth Livingstone, which is discussed in detail in her thesis.[8] Results and discussion of the gas phase time-resolved photoelectron spectra of guaiacol performed by myself will then be reported, alongside the results reported by Stavros and co-workers using time-resolved transient absorption spectroscopy.

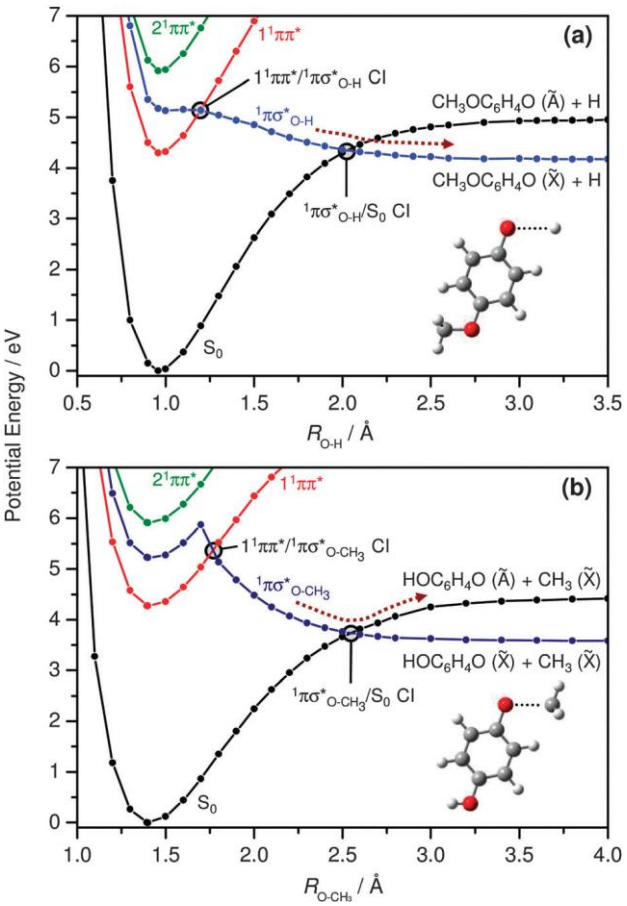

Figure 5.3 – Potential energy surfaces of mequinol along the a) OH coordinate and b) the OMe coordinate calculated using CASPT2(12/11)/aug-ccpVTZ taken from ref [28]

5.2 – Previous work

5.2.1 – Previous photoelectron study

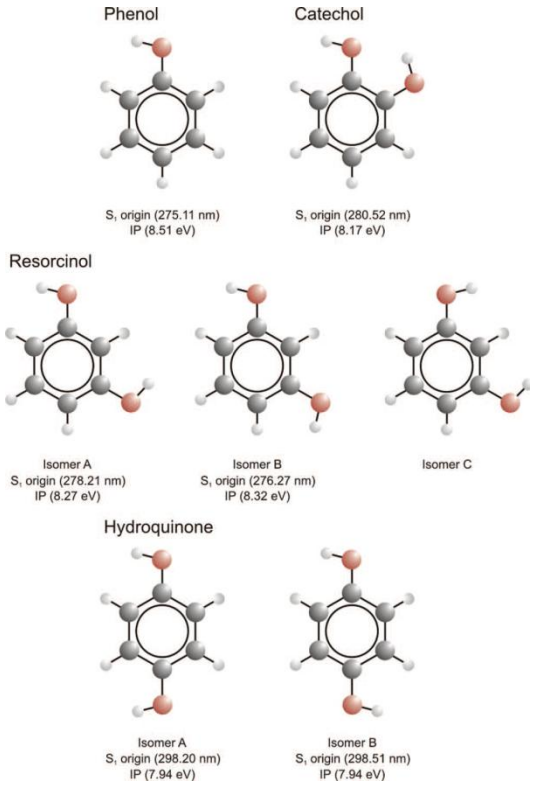

Figure 5.4 – Structures of phenol, catechol, resorcinol and hydroquinone. For catechol, resorcinol and hydroquinone only the lowest energy isomer is shown

dramatically different. The mechanism of H-atom tunnelling was put forward as route for relaxation of the $S_1(\pi\pi^*)$. This was supported by the change in the anisotropy parameter β_2, which was interpreted as a change in the electronic character of $S_1(\pi\pi^*)$ by non-adiabatic coupling of the $S_2(\pi\sigma^*)$ state, facilitating tunnelling below a potential energy barrier. What is critical to the process of H-atom tunnelling is the size of the potential energy barrier. Therefore, to verify tunnelling as the decay

With respect to the discussion of the guaiacol results later in this chapter, an understanding of the previous work performed on phenol is required in order to provide insight into the possible mechanisms observed. As such, a review of the previously reported work by Townsend and co-workers will now be presented.[8] Phenol, catechol, resorcinol and hydroquinone (shown in Figure 5.4) have previously been investigated using time-resolved photoelectron imaging. Figure 5.5 shows the time-resolved photoelectron spectra of phenol and catechol. What is clear to see is that the dynamical lifetime of the two molecules is

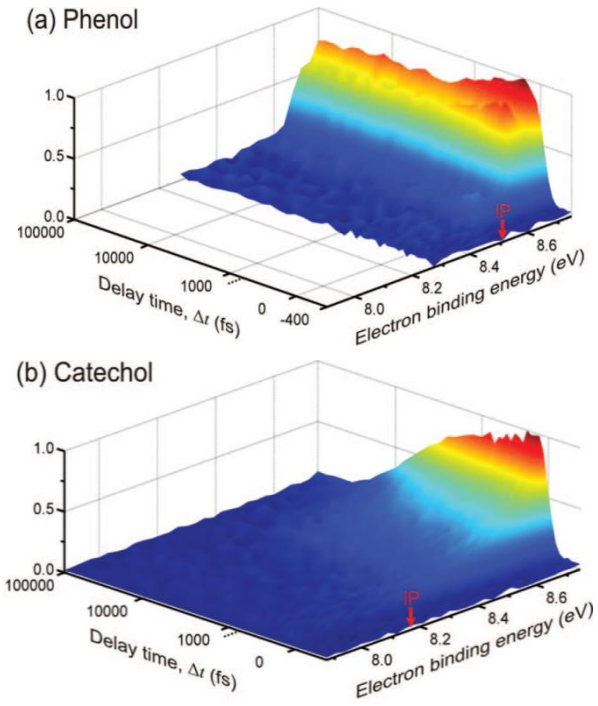

Figure 5.5 – Time resolved photoelectron spectra of phenol and catechol. The plots are shown in cation binding energy against time in a lin/log scale. The IP of both phenol and catechol is indicated on their respective plots

mechanism, it was necessary to perform potential energy surface calculations to examine the size and shape of the potential energy barrier.

5.2.2 – Theoretical work on hydroxybenzenes

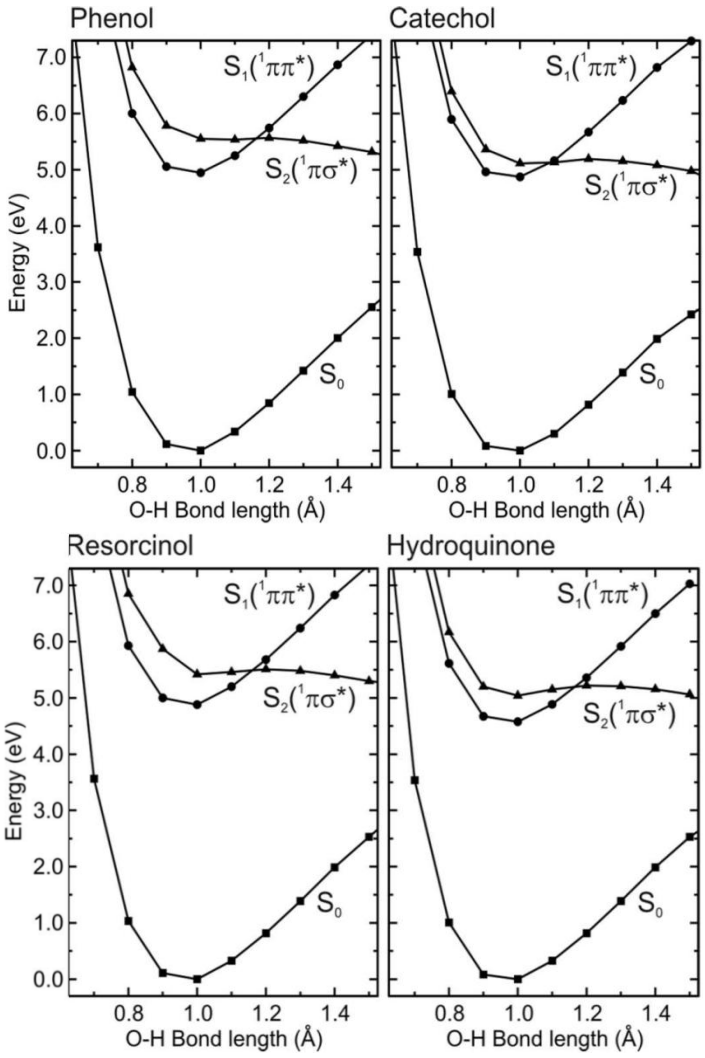

Figure 5.6 – Potential energy surfaces of phenol, catechol, resorcinol and hydroquinone generated along the OH coordinate calculated using EOM-CCSD/aug-cc-pVDZ.

As supporting evidence for the photoelectron study previously mentioned in 5.2.1,[8] I performed a series of theoretical calculations on the four hydroxybenzene species using Gaussian09.[36] From an optimised ground state configuration, calculated using B3LYP[37] with an aug-cc-pVDZ basis set, the vertical excitation energies were calculated using equation of motion couple cluster theory including single and double excitations (EOM-CCSD).[38] This was performed with the same basis set as the ground state optimisation. In this calculation, the core 1s orbitals on the carbon and oxygen atoms were frozen. The energies presented have been

Table 5.1 – Vertical excitation energies and oscillator strengths of the first two singlet excitations calculated using EOM-CCSD/aug-cc-pVDZ

	Phenol		Catechol		Resorcinol		Hydroquinone	
	E(eV)	*f*	*E*(eV)	*f*	*E*(eV)	*f*	*E*(eV)	*f*
$S_1(^1\pi\pi^*)$	4.95	0.0460	4.88	0.0580	4.90	0.0470	4.57	0.1070
$S_2(^1\pi\sigma^*)$	5.55	0.0000	5.17	0.0010	5.41	0.0010	5.12	0.0000

adjusted using a non-iterative correction of 0.15 eV, determined by calculating the effect of perturbative triples on the excitation energies of phenol and catechol, using the CCR(3) method (performed using Dalton). The results of calculating the singlet excitation energies and their oscillator strengths are displayed in Table 5.1. It should be noted that for resorcinol and hydroquinone the values quoted are for the lowest energy isomer in the ground state.[8]

The first excited state in all four systems is the optically bright ππ* state. The energies of all these states are very similar, with the exception of hydroquinone, which is approximately 0.4 eV lower than the other systems with twice the oscillator strength. The second excited state in these systems is the dark πσ* state. In all four systems the πσ* state is dark and carries no oscillator strength. What is interesting is that the gap between the first and second singlet excitation energies is the smallest for catechol, with a gap of 0.29 eV, whilst the other systems have a larger gap that is in excess of ~0.5 eV. This can be qualitatively understood due to the internal hydrogen bonding between the O-H group and the adjacent oxygen causing a weakening in the strength of the other O-H bond. To further investigate the size of the potential energy barrier which could impact the energy flow between the two singlet states, 1D relaxed potential energy surfaces were generated using EOM-CCSD/aug-cc-pVDZ along the O-H coordinate. Specifically in catechol and resorcinol, the O-H coordinate selected was the one not involved in any internal coordination. In addition, the same starting isomers of resorcinol and hydroquinone were selected, as indicated above. This methodology has been used previously in calculating the PES of indole and 5-hydroxyindole in a previous piece of work by the group.[39] Figure 5.6 shows the potential energy cuts of the four systems. It should be noted that the predicted energy at the bottom of the $S_1(\pi\pi^*)$ well is approximately 0.65 eV higher than the experimentally known energy in all four systems. To determine the validity of these surfaces, complete-active-space self-consistent-field (CASSCF) calculations were performed to establish the positions and geometries of the $S_2(3s/\pi\sigma^*)/S_1(\pi\pi^*)$ conical intersections.[13] CASSCF inherently provides a much more accurate picture of the strong non-adiabatic coupling around the crossing of two potential energy surfaces, as well as generating the location of the $S_1(\pi\pi^*)$ minima. Figure 5.7 shows a visual presentation of the branching space vectors required to bring the two states to degeneracy. It is apparent that in all cases there is a strong movement within the O-H bond and some out of plane motion within the benzene ring, indicating that the cuts in Figure 5.6 are illustrating a coordinate that is strongly correlated with finding this conical intersection. Further to this, a more

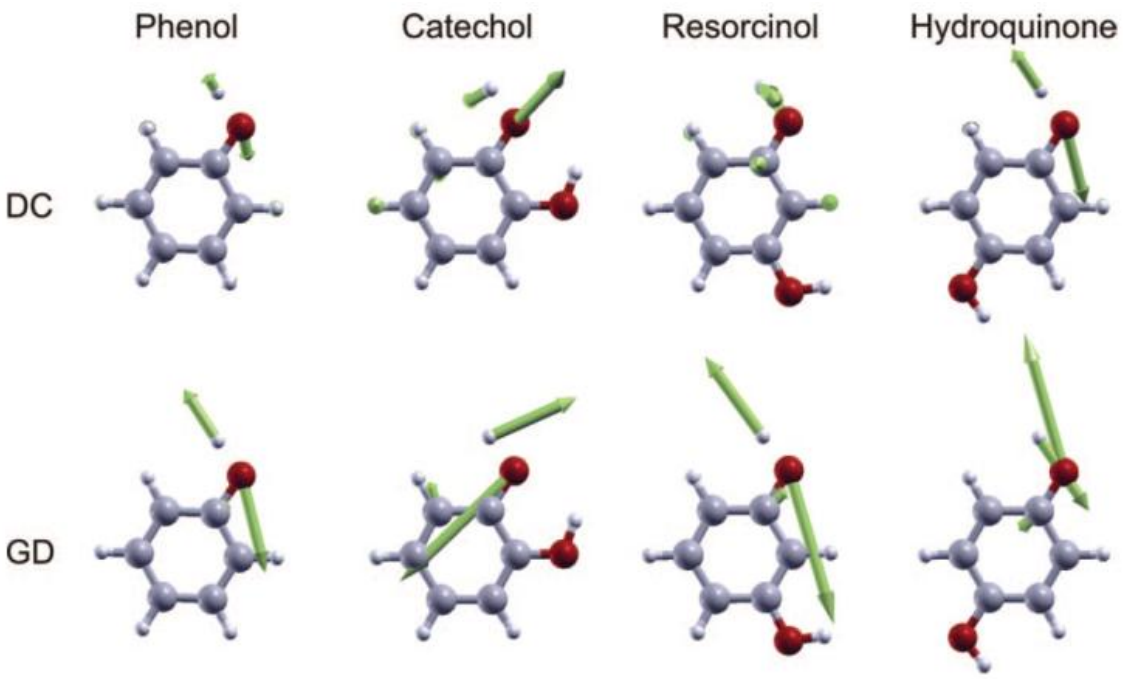

Figure 5.7 – Branching space vectors for the S_2/S_1 conical intersection for all four systems. The Derivative Coupling (DC) vectors and the Gradient Difference (GD) vectors define the motion and amplitude to bring the two surfaces to degeneracy

accurate calculation has been performed using CASPT2(10,10)/aug(O)-AVTZ on the phenol molecule by Ashfold and co-workers,[17] as shown previously in Figure 5.1.[17] This calculation has proven to be highly accurate in terms of calculating the position of the conical intersection, as well as the energy of the $S_1(\pi\pi^*)$ state. Making a comparison between the EOM-CCSD calculation presented in this chapter, and the previous CASPT2 calculation (by Ashfold and co-workers),[17] we find that the barrier height is underestimated by 0.2 eV. However, comparing the location of the conical intersection and the shapes of the $S_1(\pi\pi^*)$ and $S_2(3s/\pi\sigma^*)$ surfaces, we find that the two calculations are qualitatively similar. As such we may use the EOM-CCSD calculations to demonstrate (in a qualitative manner) the shape and depth of the potential energy barriers in all four molecules. Our work concluded that the change in the shape of the barrier between the $S_1(\pi\pi^*)$ and $S_2(3s/\pi\sigma^*)$ surface was the dominant factor that caused the *two orders of magnitude* decrease in the lifetime in the $S_1(\pi\pi^*)$ state of catechol compared to that of phenol. With this in mind, this chapter will now describe the investigation of the time-resolved photoelectron spectroscopy of Guaiacol.

5.3 – Experimental

5.3.1 – Velocity map imaging set up

The experimental set up has been described in Chapter 2 of this thesis and in previous studies.[8, 35, 40] Guaiacol, also known as 2-methoxyphenol (98%, Sigma-Aldrich), as shown in Figure 5.8, was loaded directly into the Even-Lavie (EL) pulsed molecular beam valve[41] and carried into the interaction region by 3 bar of He gas. The temperature of the EL valve was regulated to 60 °C to generate adequate vapour density for the experiment. In the interaction region between the VMI ion optics, the skimmed molecular beam was intersected by two co-linear beams of 267 and 305 nm light that had passed through a 25 cm fused silica lens to focus light onto the molecular beam. The pump beam of 267 nm light was generated using beam line 3 with a heavily attenuated power of 0.1 µJ/pulse. The 305 nm probe beam (attenuated power of 0.9 µJ/pulse) was generated using beam line 1. The two beams were combined with the use of a dichroic mirror before being introduced to the chamber. The pump-probe cross correlation of this experiment was determined to be 160 fs with use of [1 + 1′] non-resonant ionisation using pyrrole. The spectrometer was calibrated by a three photon ionisation signal from Xe using 267 nm. The time steps taken for this experiment were chosen to be 50 fs increments between -500 fs and + 500 fs with a further 20 steps at exponentially increasing intervals from + 500 fs out to + 100 ps. Images at each pump-probe delay were accumulated for 500,000 laser shots, and at each time step a pump only and probe only image were taken for background subtraction that were also acquired for the same number of laser shots.

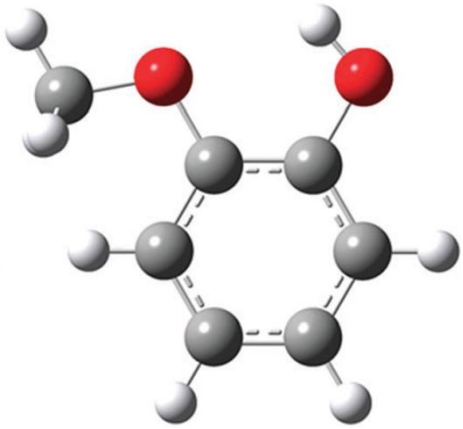

Figure 5.8 – Guaiacol in its lowest energy conformer, adapted from Ref [35]

5.3.2 – Transient absorption set-up

Complementary solution phase data was recorded by the Stavros group at the University of Warwick using a transient electronic absorption spectrometer (TEAS) setup described previously[35] and shown schematically in Figure 5.9.[42] 2-methoxyphenol (98%, Sigma-Aldrich) was dissolved in either cyclohexane (99.7%, VWR) or methanol (99.9%, Sigma-Aldrich) to a concentration of 25 mM and delivered using a liquid wire-guided jet based on the design of Tauber *et al*.[43] which provides a fresh sample volume,

~125 µm sample thickness and samples at a rate of 1 KHz (to match the laser frequency). A peristaltic pump (Masterflex) was used to circulate the sample within PFTE tubing throughout, and a large sample vat of 250 ml was used to negate concentration variance due to sample evaporation and degradation. The experiment was performed using a Ti:Sapphire femtosecond laser system (Spectra Physics, Spitfire XP, 800 nm output, 1 KHz repetition rate). The output was split to provide two beams. One beam, with an output power of 950 mW was used to produce the third harmonic (267 nm, 4.64 eV) using two BBO crystals as the non-linear media. The other 5 mW beam is used to produce a white light continuum (340 nm to 690 nm) by focussing through a CaF_2 window. The maximum pump-probe delay time of 2 ns was achieved through the use of a motorised optical delay line in the probe beam path. Pump-probe delays between -1 ps and +1 ps were measured linearly with a step size of 50 fs followed by a further 40 exponential steps out to 2 ns. The longer delay measurements of 10 ns were achieved by adding in an additional delay line consisting of moveable mounts on pre-positioned magnetic bases.

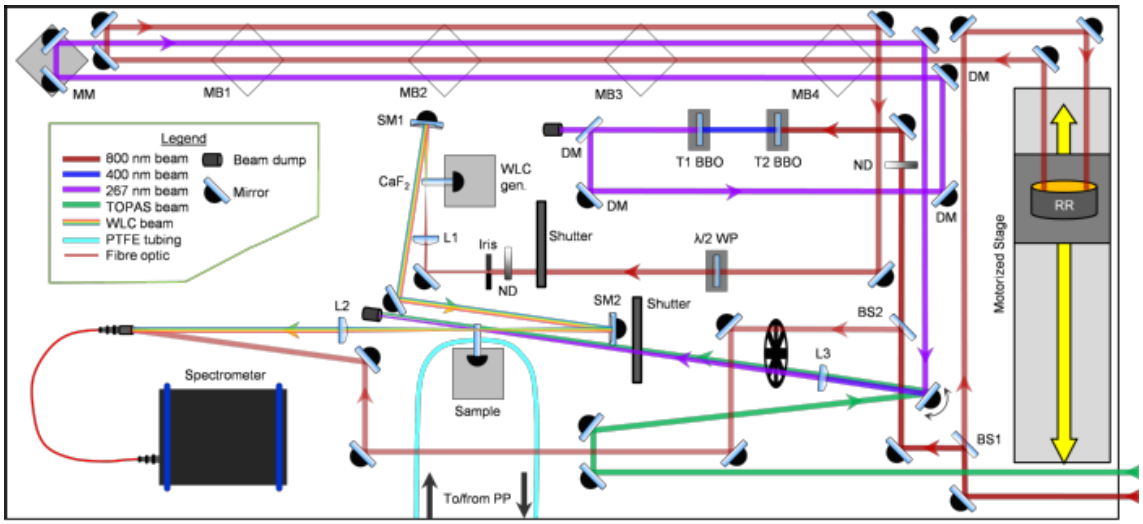

Figure 5.9 – Illustrative diagram of the TEAS set-up at Warwick University. Taken from the group website Ref [43]
http://www2.warwick.ac.uk/fac/sci/chemistry/research/stavros/stavrosgroup/overview/transient/

5.4 – Results

5.4.1 – Photoelectron images

Figure 5.10 shows a strip of images at a selection of pump-probe time delays (all values shown in femtoseconds). The upper line shows the raw photoelectron images with background subtraction to remove any pump-only or probe-only signal. The lower strip shows the matrix Abel[8, 44] transformed images (see Chapter 2 for more information).

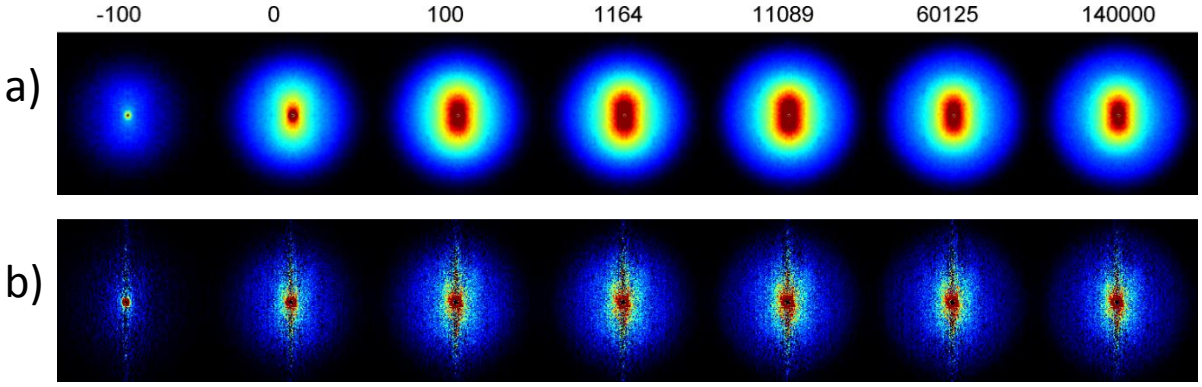

Figure 5.10 – Presents a strip of VMI images of guaiacol. The values at the top of the figure represent the delay time in femtoseconds between the pump and probe pulse. The strip labelled as a) shows the raw 4-fold symmetrised VMI images and b) the matrix Abel transformed images. In both strips the pump and probe alone background signals have been subtracted from the image. The images are presented with the laser polarisation defined as vertical with respect to the images.

5.4.2 – Time-resolved photoelectron spectra

Figure 5.11 shows the 3D time-resolved photoelectron spectra (a) of guaiacol along with its fit (b), associated residuals (c). The data was fitted using the global fit function shown in E.q 5.1 and described in Chapter 2.

$$I(E,t) = \sum_{i=1}^{n} A_i(E)\left(e^{-\frac{t}{\tau_i}}.cc(t)\right) \tag{5.1}$$

Figure 5.12 shows the decay associated spectra (DAS) of guaiacol in which two functions were required to produce a good fit. Two time constants were identified as τ_1 = 3.2 ps and τ_2 = 1.3 ns. The short time constant (τ_1) is attributed to fast IVR (internal vibrational energy redistribution) within the $S_1(\pi\pi^*)$ state. This is mediated by population from initially excited vibrational "doorway" states relaxing into a series of different states accessible by the wavepacket. This is akin to what was seen in phenol, catechol, resorcinol and hydroquinone,[8] and also in aniline.[40] This has also been reported in a number of other systems.[45, 46] It is also apparent that following this IVR

process, there is a slight increase in the photoelectron signal due to an improved Franck-Condon overlap between the excited state and the guaiacol$^+$ cation state. This has been previously observed in other work on similar molecules.[8, 40] The longer time (τ_2) component of 1.3 ns is attributed to the lifetime of the $S_1(\pi\pi^*)$ state. The mechanism of this decay is difficult to speculate by DAS alone, however, extra insight can be gathered by considering the change in anisotropy, as plotted in Figure 5.13.

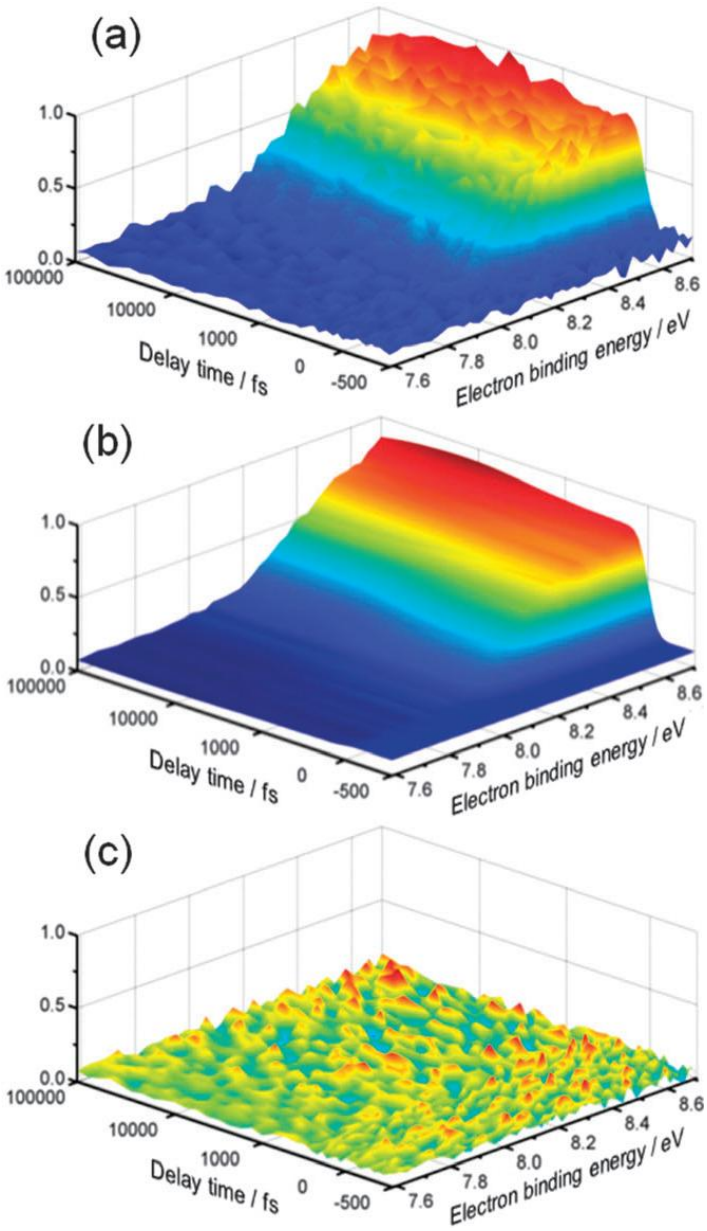

Figure 5.11 – The time resolved photoelectron spectra of guaiacol. a) shows the raw data in internal binding energy, while b) and c) display the fitted data with two exponentials in the fit, and the residuals to this fit respectively.

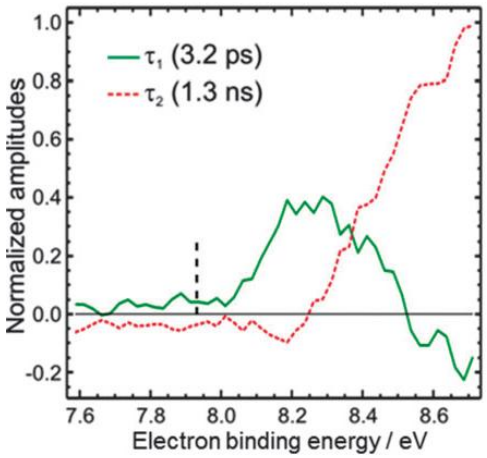

Figure 5.12 – Decay associated spectrum of guaiacol. The spectrum is plotted in binding energy with the dashed line showing the predicted cut off based on the ionisation potential (IP).

5.4.3 – Photoelectron angular distribution

Figure 5.13 shows the evolution of the β_2 parameter[47, 48] as a function of pump-probe delay. The value was averaged over all energies with significant photoelectron signal at all pump-probe times as the temporal trend is the same in all sub-regions to improve the statistics of the fits. The value of β_4 was found to be approximately zero in all regions of the spectrum.

It is clear to see that in this measurement, there is no dynamical evolution as the β_2 value is invariant as a function of time over the window investigated. This implies that there is no state mixing occurring in guaiacol at this excitation wavelength. This rationale has been used in other studies,[8, 40] and argued previously in Chapter 4.[40] In the

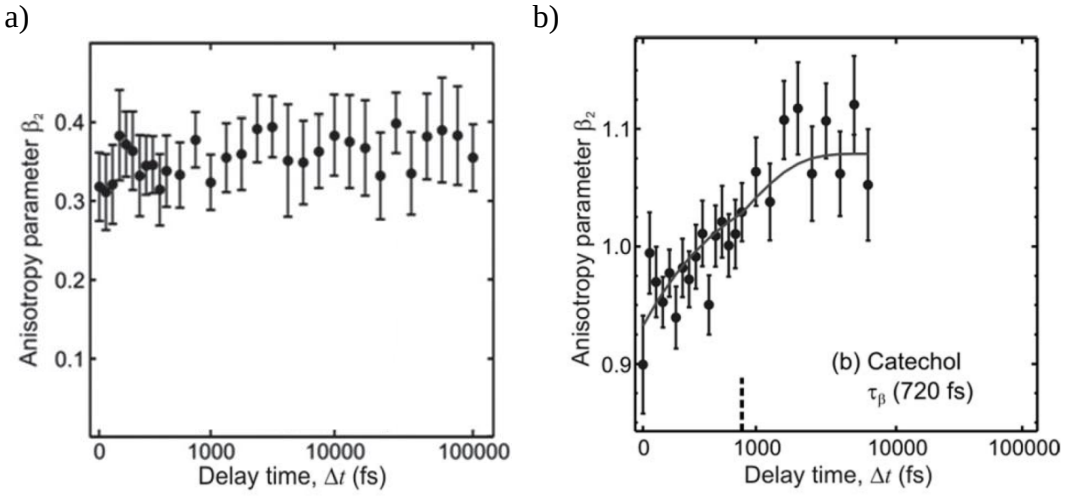

Figure 5.13 – Anisotropy parameter β_2 plotted as a function of pump probe delay for guaiacol, a), and catechol, b). Error bars plotted represent one standard deviation.

case of $S_2(\pi\sigma^*)/S_1(\pi\pi^*)$ state mixing one would expect to see an increase in the anisotropy parameter due to the 3s Rydberg character present in the $S_2(3s/\pi\sigma^*)$ state mixing into the electronic character of the $S_1(\pi\pi^*)$ state. This would lead to an increase in β_2 amplitude as, based on atomic selection rules, the increased s-like electronic character of the state would give rise to a p-type partial wave which would peak along the laser polarisation. This lack of β_2 evolution is in stark contrast to previous work on catechol (as shown in Figure 5.13 b) where, not only was the mixing active, it also greatly reduced the lifetime of the $S_1(\pi\pi^*)$ state compared to phenol. Based upon this it would seem unlikely that the $S_1(\pi\pi^*)/S_2(\pi\sigma^*)$ population transfer through internal conversion is active in guaiacol. This implies that the mechanism described by the 1.3 ns time constant would be $S_1(\pi\pi^*) \rightarrow S_0(\pi)$ relaxation either through fluorescence, internal conversion or through an intersystem crossing (ISC) to a T_n state, back to the ground state. This will be considered in the discussion after reporting the transient absorption results by Stavros and co-workers.

5.4.4 – Transient absorption data

Figure 5.14 shows the transient electronic absorption spectroscopy (TEAS) spectra of guaiacol-cyclohexane whilst Figure 5.15 shows the spectra of guaiacol-methanol. First considering the guaiacol-cyclohexane spectra, there are two main features, located at 340 nm and 620 nm. These features are assigned as the excited state absorption to $S_1(\pi\pi^*)$, and subsequent electronic state absorption (ESA) to higher lying excited states S_n similar to results previously recorded for phenol.[23, 49] Interestingly, from the spectra it is clear that in the long time window of this experiment the base line is not fully recovered. By around 8 ns, the feature at 620 nm, has relaxed and recovered the baseline absorption of the solvent. This feature is assigned to ISC from $S_1(\pi\pi^*)$ to T_n.[49] We now consider the spectra of guaiacol-methanol, shown in Figure 5.15. From first observations it is clear that there is a difference in the

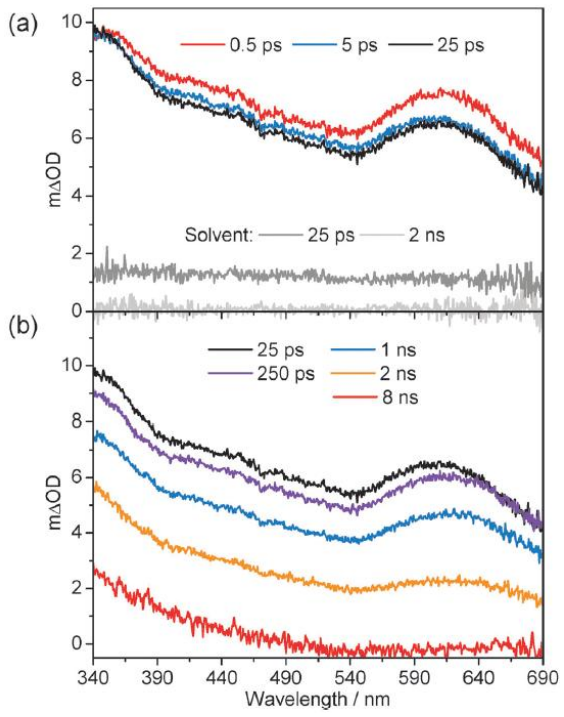

Figure 5.14 – TAS of 25 mM guaiacol in cyclohexane. Spectra a) shows the spectra from delay times from 500 fs to 25 ps, and b) delay times from 25 ps to 8 ns.

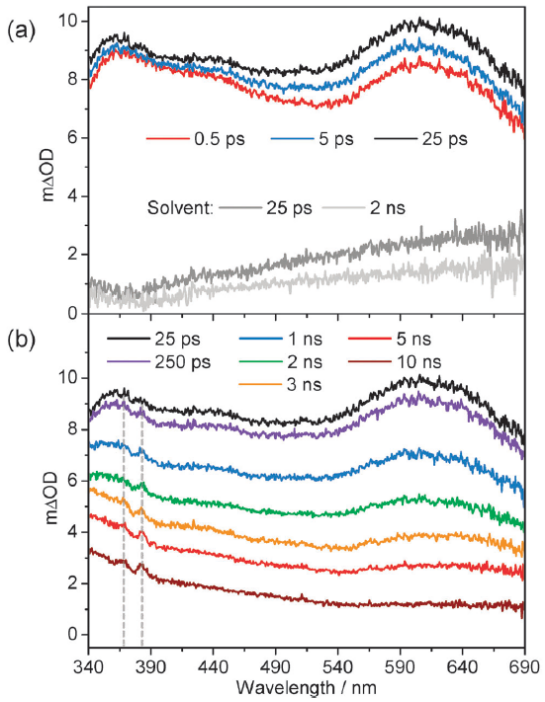

Figure 5.15 – TAS of 25 mM guaiacol in methanol. Spectra a) shows the spectra from delay times from 500 fs to 25 ps, and b) delay times from 25 ps to 8 ns.

magnitude of absorption at the red end of the spectrum when compairing the two different solvents. This is due to a background introduced by the methanol, which is not present in cyclohexane. Overall the spectra obtained from guaiacol when dissolved in the two different solvents look broadly the same. However, there are two notable differences bewteen them. There is an increase in the quantum yield of the triplet state in the methanol-solvated data. It has been previously seen in phenol that Φ_T increases with the polarity of the solvent.[49] The second difference is that of a new structural feature in the methanol data, growing in the higher energy region from 250 ps onwards (as indicated by the grey dashed lines on the spectra). Work investigating the guaiacol-tert-butoxy radical in acetonitrile has shown that this species has an absorbtion around 380 nm with structural peaks around 381 nm and 365 nm, and a lower energy broadband feature around 650 nm.[50] From this we can assign this feature as the guaiacoloxy radical. We note that the feature at 650 nm is not present in the spectra recorded for cyclohexane and surmise that this feature is hidden behind the T_n signal from guaiacol. With this in mind, the lifetime of the $S_1(\pi\pi^*)$ state has been calculated using a 5 nm slice of the spectrum around 540 nm as a kinetic trace, as shown in Figure 5.16. The lifetime of the $S_1(\pi\pi^*)$ state is 4.5 ± 0.2 ns and 2.9 ± 0.1 ns when dissolved in cyclohexane and methanol respectively. The short time dynamics (< 25 ps) of the system have been assigned as a convolution of IVR within the guaiacol molecule and intermolecular

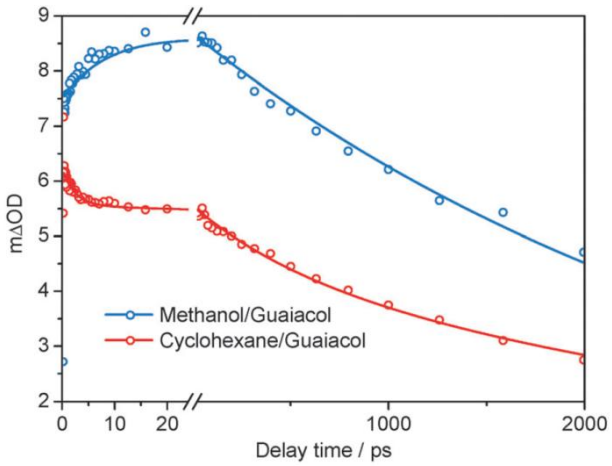

Figure 5.16 – Kinetic traces of guaiacol-methanol and guaiacol-cyclohexane solutions fitted from 0 to 2 ns with a multi exponential fit.

energy transfer (IET) between the solute and the solvent, as well as solvent-only dynamical effects. These have been collectively termed vibrational energy transfer (VET). The lifetime associated with the VET is 2.1 ± 0.4 ps and 540 ± 250 fs for cyclohexane and methanol, respectively. This is manifested as a small increase in the $S_1(\pi\pi^*)$ ESA from a presumable increase in the Franck-Condon overlap between the $S_1(\pi\pi^*)$ and S_n states. The difference in timescale is attributed to the fact that guaiacol can form intermolecular hydrogen bonds to the methanol solvent, thereby allowing more efficient and faster energy transfer, which it is unable to do effectively in cyclohexane.

5.4.5 – Computational calculations

Calculations were performed by the Stavros group using the Molpro 2010 package. The minimum energy geometry was optimised using complete-active-space self-consistent-field theory (SA4-CASSCF) with an aug-cc-pVDZ basis set. The 1D potential energy cuts calculated are shown later in Figure 5.18, in the discussion following this section. The choice of active space was heavily dependent on the O–Me and O–H ring substituents, and after careful testing an optimal active space of 12 electrons in 11 orbitals was chosen as a compromise between accuracy and computational expense.

Potential energy curves were then computed along the O–H bond extension coordinate (R_{O-H}) using the same basis set outlined above, however, it should be noted that all other coordinates were fixed at the $S_0(\pi)$ geometry (and therefore unrelaxed), using complete active space with second order perturbation theory (CASPT2). These CASPT2 calculations were based on a SA4-CASSCF reference wavefunction for both the A and B conformations (described in more detail later in this chapter and shown in Figure 5.17), and utilised the same active space as the CASSCF calculations. Since the ground state optimised geometry favours the syn conformation, all other internal degrees of freedom were fixed in the initial optimised geometry during the scan along R_{O-H}. The 1D potential energy cuts for the B conformer, along R_{O-H}, required a 180° rotation of the CCOH dihedral angle, after which the potential energy was calculated as a function of the O–H bond stretch in the same way, with all other internal degrees of freedom fixed at the ground state CASSCF geometry.

5.5 – Discussion

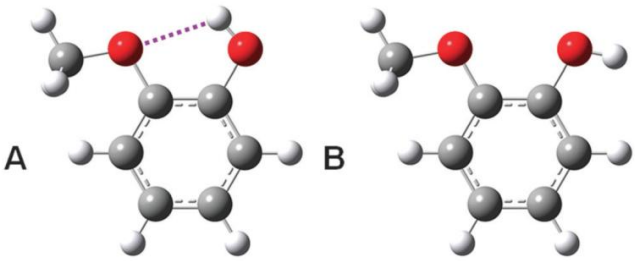

Figure 5.17 – Two conformers of guaiacol. Conformer A is the lowest energy conformer found in the gas phase and cyclohexane measurement whilst conformer B is suggested to be found in the methanol measurement.

We now compare the gas-phase measurement to the solution-phase measurements where we expect that the lowest energy conformer of guaiacol (conformer A) will dominate the dynamics in both the TRPEI and TEAS. Both the gas-phase and solution-phase data show similar results, in which direct excitation to the $S_1(\pi\pi^*)$ state results in a lifetime of >1.3 ns, which is not surprising due to the choice of solvent. Cyclohexane is non-polar and therefore weakly perturbing. As such, it creates a pseudo gas-phase environment for the guaiacol, based on a zeroth order model. What is also apparent is the lack of the guicoloxy radical species in the cyclohexane spectra, even at long time delays of around 8 ns. This would imply that just as in the gas-phase measurement, there is no significant H-atom tunnelling present in this species when excited at 267 nm. This is an interesting result when compared to phenol and catechol in the gas phase (see Section 5.2), in which clear signs of H-atom tunnelling have been observed. It was proposed that this mechanism occurred by the wavepacket produced on the $S_1(\pi\pi^*)$ surface being able to tunnel under the potential energy barrier onto the dissociative $S_2(\pi\sigma^*)$ surface. This conclusion is also supported by arguments made previously in Section 5.4.3, based upon the invariance in the anisotropy parameter β_2 as a function of time. As such, we conclude that in the gas-phase and in the 'gas-phase like solution' of cyclohexane, that the tunnelling pathway for internal relaxation in guaiacol is turned off as the barrier is too large as only the low energy conformer is present. However, this is not the case for the measurements taken for the methanol-solvated molecule, where we expect the solvent-solute hydrogen bonding interactions to play a significant role in dictating the energy of the excited states. Previous semi-empirical calculations on guaiacol suggest that the conformer distribution would shift as the dielectric constant increased with the polarity of the solvent.[51] Therefore we surmise that the high energy conformer, shown as conformer B in Figure 5.17, forms a larger proportion of the population of guaiacol in the methanol solvent. By looking at the two conformers, it is clear that from a theoretical standpoint that conformer B is more likely to form intermolecular hydrogen bonds with the solvent than conformer A. Indeed it has been shown through the use of

FTIR (Fourier transform infrared spectroscopy) that an internal hydrogen bond can be replaced by an external hydrogen bond in the presence of a proton acceptor such as methanol.[52] As such, we predict that conformer B will dominate the spectroscopy in the guaiacol-methanol measurements. The TEAS of guaiacol-cyclohexane and guaiacol-methanol are largely similar with the exception of the feature between 381 nm and 365 nm found in the guaiacol-methanol measurement. This feature was attributed to the guaiacoloxy radical and indicates that OH bond fission is active. To investigate the solvent-induced conformer specific OH bond fission, complementary theoretical calculations were performed on both guaiacol conformers, as outlined in Section 5.4.5. Figure 5.18 shows a set of 1D potential cuts for the two conformers along the O-H bond length coordinate using CASPT2(12,11)/aug-cc-pVDZ. It is worth noting that these calculations are performed on a single molecule with no solvent effects and are therefore effectively in the gas phase. However, recent work on thio-phenols and phenol have shown that these gas-phase 1D potential energy surfaces can provide useful insight in interpreting the time-resolved measurements.[20] The cuts shown in Figure 5.18 are qualitatively very similar to the potential cuts shown previously for phenol and other similar molecules. There is a notable difference in the size of the potential energy barrier when comparing conformers A and B. From previous work, it has been shown in many (but not all) phenol analogues that H-atom tunnelling occurs from the ν=0 vibrational mode.[9] Figure 5.18 b) shows an illustration of the size of the

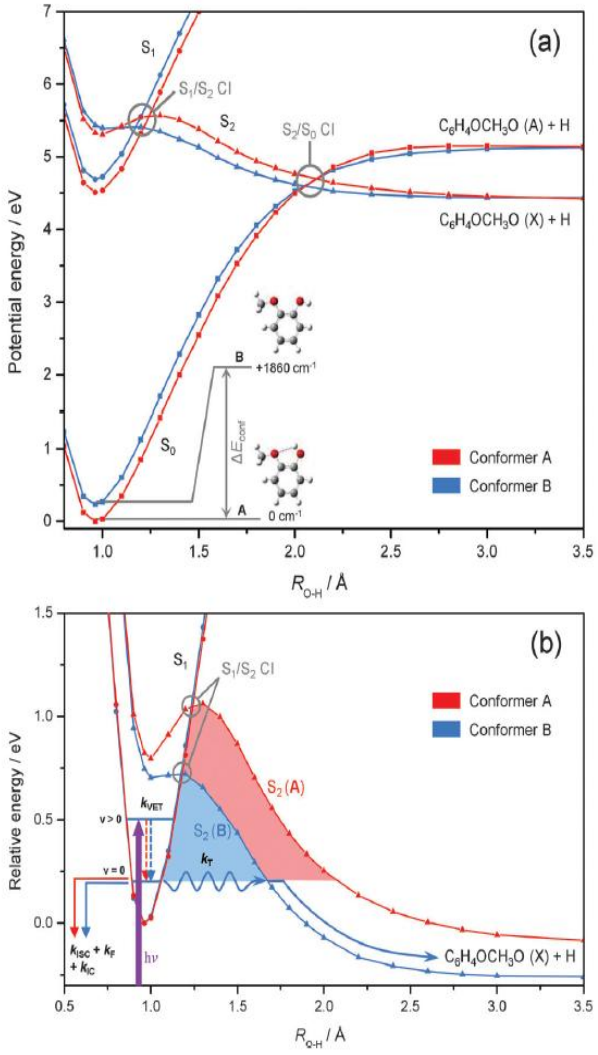

Figure 5.18 – Potential energy surface of guaiacol. The cuts shown in red are that of the lower energy conformer A and in the blue the high energy conformer B. Both of these calculations are performed using CASPT2/aug-cc-pVDZ as outlined in the text. Figure a) shows the whole surface calculated whilst b) shows a close up of the $S_1(\pi\pi^*)/S_2(\pi\sigma^*)$ CI using a relative energy scale based on the minima of conformer A's $S_1(\pi\pi^*)$ energy.

potential barrier in which conformer A (shaded in red) is approximately twice the size of the barrier for conformer B (shaded in blue). This difference in barrier size can severely impact the lifetimes of the H-atom tunnelling. In fact, performing 1D tunnelling calculations using the Wentzel-Kramers-Brillouin[9] model on these two barriers predicts tunnelling probabilities of 2.7×10^{-12} and 2.7×10^{-6} for conformers A and B, respectively. From this, in conjunction with the zero point energy of the OH stretch, it is possible to convert these probabilities into tunnelling lifetimes of 3.5 ms and 3.4 ns respectively. These tunnelling lifetimes have been predicted using the fundamental frequency of the O-H bond stretch. It should also be pointed out that the use of this 1D model to calculate tunnelling lifetimes has been shown to be qualitatively accurate in previous work.[9] With this in mind, it is now possible to explain the differences between the guaiacol-methanol and guaiacol-cyclohexane TEAS measurements, and the guaiacol TRPEI measurement. At 267 nm, conformer A is initially excited to the $S_1(\pi\pi^*)$ state, and relaxes through IVR in the gas phase (or through VET in the solution phase) in a few picoseconds. The calculations show that kinetically the process of H-atom tunnelling is unfeasible within the lifetime of the $S_1(\pi\pi^*)$ state, and as such a decay driven by ISC to a T_n, internal conversion (IC), and fluorescence back to the electronic ground state $S_0(\pi)$ would be observed. This is consistent in both the gas-phase and solution-phase experiment in which cyclohexane is the solvent. As for conformer B (which is only present in methanol due to the effects of the solvent interaction), the initially excited $S_1(\pi\pi^*)$ state relaxes through VET on a similar timescale to conformer A. However, due to the presence of signal from the guaiacoloxy radical with an onset at 250 ps, it is suggested that depopulation through H-atom tunnelling under this smaller potential barrier (when compared to conformer A), occurs on a similar kinetic timescale as other mechanisms for $S_1(\pi\pi^*)$ decay (such as ISC, IC and fluorescence).

It is worth mentioning that due to the convoluted, non-spectrally resolved signal of the guaiacoloxy signal from the $S_1(\pi\pi^*)$, TESA makes it very difficult to provide a precise onset time or lifetime for this signal. However, based on simple sequential kinetics the appearance timescale of the guaiacoloxy radical should match the decay lifetime of the $S_1(\pi\pi^*)$ state. In order to get a more accurate appearance lifetime, more experiments appropriate to examining this signal (such as transient absorption infra-red spectroscopy) are needed.[53-55] It is also worth acknowledging that our H-atom tunnelling lifetime prediction is limited to this simple 1D picture, and that even though the value of 3.4 ns shows good agreement with the experimentally derived lifetime of

2.9 ns for conformer B, a multidimensional potential energy calculation would be required to calculate a more accurate tunnelling rate under the $S_2(\pi\sigma^*)/S_1(\pi\pi^*)$ conical intersection. In addition, the theoretical calculations were devoid of any solvent based effects and how these could perturb the relative energies of the electronic states. This would also need to be taken into account in any higher level calculation to produce more accurate potential energy curves. On the other hand, the combined theoretical and experimental nature of this study highlights the solvent induced conformer specific nature of the excited state dynamics of guaiacol, and how it could potentially have significant ramifications for other biomolecule systems and their active chromophore units. It is clear that combining both geometrical and electronic structure information, together with understanding of solvation effects, will prove to be a vital role in conformer specific photochemistry.

5.6 – Conclusions

Chapter 5 has presented the highly conformer-specific photochemical dynamics of guaiacol, mediated by the hydrogen bonding nature and polarity of the solvent. This work can be discussed in terms of the dynamics of either a low energy conformer, A, or a higher energy conformer B. The dynamics of conformer A are dominated by a slow relaxation mechanism of the photoexcited $S_1(\pi\pi^*)$ state. In the case of cyclohexane, the solvent interaction with the sample is very weak, and therefore the results of the TEAS guaiacol-cyclohexane are very similar to those of the gas phase TRPEI. In this conformer, due to the internal hydrogen bonding, the mechanism for $S_1(\pi\pi^*)$ decay is that of a combination of either ISC to a T_n triplet state, or relaxation to the electronic ground state either by IC or fluorescence, with no evidence of H-atom tunnelling beneath the $S_2(\pi\sigma^*)/S_1(\pi\pi^*)$ conical intersection to form the guaiacoloxy radical due to the large barrier to dissociation.

In contrast, when dissolved in methanol, conformer B of guaiacol becomes active in solution. Due to the differences in the 1D cuts of conformer B when compared to conformer A, the H-atom tunnelling pathway to dissociation is now possible within the shortened lifetime of the $S_1(\pi\pi^*)$ state. As such, in the guaiacol-methanol measurement there is evidence of the formation of the guaicoloxy radical. It is proposed that the decrease in the lifetime of the $S_1(\pi\pi^*)$ state in methanol is in part due to this new mechanism for depopulation which is not available at this wavelength for conformer A, in addition to improved conditions for ISC due to the polarity of the solvent. This highlights the importance of the free H-atom required for intramolecular hydrogen bonding with the solvent, and allowing for tunnelling dissociation mechanisms as previously shown in phenol and catechol. The result also shows how important the investigations of solvent effects are on these small photochemical chromophores, with a combination of gas-phase and solution-phase techniques. Especially when attempting to understand how these molecules behave and react in their ultimate function in biological species.

An interesting direction for future work would be to try and investigate the $3s/\pi\sigma^*$ state of guaiacol (and by extension other similar systems such as phenol) directly. This could potentially provide a better understanding of the processes that occur on these normally optically dark states. An approach that could achieve this is a multi-photon pump scheme [2+1′]. This would allow a greater proportion of the prepared population to be placed in the one photon optically dark state and facilitate a more effective tracking of the prepared population, and thus, more rigorous interrogation of the $3s/\pi\sigma^*$ state.

5.7 – References

1. T. N. V. Karsili, A. M. Wenge, B. Marchetti and M. N. R. Ashfold, Phys. Chem. Chem. Phys. **16** (2), 588-598 (2014).
2. R. N. Dixon, T. A. Oliver and M. N. Ashfold, J. Chem. Phys. **134** (19), 194303 (2011).
3. M. G. D. Nix, A. L. Devine, R. N. Dixon and M. N. R. Ashfold, Chem. Phys. Lett. **463** (4-6), 305-308 (2008).
4. O. P. Vieuxmaire, Z. Lan, A. L. Sobolewski and W. Domcke, J. Chem. Phys **129** (22), 224307 (2008).
5. M. Miura, Y. Aoki and B. Champagne, J. Chem. Phys. **127** (8), 084103 (2007).
6. Z. Lan, W. Domcke, V. Vallet, A. L. Sobolewski and S. Mahapatra, J. Chem. Phys. **122** (22), 224315 (2005).
7. M. de Groot and W. J. Buma, Chem. Phys. Lett. **420** (4-6), 459-464 (2006).
8. R. A. Livingstone, J. O. Thompson, M. Iljina, R. J. Donaldson, B. J. Sussman, M. J. Paterson and D. Townsend, J. Chem. Phys. **137** (18), 184304 (2012).
9. G. M. Roberts, A. S. Chatterley, J. D. Young and V. G. Stavros, J. Phys. Chem. Lett. **3** (3), 348-352 (2012).
10. A. Iqbal, M. S. Cheung, M. G. Nix and V. G. Stavros, J. Phys. Chem. A **113** (29), 8157-8163 (2009).
11. G. A. King, T. A. Oliver, M. G. Nix and M. N. Ashfold, J. Phys. Chem. A **113** (28), 7984-7993 (2009).
12. M. N. Ashfold, A. L. Devine, R. N. Dixon, G. A. King, M. G. Nix and T. A. Oliver, Proc. Natl. Acad. Sci. USA **105** (35), 12701-12706 (2008).
13. M. L. Hause, Y. Heidi Yoon, A. S. Case and F. F. Crim, J. Chem. Phys. **128** (10), 104307 (2008).
14. A. Iqbal, L. J. Pegg and V. G. Stavros, J. Phys. Chem. A **112** (39), 9531-9534 (2008).
15. G. A. King, A. L. Devine, M. G. Nix, D. E. Kelly and M. N. Ashfold, Phys. Chem. Chem. Phys. **10** (42), 6417-6429 (2008).
16. C.-M. Tseng, Y. T. Lee, M.-F. Lin, C.-K. Ni, S.-Y. Liu, Y.-P. Lee, Z. F. Xu and M. C. Lin, J. Phys. Chem. A. **111** (38), 9463-9470 (2007).
17. M. G. Nix, A. L. Devine, B. Cronin, R. N. Dixon and M. N. Ashfold, J. Chem. Phys. **125** (13), 133318 (2006).
18. C. M. Tseng, Y. T. Lee and C. K. Ni, J. Chem. Phys. **121** (6), 2459-2461 (2004).
19. C. P. Schick and P. M. Weber, J. Phys. Chem. A **105** (15), 3725-3734 (2001).
20. Y. Zhang, T. A. A. Oliver, M. N. R. Ashfold and S. E. Bradforth, Faraday. Discuss. **157**, 141-163 (2012).
21. R. J. Lipert, G. Bermudez and S. D. Colson, J. Phys. Chem. **92** (13), 3801-3805 (1988).
22. R. J. Lipert and S. D. Colson, J. Phys. Chem. **92** (5), 3240-3241 (1990).
23. D. V. Bent and E. Hayon, J. Am. Chem. Soc. **97** (10), 2599-2606 (1975).
24. M. N. Ashfold, G. A. King, D. Murdock, M. G. Nix, T. A. Oliver and A. G. Sage, Phys. Chem. Chem. Phys. **12** (6), 1218-1238 (2010).
25. A. L. Sobolewski, W. Domcke, C. Dedonder-Lardeux and C. Jouvet, Phys. Chem. Chem. Phys. **4** (7), 1093-1100 (2002).
26. M. N. R. Ashfold, B. Cronin, A. L. Devine, R. N. Dixon and M. G. D. Nix, Science **312** (5780), 1637-1640 (2006).
27. R. Matsumoto, K. Sakeda, Y. Matsushita, T. Suzuki and T. Ichimura, J. Mol. Struct. **735**, 153-167 (2005).
28. D. J. Hadden, G. M. Roberts, T. N. Karsili, M. N. Ashfold and V. G. Stavros, Phys. Chem. Chem. Phys. **14** (38), 13415-13428 (2012).

29. T. N. V. Karsili, A. M. Wenge, S. J. Harris, D. Murdock, J. N. Harvey, R. N. Dixon and M. N. R. Ashfold, Chem. Sci. **4** (6), 2434-2446 (2013).
30. J. C. Dean, P. Navotnaya, A. P. Parobek, R. M. Clayton and T. S. Zwier, J. Chem. Phys. **139** (14), 144313 (2013).
31. A. S. Chatterley, J. D. Young, D. Townsend, J. M. Zurek, M. J. Paterson, G. M. Roberts and V. G. Stavros, Phys. Chem. Chem. Phys. **15** (18), 6879-6892 (2013).
32. J. D. Young, M. Staniforth, A. S. Chatterley, M. J. Paterson, G. M. Roberts and V. G. Stavros, Phys. Chem. Chem. Phys. **16** (2), 550-562 (2014).
33. W. B. Tzeng, K. Narayanan, C. Y. Hsieh and C. C. Tung, Spectrochim. Acta A **53** (14), 2595-2604 (1997).
34. C. Agache and V. I. Popa, Mon. Fur Chem. **137** (1), 55-68 (2006).
35. S. E. Greenough, M. D. Horbury, J. O. Thompson, G. M. Roberts, T. N. Karsili, B. Marchetti, D. Townsend and V. G. Stavros, Phys. Chem. Chem. Phys. **16** (30), 16187-16195 (2014).
36. M. J. Frisch, G. W. Trucks, H. B. Schlegel, G. E. Scuseria, M. A. Robb, J. R. Cheeseman, G. Scalmani, V. Barone, B. Mennucci, G. A. Petersson, H. Nakatsuji, M. Caricato, X. Li, H. P. Hratchian, A. F. Izmaylov, J. Bloino, G. Zheng, J. L. Sonnenberg, M. Hada, M. Ehara, K. Toyota, R. Fukuda, J. Hasegawa, M. Ishida, T. Nakajima, Y. Honda, O. Kitao, H. Nakai, T. Vreven, J. J. A. Montgomery, J. E. Peralta, F. Ogliaro, M. Bearpark, J. J. Heyd, E. Brothers, K. N. Kudin, V. N. Staroverov, R. Kobayashi, J. Normand, K. Raghavachari, A. Rendell, J. C. Burant, S. S. Iyengar, J. Tomasi, M. Cossi, N. Rega, J. M. Millam, M. Klene, J. E. Knox, J. B. Cross, V. Bakken, C. Adamo, J. Jaramillo, R. Gomperts, R. E. Stratmann, O. Yazyev, A. J. Austin, R. Cammi, C. Pomelli, J. W. Ochterski, R. L. Martin, K. Morokuma, V. G. Zakrzewski, G. A. Voth, P. Salvador, J. J. Dannenberg, S. Dapprich, A. D. Daniels, Ö. Farkas, J. B. Foresman, J. V. Ortiz, J. Cioslowski and D. J. Fox, (Gaussian, Inc., Wallingford CT, 2009).
37. A. D. Becke, J. Chem. Phys. **98** (2), 1372-1377 (1993).
38. O. Christiansen, H. Koch and F. Jorgensen, J. Chem. Phys. **105** (4), 1451-1459 (1996).
39. R. Livingstone, O. Schalk, A. E. Boguslavskiy, G. Wu, L. T. Bergendahl, A. Stolow, M. J. Paterson and D. Townsend, J. Chem. Phys. **135** (19) (2011).
40. J. O. F. Thompson, R. A. Livingstone and D. Townsend, J. Chem. Phys. **139** (3), 034316 (2013).
41. U. Even, J. Jortner, D. Noy, N. Lavie and C. Cossart-Magos, J. Chem. Phys. **112** (18), 8068-8071 (2000).
42. V. G. Stavros and G. Costantini, (Warwick, 2015).
43. M. J. Tauber, R. A. Mathies, X. Y. Chen and S. E. Bradforth, Rev. Sci. Inst. **74** (11), 4958-4960 (2003).
44. Y. T. Cho and S. J. Na, Meas. Sci. Technol. **16** (3), 878-884 (2005).
45. Y. Yamada, N. Mikami and T. Ebata, J. Chem. Phys. **121** (23), 11530-11534 (2004).
46. T. Ebata, M. Kayano, S. Sato and N. Mikami, J. Phys. Chem. A. **105** (38), 8623-8628 (2001).
47. K. L. Reid, Annu. Rev. Phys. Chem. **54**, 397-424 (2003).
48. K. L. Reid, Mol. Phys. **110** (3), 131-147 (2012).
49. R. Hermann, G. R. Mahalaxmi, T. Jochum, S. Naumov and O. Brede, J. Phys. Chem. A. **106** (11), 2379-2389 (2002).
50. A. B. Berinstain, M. K. Whittlesey and J. C. Scaiano, in *Photochemistry of Lignocellulosic Materials*, edited by C. Heitner and J. C. Scaiano (1993), Vol. 531, pp. 111-121.
51. M. Shigematsu, T. Kobayashi and M. Tanahashi, Japan. Chem. Prog. Exc. **13**, 177 (2001).

52. M. A. Varfolomeev, D. I. Abaidullina, A. Z. Gainutdinova and B. N. Solomonov, Spectrochimica Acta Part a-Molecular and Biomolecular Spectroscopy **77** (5), 965-972 (2010).
53. S. J. Harris, D. Murdock, Y. Zhang, T. A. A. Oliver, M. P. Grubb, A. J. Orr-Ewing, G. M. Greetham, I. P. Clark, M. Towrie, S. E. Bradforth and M. N. R. Ashfold, Phys. Chem. Chem. Phys. **15** (18), 6567-6582 (2013).
54. S. J. Harris, D. Murdock, M. P. Grubb, G. M. Greetham, I. P. Clark, M. Towrie and M. N. R. Ashfold, Chem. Sci. **5** (2), 707-714 (2014).
55. D. Murdock, S. J. Harris, T. N. V. Karsili, G. M. Greetham, I. P. Clark, M. Towrie, A. J. Orr-Ewing and M. N. R. Ashfold, J. Phys. Chem. Lett. **3** (24), 3715-3720 (2012).

Chapter 6 – The excited state dynamics of simple aliphatic amines

6.1 – Introduction

This final results chapter will report work that is in a slightly different vein to that previously discussed. Instead of studying the interplay between the ππ* and 3s/πσ* states in heteroaromatic systems, this chapter will report work performed on simple aliphatic amines, and the interesting (and quite complex) dynamics that can occur in these molecules. This work was born out of collaboration with Theis Sølling's group in Copenhagen, Denmark.

Tertiary amines are useful model systems for studying the interactions between high-lying electronic states, and the interplay between molecular structure, electronic relaxation and fragmentation patterns when breaking covalent bonds in large polyatomic molecules. Simple amines provide models for the nitrogen chromophore centres in peptides, nucleotide bases and other naturally occurring systems. Broad absorption UV spectra of tertiary amines indicate that the dynamics in these systems happen on an ultrafast timescale,[1] making them ideal for femtosecond time-resolved studies. The excited states of amines are of the Rydberg type,[2] which has advantages for spectroscopic measurements, and also make them ideal for study. These ideas will be drawn upon heavily in both the theoretical and results sections of this chapter.

For longer-chain aliphatic amines, the main fragmentation pattern in mass spectrometry is α–cleavage, that is rupture of the first carbon-carbon bond from the amine group[3-5] (as identified in Figure 6.1). Over the last decade, considerable interest has been given to the study of structural influence on the photophysical properties of different amines, with a particular focus on tertiary species.[6-12] In most of these studies, the focus is on excitation to a higher-lying optically bright 3p Rydberg state and the subsequent relaxation dynamics evolving via non-adiabatic coupling to the lower-lying 3s state. It has been well documented since the 1970s that tertiary amines decay via fluorescence, typically quoted with a very high quantum yield.[1, 13, 14] However, based upon these previous studies, such as a report by Cureton *et al.*,[1] it appears that the overall fluorescence quantum yield of tertiary amine

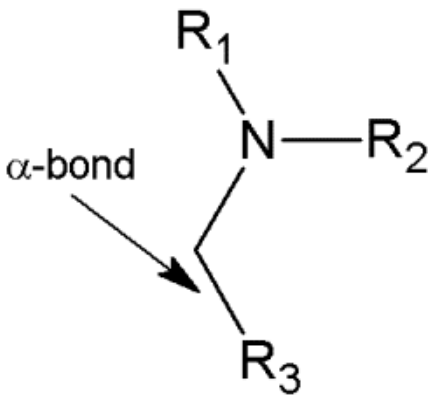

Figure 6.1 – Diagram depicting location of an "α bond" in α bond cleavage mechanisms

systems is highly wavelength dependent. In the study by Cureton *et al.*,[1] the three amines trimethylamine (TMA), trimethylamine (TEA) and tripropylamine (TPA) were investigated at a range of wavelengths. It was found that at higher pump energies, the fluorescence quantum yield and the lifetime of the systems fell dramatically. Following excitation at 220 nm, it was found in all cases that the overall fluorescence quantum yield was reduced to just 0.01. This would indicate that at higher energy pump wavelengths, additional decay pathways become available and eventually dominate the relaxation dynamics of these systems.

For the remainder of this section, a rigorous review of recent work on amine systems will be presented. As this review will encompass a number of molecular systems, for clarity, these are shown in Figure 6.2. Zewail and co-workers studied a large number of aliphatic amines using femtosecond time-resolved mass spectrometry (TR-MS) and found differences in the decay time constants and shapes of the ion transients, depending on the degree of alkylation.[7] The most remarkable difference was that the fragment ion transients of the primary amines were very similar to those of the parent

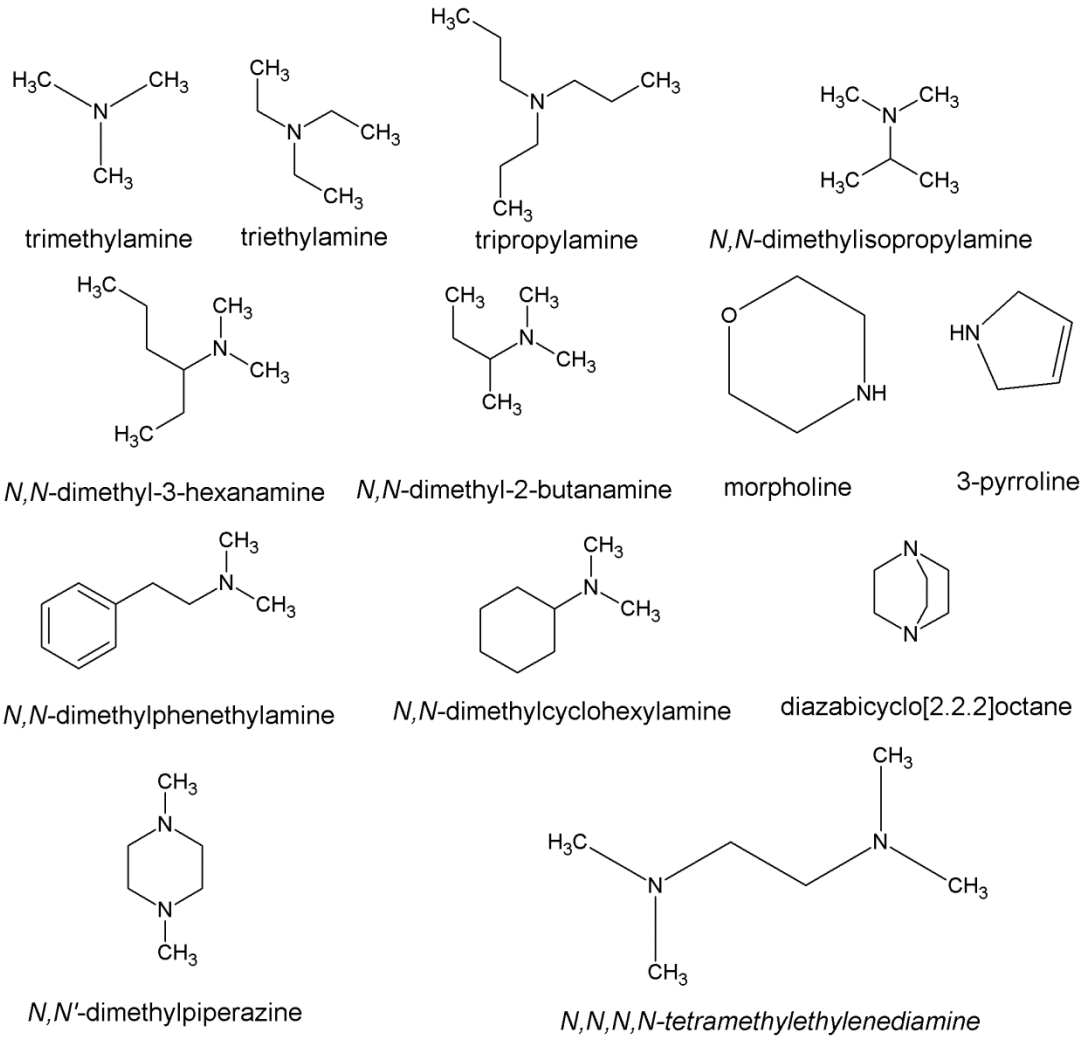

Figure 6.2 – Structures of amines reviewed in Section 6.1

ion and could be fitted with one time constant, whereas for the corresponding tertiary amines, the fits to the fragment ion currents needed an additional time constant.[7] This work used a total two-photon pump excitation energy around 8 eV, and as such, focussed on high-lying Rydberg states of the amines. The decay mechanism is proposed to be dissociation *on the excited state surface*, by an alpha cleavage mechanism.

Following this, Gosselin *et al*. studied the tertiary amine *N*,*N*-dimethylisopropylamine (DMIPA) (see Fig 6.2), a molecule that has been investigated in other studies,[7, 8] and concluded that the initially excited 3p Rydberg state decays into the lower 3s state by ultrafast internal conversion.[8] From the fragmentation pattern it was determined that, its dissociation occurs solely on the ionic surface. The reasoning put forwards is as follows; ionization out of the initially excited 3p state results in parent ions, whilst ionization after internal conversion (producing a more highly-vibrationally excited 3s state) gave rise to significant cation fragmentation due to the increase in vibrational energy in the prepared cation state[8]. A subsequent study (by the same group) has also investigated the photophysics of DMIPA under conditions where cluster formation is favoured. Photoelectron bands were broadened and shifted to lower binding energies. Changes observed in the dynamics were attributed to the significant lowering of the 3s Rydberg state energy, and fast proton transfer on the ion surface was also inferred.[12] Recently, Weber and co-workers have shown that the lifetime of the 3s state in DMIPA decreases exponentially with increasing amount of excess vibrational energy from the pump pulse,[15] which is in agreement with previous work[1, 13, 14].

Another tertiary amine, trimethylamine, was investigated by Cardoza *et al.*[10] This study postulated that electronic relaxation proceeded via internal conversion between the $3p_z$ state and the $3p_{x,y}$ states. It was concluded from this study that internal conversion within the P manifold occurred in 539 fs, from which subsequent internal conversion from the 3p states to 3s in 2.9 ps. Internal conversion between different states in the P Rydberg manifold was also found in triethylamine, on a slightly different timescale reflecting reorientation of the carbon chains, caused by the vibrational energy deposited in the 3s state by the 3p/3s internal conversion.[16] This is evidence of conformational dynamics occurring on a similar timescale as the non-adiabatic dynamics.

Additional evidence of conformational dynamics has been identified in *N*,*N*-dimethyl-2-butanamine (DM2BA) and *N*,*N*-dimethyl-3-hexanamine (DM3HA).[9] In contrast to triethylamine, for DM2BA and DM3HA only two conformers are involved, and these remain frozen in their room temperature distribution. Similarly, using H(Rydberg) atom

photofragment translational spectroscopy, excitation of both morpholine[17] and 3-pyrroline[18] have been shown to result in photofragments originating from both of the molecules' ground state chair conformers.

Conformeric structural dynamics have also been investigated in *N*,*N*-dimethylphenethylamine (PENNA), where the conformeric rearrangement over 5.3 ps is induced by interactions between the π-system and the cationic amine moiety.[11, 19] This is revealed by a rapid, non-exponential decay of the 3s state together with shifts of about 30 meV in the Rydberg binding energies. The similar *N*,*N*-dimethylcyclohexethylamine (CENNA), lacking the aromatic group, behaves much like other tertiary amines, simply decaying with a 913 fs time constant from 3p to a long lived 3s state.[11] For both PENNA and CENNA, an initial shift in the 3p state to higher Rydberg binding energies is ascribed to the planarization of the amine group that follows excitation to Rydberg states.

The effect of a second amino group in amine systems has also been investigated. In particular, the extremely constrained diazabicyclo[2.2.2]octane (DABCO) and related molecules have been the focus of many studies in order to investigate the interaction between the two lone pairs.[13, 20-22] Additional work on DABCO has also identified several conical intersections, which promote internal conversion between the excited Rydberg states.[22] In a recent study of the rigid *N*,*N'*-dimethylpiperazine (DMP), Cheng *et al.* found that internal conversion from the 3p state leads to several conformers where equilibrium is established in 2.65 ps.[23] The similar but more flexible *N*,*N*,*N*,*N*-tetramethylethylenediamine (TMEDA) shows a much faster equilibrium between folded and extended structural conformers in the excited state, possibly due to strong interaction between the Rydberg state's positively charged core interacting with lone pair on the other nitrogen.[24]

Recent results from TR-MS experiments on two series of amines with varying degrees of deuteration showed that the lifetime of the parent ion in both primary and tertiary species increases with increasing mass of the *N*-substituents.[25] This has been interpreted as an indication that amines, like ketones,[26-28] undergo non-ergodic internal conversion, i.e. the concept that the nuclear dynamics only sample a reduced phase space before internal conversion. This phenomenon has been observed in a number of different molecular systems,[29] and is also supported by the results from the diamine TMEDA.[24] However, the TR-MS experiments do not allow certain identification of the excited states involved, and so we seek to obtain further details of the photophysical processes by studying the ejected photoelectrons.

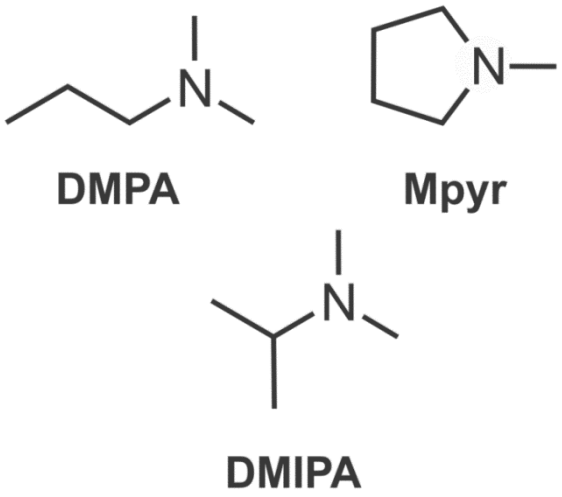

Figure 6.3 – Structures of *N*,*N*-dimethylisopropylamine (DMIPA), *N*,*N*-dimethylpropylamine (DMPA) and *N*-methylpyrrolidine (Mpyr)

As shown by all the aforementioned studies, work investigating relaxation pathways of these simple amines is quite extensive; however, no studies using photoelectron imaging have been performed on these systems. As such, this chapter will report an imaging study (that also incorporates an extensive quantity of complementary theoretical calculations) to investigate the interplay between the molecular structure and relaxation dynamics in tertiary systems. Specifically these are *N*,*N*-dimethylisopropylamine (DMIPA), *N*,*N*-dimethylpropylamine (DMPA) and *N*-methylpyrrolidine (Mpyr), all tertiary systems of the same size, but varying in structure i.e. branched, straight-chain or cyclic (see Figure 6.3). The goal is to investigate what influence, if any, constraints imposed by the structure of these systems can have on the dynamics of these simple systems.

6.2 – Experimental

With the exception of DMPA, the samples used in the present study were purchased from Sigma-Aldrich (both 99% purity). DMPA was synthesized by Theis Sølling's group through dimethylation of isopropylamine in a standard Eschweiler-Clarke reaction.[30, 31] Identity and purity was confirmed by ^{1}H-NMR. Prior to commencing collection of the time-resolved photoelectron data, preliminary UV/VIS vapour-phase spectra were obtained for all three molecules at room temperature using a commercial bench-top spectrophotometer (Camspec M550).

The experimental setup for time-resolved photoelectron imaging is discussed in great detail in Chapter 2 and in other work,[32] this section will now, therefore, discuss the specific details of the set-up considerations for the results presented in this chapter. In order to help eliminate the possibility of forming unwanted clusters, all samples were placed in an external bubbler maintained at 0 °C. Helium at a pressure of 1 bar was flowed through the liquid sample reservoir and then introduced into the source chamber of the differentially pumped photoelectron spectrometer via an Even-Lavie pulsed valve (150 μm nozzle diameter) operating at 1 kHz.[33] After travelling through a skimmer, the molecular beam passed into the main interaction chamber and was intersected at 90° by co-propagating UV pump and probe pulses. The pump beam (200 nm, attenuated to ~0.5 μJ/pulse) generated using beam line 3 and probe beam (267 nm, attenuated to ~2.0 μJ/pulse) generated using beam line 2 (bypassing the TOPAS) were provided by generating the fourth and third harmonics of this output, respectively. The pump and probe were combined on a thin dichroic mirror and focussed through a 2.0 mm thick CaF_2 window into the spectrometer using a 50 cm focal length UV-enhanced concave aluminium mirror.

The interaction between the UV light pulses and the molecular beam took place between the repeller and extractor electrodes of a magnetically shielded electrostatic lens set-up optimised for the velocity-map imaging of photoelectrons produced following [1+1′] ionization.[34] A 40 mm dual micro-channel plate/P47 phosphor screen detector was positioned at the end of the photoelectron flight tube and photoelectrons impacting on the detector were imaged using a CCD camera (640 × 480 pixel array). In order to reduce unwanted signal caused by the background scatter originating from the 200 nm pump light, the entrance and exit windows were deliberately positioned as far away from the interaction region as possible by extending side arms off the main vacuum chamber. In addition, small-aperture (2 mm diameter) conical "baffles" were

placed inside these arms as close to the interaction region as practically possible. Before commencing photoelectron acquisition for a given sample, the spectrometer was switched to ion detection mode. This allowed the opening duration and timing conditions of the pulsed valve to be adjusted to ensure that no significant cluster formation was observed in the molecular beam, as discussed in Chapter 2

Photoelectron data collection runs consisted of scanning the translation stage repeatedly between pump-probe delays of -500 fs to +1000 fs in 50 fs increments and then 19 exponentially increasing steps out to +100 ps (giving 50 time steps per data set in total). At each repeatedly sampled delay position, pump-probe photoelectron images were recorded for 150,000 laser shots, along with images of the time-invariant one-colour pump-alone and probe-alone signals (for subsequent background subtraction). Typical data accumulation runs for each molecule under study constituted approximately 30-50 scans. A pump-probe cross-correlation of 180 ± 20 fs was obtained directly inside the spectrometer from non-resonant, two-colour [1 + 1′] multiphoton ionization of butadiene. Energy calibration data was obtained from three-photon, non-resonant 267 nm ionisation of xenon and the central wavelengths of both the pump and probe beams were accurately monitored using a USB grating spectrometer.

6.3 – Theoretical

Supporting calculations for the three amine systems under study were performed using the Gaussian09 software suite[35] and Dalton2013[36] and visualised using the GaussView 5.0 program.[37] In this work Prof. Martin Paterson was responsible for the coupled cluster calculations, whilst I performed all other calculations presented in this section. In the first instance, each of the three amines were treated to a number of different coupled cluster methods to calculate the energies of the first four excited states. Initial ground state geometry optimisations were performed using density functional theory (B3LYP)[38] with a cc-pVTZ basis set. To calculate the vertical excited state energies, equation of motion coupled cluster theory including singles and doubles (EOM-CCSD)[39] with an aug-cc-pVDZ basis set and linear response coupled cluster theory including singles and doubles with triples corrections, using an aug-cc-pVDZ + (l_{max}=1, n=2-3.5) basis set, were both performed in Gaussian09. Additionally, coupled cluster calculations including singles and doubles with triples corrections were performed on Dalton2013 with both an aug-cc-pVDZ basis set and an aug-cc-pVDZ + (l_{max}=1, n=2-3.5) basis set. In all cases the excited state geometry was not relaxed and no additional corrections were applied. Table 6.1 shows the vertical excitation energies, oscillator strengths and assignments with each of the aforementioned methods. The standard

Table 6.1 - Calculated excitation energies and oscillator strengths for the three tertiary amines, calculated using A: CAM-B3LYP/aug-cc-pVDZ, B: CAM-B3LYP/aug-cc-pVTZ, C: EOM-CCSD/aug-cc-pVDZ, D: LR-CCSD/aug-cc-pVDZ + (l_{max}=1, n=2-3.5), E: CCSDR(3)/aug-cc-pVDZ & F: CCSDR(3)/aug-cc-pVDZ + (l_{max}=1, n=2-3.5). For further details, see main text

		A		B		C		D		E		F	
		***E*/eV**	***f***	***E*/eV**	***f***	***E*/eV**	***f***	***E*/eV**	***f***	***E*/eV**	***f***	***E*/eV**	***f***
DMIPA	3s←n	5.22	0.003	5.24	0.003	5.136	0.003	5.135	0.003	5.163	-	5.143	-
	$3p_x$←n	5.76	0.009	5.77	0.009	5.689	0.012	5.619	0.012	5.702	-	5.645	-
	$3p_z$←n	5.88	0.027	5.88	0.028	5.809	0.031	5.717	0.021	5.826	-	5.747	-
	$3p_y$←n	5.91	0.010	5.90	0.006	5.847	0.003	5.778	0.006	5.858	-	5.795	-
DMPA	3s←n	5.47	0.018	5.49	0.0170	5.435	0.012	5.407	0.017	-	-	5.415	-
	$3p_x$←n	6.00	0.004	6.00	0.004	5.968	0.011	5.895	0.072	-	-	5.924	-
	$3p_y$←n	6.06	0.101	6.05	0.092	5.988	0.093	5.910	0.100	-	-	5.931	-
	$3p_z$←n	6.10	0.008	6.10	0.008	6.114	0.013	6.066	0.010	-	-	6.071	-
Mpyr	3s←n	5.44	0.014	5.46	0.014	5.390	0.016	5.354	0.014	5.366	-	5.354	-
	$3p_y$←n	6.01	0.080	6.01	0.084	5.946	0.100	5.840	0.084	5.872	-	5.838	-
	$3p_z$←n	6.06	0.034	6.07	0.021	6.014	0.014	5.943	0.012	5.954	-	5.938	-
	$3p_x$←n	6.08	0.001	6.08	0.001	6.031	0.003	5.942	0.002	5.978	-	5.940	-

GaussView labelling conventions of the *x*, *y* and *z* axis were used in the assignment. Additionally, a series of CAM-B3LYP calculations were performed. From Table 6.1 it is clear to see that the density fucntional theory calculations produced qualitatively similar values for both the excitation energies and the oscillator strengths of the various excited states. This firmly established that for these systems CAM-B3LYP provides sufficient computational accuracy to use for discussion later in this chapter. As such, to save on computational expense, CAM-B3LYP will be used to further investigate the excited states of these systems.

The results of the six calculations are very consistent with one another, although the results for DMIPA are about 0.1 – 0.2 eV higher than those previously reported by Sølling *et al.*,[7] most likely due to the difference in the levels of theory used. The character of the excited state is generally mixed between several Rydberg type orbitals, but the main character is clearly identifiable and this forms the basis of the assignment given in Table 6.1. Mixed character of Rydberg states in amines have been reported before.[40] Other points of note in Table 6.1 are that the excitation energies for the tertiary DMPA and Mpyr systems are very similar, with those of DMIPA being somewhat lower. Additionally, all the oscillator strengths are rather low. This is typical for transitions involving states with predominantly Rydberg character, which are generally of weaker intensity than valence state transitions.[41] Ground state optimisations revealed a number of ground state conformers for each system. Calculations were performed to precisely predict the energies of these structures and characterise the population of these conformers in the molecular beam of the TR-PEI experiment. For all systems, initial conformer searches were performed in Gaussian using B3LYP with an aug-cc-pVDZ basis set. Following the identification of these structures, the geometries were optimized using second order Møller-Plesset perturbation theory (MP2)[42] with a aug-cc-pVTZ basis set. The results from these calculations show that it is very unlikely that multiple conformers will be present in the molecular beam due to the large separation < ~300 cm^{-1} in energy between the global minima and the next lowest energy conformer. These values are shown in Table 6.2

Table 6.2 – Energy difference in ground state minimum conformers. Values calculated with MP2/aug-cc-pVTZ level of theory. See text for more details

	DMIPA		DMPA			Mpyr	
	Con 1 (min)	Con 2	Con 1 (min)	Con 2	Con 3	Con 1	Con 2 (min)
Energy Difference (eV)	0	0.0250	0	0.1395	0.0538	0.1855	0

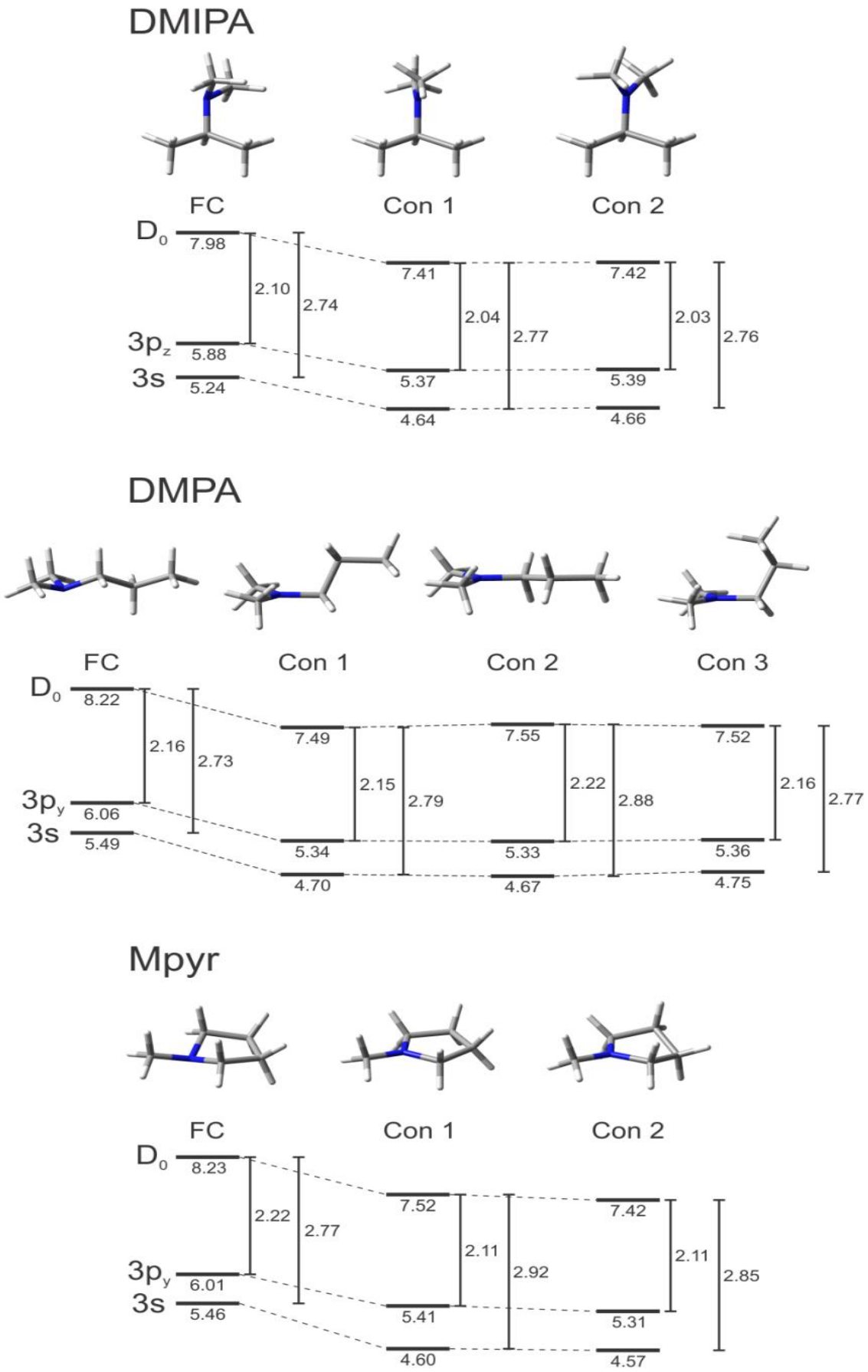

Figure 6.4 – Conformational energy relaxation for the three amine structures. Each diagram depicts the transition energies in both the Franck-Condon window and the two (or 3 for DMPA) excited state conformers along with the change in the relative transition from excited state to the cation. In each case only the optically active 3p state is shown and all transitions are quoted in eV.

Additional calculations were then performed to identify conformer geometries in the excited states of the three systems. To do so, initial geometries for the excited state conformers were generated on the ground electronic state of the cation (D_0) using unrestricted DFT (UB3LYP) in combination with an aug-cc-pVDZ basis set. This approach was utilised as the excited states identified in all three systems are Rydberg states. It therefore is valid to consider the geometry of the cation to be a good approximation for the geometry of the excited states. This method has been previously employed by Webber and co-workers in their study of trimethylamine.[43] The generated structures were then further optimised with unrestricted UCAM-B3LYP with an aug-cc-PVTZ basis set on the cation surface. Using this geometry, the energies of the first five excited states were calculated. The results of these calculations are shown in Figure 6.4. It should be noted that the transition energy of the excited states were all measured from the S_0 global minimum geometry. To test the validity of this method for producing adiabatic energies of the excited states, the geometry was subsequently optimised on the 3s excited state using CAM-B3LYP in conjunction with an aug-cc-pVTZ basis set for Mpyr in both its excited state conformers. The difference in energy was subsequently shown to be < 0.5% of the total excitation energy (~0.015 ±0.005). This showed that this method was appropriate for the arguments used in the discussion later in this chapter. To confirm that the energies calculated using CAM-B3LYP were valid, vertical CAM-B3LYP calculations using an aug-cc-pVTZ basis set were performed and compared to the previous coupled cluster calculations. These results are shown in Table 6.1 and in Fig 6.4. In all cases the CAM-B3LYP energies calculated were higher than those predicted by coupled cluster, however, considering the small increase of energy of ~0.06 eV, ~0.07 eV and ~0.03 eV for Mpyr, DMIPA and DMPA, respectively, the CAM-B3LYP energies are sufficiently reliable for the qualitative discussion in which they will be drawn upon.

Finally, to investigate the possibility of a dissociative relaxation channel, rigid potential energy cuts were generated using the S_1 minimum energy conformer of DMIPA along (a) the C-Me bond (corresponding to alpha cleavage, as shown in Figure 6.1), (b) the nitrogen-isopropyl group (N-iso) bond and (c) the nitrogen-methyl (N-Me) co-ordinate. These cuts are shown in Figure 6.5. In all cases there is a crossing between the dissociative state and the Rydberg states. It is also noted that the cuts along the N-Me and N-iso bond are fairly similar to each other in terms of the shape of the potential and the approximate location of the crossing point. However, a cut along the C-C α-cleavage co-ordinate is different to the other two cuts in that, upon inspection, the

potential energy surface of the 3p(x) Rydberg state along the C-Me co-ordinate evolves into this dissociative state. This is analagous to the 3s/πσ* states discussed in detail in Chapters 3 & 4.

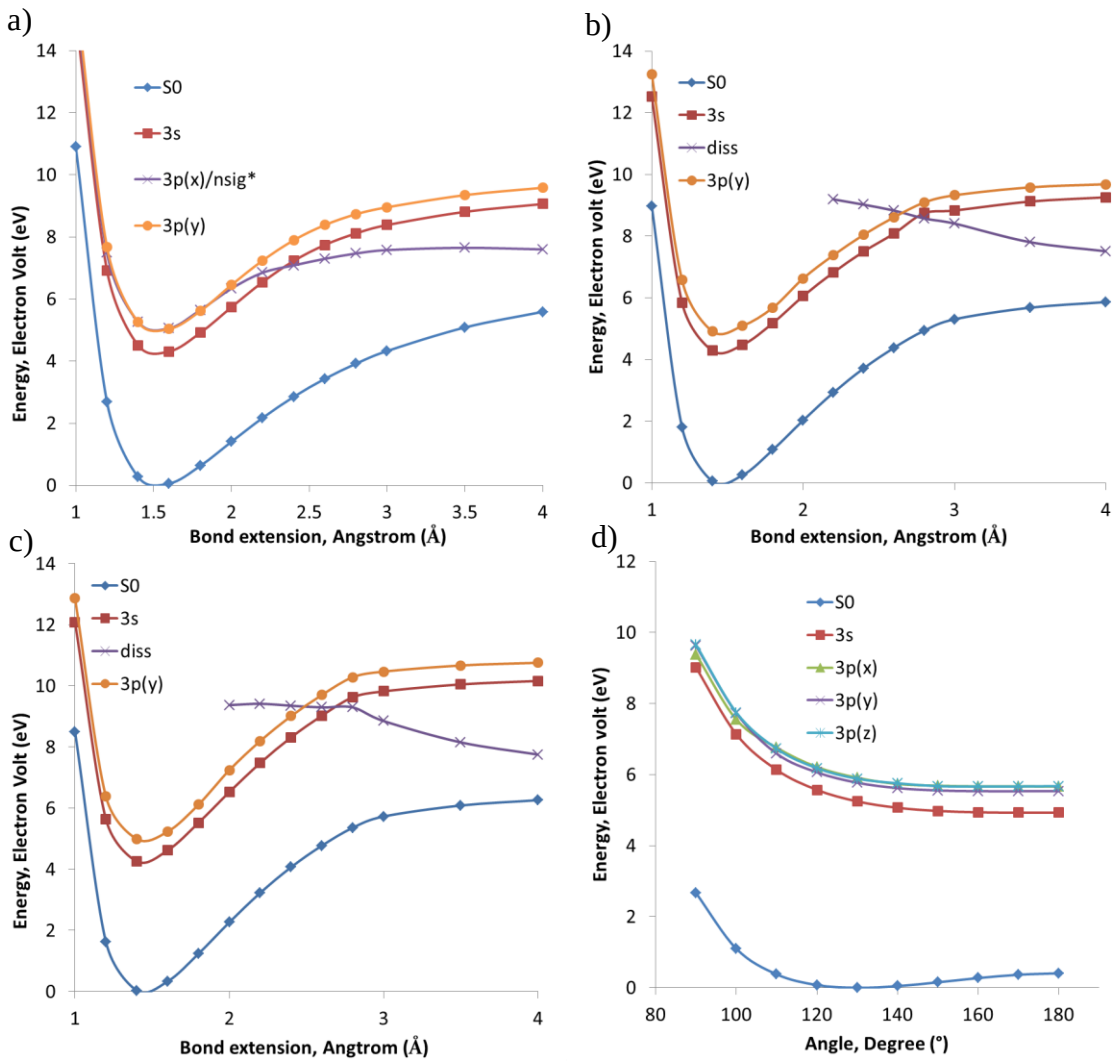

Figure 6.5 – Potential energy cuts of DMIPA using CAM-B3LYP/aug-cc-pVTZ along the C-C alpha co-ordinate (a), the N-Me co-ordinate (b), the N-iso co-ordinate (c) & along the planarization co-ordinate (d). See text for more details

6.4 – Results

6.4.1 - Vapour phase UV/VIS spectra

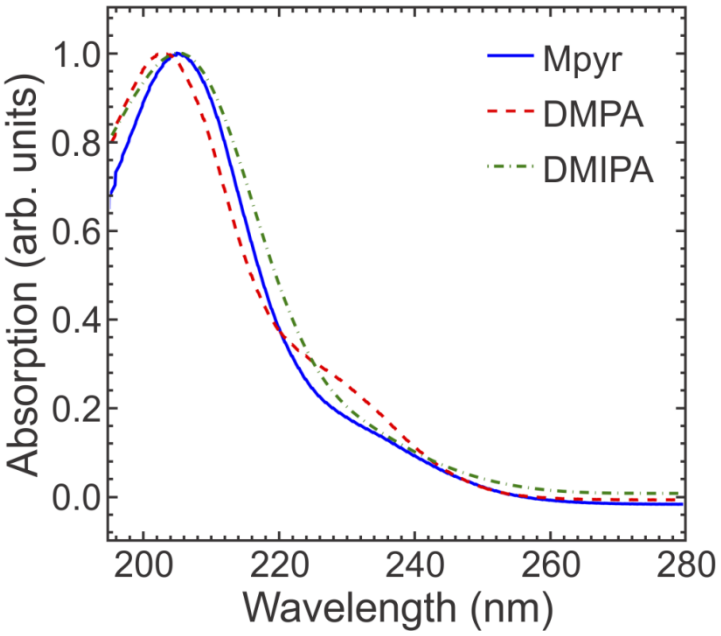

Figure 6.6 - UV/VIS vapour-phase absorption spectra of DMIPA, DMPA & Mpyr. The spectra have been normalized with respect to the most intense peak.

Preliminary UV/VIS vapour-phase spectra obtained for the three amines under study are displayed in Fig. 6.6. The spectra are very similar, showing an intense second absorption band around 204 nm and a weaker first absorption band as a shoulder at slightly longer wavelengths. The shoulder is more pronounced in DMPA than in the other two, but even here it is not possible to discern the position of the maximum. The close lying bands in tertiary amines have been observed previously for the smallest tertiary amines, trimethylamine and triethylamine.[44]

The weaker first and stronger second absorption band agrees with our calculated oscillator strengths, shown in Table 6.1. In general, the spectra are in good agreement with our theoretical results. In all of the three amines, the first band is assigned to 3s←n_N excitation, and the second band to 3p←n_N, in accordance with earlier spectral assignments for methylamine and ethylamine,[2, 40, 44-46] and our own calculations. On the basis of the spectra shown in Fig. 6.6, and given the pump wavelength of 200 nm used in the present study, we therefore assume that in all cases the initial excitation is predominantly 3p manifold, as has also been seen for DMIPA by Weber and co-workers.[8, 12, 15]

6.4.2 – Time resolved photoelectron spectra

Fig. 6.7 presents a series of photoelectron images resulting from [1 + 1′] ionization of the three amine systems at selected pump-probe time delays. In all cases, the pump only and probe only background signals were subtracted from the images and were 4-fold symmetrised. The right hand half of the image shows the raw image whilst the left hand half of each image shows the result following application of the rapid matrix

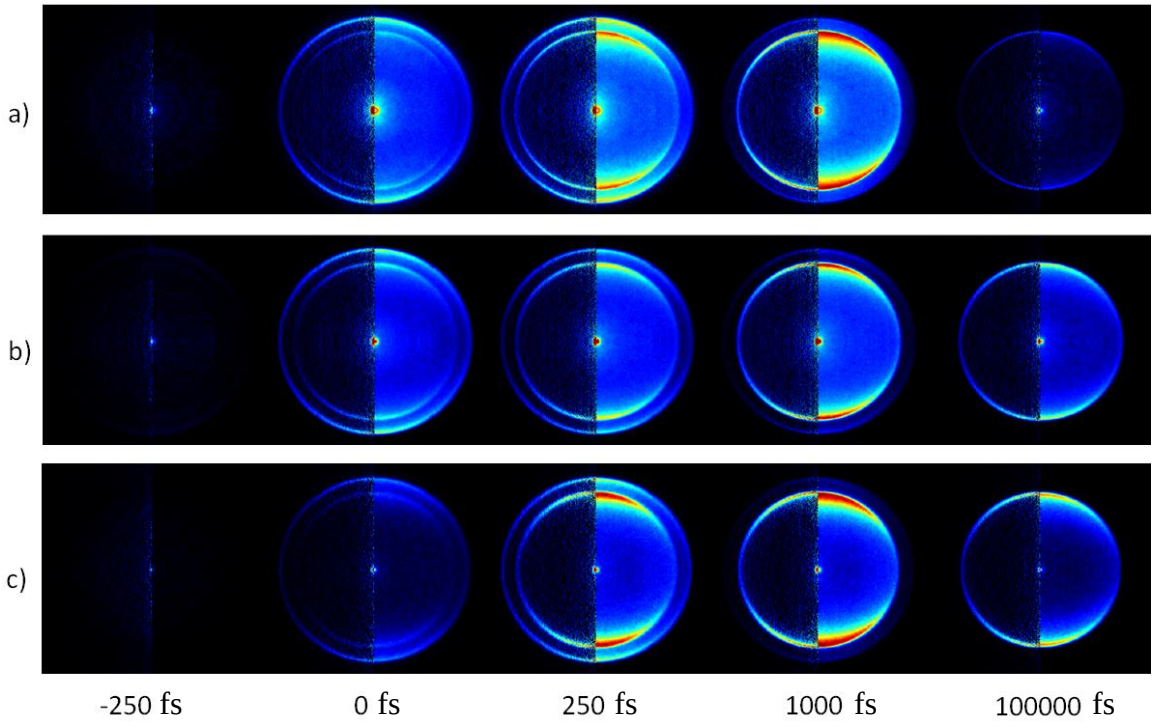

Figure 6.7 – Strip of 4-fold symmetrised photoelectron images of DMIPA, DMPA and Mpyr (a-c respectively) at pump-probe time delays of -250, 0, 250, 1000, 100000 fs. For illustrative purposes the right hand side of each image shows half the raw photoelectron image whilst the left hand side shows half the image after the matrix Abel transform has been performed. In all images the pump and probe background images have been subtracted. It should also be noted that the laser polarisation is vertical in each image.

inversion approach that has been described in detail elsewhere[32] and in Chapter 2. Of particular note is that all systems exhibit sharp ring features with significant anisotropy peaking along the direction of the pump and probe laser polarization.

Using appropriate time-of-flight to energy calibration data, time-resolved photoelectron spectra were generated from the full set of background-subtracted image data recorded for each amine system over the full range of pump-probe delay times. These plots are shown in Fig. 6.8 (note the mixed linear-logarithmic time axis). For ease of comparison with previously reported studies by Weber and co-workers on DMIPA,[8] the energy axes are plotted in terms of excited state binding energy, defined as the energy of the probe photon minus the kinetic energy of the ejected photoelectron[47] as shown in Eq. 6.1.

$$E_B = E_{hv(probe)} - E_{electron} \tag{6.1}$$

The total pump + probe energy used was 10.8 eV. From an initial inspection of the spectra recorded for the three amines, it is clear that all three molecules exhibit two, relatively narrow spectroscopic features in all cases; a rapidly decaying (< 1 ps) signal

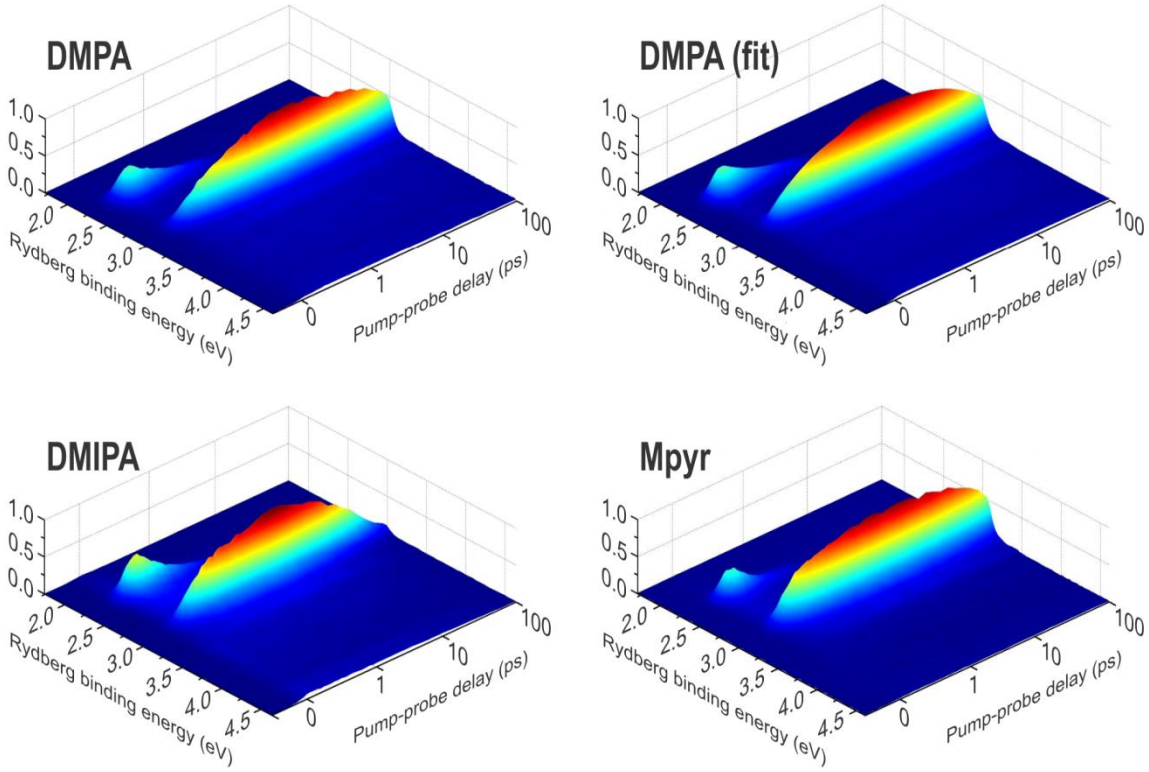

Figure 6.8 - 3D photoelectron spectra of the amines, including representative fits to the DMPA spectrum. The delay times are given on lin-log time scales, changing over at 1000 fs.

at ~2.3 eV, assigned as decay from the 3p manifold, and a signal at ~3.0 eV, assigned to subsequent population of the 3s state, that has a delayed onset from the zero pump-probe delay time. The subsequent decay of the 3s state occurs on an extended timescale and, in the case of DMIPA, this longer-time decay is noticeably faster than in DMPA or Mpyr.

Additionally, there is a more subtle feature in these spectra that cannot be clearly displayed in a normal linear intensity scale. As shown in Figure 6.10 there is a clear "bend" in some of the photoelectron signal at early time delays. In the case of DMIPA and DMPA, this bend is shown in the signal originating from the 3p manifold, whilst in Mpyr it is shown in the signal attributed to 3s. To further identify the magnitude of the bend, an inspection of the data was perfiormed to identify the average kinetic energy of each time step of the photoelectron data. It

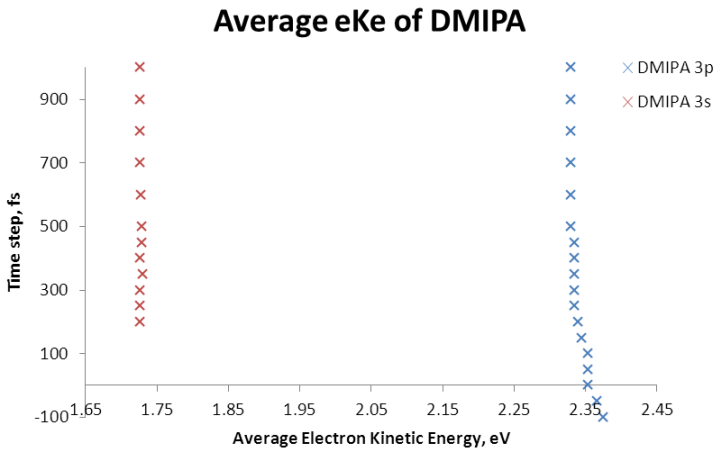

Figure 6.9 – Plot to show average electron kinetic energy as a function of time in DMIPA.

was found that in the positions identified by the arrows in Figure 6.10 the bend could be quantified as a movement of average kinetic energy of around 30 meV. An example of this trace is shown in Figure 6.9 for DMIPA.

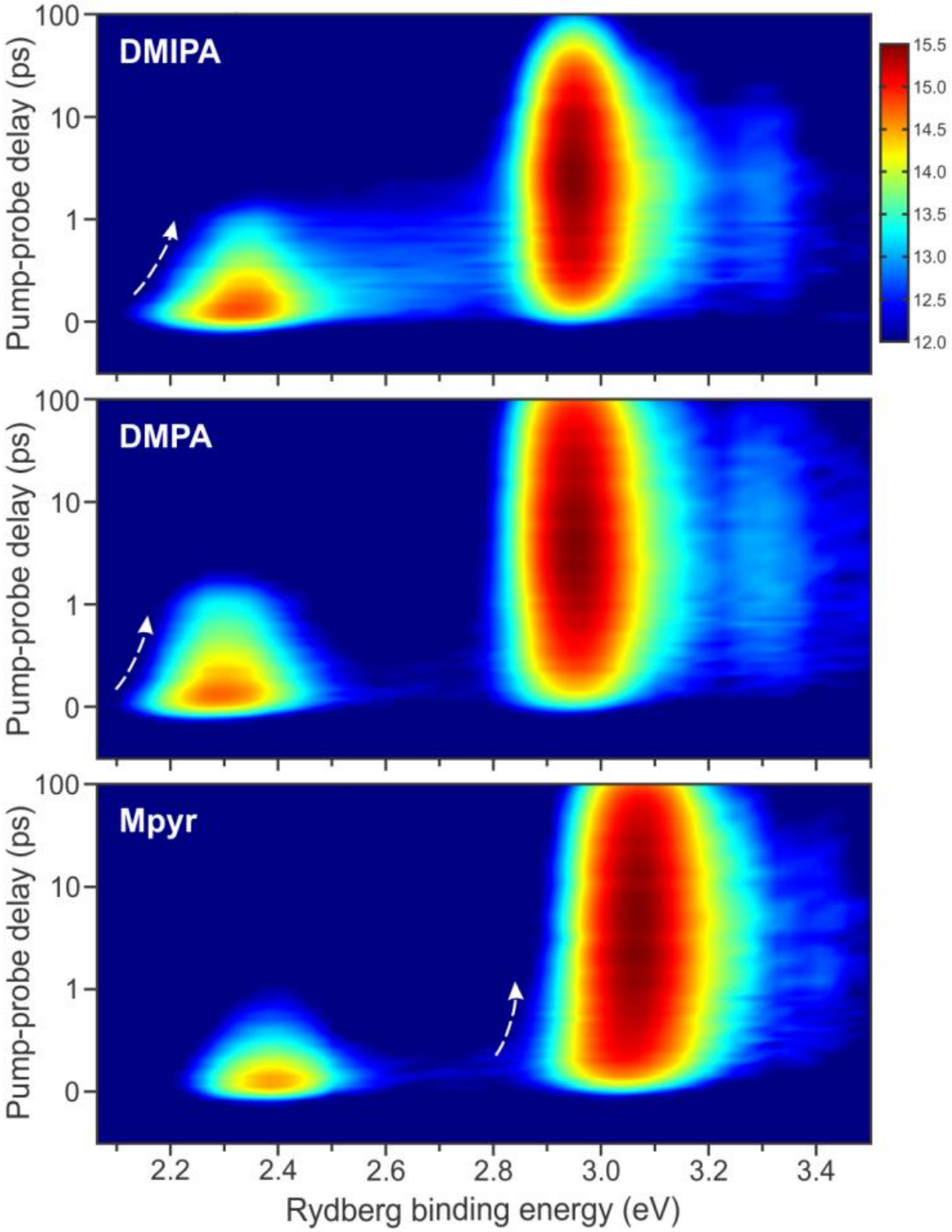

Figure 6.9 – 2D time resolved photoelectron spectra of the three amines. The time axis is shown in the same mixed lin/log scale as the previous figure and the Rydberg binding energy axis is also on the same scale. The intensity axis is plotted on a natural log scale of the raw data signal (as indicated by the colour bar on the top right of the figure). The arrows drawn on the figure indicate the site of the prevalent "bend" in the photoelectron spectra

6.4.3 – Decay associated Spectra

All three data sets were *sequentially* fitted using a standard Levenberg-Marquardt global fitting routine to analyse the time-dependence of the photoelectron data in detail. This method is somewhat different to the approach used in the previous three chapters (a full explanation of the difference between the sequential fit and the normal fit is provided in Chapter 2). However, this method was selected as the procedure utilised previously (in which all exponential functions are fitted from time zero in parallel) did not fit the data in a satisfactory manner. This was due to multiple processes occurring on similar timescales in the same region of the spectra, i.e. not sufficiently spectrally resolved from one another, such as the bending seen in the photoelectron spectra in Fig. 6.8. Here the 2D data $S(E, \Delta t)$ are expressed as:[48]

$$I(E,t) = \sum_{i=1}^{n} A_i(E)\left(e^{-\frac{t}{\tau_i}} \otimes r_i(t).cc(t)\right) \tag{6.2}$$

Where

$$r_i(t) = 1 - e^{-\frac{t}{\tau_j}} \tag{6.3}$$

In the above expression $A_i(E)$ is the decay associated photoelectron spectrum of the i^{th} data channel, which has a time dependent population $P_i(\Delta t)$. This is described by a series of exponentially decaying functions, all of which are taken to originate from the previous function in this case. The experimentally determined Gaussian cross-correlation function is denoted $cc(t)$ and $r_i(t)$ applies the offset to the i^{th} function with an exponential related to the j^{th} function, as discussed previously in Chapter 2. This approach constrains the possible values of $A_i(E)$ to positive values and as such was able to fit the data more adequately. This approach yields a series of decay associated spectra (DAS) that show the relative amplitude of each exponential component as a function of Rydberg binding energy. Figure 6.11 shows the DAS of the three amine systems. In all cases τ_1 has a large amplitude feature at around ~2.25 eV with a relative amplitude of ~0.5 at its maximum. As stated previously, this is assigned as signal arising from the 3p manifold. There is also an additional small amplitude feature at

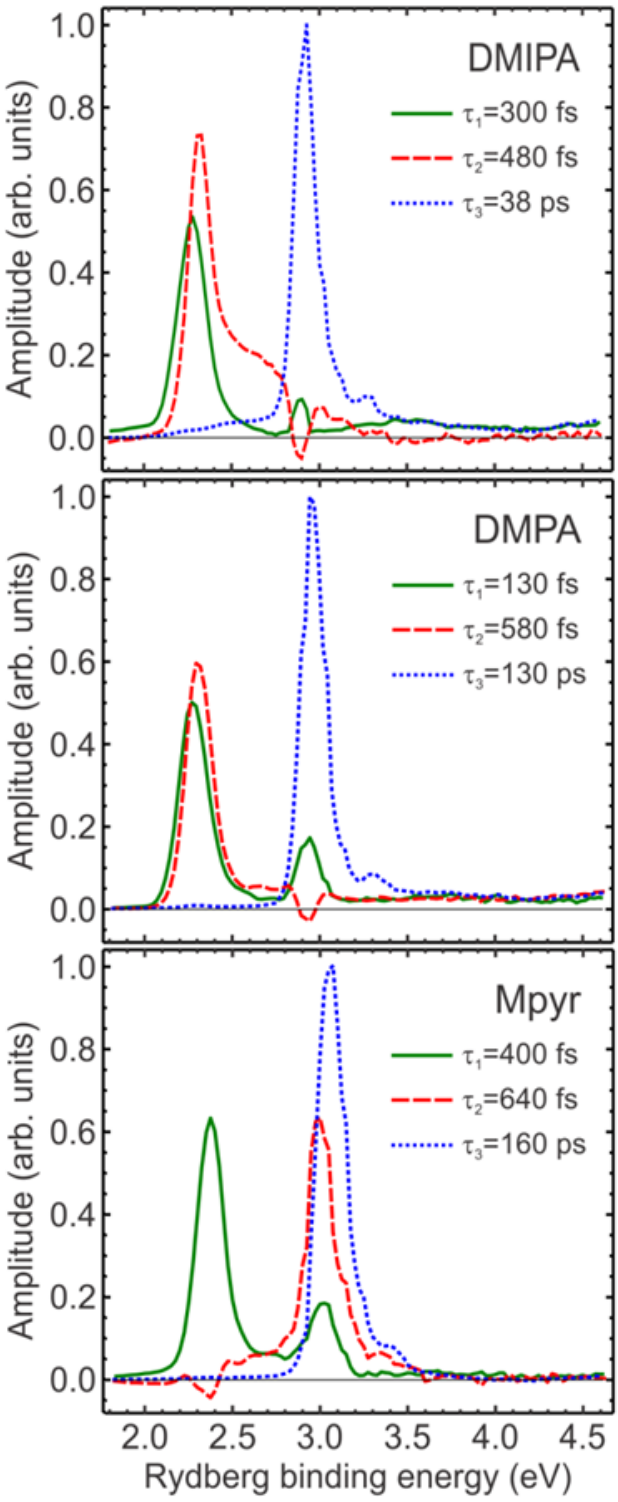

Figure 6.11 – Decay associated spectra of DMIPA, DMPA & Mpyr. The fits show the contributions of the different time constants. The vertical dashed line indicates the binding energy cut-off (where known). The quoted time-constants all have an uncertainty of ±10%.

~3.0 eV which is assigned as some initial excitation to the 3s state. The second time constant τ_2 is very similar in all cases in terms of its lifetime, with values of 0.48 ps, 0.64 ps and 0.58 ps for DMIPA, Mpyr and DMPA respectively. However, as shown in Figure 6.11, the position of the region of significant amplitude is different in Mpyr when compared to DMPA and DMIPA. In the case of DMPA and DMIPA, the feature is placed to slightly higher binding energy of the main τ_1 feature. In the case of Mpyr, the position of the feature is different, this feature is now located at slightly lower binding energy then the main τ_3 feature. Finally, the third time constant (τ_3) in all cases contains the largest amplitude, ~1.0, centred at around ~3.0 eV and, additionally, always had the longest life time (38 ps, 160 ps and 130 ps for DMIPA, Mpyr and DMPA respectively), as such, this is assigned as describing the ultimate decay of the 3s Rydberg state.

As stated above, we assign the features at ~2.3 and ~3.0 eV as signal resulting from the 3p manifold and 3s state respectively.

In further support of these assignments, the lifetime of the 3s state (corresponding to τ_2) has been shown to depend exponentially on the pump wavelength,[15] with the time constant for 202 nm of 39.5 ps being very close to the 38 ps we have obtained using 200 nm. Additional previously

reported time-resolved mass spectrometry measurements on DMIPA and DMPA using a 200 nm pump gave values of 619 fs and 739 fs, respectively, for the decay time-constant of the parent ion,[25] in good agreement with the current findings.

The ionization potentials of amines are relatively low, especially for tertiary systems. Previously reported vertical ionization potentials are 8.20 eV for DMIPA[49] and 8.41 eV for Mpyr,[50, 51] and these values may be used to predict binding energy cut-offs at about 2.1-2.2 eV for the tertiary amines. No ionization potentials could be found in the literature for DMPA, however, we might reasonably expect it to be very similar to (but possibly slightly larger than) that of DMIPA, as is the case when going from isopropylamine to propylamine.[52, 53] From the DAS plot in Fig. 6.10 we estimate the ionization potential of DMPA to be about 8.25 ± 0.05 eV from a binding energy cut-off at 2.05 eV, which indeed seems very close to the other amines.

6.4.4 – Photoelectron angular distributions

As previously stated, in the case of a two-photon ionization scheme using linear polarization, time-dependent PADs may be expressed as a function of the excited state electron binding energy E and the pump-probe delay time Δt in terms of the well-known anisotropy parameters β_2 and β_4:[54, 55]

$$I(E,t,\theta) \propto 1 + \beta_2(E,t)P_2(\theta) + \beta_4(E,t)P_4(\theta) \tag{6.3}$$

Fits to our data using Eq. 6.3, in which the anisotropy values (β_2 and β_4) are plotted as a function of both time (in a mixed linear and logarithmic axis) and energy (plotted in bins of 0.02 eV). From these fits, regions which contained significant photoelectron signal were averaged and plotted as a function against time. These are shown in Figure 6.12. In all three systems, the β_2 and β_4 values follow the same trend as each other. For the initially prepared 3p Rydberg manifold in all three molecules, both β_2 and β_4 start with large positive amplitudes which, as the state decays, lowers as a function of time. The most obvious change is shown in Mpyr with a drop from 1.4 to 1.0 in β_2 and a drop of 0.6 to 0.2 in β_4. Next, considering the trend in the 3s Rydberg states signal, in all cases there is a large drop in the first picosecond of the lifetime. By eye it can be shown that this decay occurs on a similar timescale to the decay of the anisotropy in the 3p manifold. In addition to the short time features in the traces, in the long time region there is a slow increase in both the β_2 and β_4 parameters starting from 10 ps in DMPA

and Mpyr and around 2 ps in DMIPA. The significance of both the initial fall in β_2 and β_4 and the long-time subsequent rise will be considered in detail in the next section.

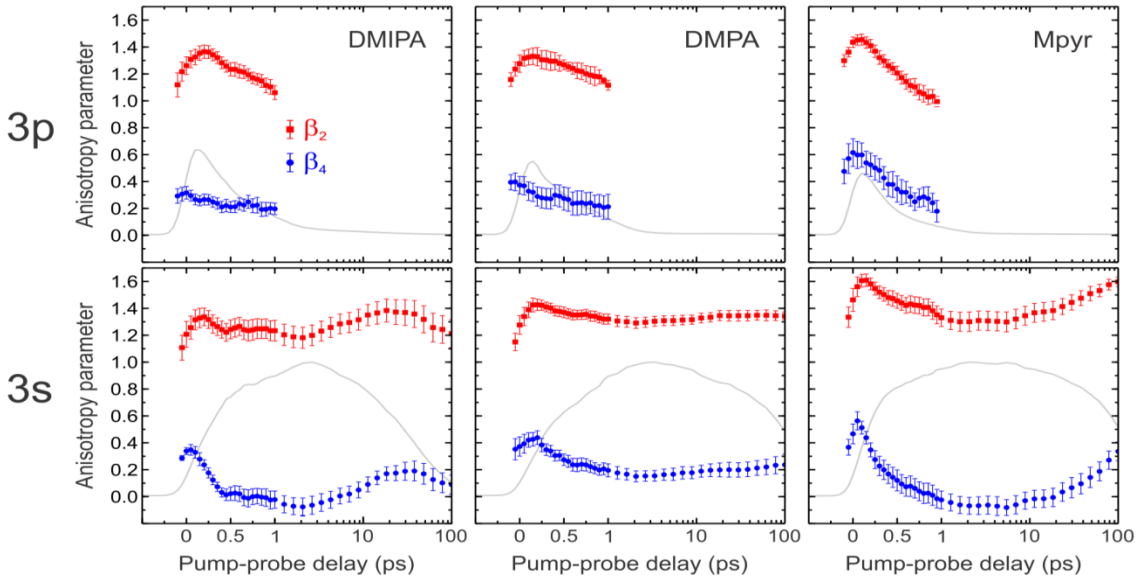

Figure 6.12 – Cut through traces of the normalised anisotropy parameters β_2 & β_4 as a function of time over the 3p and 3s regions of the photoelectron spectrums of all three amines. The time axis has been plotted on a mixed lin/log axis with the cross over point at 1 ps.

6.5 – Discussion

6.5.1 – Relaxation dynamics of the 3p manifold

The discussion begins with consideration of the photoelectron spectra presented in Figure 6.10, which looks similar in many respects to work reported previously.[8, 10] Both of the observed peaks in all three spectra are sharp, which is a reflection of the Rydberg nature of the corresponding excited states (i.e. a strong propensity for vertical ionization). As stated previously, the DAS peak at lower Rydberg binding energy, attributable to the initially prepared 3p manifold, which decays on a sub-picosecond timescale giving rise to the peak at higher Rydberg binding energies, which is assigned as signal arising the lower lying 3s state.

First considering the 3p manifold signal, it is clear from the shape and relative amplitudes of the DAS that DMPA and DMIPA behave very similarly to each other. From inspection of the photoelectron spectra (see Figure 6.9) it can be seen that there is a clear "bend" in the photoelectron signal in early time on the signal originating from the 3p manifold. It should be pointed out that the magnitude of the movement of the average kinetic energy is of the order of 30 meV which is at the resolution sensitivity limit of the VMI apparatus. As such, the τ_1 lifetime describes the bend in the photoelectron spectra in DMPA and DMIPA (with a decay time of 130 and 300 fs respectively).

It has been previously reported that this bend in the photoelectron signal can be the result of geometry relaxation[15, 16] or internal conversion within the P manifold.[10, 16] From the calculations presented in Section 6.3 it is clear to see that there are a number of conformers that can be accessed on the excited state surface. As shown in Figure 6.4, as conformational relaxation occurs the excited state and cation minimum energy lowers. Due to this evolution in the relative difference between the excited state and the cation minimum energy, the amount of energy imparted into the outgoing photoelectron changes. If the gap gets larger, the amount of energy removed by the photoelectron will be reduced, resulting in an increase in the observed photoelectron binding energy. In the case of DMIPA, the calculations would suggest that the bend would shift in the other direction then what is observed in the photoelectron data. However, in the case of DMPA, the calculations suggest that the conformational relaxation could account for the bend in the photoelectron spectrum.

In addition to predicting conformational relaxation, the calculations presented in Table 6.1 predict there is a lower lying 3p state below that of the optically bright state.

However, in DMPA the change in the local transition energy from the 3p state to the cation is small and suggests that a bend in the photoelectron signal would not be observed. Whilst in DMIPA, the change is large enough that it could potentially be observed. As such, we suggest that the bend in the photoelectron spectra is a result of *both or either* internal conversion within the P manifold and conformational relaxation on the excited state surface. In the case of Mpyr, there is no bend apparent within the 3p signal and as such τ_1 describes the decay of the initially excited 3p(y) state.

Next we will now consider the decay of the signal originating from the 3p manifold. In the Mpyr DAS there is only one exponential with amplitude in the 3p region of the spectrum (τ_1). Therefore we assign τ_1 to the decay of the 3p(y) state which takes place in 400 fs. In the case of DMPA and DMIPA, there are two exponentials with significant amplitude in the 3p region of the spectra (τ_1 & τ_2). As the τ_1 lifetime in DMPA and DMIPA has been assigned previously to the bend in the photoelectron spectra. The second decay (τ_2) is therefore assigned as the decay 3p manifold (after the motion assigned to τ_1) which takes place in 480 and 580 fs for DMIPA and DMPA respectively. As such, the overall decay time of the 3p manifold is given by τ_1 in Mpyr, and $\tau_1 + \tau_2$ in DMPA and DMIPA (as these are the only two time constants that have any meaningful amplitude in this region). Therefore the decay time of the 3p manifold is concluded to be 400 fs in Mpyr, 780 fs in DMIPA and 710 fs in DMPA. The decay process of the 3p manifold in all three systems is summarised in Figure 6.12. Additionally, for DMIPA, Weber and co-workers have previously reported values corresponding to $\tau_1 + \tau_2$ in our data of 701 fs using a pump wavelength of 208.5 nm[8]

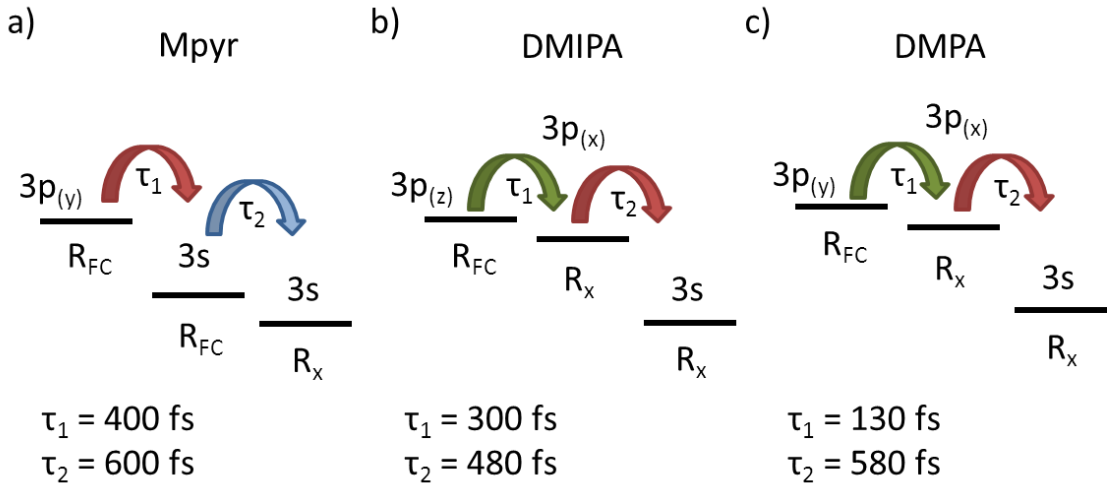

Figure 6.12 – The relaxation dynamics of Mpyr, DMIPA and DMPA (a-c). In each case R_{FC} represent the molecule in the initial Frack-Condon geometry whilst R_X indicates the molecule is in its excited state conformer(s). The red arrow indicates internal conversion between a 3p and 3s state, the blue arrow indicates conformation change on the 3s surface and the green arrow indicates some combination of conformational change and internal conversion between two 3p states. The time constants for each system is listed below each panel

which is in good agreement with our results. Based upon the DAS we postulate that the decay of the 3p manifold is driven by an internal conversion to the 3s state. This conclusion is also supported by the PADs. Upon examining Figure 6.11, each of the systems contain significant contribution from β_2 and β_4 to the total PADs, which is not unsurprising, when considering that the ionised photoelectron from the initial 3p Rydberg state should be described by a set of partial waves with significant amplitude in both s and d (as *l* must change by ±1), but, based upon this assumption, no significant β_4 would be expected in the 3s signal. However, the contribution of β_4 in the 3s state can best be explained by the following. As argued by ourselves previously[32, 56] and by others[57-59] and in previous chapters, that when two states are coupled together their respective electronic character mix. As such, based upon these arguments it is concluded that the initial early time rise and fall in β_2 and β_4 amplitudes is due to state mixing between the initially excited 3p state and the 3s state. This ties in well with the internal conversion mechanism between the 3p and 3s states. However, the PADs do not reveal any additional insights into the 3p/3p coupling in DMPA and DMIPA, which is most likely due to the partial wave expansion of the electrons ionised from these two states being very similar.

6.5.2 – Relaxation dynamics of the 3s state

In DMPA and DMIPA the decay of the 3s state is described by a single decay process (τ_3), whilst in Mpyr there are two features in this region of the DAS. The decay feature with a time constant, τ_2, in Mpyr is assigned as describing the bend in the 3s photoelectron spectrum, with a life time of 640 fs. As the bend in the 3s signal it can only be attributed to the conformational relaxation on the 3s excited state surface. This is based upon the arguments presented previously regarding the conformational relaxation on the 3p state. The calculation results presented in Figure 6.4 support the assignment of τ_2 in Mpyr. Finally, in all three systems, the third decay time (τ_3) is assigned to the decay of the 3s state, which is found to be 38 ps, 130 ps & 160 ps for DMIPA, DMPA and Mpyr respectively.

This observation of the difference in lifetimes of the 3s state can be explained through the calculations presented in Table 6.1. By inspection of the average energy gaps ΔE (taken from the two levels of theory used) between the 3s state and the 3p state carrying most oscillator strength in each case, the difference is found to be significantly larger for DMIPA (1.11 eV) than for DMPA (0.93) and Mpyr (0.89). After internal conversion from 3p to 3s, DMIPA will therefore possess a higher level of vibrational excitation

than the other tertiary amines. For DMIPA, Weber has demonstrated an exponential decrease in 3s lifetime with increasing excess vibrational energy resulting from different pump wavelengths,[15] and our value of 38 ps for DMIPA when using a 200 nm pump photon fits perfectly with this observed trend. The longer 3s lifetimes of DMPA and Mpyr is explained in the same way; less excess vibrational energy results in longest 3s lifetime. In additional support to the arguments presented above, the dependency of both radiative and non-radiative rate constants on excess energy has been established for a number of systems. Examples of this include a decrease of fluorescence lifetime with increasing vibrational energy in small alkoxy radicals[60] and some aromatic systems,[61] with relations also observed for naphthalene vapour,[62] SO_2,[63] N_2,[64] and various benzenes.[65, 66] Based upon the previously cited work investigating the fluorescence quantum yield of similar systems,[1, 13, 14] it would seem unlikely that this process is contributing the most to the overall decay of the 3s state in these systems. This would imply that an additional process is occurring. On the basis of El-Sayad's rules[67] and the lack of additional features in the photoelectron spectrum, it would seem unlikely that this is due to an intersystem crossing to a triplet state, in agreement with other work.[25] It is at this point we will now consider the information provided by the time-resolved photoelectron angular distribution of these systems.

The PADs reveal an extra feature in the long time region of the data that is not present in the DAS of the three systems. In all three cases there is a relatively long time rise in both β_2 and β_4. Now considering that the molecules are now in a state that is predominantly 3s Rydberg in character, it would seem unlikely that this is due to some geometry change not seen in the PES, and must be in fact due to some additional non-adiabatic coupling process. As stated previously, on the basis of El-Sayad's rules,[67] it seems reasonable to conclude that this change is not due to some intersystem crossing to a triplet state. As such, we suggest that the state coupling to the 3s Rydberg state must be a singlet state. However, location of conical intersections in amine systems is a point of contention in the literature. Many articles have stipulated that the critical mode to access these conical intersections is planarization around the nitrogen.[7, 8, 15, 16, 25] However, only in the work by Zewail and co-workers is a PES along this co-ordinate shown[7] and, much like the surface calculated in Figure 6.5d, there is no evidence of any crossing of the potential energy surfaces. As such, we must draw the conclusion that planarization is not a critical co-ordinate in accessing the conical intersections of these systems. Nevertheless, the calculations provided some insight into a possible co-

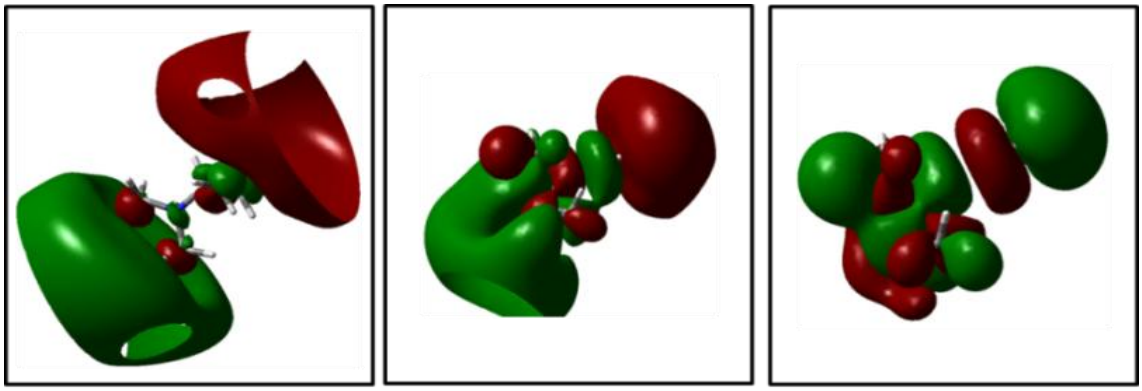

Figure 6.13 – Snap shots of the MO character of the 3p(x) state as it evolves into the dissociative σ* corresponding to α-cleavage. The image at 1.6 Å represent the orbital in region near to the 3s Rydberg minima whilst 2.4 Å shows the 3p(x) orbital at the 3s/3p(x)σ* conical intersection and the MO at 3.0 Å is the pure dissociative σ* orbital

ordinate that could allow the internal conversion to occur, which will now be elaborated on.

As shown in Figure 6.5a-c, cuts along dissociative coordinates (N-C in Fig. 6.5a & b, C-C in Fig. 6.5c) have provided evidence of the existence of conical intersections in the molecule DMIPA. On the basis of these calculations, the dissociative state along the C-C stretch (corresponding to α-cleavage) would seem to be the active pathway for dissociation, in agreement with as Zewail and co-workers[7] and Weber and co-workers[8] in similar molecules. In addition to the supporting evidence from Zewail and co-workers,[7] investigating the character of the 3p(x) molecular orbital (MO) as a function of α-cleavage C-C bond distance finds that the 3p(x) MO evolves into the dissociative α-cleavage C-C σ* orbital, as shown in Figure 6.13. This is analogous to that seen in the 3s/πσ* which is discussed in great detail in Chapter 4 in regards to aniline. As such, this state may be considered as a 3p(x)/nσ* state. Based upon this, it is concluded that in the long time region, non-adiabatic coupling between the 3s state and the 3p(x)/nσ* state is active, providing a route for relaxation via dissociation. This conclusion is supported experimentally by the evolution of both β_2 and β_4 which is of direct consequence to the progression of the non-adiabatic coupling between the 3s Rydberg state and the 3p(x)/nσ* state. Above the conical intersection (which based upon the DFT potential energy surface) is predicted to be somewhere around 7 eV, then dissociation could occur rapidly, which ties into the fast dissociation reported by Zewail and co-workers.[7] However, even though the wavelength used to excite the three systems in the experiments reported in this chapter (200 nm) lies below the predicted conical intersection, it is clear that this relaxation pathway is active due to the change in

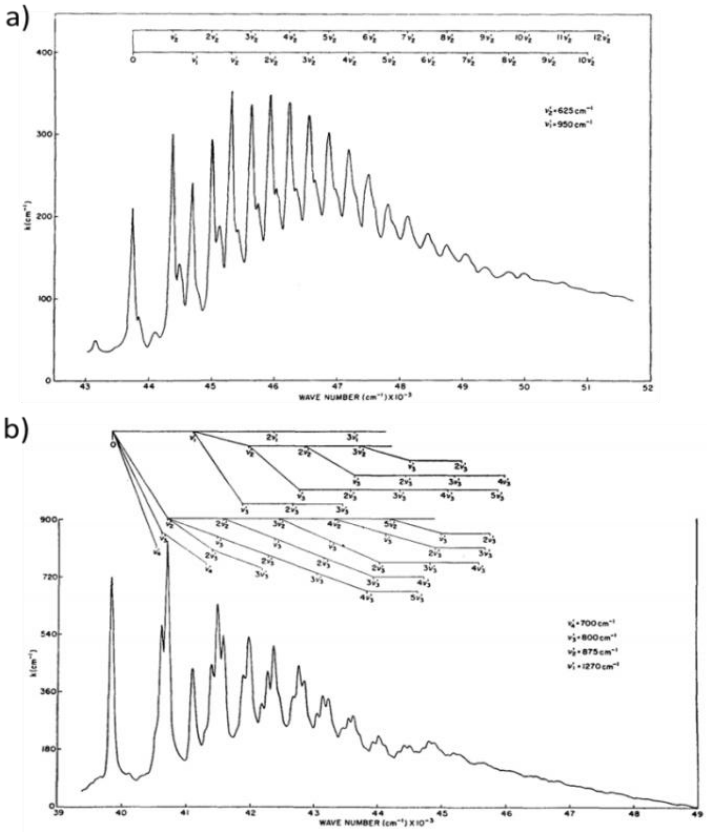

Figure 6.14 – High resolution vapour phase spectra of ABCO (a) and DABCO (B) taken from ref [72]

the PADs. As to why this is, and the time required to access the conical intersection is somewhat of an open question which we will try to address.

On the basis of the large amount of vibrational energy in the 3s state it would seem unlikely that this delay is due to some slow IVR interaction as the IVR occurring on the 3s state would occur very rapidly, applying a density of states arguement.[68, 69] Therefore, a possible reason suggested for this apparent delay in the rise of the β_2 and β_4 parameters is that the non-adiabatic coupling between the 3s Rydberg state and the 3p(x)/nσ* is slow, most likely due to the region of the surface in which the coupling is turned on is difficult to access, and as such, the time scale on which the change in the overall electronic character of the state is also long.

In addition to the evidence based upon the C-C bond stretch co-ordinate, we also propose that the other co-ordinate to bring the system to degeneracy is in fact the waggling mode around the nitrogen, but not for the planarisation as inferred by others.[7, 8, 15, 16, 25] To rationalise this, consider DABCO, a caged tertiary amine system has been studied by a number of groups in recent years.[13, 20-22] Work by Stolow and co-workers[22] have shown that the critical co-ordinates in reaching the conical intersection between the 3p and 3s states in DABCO are a combination of the umbrella mode on the nitrogen, the N-C stretching mode and a C-C stretching mode. Due to the similarities reported by all tertiary amine systems, we suggest that this system illustrates that the planarization of the system cannot be critical as the cage structure of DABCO prohibits the system from achieving planarity, rather it is the umbrella motion that is important. However, for this argument to hold we must verify that the double amine structure is not influencing this mechanism. Therefore, we will now consider the molecule ABCO (the

single amino group equivalent of DABCO). Weiss and co-workers[70] recorded high resolution vapour spectra of both DABCO and ABCO, as shown in Figure 6.14 in which both of the spectra are able to resolve the vibrational structure of the electronic states. Based upon the work by Stolow and co-workers[22] it is shown that the lifetime of the 3p state is short, much like in the results reported in this chapter. Considering the line widths in the DABCO spectrum by Weiss and co-workers[70], the lines are reasonably broad, in the region of ~150 cm^{-1}, which based upon arguments presented in Chapter 3, would imply that the state is very short lived. This would seem to be in qualitative agreement with the time resolved measurement. Now comparing the ABCO spectrum to the DABCO spectrum, it is clear that the line widths of the vibrational structure on in both spectra are very similar. Therefore, ABCO would be expected to behave in a similar manor. This verifies that using DABCO to illustrate the potential motions required to bring the 3p and 3s states to degeneracy is meaningful, but, additional computational and time-resolved photoelectron imaging are needed to fully explore this conclusion. Nevertheless, the insight gained by the PADs into the decay pathways of these simple tertiary amine systems has proven to be invaluable into understanding the dynamics of these systems.

6.6 – Conclusion

Using a state of the art VMI spectrometer, a series of three small aliphatic tertiary amines with approximately the same molecular formula have been studied in order to investigate the effects of structure on the photo-physics. Following excitation with 200 nm light, DMIPA and DMPA were prepared primarily in the optically bright 3p Rydberg state which decays on an ultrafast timescale followed to a lower energy 3p state by internal conversion, with additional to a conformational changes occurring simultaneous, which then finally relaxation to the 3s Rydberg state by internal conversion. For Mpyr the story is a little different, with the initially prepared 3p state undergoing electronic relaxation directly to the 3s state on a faster timescale than the geometry relaxation of the system.

In all three cases, the data suggests that fluorescence is not the major decay mechanism of the 3s state and, based upon the agreements set in this chapter; suggest that dissociation along the α-cleavage bond is the major dynamical pathway for relaxation. This is justified by a combination of additional information provided by investigating the photoelectron angular distributions (PADs), in-depth theoretical calculations alongside arguments drawn from a large number of sources from the literature. From these arguments it is suggested that the decay of the 3s state is promoted via non-adiabatic coupling to a 3p(x)/nσ* state.

This chapter has highlighted the additional benefits of imaging over other photoelectron spectroscopic techniques as the additional information gained from the investigation of the PADs has proven to be invaluable and provided further insight into the dynamics of these systems.

Following on from this chapter, this thesis will now move on to Chapter 7, in which, some potential ideas for future work and instrumental methods that could be employed to further the understanding of the work detailed in this thesis are presented.

6.7 - References

1. C. G. Cureton, K. Hara, D. V. O'Connor and D. Phillips, Chem. Phys. **63**, 31-49 (1981).
2. M. B. Robin, *Higher Excited States of Polyatomic Molecules I*. (Academic Press, New York, 1974).
3. R. S. Gohlke and F. W. McLafferty, Anal. Chem. **34**, 1281-1287 (1962).
4. S. Hammerum, Tetahedron Lett. **22**, 157-160 (1981).
5. R. D. Bowen and A. Maccoll, Org. Mass. Spectrom. **20**, 331-335 (1985).
6. J. E. Mathis and R. N. Compton, J. Chem. Phys. **104**, 8341-8347 (1996).
7. T. I. Sølling, C. Kötting and A. H. Zewail, J. Phys. Chem. A **107**, 10872 (2003).
8. J. L. Gosselin, M. P. Minitti, F. M. Rudakov, T. I. Sølling and P. M. Weber, J. Phys. Chem. A **110**, 4251 (2006).
9. M. P. Minitti and P. M. Weber, Phys. Rev. Lett. **98**, 253004 (2007).
10. J. D. Cardoza, F. M. Rudakov and P. M. Weber, J. Phys. Chem. A **112**, 10736 (2008).
11. J. C. Bush, M. P. Minitti and P. M. Weber, J. Phys. Chem. A **114**, 11078-11084 (2010).
12. S. Deb, M. P. Minitti and P. M. Weber, J. Chem. Phys. **135**, 044319 (2011).
13. A. M. Halpern and T. Gartman, J. Am. Chem. Soc **96** (1393-1398), 1393 (1974).
14. C. G. Freeman, M. J. McEwan, R. F. C. Claridge and L. F. Phillips, Chem. Phys. Lett. **8** (1), 77-78 (1971).
15. F. Rudakov, Y. Zhang, X. Cheng and P. M. Weber, Opt. Lett. **38** (21), 4445-4448 (2013).
16. S. Deb, B. A. Bayes, M. P. Minitti and P. M. Weber, J. Phys. Chem. A **115**, 1804-1809 (2011).
17. T. A. A. Oliver, G. A. King and M. N. R. Ashfold, Chem. Sci. **1**, 89-96 (2010).
18. T. A. A. Oliver, G. A. King and M. N. R. Ashfold, J. Chem. Phys. **133**, 194303 (2010).
19. J. C. Bush, M. P. Minitti and P. M. Weber, J. Photochem. Photobiol. A **213**, 70-72 (2010).
20. E. Heilbronner and K. A. Muszkat, J. Am. Chem. Soc **92**, 3818-3821 (1970).
21. A. M. Halpern and A. Taaghol, J. Phys. Chem. **93**, 144-149 (1989).
22. A. E. Boguslavskiy, M. S. Schuurman, D. Townsend and A. Stolow, Faraday Discuss. **150**, 419-438 (2011).
23. S. Deb, X. Cheng and P. M. Weber, J. Phys. Chem. Lett. **4**, 2780-2784 (2014).
24. X. Cheng, Y. Zhang, S. Deb, M. P. Minitti, Y. Gao, H. Jónsson and P. M. Weber, Chem. Sci. **5**, 4394-4403 (2014).
25. L. B. Klein and T. I. Sølling, Chem. Phys. **442**, 62-67 (2014).
26. E. W. G. Diau, J. Herek, Z. H. Kim and A. H. Zewail, Science **279**, 847-851 (1998).
27. T. S. Kuhlman, T. I. Sølling and K. B. Møller, ChemPhysChem **13**, 820-827 (2012).
28. T. S. Kuhlman, M. Pittelkow, T. I. Sølling and K. B. Møller, Angew. Chem. Int. Ed. **52**, 2247-2250 (2013).
29. T. I. Sølling, T. S. Kuhlman, A. B. Stephansen, L. B. Klein and K. B. Møller, ChemPhysChem **15**, 249-259 (2014).
30. W. Eschweiler, Ber. Dtsch. Chem. Ges. **38**, 880-882 (1905).
31. H. T. Clarke, H. B. Gillespie and S. Z. Weisshaus, J. Am. Chem. Soc. **55**, 4571-4587 (1933).
32. R. A. Livingstone, J. O. F. Thompson, M. Iljina, R. J. Donaldson, B. Sussman, M. J. Paterson and D. Townsend, J. Chem. Phys. **137**, 184304-184317 (2012).

33. U. Even, J. Jortner, D. Noy, N. Lavie and C. Cossart-Magos, J. Chem. Phys. **112**, 8068-8071 (2000).
34. A. T. J. B. Eppink and D. H. Parker, Rev. Sci. Instrum. **68**, 3477 (1997).
35. M. J. Frisch, G. W. Trucks, H. B. Schlegel, G. E. Scuseria, M. A. Robb, J. R. Cheeseman, G. Scalmani, V. Barone, B. Mennucci, G. A. Petersson, H. Nakatsuji, M. Caricato, X. Li, H. P. Hratchian, A. F. Izmaylov, J. Bloino, G. Zheng, J. L. Sonnenberg, M. Hada, M. Ehara, K. Toyota, R. Fukuda, J. Hasegawa, M. Ishida, T. Nakajima, Y. Honda, O. Kitao, H. Nakai, T. Vreven, J. J. A. Montgomery, J. E. Peralta, F. Ogliaro, M. Bearpark, J. J. Heyd, E. Brothers, K. N. Kudin, V. N. Staroverov, R. Kobayashi, J. Normand, K. Raghavachari, A. Rendell, J. C. Burant, S. S. Iyengar, J. Tomasi, M. Cossi, N. Rega, J. M. Millam, M. Klene, J. E. Knox, J. B. Cross, V. Bakken, C. Adamo, J. Jaramillo, R. Gomperts, R. E. Stratmann, O. Yazyev, A. J. Austin, R. Cammi, C. Pomelli, J. W. Ochterski, R. L. Martin, K. Morokuma, V. G. Zakrzewski, G. A. Voth, P. Salvador, J. J. Dannenberg, S. Dapprich, A. D. Daniels, Ö. Farkas, J. B. Foresman, J. V. Ortiz, J. Cioslowski and D. J. Fox, (Gaussian, Inc., Wallingford CT, 2009).
36. K. Aidas, C. Angeli, K. L. Bak, V. Bakken, R. Bast, L. Boman, O. Christiansen, R. Cimiraglia, S. Coriani, P. Dahle, E. K. Dalskov, U. Ekström, T. Enevoldsen, J. J. Eriksen, P. Ettenhuber, B. Fernández, L. Ferrighi, H. Fliegl, L. Frediani, K. Hald, A. Halkier, C. Hättig, H. Heiberg, T. Helgaker, A. C. Hennum, H. Hettema, E. Hjertenæs, S. Høst, I.-M. Høyvik, M. F. Iozzi, B. Jansik, H. J. A. Jensen, D. Jonsson, P. Jørgensen, J. Kauczor, S. Kirpekar, T. Kjærgaard, W. Klopper, S. Knecht, R. Kobayashi, H. Koch, J. Kongsted, A. Krapp, K. Kristensen, A. Ligabue, O. B. Lutnæs, J. I. Melo, K. V. Mikkelsen, R. H. Myhre, C. Neiss, C. B. Nielsen, P. Norman, J. Olsen, J. M. H. Olsen, A. Osted, M. J. Packer, F. Pawlowski, T. B. Pedersen, P. F. Provasi, S. Reine, Z. Rinkevicius, T. A. Ruden, K. Ruud, V. Rybkin, P. Salek, C. C. M. Samson, A. S. d. Merás, T. Saue, S. P. A. Sauer, B. Schimmelpfennig, K. Sneskov, A. H. Steindal, K. O. Sylvester-Hvid, P. R. Taylor, A. M. Teale, E. I. Tellgren, D. P. Tew, A. J. Thorvaldsen, L. Thøgersen, O. Vahtras, M. A. Watson, D. J. D. Wilson, M. Ziolkowski and H. Ågren, WIREs Comp. Mol. Sci. **4**, 269 (2014).
37. R. Dennington, T. Keith and J. Millam, (Semichem Inc., Shawnee Mission, KS, 2009).
38. A. D. Becke, J. Chem. Phys. **98**, 5648-5652 (1993).
39. H. Koch and P. Jørgensen, J. Chem. Phys. **93**, 3333-3344 (1990).
40. A. Osted, J. Kongsted and O. Christiansen, J. Phys. Chem. A **109**, 1430-1440 (2005).
41. E. Kassab and E. M. Evleth, in *The Role of Rydberg States in Spectroscopy and Photochemistry*, edited by C. Sándorfy (Kluwer Academic Publishers, Hingham, MA, USA, 1999), pp. 231.
42. M. Headgordon, J. A. Pople and M. J. Frisch, Chem. Phys. Lett. **153** (6), 503-506 (1988).
43. S. Deb, B. A. Bayes, M. P. Minitti and P. M. Weber, J. Phys. Chem. A **115** (10), 1804-1809 (2011).
44. E. Tannenbaum, E. M. Coffin and A. J. Harrison, J. Chem. Phys. **21**, 311 (1953).
45. M.-J. Hubin-Franskin, J. Delwiche, F. Tollet, M. Furlan and J. E. Collin, J. Phys. B: At. Mol. Opt. Phys. **21**, 189-202 (1988).
46. P. Avouris and A. R. Rossi, J. Phys. Chem. **85**, 2340-2344 (1981).
47. W. Cheng, N. Kuthirummal, J. L. Gosselin, T. I. Sølling, R. Weinkauf and P. M. Weber, J. Phys. Chem. A **109**, 1920-1925 (2005).
48. O. Schalk, A. E. Boguslavskiy and A. Stolow, J. Phys. Chem. A **114**, 4058-4064 (2010).
49. S. F. Nelsen, J. Org. Chem. **49**, 1891-1897 (1984).
50. D. H. Aue, H. M. Webb and M. T. Bowers, J. Am. Chem. Soc. **98**, 311 (1976).

51. I. Morishima, K. Yoshikawa, M. Hashimoto and K. Bekki, J. Am. Chem. Soc **97**, 4283-4288 (1975).
52. K. Watanabe and J. R. Mottl, J. Chem. Phys. **26**, 1773 (1957).
53. S. Katsumata, T. Iwai and K. Kimura, Bull. Chem. Soc. Jpn. **46**, 3391-3395 (1973).
54. K. L. Reid, Annu. Rev. Phys. Chem. **54**, 397-424 (2003).
55. T. Suzuki, Annu. Rev. Phys. Chem. **57**, 555-592 (2006).
56. J. O. F. Thompson, R. A. Livingstone and D. Townsend, J. Chem. Phys. **139**, 034316 (2013).
57. C. Z. Bisgaard, O. J. Clarkin, G. Wu, A. M. D. Lee, O. Gessner, C. C. Hayden and A. Stolow, Science **323**, 1464 (2009).
58. Y. Suzuki, T. Horio, T. Fuji and T. Suzuki, J. Chem. Phys. **134** (18), 184313 (2011).
59. H. Reisler and A. I. Krylov, Int. Rev. Phys. Chem. **28**, 267 (2009).
60. S. Gopalakrishnan, L. Zu and T. A. Miller, Chem. Phys. Lett. **380**, 749-757 (2003).
61. G. S. Beddard, G. R. Fleming, O. L. J. Gijzeman and G. Porter, Proc. R. Soc. Lond. A **340**, 519-533 (1974).
62. E. C. Lim and J. O. Uy, J. Chem. Phys. **56**, 3374 (1972).
63. M. H. Hui and S. A. Rice, Chem. Phys. Lett. **17**, 474 (1972).
64. M. Jeunehomme, J. Chem. Phys. **45**, 1805 (1966).
65. K. G. Spears and S. A. Rice, J. Chem. Phys. **55**, 5561-5581 (1971).
66. A. S. Abramson, K. G. Spears and S. A. Rice, J. Chem. Phys. **56**, 2291 (1972).
67. M. A. Elsayed, J. Chem. Phys. **38** (12), 2834 (1963).
68. M. Gruebele and R. Bigwood, Int. Rev. Phys. Chem. **17** (2), 91-145 (1998).
69. D. J. Nesbitt and R. W. Field, J. Phys. Chem. **100** (31), 12735-12756 (1996).
70. A. M. Halpern, J. L. Roebber and K. Weiss, J. Chem. Phys. **49** (3), 1348 (1968).

Chapter 7 – Conclusions, outlook & future work

7.1 – Investigation of model biological systems

Throughout this thesis, the discussion has followed a general theme; understanding energy redistribution in small, model chromophore systems found throughout nature. Through the use of a state-of-the-art velocity map imaging (VMI) spectrometer[1] and high quality quantum chemistry calculations, the work presented in this thesis highlights the importance of ultrafast, non-adiabatic coupling between electronic states, in the relaxation dynamics mechanisms in these model chromophore systems. This work, in tandem with work performed by a number of other groups both in the UK and internationally, explores possible explanations for the evolution of the photo-protective or photo-resistant properties of any molecules found in nature. Work in Chapter 5 highlights the importance of both gas-phase and liquid-phase measurements in providing a benchmark for a more detailed understanding of the effects of solvation upon the dynamics of molecular systems.[2] Chapter 6 highlighted the effects of geometry rearrangement in excited state species, as well as the sensitivity of the VMI technique to detect subtle changes in potential energy surfaces. Through the work on the aniline system presented in Chapters 3 and 4, both structure and energy specific dynamics have been identified, which provide further insight into the competition between alternative relaxation pathways.[3] Additionally, these chapters have all shown how the use of a position sensitive imaging technique can be used to investigate the electronic character of molecular excited states, by examination of the photoelectron angular distributions, in combination with time-resolved photoelectron spectra, to provide an insight into the processes occurring as a function of time.

This chapter will discuss possible avenues for future work, based upon the results described previously, and will follow similar themes to those already discussed, focusing on model chromophore systems. This discussion will, however, be limited to the development of gas-phase experiments, although the benefits of performing solution phase measurements have been identified previously in Chapter 5.

7.2 – Cyclohexenone, a model for mycosporine-like amino acids (MAAs)

Since the work of Domcke and co-workers[4, 5] in the late 1990s and early 2000s, research into the ultrafast relaxation pathways of model chromophore systems has expanded into a large field. The majority of this research investigates systems that contain aromatic components with an X-H substituent (such as an O-H, alcohol group, or N-H, amine group).[6, 7] These molecules include those described previously in this thesis such as guaiacol[2] and aniline[3], but also include systems such as pyrroles,[8-10] indoles,[11-14] imidazoles[15-18] and phenols.[19-22] This, however, does not exhaust the list of model chromophore systems that could be studied. An example of a molecular system that has yet to be investigated in detail is 2-cyclohexen-1-one. This molecule (as shown in Figure 7.1) contains a conjugated π system over its alkene and ketone functional groups and is a model chromophore for mycosporine-like amino acids (MMAs).[23] These have been implicated as the photo-protectors in microbial systems.[24] It should be noted that there are over 30 of these systems found in nature, all of which share a common structure. To highlight the structural similarities, a selection of MAA have been depicted in Figure 7.1,[25] alongside the model 2-cyclohexen-1-one chromophore. Interestingly, all these systems are heavily functionalised, however, there is no substitution on the 4th and 6th positions of the 6-member carbon ring.[23] This naturally leads to questioning why this specific structure is employed.

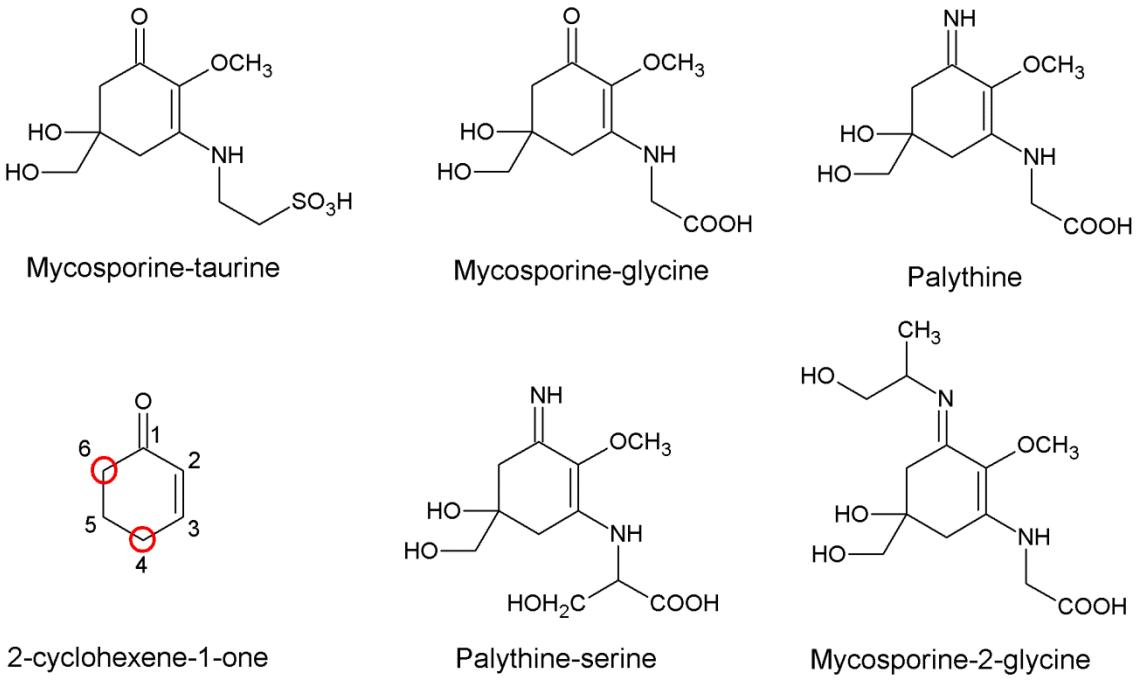

Figure 7.1 – Structures of a small subset of mycosporine-like amino acids and the model chromophore 2-cyclohexene-1-one. The positions around the cyclohexeneone structure have been marked for clarity. See text for further details.

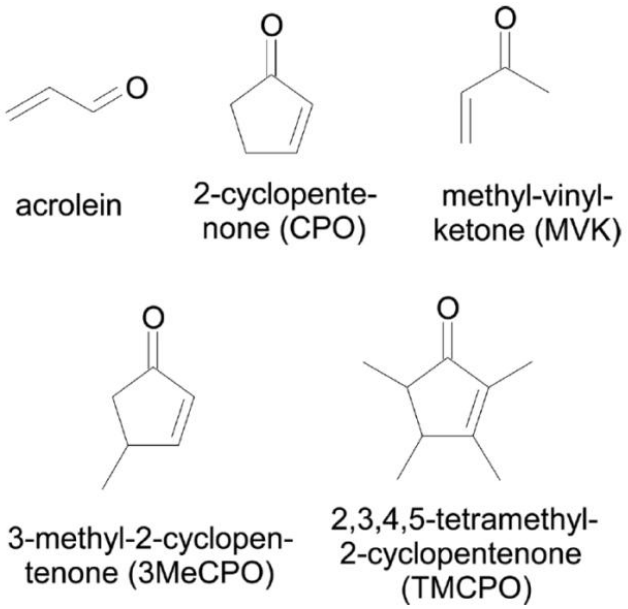

Figure 7.2 – Structures of the α,β-enone systems investigated by Stolow and co-workers[26]

Recent work by Stolow and co-workers[26] has investigated a series of α,β-enones using time-resolved photoelectron spectroscopy. These systems (shown in Figure 7.2) are structurally similar to that of 2-cyclohexen-1-one, the MMA chromophore. In this work, two possible channels for relaxation of the systems were identified after excitation to the lowest ππ* state. It was determined that both intersystem crossing and internal conversion were active mechanisms in all of the systems studied and, depending upon the structure of the enone, it was possible to influence the quantum yield of the different relaxation schemes.

Preliminarily experimental time-resolved photoelectron imaging experiments of 2-cyclohexen-1-one (and a number of methylated cyclohexenone systems) were undertaken during the course of my thesis work. Figure 7.3 shows the structure of 2-cyclohexen-1-one, 4,4-dimethyl-2-cyclohexen-1-one and 5,5,3-trimethyl-2-cyclohexen-1-one (henceforth as abbreviated to chx, 44-chx and 553-chx respectively), which were used to investigate the relaxation dynamics of the model chromophore of mycrosporine-like amino acids. This method of selective methylation to investigate the effects of slowing down specific vibrational and rotational motion has been presented before in Chapter 6. In which, it was shown that the methylation did not significantly affect the spacing between the excited state energy levels in aniline, when compared to *N*,*N*-dimethylaniline & 3,5-dimethylaniline. Theoretical calculations on these model

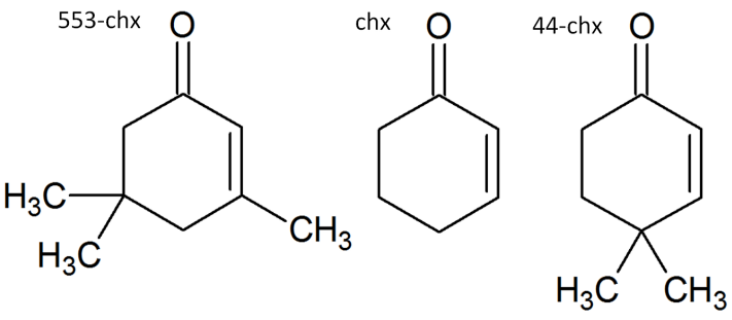

Figure 7.3 – Structure of 5,5,3-trimethyl-2-cyclohexen-1-one (553-chx), 2-cyclohexen-1-one (chx) and 4,4-dimethyl-2-cyclohexen-1-one (44-chx)

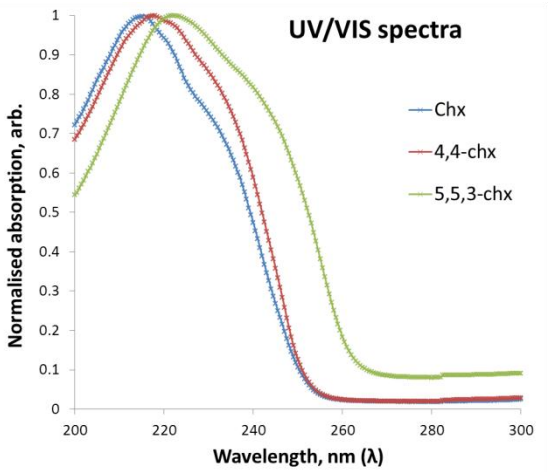

Figure 7.4 – Normalised UV/VIS vapour phase spectra of chx, 44-chx & 553-chx between 200 – 300 nm.

chromophore systems found that upon methylation, the spacing between the S_2 and S_1 states barely changed. This suggests that any change in the observed timescales of the relaxation dynamics of the systems is purely a dynamical effect. To verify the results of the calculations, vapour phase UV/VIS spectra of chx, 44-chx and 553-chx were recorded using a Shimadzu UV-2550 spectrometer. The experimental procedure was performed in the same manner as what was described previously in Section 4.2.1. Figure 7.4 presents the UV/VIS absorption spectra of the three model chromophores. As seen from the spectra although there is slight red shift of the 5,5,3-chx spectrum, the spectra all seem to peak around the same wavelength. Figure 7.5 presents the time-resolved photoelectron spectra of these systems obtained following excitation at 220 nm and subsequent ionisation using a 267 nm pulse (in a [1+1′] REMPI scheme), attained via the set-up described in great detail previously in this thesis (using beam lines 1 & 3 to generate the pump and probe light, respectively). These spectra are plotted as a function of kinetic energy and calibrated using a 1,3-butadiene image. The time axis of this data is plotted on a mixed linear-logarithmic scale, in which linear steps were taken from 500 fs to +1000 fs, in 50 fs increments, followed by 17 exponential steps, were taken up to 100 ps. It is clear to see in all the spectra that at shorter time delays there is a large, broad photoelectron signal spanning the region from 0 – 1.2 eV. This is attributed to signal arising from direct excitation to the optically bright ππ* state. In the longer time range, there is a very small amplitude signal in the low energy region of the spectra. This is attributed to populating a lower-lying nπ* state by internal conversion from the ππ* state, a similar observation to that reported previously by Stolow and co-workers.[26] The feature is too weak to produce a meaningful lifetime for this long-term dynamic effect (as shown in Figure 7.6), however, the fits have pulled out time constants for the initial process of <100 fs, <100 fs and 140 fs for chx, 553-chx and 44-chx respectively. As such, in order to fully investigate these molecules, a higher energy photon probe (i.e. > 267 nm) is required to interrogate the system, to investigate the dynamics of the molecules further along the reaction co-ordinate more effectively. This could be achieved using a VUV photon as the probe, which will be discussed in more detail later

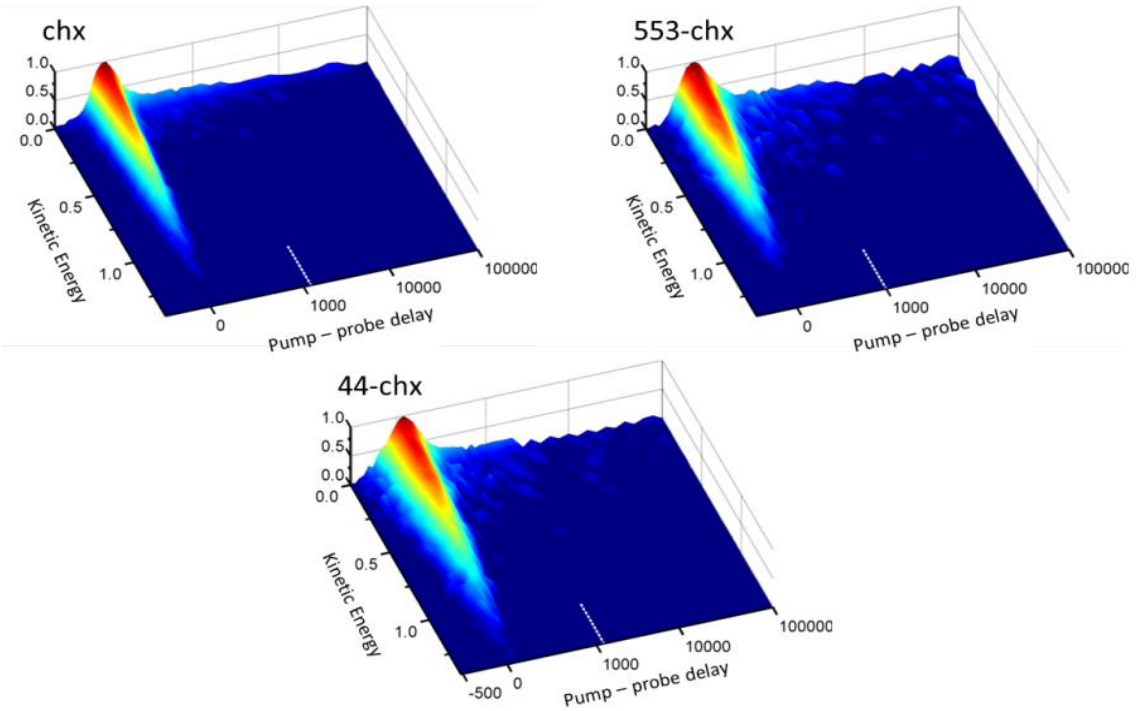

Figure 7.5 – Time resolved photoelectron spectra of 2-cyclohexen-1-one (chx), 5,5,3-trimethyl-2-cyclohexen-1-one (553-chx) and 4,4-dimethyl-2-cyclohexen-1-one (44-chx). The spectra are plotted in kinetic energy with bins of 0.05 eV. The pump probe delay axis is plotted as a lin/log scale with -500 to 1000 fs plotted linearly in 50 fs steps and the region between 1000 fs and 100 ps plotted as a logarithmic scale.

in this chapter. Based upon the time constants identified in the fits, all these molecules show very similar behaviour and that methyl substitution has had no effect on the dynamics of these systems, however, it should be pointed out that, due to availability of the chemical, any experiments on substituted 6th position have yet to be performed, which could yet prove critical in influencing the relaxation lifetime of these systems. The notion that the 6th position maybe a critical co-ordinate is also supported by additional theoretical work has also been performed by the group.[27] In which, complete active space self-consistent field (CASSCF) calculations were performed on the 2-cyclohexen-1-one system to identify the branching space vectors to acsess the ππ*/nπ* conical intersection. These calculations identified that motion around the 4th position on the ring was indeed not ciritical, however, large motion around the 6th position of the ring was identified as being important as to allowing population transfer between the ππ*/nπ*, via a concial intersection

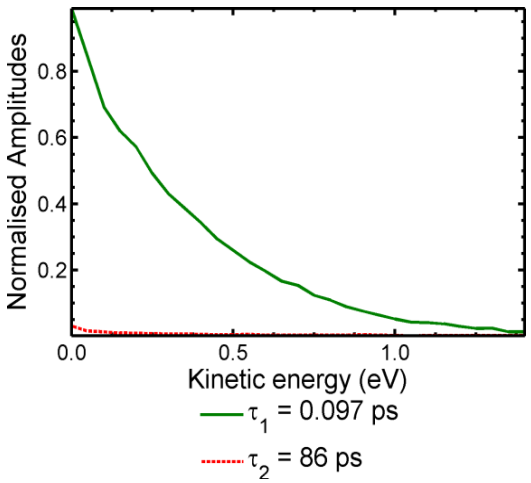

Figure 7.6 – Decay associated spectra of 2-cyclohexen-1-one (chx)

7.3 – Laser induced acoustic desorption

A key motivation for the work in this thesis, as described in Chapter 1, is to attain an understanding of model chromophore species in order to comprehend the photo-protection mechanism and photo-resistivity of natural systems to ultraviolet light. However, to investigate larger, more complex systems, it is necessary to start systematically adding on additional functional groups, so as to accurately simulate the true chromophore. However, these larger systems are often difficult to investigate utilising gas phase spectroscopy.

Gas-phase spectroscopy provides an excellent starting platform to investigate and understand the ultrafast molecular dynamics of model chromophore species. The use of a supersonically expanded molecular beam to produce cooled molecules in the gas phase provides many advantages in simplifying the spectroscopy, by reducing the likelihood of spectral hot bands and removing intermolecular interactions. Additionally, gas-phase techniques allow highly differential measurements to be performed that are very sensitive to subtle dynamical effects. However, the effectiveness of this technique is limited by the vapour pressure of the target species. For example, the molecules studied for this thesis have a vapour pressure in the region of 0.01 – 10 mbar at room temperature, which is ample to produce a highly concentrated molecular beam for the VMI experiment. However, larger, more complex chromophore species often have much lower vapour pressures than their smaller, simpler counterparts. As such, performing experiments on these systems is challenging as, due to the reduction in sample density, imaging experiments can be difficult to perform reliably as the signal-to-noise ratio becomes unfavourable. Many of these systems are unsuitable for techniques such as laser ablation or oven heating to improve the sample density as the system may fragment. There are techniques that exist at present which seek to overcome this issue, for example electrospray ionisation. Electrospray ionisation produces charged gas phase species,[28] which is of limited use for our specific application. This being said however, electrospray ionisation has been successfully employed by others to investigate similar molecular systems as discussed in this thesis.[29, 30] MALDI (matrix assisted laser desorption/ionisation), is a technique in which the target is initially crystallised on a suspended matrix of solvent and then ablated with a laser to produce a gas-phase plume of molecules.[31] The target molecule is cooled as thermal energy is transferred from the sample to the surrounding matrix as the ablation occurs. However, the plume produced contains not only the target system, but other

molecules from the matrix and, as such, means that photoelectron studies become impractical.

For these reasons, a strategy for "soft" desorption is required to allow gas-phase measurements on larger neutral systems without need of a solvent. A promising technique for driving these systems into the gas phase is LIAD (laser induced acoustic desorption).[32-36] LIAD produces a plume of gas phase molecules similar to that of traditional desorption techniques. Instead of directly targeting the sample, however, the desorption laser irradiates the back of a foil on which the sample is prepared. It was originally thought that this irradiation induces an acoustic wave that travels through the foil, resulting in some of the sample being "shaken off" into the gas phase. However, it has also been suggested that this may not be the case and that the mechanism could be explained though a localised heating model as opposed to an acoustic wave propagation.[37] Even though the exact mechanism of the process is not completely understood and requires more rigorous investigation; the technique shows great promise in allowing gas-phase experiments to be performed on low vapour pressure systems. Once in the gas phase, the molecules can then either be picked up by a carrier gas and delivered to an interaction region, or be interrogated next to the site of desorption. Figure 7.7 provides a simple schematic of the LIAD process. LIAD has some key advantages over other techniques which produce molecular sources of larger low vapour systems, as the molecular plume is, in principle, free of contaminants. However, this process is not yet well understood, with factors such as the effects of foil thickness, laser power and wavelength, and foil material needing further investigation before the technique can be fully exploited.

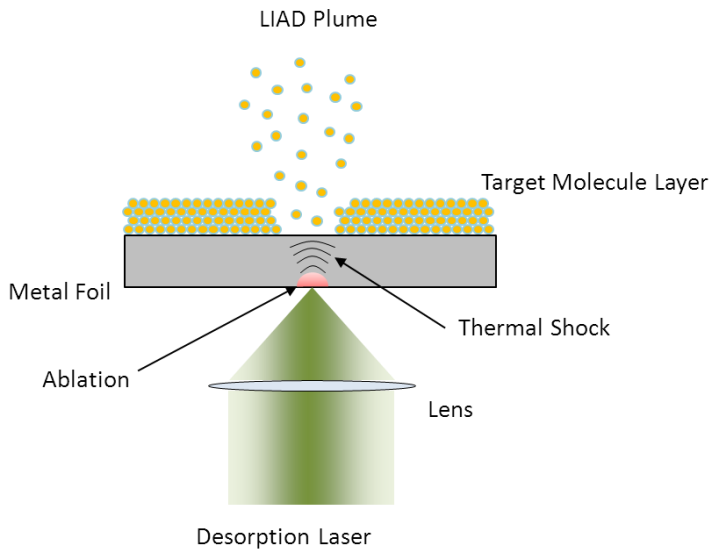

Figure 7.7 – Cartoon schematic of LIAD

Incorporating the LIAD technique in to the existing experimental set up, as discussed in Chapter 2, could be achieved in one of two ways. The first is to employ a LIAD source in the method used by Greenwood and co-workers,[38, 39] in which the metal foil is placed

directly behind the interaction region of the photo-ion spectrometer. This maximises the effective density of the molecules in the interaction region by sampling the entire plume. However, the method provides no additional cooling to the sample, which may lead to the potential complication of hot-bands within the photoelectron spectrum. The second disadvantage with this method is the proximity to the detector. In this setup, the VMI optics and MCP detector would have to be positioned in the same chamber as the metal foil, meaning that the turn-around time for sample changing would increase. Furthermore, it may not be possible to bake the vacuum chamber as this may lead to the sample being driven away. The second method of employing the LIAD source would be to integrate it into the current molecular beam setup through coupling it with the Even-Lavie (EL) valve.[40] This could be achieved, for example, using a flow pick-up just after leaving the valve in the initial expansion with the LIAD laser delivered into the vacuum chamber via a optical fibre. A schematic of this set-up is shown in Figure 7.8.

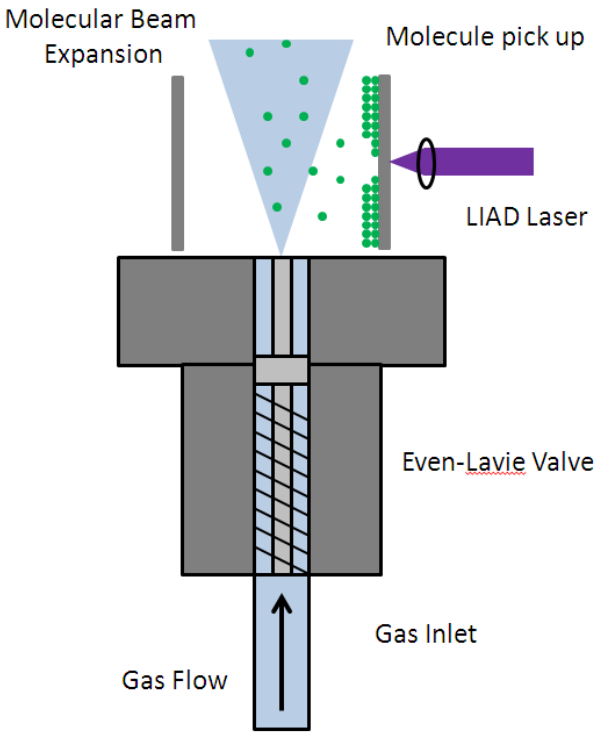

Figure 7.8 –schematic of pick up mechanism for integrating LIAD into current experimental set-up.

7.4 – Vacuum ultraviolet light source

The true aim of a time-resolved dynamical study is to follow the reaction from the initial excitation step through to the final products being formed. With reference to the model chromophores presented in this thesis, photochemical reactions can conclude with the recovery of the ground state after all relaxation mechanisms have taken their course. However, if a state is prepared with a set of highly excited vibrational modes then the system will in principle preferentially ionise to a highly excited set of vibrational modes in the cation (assuming a high propensity for diagonal ionisation). Thus, for effective ionisation to occur, these vibrational levels need to be accessible by the energy provided by the probe UV laser light. Consider a wavepacket that has non-adiabatically travelled to another excited state surface, through some intersystem crossing mechanism or conical intersection (as described in Chapter 1). As the energy within the system must be conserved, any lower energy electronic state accessed through non-adiabatic coupling must be prepared with a combination of more excited vibrational modes. As such, depending upon the probe laser energy provided, the experiment may be effectively blind to this new state as the Franck-Condon overlap with the cation may become unfavourable. Figure 7.9 illustrates the role of the Franck-Condon principle in relation to the ionisation cross-section along some generalised reaction co-ordinate. This figure illustrates that as the relaxation of the system progresses, a single photon of the probe pulse is unable to efficiently ionise the wavepacket in the S_1 state, however, two photons of the probe pulse, or a single photon of VUV

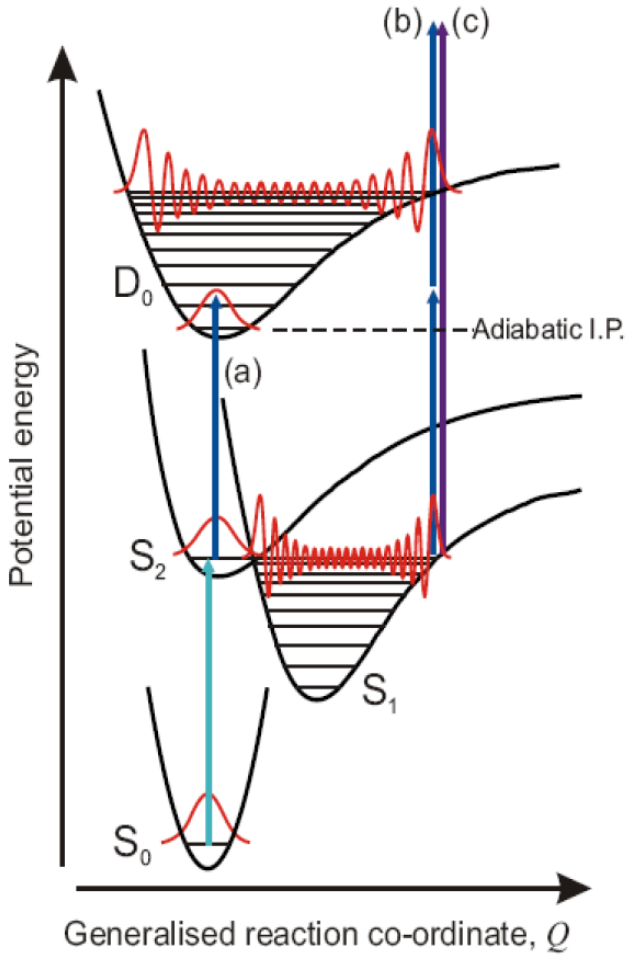

Figure 7.9 – llustration of the Franck-Condon principle in photoelectron spectroscopy. Schematic vibrational wavefunctions are shown in red. For instructive simplicity, a stationary state representation is used in place of a wavepacket picture.

light can ionise the highly vibrationally excited S_1 state, therefore allowing observation of its dynamics. A [1+2′] experiment performed by Stolow and Townsend (unpublished) on 1,3–butadiene may be used to demonstrate what insight can be gained. The results are seen in Figure 7.10. Through the use of a two photon probe it was possible to interrogate the system as it relaxed from the S_1 state into the lower-lying S_0 electronic state and, in doing so, acquire more information about the relaxation mechanism of the molecule. There are, however, complications with the use of a multiphoton probe scheme. Firstly, there is a risk that the dynamics observed are influenced by an intermediate state accessed by the first probe photon. Additionally, a two photon ionisation process adds further complexity in the deconvolution of the photoelectron data, as the signal from the [1+1′] and [1+2′] may not be spectrally separated. Furthermore, the cross correlation for the [1+2′] process would be different to the [1+1′], meaning that the temporal response of the two processes would differ. Finally, an additional photon adds an extra layer of complexity to fitting the anisotropy parameters. In a three photon process, as well as determining the values of β_2 and β_4, the value of β_6 would also have to be included in the fitting. Evidently, to see further potential dynamics as the system relaxes, without any of the other drawbacks discussed, a higher energy probe is required. This can be achieved through the use of vacuum ultraviolet light (VUV).

Vacuum ultraviolet light is a form of ultraviolet radiation that cannot propagate in normal atmospheric conditions, due to it propensity to be absorbed by N_2 and O_2 (typically 200 – 10 nm). The generation, propagation, and diagnostics of the VUV light must therefore be performed under vacuum conditions. Noack and co-workers have demonstrated the ability to produce femtosecond VUV light through the use of a four-wave frequency mixing process using a gas cell filled with argon.[41-43] The technique requires the combination of two photons of 267 nm and one photon of 800 nm to generate 160 nm light in the gas cell. A VUV system attached to the setup described in

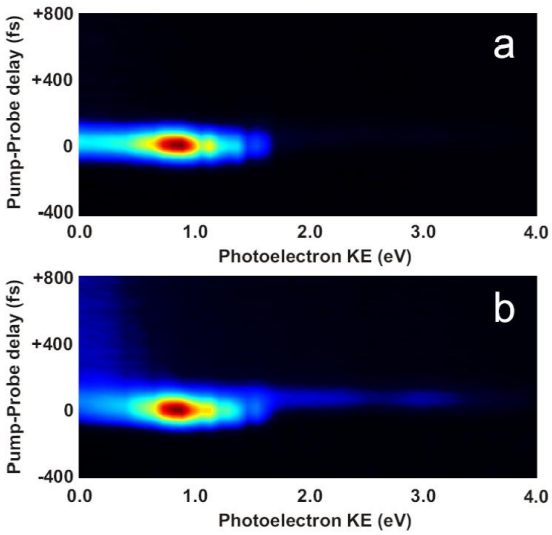

Figure 7.10 – Time-resolved photoelectron spectra of 1,3-butadiene. a) displays data resulting from [1+1′] ionisation whilst b) shows data acquired with both [1+1′] and [1+2′] ionisation

Chapter 2, would allow the TRPEI experiment to reveal further insights into the relaxation dynamics of the model chromophore systems. Such a system is currently under development in our group. Figure 7.11 shows an AutoCAD image of the vaccum chamber used to generate the VUV light, which is directly atatched onto the side of the TRPEI vacuum chamber described in Chapter 2. The chamber also contains all the required diagnostic tools such as power meter, spectrometer and alignment targets to control and maintain the VUV light generated in vacuum, all of which are positioned on motarised mounts. Once produced, the VUV would be sent into the VMI chamber with an additional of co-propagating UV beam to perform experiments similar to those discussed in this thesis.

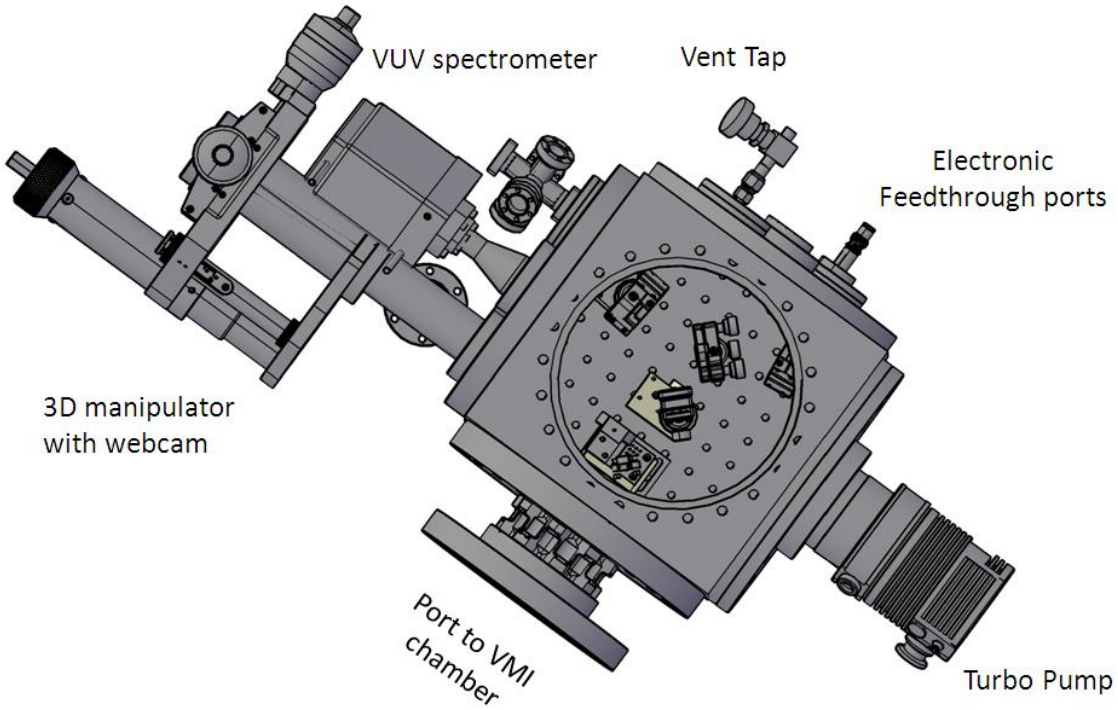

Figure 7.10 – AutoCAD design of VUV vacuum chamber. The window port on the top of the chamber has been made transparent to view the optomechanics inside. Figure courtesy of Dr M. Candelaresi

7.5 – Concluding remarks

The aim of this thesis has been to provide an overview and detailed discussion of work I have performed over the last three years. Throughout the work conducted for this thesis, a number of experiments have been undertaken to understand the relaxation mechanisms of numerous model chromophore systems. As discussed in Chapter 1, these model systems are used to provide a "bottom-up" understanding of a wide range of larger biological chromophores. They are used to give support to the theory that natural systems are designed to be capable of ultrafast internal energy relaxation, as a way to make these systems inherently UV resistant. Although, this being said, there is still a long way to go in reaching definitive conclusions in the full bio-systems.

The experiments discussed in Chapters 3 through 6 all take advantage of both the energy and angle-resolved information obtained through the use of a velocity map imaging spectrometer. Time-resolved photoelectron imaging was used to investigate various dynamical processes involving non-adiabatic coupling between electronic states and IVR through interrogation of the lifetime of photoelectron signals and the evolution of photoelectron angular distributions. Finally, this chapter has suggested improvements to the set-up and techniques described in Chapter 2 and possible molecules for future experiments.

7.6 - References

1. R. A. Livingstone, J. O. Thompson, M. Iljina, R. J. Donaldson, B. J. Sussman, M. J. Paterson and D. Townsend, J. Chem. Phys. **137** (18), 184304 (2012).
2. S. E. Greenough, M. D. Horbury, J. O. Thompson, G. M. Roberts, T. N. Karsili, B. Marchetti, D. Townsend and V. G. Stavros, Phys. Chem. Chem. Phys. **16** (30), 16187-16195 (2014).
3. J. O. F. Thompson, R. A. Livingstone and D. Townsend, J. Chem. Phys. **139** (3), 034316 (2013).
4. A. L. Sobolewski, W. Domcke, C. Dedonder-Lardeux and C. Jouvet, Phys. Chem. Chem. Phys. **4** (7), 1093-1100 (2002).
5. A. L. Sobolewski and W. Domcke, Chem. Phys. Lett. **315** (3-4), 293-298 (1999).
6. G. M. Roberts and V. G. Stavros, Chem. Sci. **5** (5), 1698-1722 (2014).
7. M. N. Ashfold, G. A. King, D. Murdock, M. G. Nix, T. A. Oliver and A. G. Sage, Phys. Chem. Chem. Phys. **12** (6), 1218-1238 (2010).
8. M. N. Ashfold, B. Cronin, A. L. Devine, R. N. Dixon and M. G. Nix, Science **312** (5780), 1637-1640 (2006).
9. M. Barbatti, M. Vazdar, A. J. Aquino, M. Eckert-Maksic and H. Lischka, J. Chem. Phys. **125** (16), 164323 (2006).
10. R. Montero, A. Peralta Conde, V. Ovejas, M. Fernandez-Fernandez, F. Castano, J. R. Vazquez de Aldana and A. Longarte, J. Chem. Phys. **137** (6), 064317 (2012).
11. R. Livingstone, O. Schalk, A. E. Boguslavskiy, G. Wu, L. T. Bergendahl, A. Stolow, M. J. Paterson and D. Townsend, J. Chem. Phys. **135** (19) (2011).
12. M. G. Nix, A. L. Devine, B. Cronin and M. N. Ashfold, Phys. Chem. Chem. Phys. **8** (22), 2610-2618 (2006).
13. A. Iqbal and V. G. Stavros, J. Phys. Chem. A **114** (1), 68-72 (2010).
14. R. Montero, A. P. Conde, V. Ovejas, F. Castano and A. Longarte, J. Phys. Chem. A. **116** (11), 2698-2703 (2012).
15. A. L. Devine, B. Cronin, M. G. Nix and M. N. Ashfold, J. Chem. Phys. **125** (18), 184302 (2006).
16. D. J. Hadden, K. L. Wells, G. M. Roberts, L. T. Bergendahl, M. J. Paterson and V. G. Stavros, Phys. Chem. Chem. Phys. **13** (21), 10342-10349 (2011).
17. R. Crespo-Otero, M. Barbatti, H. Yu, N. L. Evans and S. Ullrich, Chemphyschem **12** (17), 3365-3375 (2011).
18. R. Montero, A. Peralta Conde, V. Ovejas, M. Fernandez-Fernandez, F. Castano and A. Longarte, J. Phys. Chem. A. **116** (44), 10752-10758 (2012).
19. M. G. Nix, A. L. Devine, B. Cronin, R. N. Dixon and M. N. Ashfold, J. Chem. Phys. **125** (13), 133318 (2006).
20. G. M. Roberts, A. S. Chatterley, J. D. Young and V. G. Stavros, J. Phys. Chem. Lett. **3** (3), 348-352 (2012).
21. M. L. Hause, Y. Heidi Yoon, A. S. Case and F. F. Crim, J. Chem. Phys. **128** (10), 104307 (2008).
22. T. N. V. Karsili, A. M. Wenge, B. Marchetti and M. N. R. Ashfold, Phys. Chem. Chem. Phys. **16** (2), 588-598 (2014).
23. K. H. Cardozo, T. Guaratini, M. P. Barros, V. R. Falcao, A. P. Tonon, N. P. Lopes, S. Campos, M. A. Torres, A. O. Souza, P. Colepicolo and E. Pinto, Comp. Biochem. Physiol. C. Toxicol. Pharmacol. **146** (1-2), 60-78 (2007).
24. T. Rezanka, M. Temina, A. G. Tolstikov and V. M. Dembitsky, Folia Microbiol (Praha) **49** (4), 339-352 (2004).
25. S. P. Singh, S. Kumari, R. P. Rastogi, K. L. Singh and R. P. Sinha, Indian. J. Exp. Biology. **46** (1), 7-17 (2008).

26. O. Schalk, M. S. Schuurman, G. Wu, P. Lang, M. Mucke, R. Feifel and A. Stolow, J. Phys. Chem. A **118** (12), 2279-2287 (2014).
27. E. Burgess, Private communications, edited by J. O. Thompson (2015).
28. J. B. Fenn, M. Mann, C. K. Meng, S. F. Wong and C. M. Whitehouse, Science **246** (4926), 64-71 (1989).
29. J. Lecointre, G. M. Roberts, D. A. Horke and J. R. R. Verlet, J. Phys. Chem. A. **114** (42), 11216-11224 (2010).
30. D. A. Horke and J. R. R. Verlet, Phys. Chem. Chem. Phys. **13** (43), 19546-19552 (2011).
31. M. Karas, D. Bachmann and F. Hillenkamp, Anal. Chem. **57** (14), 2935-2939 (1985).
32. V. V. Golovlev, S. L. Allman, W. R. Garrett and C. H. Chen, App. Phys. Lett. **71** (6), 852-854 (1997).
33. V. V. Golovlev, S. L. Allman, W. R. Garrett, N. I. Taranenko and C. H. Chen, Int. J. Mass. Spec. **169**, 69-78 (1997).
34. R. C. Shea, C. J. Petzold, J. A. Liu and H. I. Kenttamaa, Anal. Chem. **79** (5), 1825-1832 (2007).
35. J. Perez, L. E. Ramirez-Arizmendi, C. J. Petzold, L. P. Guler, E. D. Nelson and H. I. Kenttamaa, Int. J. Mass. Spectrom. **198** (3), 173-188 (2000).
36. I. Bald, I. Dabkowska and E. Illenberger, Angew. Chem. Int. Ed. Engl. **47** (44), 8518-8520 (2008).
37. A. Zinovev, I. Veryovkin and M. Pellin, in *Acoustic Waves - From Microdevices to Helioseismology*, edited by M. G. Beghi (InTech, 2011), Vol. 1, pp. 343-368.
38. C. R. Calvert, O. Kelly, M. J. Duffy, L. Belshaw, R. B. King, I. D. Williams and J. B. Greenwood, J. Phys. Conf. Ser. **388** (2012).
39. C. R. Calvert, L. Belshaw, M. J. Duffy, O. Kelly, R. B. King, A. G. Smyth, T. J. Kelly, J. T. Costello, D. J. Timson, W. A. Bryan, T. Kierspel, P. Rice, I. C. Turcu, C. M. Cacho, E. Springate, I. D. Williams and J. B. Greenwood, Phys. Chem. Chem. Phys. **14** (18), 6289-6297 (2012).
40. U. Even, J. Jortner, D. Noy, N. Lavie and C. Cossart-Magos, J. Chem. Phys. **112** (18), 8068-8071 (2000).
41. M. Beutler, M. Ghotbi and F. Noack, Opt. Lett. **36** (19), 3726-3728 (2011).
42. M. Beutler, M. Ghotbi, F. Noack and I. V. Hertel, Opt. Lett. **35** (9), 1491-1493 (2010).
43. M. Ghotbi, M. Beutler and F. Noack, Opt. Lett. **35** (20), 3492-3494 (2010).